DEVELOPMENT OF X-RAY & NEUTRON MICRO-IMAGING TECHNIQUES AND THEIR APPLICATIONS IN MATERIAL SCIENCE

By

ASHISH KUMAR AGRAWAL

PHYS01201004002

Bhabha Atomic Research Centre, Mumbai, India

A thesis submitted to the

Board of studies in Physical Sciences

In the partial fulfilment of requirements

For the Degree of

DOCTOR OF PHILOSOPHY

of

HOMI BHABHA NATIONAL INSTITUTE

April 2017

STATEMENT BY AUTHOR

This dissertation has been submitted in partial fulfilment of requirement for an advanced degree at Homi Bhabha National Institute (HBNI) and is deposited in the library to be made available to borrowers under rules of HBNI.

Brief quotations from this dissertation are allowable without special permission, provided that accurate acknowledgement of source is made. Request for permission for extended quotation from or reproduction of this manuscript in whole or part may be granted by Competent Authority of HBNI when in his or her judgement the proposed use of the material is in the interest of scholarship. In all other instances, permission must be obtained from the author.

Signature

Ashish Kumar Agrawal

DECLARATION

I, hereby declare that the investigation presented in the thesis has been carried out by me. The work is original and has not been submitted as a whole or in part for a degree/diploma at this or any other Institution/University.

Signature

Ashish Kumar Agrawal

List of publications arising from the thesis

Journal

1. "Application of X-ray micro-CT for micro-structural characterisation of APCVD deposited SiC coatings on graphite conduit", A.K. Agrawal, P.S. Sarkar, B. Singh, Y.S. Kashyap, P.T. Rao, A. Sinha, App. Rad. & Isotopes; **2016**,108,133-142.
2. "Application of X-ray CT for non-destructive characterization of graphite fuel-tube", A. K. Agrawal, P.S. Sarkar, Y.S. Kashyap, B. Singh, A. Sharma, R. Kumar, A. Sinha, J Non-destruct Eval., **2016**, 35:36.
3. "Design, development and first experiments on the X-ray Imaging Beamline at Indus-2 synchrotron source RRCAT, India", A. K. Agrawal, B. Singh, Y.S. Kashyap, M. Shukla, P. S. Sarkar, A.Sinha; J. Synchrotron Rad. **2015**, 22,1531–1539.
4. "Micro-structural Characterization of Materials Using Synchrotron Hard X-ray Imaging Techniques", Ashish Kumar Agrawal, Balwant Singh, Yogesh Kashyap, P S Sarkar, Mayank Shukla, Amar Sinha, AIP conference proceeding **2015**,1665,060020
5. "Application of atmospheric CVD for internal surface coating of graphite conduit by Silicon carbide", P. T. Rao, U. Jain, P.K. Mollick, A. Agrawal, J.K. Chakrabortty, Sanjay Kumar, Journal of nuclear materials, **2015** 456, 200-205.
6. "Visualization of Lead Melting and Solidification using Neutron Radiography", Partha Sarkar, Ashish Agrawal, Y. Kashyap, M. Shukla, A.Sinha, Lokendra Kumar, B. S. Manjunath, S. V. Prabhu, S.G. Markandeya, Int. J. of Nucl. Energy Sci. and Eng., **2013**, 3(1), 7-14.
7. "Neutron imaging experiments at E-12 beam-line of CIRUS"; Ashish Agrawal, Yogesh Kashyap, Mayank Shukla, P. S. Sarkar, and Amar Sinha; AIP Conf. Proc. **2013,**1512, 482-483.
8. "Development of neutron tomography and PCI technique"; Y. S. Kashyap; Ashish Agrawal, P. S. Sarkar, Mayank Shukla, and Amar Sinha; AIP Conf. Proc. **2013**,1512, 452-453.
9. "Neutron PCI beamline at CIRUS, reactor India", Yogesh S. Kashyap, Ashish Agrawal, P. S. Sarkar, Mayank Shukla, Tushar Roy, Amar Sinha, App. Rad.& Isotopes, **2012**,70, 625-631.

10. “Study of Hydride blisters in Zr-alloy using Neutron tomography”, Ashish Agrawal, Yogesh Kashyap, P. S. Sarkar, A. N. Behra, M. Shukla, R. N. Singh, Amar Sinha, J. K. Chakravartty, Journal of Nuclear materials, **2012**, 421,47-53.
11. “Experimental Investigations on Melting of Lead in a cuboid with constant heat flux boundary condition using thermal neutron radiography”, Lokendra Kumar, B.S. Manjunath, R.J. Patel, S. G. Markandeya, R.G. Agarwal, Ashish Agrawal, Y. Kashyap, P. S. Sarkar, Amar Sinha, Kannan Iyer, S.V. Prabhu; Int. Jour. of Thermal Sciences, **2012**, 61,15–27.
12. “Study of pyro-carbon coated alumina kernel using mixed contrast transfer based phase retrieval technique”, Y. S. Kashyap, Ashish Agrawal, P. S. Sarkar, Mayank Shukla, Tushar Roy, Amar Sinha, NDT & E International, **2011**, 44, 41-46.
13. “A variable wavelength based approach of phase retrieval for contrast transfer function based methods” Yogesh Kashyap, Ashish Agrawal, P.S. Sarkar, Mayank Shukla, Tushar Roy and Amar Sinha, J. Synchrotron Rad. , **2010**, 17, 799-803.
14. “High Resolution X-ray Microscopy for Nano-Resolution Imaging; Y. S. Kashyap”, Ashish Agrawal, P. S. Sarkar, Mayank Shukla T. Roy and Amar Sinha, AIP conference proceedings, **2010**,149, 1313.

Conference Presentations

1. Diffraction Enhance X-ray Imaging for Quantitative Phase Contrast Studies; A.K. Agrawal, B. Singh, Y.S. Kashyap, M. Shukla, P. S. Sarkar, Amar Sinha SSPS 2016.
2. Observation of de-cohesion damage in Aluminium Metal Matrix Composite at INDUS-2 Imaging beamline using Micro-Tomography; Chiradeep Gupta, Ashish K Agarwal, Balwant Singh, P.S. Sarkar, Amar Sinha, J. K. Chakravartty; NMD ATM Pune, Nov 2014.
3. Phase Imaging with polychromatic Neutrons; Yogesh Kashyap, Ashish Agrawal, P. S. Sarkar, Mayank Shukla and Amar Sinha; International Symposium on Neutron Scattering, January 14-17,2013
4. Compressibility and PCI of γ irradiated polyurethane foam blocks; Y. Naik, S.G. Kulkarni, B.S. Manjunath, R.J, Patel, A.K. Agrawal, Y. Kashyap and A. Sinha; NSRP 2013, march 20-22 Shillong, India.
5. Development of synchrotron source based X-ray imaging facility at RRCAT, India; Yogesh Kashyap, Ashish Agrawal, Mayank Shukla, Balwant

Singh, P.S. Sarkar, Tushar Roy and Amar Sinha; National symposium on Non Destructive Evaluation-2012,December 10 to 13, 2012.

6. Development of Neutron Imaging Beam Line for NDT applications; Mayank Shukla, Yogesh Kashyap, Ashish Agrawal and Amar Sinha; National symposium on Non Destructive Evaluation-2012, December 10 to 13, 2012
7. Experimental and Numerical Investigations on Lead Melting; Lokendra Kumar, B.S. Manjunath, R.J. Patel, S.G. Markandeya, R.G. Agrawal, Ashish Agrawal, Y. Kashyap, P.S. Sarkar, Amar Sinha, K.N. Iyer and S.V. Prabhu; International Congress on Computational Mechanics and Simulation (ICCMS), IIT Hyderabad, 10-12 December 2012
8. Development of Neutron tomography and its applications in Non-destructive analysis; Ashish Agrawal, Yogesh Kashyap, P.S. Sarkar, A.N. Behra, Mayank Shukla, R.N. Singh, Amar Sinha and J.K. chakravartty; NDE-2011, December 8-10, 2011 at Chennai.
9. Development of neutron phase contrast-imaging technique at CIRUS reactor, India; Yogesh Kashyap, Ashish Agrawal, Mayank Shukla, P.S. Sarkar, Tushar Roy and Amar Sinha; NDE-2011, December 8-10, 2011 at Chennai.
10. Neutron PCI, Yogesh S. Kashyap, Ashish Agrawal, Mayank Shukla, P. S. Sarkar, Tushar Roy, and Amar Sinha; DAE SSPS 2011.

Signature

Ashish Kumar Agrawal

In the memory of my father,

who taught me science, mathematics, social science

and many lessons of life

And, inspired me to take physics a major for study

I dedicate this thesis to everyone in my family, whose support, affection, prays and love of day and night made me able to complete this thesis successfully.

ACKNOWLEDGEMENTS

It is a great pleasure to express deep sense of gratitude and sincere thanks to my research guide, Dr. Amar Sinha, RRF & former Head, NXPD, for his constant support, valuable guidance, constant encouragement and valuable suggestions throughout my research tenure. I am also grateful to all the members of doctoral committee for their valuable suggestions and review of progress time to time.

It gives me immense pleasure to express my gratitude to Dr. Mayank Shukla, Dr. P.S. Sarkar and Dr. Yogesh Kashyap for providing their continuous guidance in the course of this research work. I also thank my colleagues Shri Balwant Singh and Ms. Anis Fatima for the valuable discussions during the preparation of this thesis. I also wish to express heart filled thanks to all my colleagues from NXPD for providing constructive suggestions throughout this work. I also acknowledge the cooperation extended to me by colleagues from other divisions by providing their valuable sample for study in my research activities.

I wish to express my sincere gratitude and indebtedness to my late father Shri G.S. Agrawal for his blessings, teachings, guidance and support. I also wish to express my deepest thanks to my mother, wife and sisters for their love, support, patience and understanding. I am extremely thankful to my loving daughter Yashshwi for her love and delightful smile which is a great source of energy in my life. Last but not the least, I also wish to thank God almighty, all my friends and everyone whom I might have forgotten to mention for their constant and unconditional support.

Ashish Kumar Agrawal

CONTENTS

SYNOPSIS 12

LIST OF TABLES 20

LIST OF FIGURES 21

LIST OF ABBREVIATIONS 27

1 INTRODUCTION 28

1.1 MOTIVATION 28

1.2 HIGHLIGHTS OF THE THESIS 30

1.3 OVERVIEW OF MICRO-IMAGING TECHNIQUES 32

1.3.1 Absorption contrast imaging 33

1.3.2 Phase contrast imaging 34

1.3.3 Tomography 38

1.4 MECHANISM OF CONTRAST GENERATION 41

1.5 EFFECTS OF EXPERIMENTAL PARAMETERS ON IMAGE QUALITY 45

1.6 OPTIMIZATION OF IMAGE QUALITY IN EXPERIMENTAL CONDITION 51

1.7 LITERATURE REVIEW 53

2 SIMULATION STUDIES 57

2.1 THEORY OF PHASE RETRIEVAL 57

2.2 SIMULATION STUDIES ON PHASE RETRIEVAL 66

2.2.1 Multi-distance phase retrieval 67

2.2.2 Multi energy phase retrieval 71

2.2.3 Single image phase retrieval 73

2.3 SIMULATION STUDIES ON TOMOSYNTHESIS 81

2.3.1 Translational Geometry *82*

2.3.2 Iso-centric Geometry *83*

2.3.3 Shift and add method of Slice reconstruction *84*

3 DEVELOPMENT OF ADVANCED MICRO-IMAGING FACILITIES 88

3.1 BASIC DESIGN OF A MICRO-IMAGING SYSTEM 89

3.2 DEVELOPMENT OF SYNCHROTRON IMAGING BEAMLINE AT INDUS-2 91

3.2.1 Indus-2 Synchrotron source *94*

3.2.2 Beamline optics *94*

3.2.3 Experimental Station *97*

3.2.4 Characterisation of imaging beamline *102*

3.2.5 Feasibility experiments *107*

3.3 DEVELOPMENT OF NEUTRON IMAGING BEAMLINE AT CIRUS REACTOR 114

3.3.1 Neutron source: CIRUS reactor *116*

3.3.2 Collimator *116*

3.3.3 Shielding hutch *118*

3.3.4 Experimental station *119*

3.3.5 Neutron beam characterisation *121*

3.4 FEASIBILITY EXPERIMENTS 122

4 APPLICATION OF MICRO-FOCUS BASED IMAGING SYSTEM 126

4.1 MICRO-IMAGING REQUIREMENTS IN CHTR 126

4.2 MICRO-STRUCTURE OF SIC COATINGS 129

4.3 GRAPHITE FUEL-TUBE OF CHTR 144

4.4 TRISO COATED FUEL PARTICLES 152

5 APPLICATION OF SYNCHROTRON IMAGING BEAMLINE 156

5.1 POLYMERIC BEADS 156

5.2 POLYURETHANE FOAM 164

5.3 METAL MATRIX COMPOSITE 175

5.4 CARBON-CARBON COMPOSITES 183

6 APPLICATIONS OF NEUTRON IMAGING BEAMLINE 191

6.1 STUDY OF HYDRIDE BLISTERS FORMATION USING NEUTRON TOMOGRAPHY 191

6.1.1 Detection of hydride blister in a matrix of zirconium pressure tube 193

6.1.2 Quantitative analysis of hydride concentration: 200

6.2 NON-DESTRUCTIVE EVALUATION OF PHWR FUEL ROD 205

6.3 STUDY OF LEAD MELTING AND SOLIDIFICATION 206

7 CONCLUSIONS 216

8 REFERENCES 222

9 APPENDICES 243

SYNOPSIS

X-ray & neutron imaging play an important role in the visualization and measurement of spatial and/or temporal distribution of objects' internal structure and density. In particular, understanding of macroscopic properties of materials often requires a detailed knowledge of its internal structure at micron to sub-micron scale[1–4]. Qualitative observation of images obtained allows visualization of distributed phases, detection of imperfections & enclosed particles, identification of geometry and morphology of subcomponents etc. Similarly, quantitative analysis of image provides measurement of density and structural features such as distribution of area/volume/surface of subcomponents/material phases, porosity, tortuosity, anisotropy, fractal dimension etc. [5,6]. Quantitative microstructure determination of materials also plays important role in the optimization of their manufacturing parameters and modelling of macroscopic behaviour through structure property correlation[7,8]. It may be noted that analysis of images for microstructure study is strongly dependent on two parameters, image resolution and contrast respectively. While high resolution is necessary to see the smallest features of the object with good clarity, high contrast allows distinction between material phases of closest density, atomic number and thickness[4,6].

In the last few decades, quality of images in X-ray & neutron imaging (measured in terms of resolution and contrast) has enhanced tremendously. This is principally due to development of new modes of image contrast generation based on refraction, reflection, diffraction and scattering of the beam instead the simple attenuation [9–12];

and instrumental improvements in imaging systems due to development of highly brilliant and coherent sources, advanced optics and high efficiency, high-resolution imaging detectors[13–15]. The objective of present thesis is to develop micro-imaging capabilities in X-ray and neutron imaging by improving their resolution and contrast through both methodological and instrumental routes and apply them in micro-structural characterisation of advanced nuclear materials to study their composition, geometry, and internal structure. Since X-ray and neutron have different interaction mechanism and provide complementary information in terms of penetration depth and sensitivity to material density, structure; both X-ray and neutron imaging are included in the scope of study to identify their relative merits and demerits when applied in material science applications. Thus the objectives of present thesis are

1) Study of principles of X-ray & neutron micro-imaging techniques, strategies for image quality optimization and development/computer simulation of quantitative analysis/reconstruction methods.
2) Design, development, and characterisation of state of the art X-ray & neutron micro-imaging facilities and implementation of various advanced micro-imaging techniques.
3) Applications of X-ray & neutron imaging in micro-structural characterisation of advanced nuclear materials differing in their composition, geometry, and internal structure.

In the methodological domain, there has been a paradigm shift in capabilities of X-ray and neutron imaging due to switching from attenuation based imaging to phase based

imaging, which utilized coherence properties of new sources. Adopting phase contrast imaging has resulted in unprecedented improvement in contrast and resolution. This allowed imaging of materials such as polymers, soft composites (carbon), biomaterials, soft tissue organs etc, which until now were difficult to be imaged with X-rays. Similarly, neutron phase imaging has opened up imaging of two very similar low neutron-attenuating materials. This thesis examines various modes of phase imaging, starting from simple propagation based imaging to advanced techniques like diffraction enhanced imaging. Propagation based PCI (PB-PCI) is the simplest in terms of implementation and I have evaluated optimization various experimental parameters under exact experimental conditions.

The images acquired in PB-PCI do not readily provide the object phase information. Computational methods are required for retrieving phase at object plane. Existing methods of phase retrieval based on multiple projections data are applicable under certain conditions and possess one or more limitation. We have carried out simulation studies on existing multi-distance phase retrieval methods to study their applicability on experimental data of pyro carbon coated alumina particles. A new algorithm has been developed where variable wavelength based ‘contrast transfer function’ approach was applied for the quantitative phase retrieval from simulated and experimental data of fibre materials[16,17]. The performance of both of these multi-distance and energy methods is found reasonably good for experimental data, however, their application to tomographic imaging is somewhat limited due to requirement of multiple image acquisition and stringent system alignment. As an alternative, single image phase

retrieval methods can be used. These algorithms are simple in implimatation but impose very stringent conditions on sample composition and experimental parameters. To find out the applicability of single image phase retrival algorithms for tomography under experimental conditions, we have compared the performance of various phase retrieval algorithms on real experimental data. Similarly, we have worked on the development of three-dimensional image reconstruction method from limited scan projection data also called tomosynthesis which is important for fast tomography, reduced dose imaging, and samples with laminar geometry. We have carried out computer simulations for two acquisition geometries using shift and add algorithm.

For the implementation of advanced micro-imaging techniques, state of the art imaging facilities have been designed and developed utilizing synchrotron based X-ray sources and nuclear reactor based neutron source. These facilities have been uniquely designed to implement a large variety of micro-imaging techniques in the same experimental station. For X-ray, the synchrotron imaging beamline is designed, developed, installed and commissioned at Indus-2 synchrotron source India. This beamline can work in monochromatic & white beam mode and we have implemented techniques like high-resolution radiography and tomography; PB-PCI, Diffraction enhanced imaging, holotomography, laminography, dual energy imaging and real-time imaging [18]. Similarly, the neutron imaging facility was designed and developed at CIRUS reactor India, for the implementation of high-resolution digital neutron radiography, tomography, and PB-PCI [19]. The performance of these experimental facilities is evaluated by several system characterization and feasibility experiments.

X-ray and neutron micro-imaging has been applied to solve some of the innovative problems in materials science related to measurement of 3D microstructure and density distribution. In this thesis, we have primarily focused on microstructure determination and non-destructive evaluation studies of nuclear materials, either being used in the conventional reactors such as PHWRs or proposed to be used in the advanced reactors such as CHTRs. Laboratory based X-ray μ-CT has been uniquely applied to study microstructure variations of thickness and porosity caused by reactant depletion during chemical vapour deposition process of oxidation protective SiC coating over the internal surface of bore in thick graphite tube sample, which is a prototype of several components of compact high temperature reactor (CHTR)[20,21]. Fuel tube of CHTR has also been studied to find bore area, inter-spacing, and their variation along the tube axis. Microstructure of TRISO coated fuel particles having layers of pyro-carbon, SiC over zirconia core has been characterised to find out their layer thickness, and uniformity using propagation based PCI and tomography.

Synchrotron based micro imaging and tomography has been applied in the studies of several advanced materials such as carbon composites, polyurethane foam, Al-SiC metal matrix composites, and metal adsorbent polymer beads to find out their micro-structure and effect on them caused by various external factors[22]. Several types of carbon-carbon composites, which are the potential structural material for high temperature reactors and manufactured using different preparation processes have been characterised to study distribution and geometries of pores and carbon layers in epoxy matrix. Polyurethane foam used as a packing material in the transportation of nuclear

waste has been characterised for its porous microstructure and effect thereon due to different gamma irradiation dose. The microstructure variation is also shown to have correlation with the mechanical strength of the polyurethane foam. Microstructure of glassy carbon has been studied using phase contrast micro-tomography. Polymer beads used as adsorbent materials for the extraction of metallic impurities from solution during processing of nuclear waste have also been characterised for its porous microstructure. The advantage of holotomography over phase & absorption contrast μ-CT has been evaluated in the Al-SiC metal matrix composite to study damages caused by external compressive load.

Neutron tomography was used for the detection of hydride blisters in the Zr-alloy pressure tube of PHWR and study their shape, size, and distribution of hydride in the vicinity [23]. We have used neutron tomography images to calibrate hydride concentration with the gray values to determine hydride concentration from the images of unknown sample. It was established that neutron tomography is a valuable tool to study diffusion of hydride in the Zr-alloy matrix during blister formation. Neutron imaging was applied for the non-destructive evaluation of fuel tubes of Pressurised Heavy Water Reactor (PHWR). Neutron dynamic imaging was applied to study lead melting and solidification under external heating to study the effects of natural convection and heating rate on molten fraction and curvature of molten-solid interface[24,25].

The thesis consists of seven chapters and is organised to show methodological studies in chapter 1 and 2 followed by instrumental development of micro-imaging facilities

and their characterisation in chapter 3 and finally applications of X-ray and neutron imaging in chapters 4, 5 and 6. Chapter 7 summarises the outcome of the thesis and future prospects of the study. The outline of each chapter of the thesis is given here –

Chapter-1 Introduction - This chapter provides an overview of X-rays and neutrons micro-imaging techniques with their relative advantages and limitations. Mechanism of contrast generation and effects of various experimental parameters on image quality is discussed. Finally a literature review of recent developments in X-rays and neutron micro-imaging techniques is given.

Chapter-2 Simulation studies - In this chapter a comparative study of various single and multi-image phase retrieval methods applicable to propagation based PCI is then presented based with their simulations and experimental results. Finally, simulation studies on tomosynthesis reconstruction are discussed using shift and add method.

Chapter-3 Development of advanced micro-imaging facilities - This chapter discusses design, characteristics and performance evaluation of various micro-imaging facilities developed using synchrotron based X-ray sources, and nuclear reactor based neutron source. Results of feasibility experiments on different micro-imaging techniques implemented are also presented.

Chapter-4 Applications of micro-focus based imaging system - This chapter discusses the application of X-ray PCI and μ-CT using micro-focus tube source for the non-destructive micro-structural evaluation of CHTR components such as SiC coating on graphite fuel tube, TRISO coated fuel particles, fuel tube etc. Quantitative image

analysis of micro-CT data is applied for measurement of shape, size, homogeneity, deformations, and porosity distribution.

Chapter-5 Application of synchrotron imaging beamline - This chapter discusses application of synchrotron X-ray μ-CT in the studies of microstructure and density variation of carbon composites, polymer beads, and polymer foam. Results for 3D visualization and quantitative measurements of various structural properties are given. Effects of various external factors to their micro-structural properties have also been shown through differences in images or measured quantitative parameters.

Chapter-6 Applications of neutron imaging beamline - This chapter discusses the application of neutron tomography in the detection of small hydride blister in Zr-alloy pressure tube of PHWR and calibration of hydride concentration in Zr-alloy coupons against tomography image gray values. Application of dynamic radiography to study the lead melting and its solidification is also discussed.

Chapter-7 Summary and conclusions- This chapter summarises the thesis outcome and future scopes of the study. Relative merits of different micro-imaging techniques have also been discussed.

List of Tables

Table 2.1 Comparison of real and imaginary part of refractive index of alumina and carbon materials of phantom used in the experimental studies 69

Table 2.2 Density and thickness of coating layers in TRISO coated fuel particle. 76

Table 2.3 Description of mathematical phantoms used in the simulation study 86

Table 3.1 Beamline Characteristics 93

Table 3.2 Different experimental techniques at imaging beamline 93

Table 3.3 Resolution and field of view of X-ray microscope with different objective lenses used with PCO-2000 Camera 100

Table 3.4 Neutron flux measurement 121

Table 3.5 Measurement of contrast as a function of neutron aperture 122

Table 4.1 Process parameters of Sic coating deposition using APCVD 132

Table 4.2 Comparison of microstructure measurements on SiC coating on B1 and B2 144

Table 4.3 Measured parameters of fuel tube for high-resolution tomography system 150

Table 6.1 Comparison of transient behaviours of lead melting and solidification under various cases of natural convection 213

Table 6.2 Comparison of transient behaviour of lead melting and solidification caused by different heating rates 215

List of Figures

Figure 1.1 Schematic of different PCI techniques (a) PB-PCI (b) DEI (c) GI [30] 35

Figure 1.2 Sequence of operations in a typical tomography experiment[39] 40

Figure 1.3 Contrast transfer variation with respect to distance and wavelength.[31] 44

Figure 2.1 Mathematical phantom used for simulation studies on phase retrieval 67

Figure 2.2 PB-PCI images of phantom at 2, 15, & 35 cm propagation distances 67

Figure 2.3 Phase map retrieved at object plane using multi-distance method 68

Figure 2.4 Experimental PB-PCI images of alumina particles at 15, 35 and 50 cm. 69

Figure 2.5 Phase map retrieved from the experimental images of alumina particle and its profile plot along the central row 70

Figure 2.6 Thickness map of the alumina particle calculated from the phase retrieved 70

Figure 2.7 PB-PCI images of simulated phantom at beam energies 16, 18, 20 keV. 71

Figure 2.8 Phase retrieved using variable wavelength approach for simulated phantom 71

Figure 2.9 Experimental propagation phase contrast projection images of Silicon aerogel with fiberous structure with beam energies at 16, 18 and 20 keV. 73

Figure 2.10 Phase Retrieved of silicon aerogel using variable wavelength algorithm 73

Figure 2.11 Comparison of various single image phase retrieval methods for Polymer Bead and TRISO coated fuel particle. [Scale bar = 200μm for all images] 77

Figure 2.12 Data acquisition geometries considered for tomosynthesis simulation under limited angle projection (a) Iso-centric geometry (b) Translational geometry 83

Figure 3.1 Schematic of X-ray or neutron micro-imaging system 90

Figure 3.2 Optical layout of imaging beamline with component distances from source. 91

Figure 3.3 Experimental station of imaging beamline Indus-2 at RRCAT India 97

Figure 3.4 (a, b) Lens coupled X-ray imaging microscope. (c) Quantum efficiently of (PCO2000) CCD with wavelength (d) Photo-luminescence of various scintillators 99

Figure 3.5 Characteristics of White beam at imaging beamline (a) Calculated spectra of synchrotron white beam (b) Beam divergence (FWHM) with energy (c) Beam profile at 18 m (FWHM 4.5 mm) (d) Rocking curve of DCM at 12 keV(FWHM 53.53 µrad). 102
Figure 3.6 Characteristics of Monochromatic beam (a) Beam size (FWHM) variation with energy) (b) Beam flux variation with energy 104
Figure 3.7 Measurement of beam uniformity (a) Flat image of synchrotron beam at 12 keV acquired using CCD detector. The figure also shows horizontal and vertical profile plots and its histogram. (b) Image (a) after flat field correction 105
Figure 3.8 Spatial resolution measurement using JIMA pattern (a) Fiber optic coupled CCD detector (b) Lens coupled CCD detector. 106
Figure 3.9 Full field high-resolution absorption contrast image of beehive. 107
Figure 3.10 (a) PB-PCI image of silicon aerogel (b) Profile plot along the red line 108
Figure 3.11 High-resolution PB-PCI using X-ray microscope of (a) Flower (b) Anther 109
Figure 3.12 (a) PB-PCI projection image (b) µ-CT slice image (c) 3D image of bone..... 109
Figure 3.13 Characteristics of analyser crystal used in diffraction enhanced imaging (a) Rocking curve (b) Gradient of rocking curve 111
Figure 3.14 DEI of Rose petals. (a) Apparent absorption image (b) Refraction image. 111
Figure 3.15 Dual energy imaging of Arsenic (As) [Absorption edge 11.87 keV] in Rice using X-ray CCD Projection image acquired at (a) 11.5 keV (b) 12.0 keV (c) difference of logarithmic images(a and b) to visualize distribution of As..... 113
Figure 3.16 High-resolution large FOV imaging of Zebra fish..... 114
Figure 3.17 Neutron imaging beamline at CIRUS reactor, INDIA 114
Figure 3.18 Design (left) and photograph (right) of main collimator for neutron imaging and tomography and the conical insert for neutron PCI 117
Figure 3.19 Schematic of imaging camera used for neutron tomography experiment. 120
Figure 3.20 Sharp edge image and plot of Modulation transfer function (MTF) for CCD 122

Figure 3.21 (a) Measurement of resolution using test pattern (b) contrast variation in with object disc thickness (Horizontal) and diameter (vertical). (c) and (d) show the profile plot for (b) along right most vertical and bottom most horizontal series of disks 123
Figure 3.22 Neutron Radiography images acquired at neutron imaging beamline at CIRUS (a) nozzle of a gas cylinder (b) Hard disk..... 124
Figure 3.23 Comparison of (a) neutron absorption and (b) PCI of syringe and their profile plots along the line shown. 125
Figure 4.1 Schematic of CHTR core to show lattice subcomponents of the reactor 128
Figure 4.2 Schematic of Prototype fuel tube with SiC coating over its internal surface of the central bore. B1 and B2 are the tube domains for microstructure characterization. 130
Figure 4.3 Micro-focus based imaging system used in this study 133
Figure 4.4 Horizontal (a) and vertical (b) slice images of µ-CT reconstructed graphite tube domain B2 (c) 3D micro-graph of coated fuel tube section B2 (d) 3D cropped view to show substrate coating interface (e) 3D segmented view of coating only showing granular morphology (f) a close view of (e)..... 135
Figure 4.5 Comparison of horizontal and vertical region of interests in slice images of SiC coating of domains B1 (a, b) and B2 (c, d) 136
Figure 4.6 Sequence of image processing operations for quantitative analysis of slice images (a) Reconstructed raw (b) Threshold (c) segmented and outlined..... 139
Figure 4.7(a) Pore frequency distribution for domains B1 and B2 (b) Pore frequency variation along the tube axis 141
Figure 4.8 (a) Pore area distribution for B1 and B2 (b) its variation along the tube axis 141
Figure 4.9 (a) Pore Size distribution (b) Surface area of the coating in B1 and B2 142
Figure 4.10 Slice image to show method of coating thickness measurement using grid lines and their profile plots. One profile plot along the vertical line is shown. 142
Figure 4.11 Coating thickness variation along axial direction for B1 and B2..... 143
Figure 4.12 Schematic of the samples fuel tube studied (a) and its actual photograph (b) 147

Figure 4.13 Sequence of digital image processing operations to carry out structural and morphological analysis of X-ray CT data. 148
Figure 4.14 Section of fuel tube (a) XZ slice (b) shows the YZ slice (c) XY slice (d) 3D image of fuel tube section show surface roughness. 148
Figure 4.15 Histogram of bore area (a) central (b) peripheral 149
Figure 4.16 Histogram of bore inter-spacing (a) central (b) peripheral 149
Figure 4.17 Histogram of bore circularity of peripheral and central bore 151
Figure 4.18 Histogram of length of major and minor axis of ellipse fitted in the micro-imperfection of the graphite matrix 152
Figure 4.19 TRISO coated fuel particles showing core radius and thickness of layers 152
Figure 4.20 Comparison of absorption and phase contrast images of TRISO coated fuel particles showing different layers (a) Absorption contrast image (b) Propagation phase contrast image (c) The edge enhanced image clearly showing all the interfaces. [Scale bar = 200µm for all images] 153
Figure 4.21 X-ray µ-CT slice images of TRISO coated fuel particle at different planes of elevation. [Scale bar = 200µm for all images] 154
Figure 4.22 Different view of phase contrast µ-CT of TRISO coated fuel particle (a) Slice image (b) Orthonormal view (c) 3D volume rendered view. [Scale bar = 200µm for all images] 155
Figure 5.11 Compressibility test on polyurethane foam samples exposed with different gamma doses of 5, 10, 15, 20 kgray. 172
Figure 5.12 SRµ-CT images showing the effect of gamma dose on microstructure of polyurethane foam exposed with different gamma doses of 0,5, 10, 15, 20 kgray. 174
Figure 5.13 Comparison of absorption and phase contrast imaging - projection images, reconstructed slices of the same plane, plot profiles of projection (along the central row) and reconstructed slices (along the line shown) and histograms of slice 178
Figure 5.14 Comparison of reconstructed slice images of absorption contrast tomography (left) and phase contrast tomography (right). [Scale bar = 500µm] 180

Figure 5.15 Comparison of flat field corrected phase contrast image and phase map retrieved using PAD-MBA at object plane for Al-SiC composite 181
Figure 6.1 Experimental set-up for hydride blisters preparation in pressure tube and picture of sample prepared. 193
Figure 6.2 Neutron tomography of Zr-alloy pressure tube to detect hydride blisters (a) Flat field corrected radiograph (b) Vertical slice showing cross section of the detected blister (c) Horizontal slice showing relative location of three blisters (d) 3D image showing hydride blisters and their nearby regions with low hydride concentration caused by migration. 196
Figure 6.3 Enlarged vies of hydride blisters formed in Zr-alloy pressure tube. The figure also shows the intensity profile plots of one of the blisters to confirm the inhomogeneity of hydride concentration in the nearby region of the blister. 197
Figure 6.4 3D images near blister showing hydride migration towards blister formation 200
Figure 6.5 Neutron tomography of Zr-alloy coupons charged with hydride concentration 0, 50, 100 wppm. (a) Projection image (b) reconstructed slice (c) 3D image showing hydride in red and Zr-alloy in green colour (d) 3D image showing only hydride concentration. 201
Figure 6.6 Neutron tomography of Zr-alloy coupons charged with 25, 50, 75, 100 wppm of hydride concentration. (a) Projection image (b) YZ slice (c) XZ slice (d) XY slice (e) 3D image showing hydride in red colour and Zr-alloy in green (f) 3D image showing only hydride concentration. .. 202
Figure 6.7 Calibration of hydride concentration against gray values (a) Histogram distribution of gray values for Zr-alloy coupons charged with different hydride concentrations (b) Linear fit of mode of gray values and hydride concentration 204
Figure 6.8 Fuel rod sample of PHWR and its projection image. Images in right show (a) region of interest (b) 3D image showing Zr-alloy cladding and end-cap in green and fuel pellet in red. (c) Segmented image of Zr-alloy cladding and end-cap (d) 3D image showing the defective fuel pellet. 205

Figure 6.9 Lead solidification: Neutron radiography images acquired at different time after initiation of cooling. Images show movement of solid-liquid interface after heating from different surfaces was put-off. 212
Figure 6.10 Contours showing the movement of solid-liquid interface with time for different cases of heating and solidification (a,b) side (c,d) bottom (e,f) top 214
Figure 6.11 Molten fraction vs. time in different cases of lead melting and solidification 214
Figure 6.12 Effect of heating rate on lead melting & solidification though images acquired after fixed time of heating & cooling initiation (a)16.3 (b) 22.7 (c)35.1 kW/m^2 215

List of abbreviations

PCI- Phase Contrast Imaging

PB-PCI- Propagation Based Phase Contrast Imaging

DEI – Diffraction Enhanced Imaging

CI- Crystal Interferometry

µ-CT- Micro Computed Tomography

CT - Computed Tomography

CTF – Contrast Transfer Function

TIE – Transport of Intensity Equation

3D – Three Dimensional

PHWR – Pressurised Heavy Water Reactor

CHTR – Compact High Temperature Reactor

TRISO- Tri ISO

NDT – Non-Destructive Testing

CRL- Compound Refractive Lenses

SNR-Signal to Noise Ratio

CCD – Charge Coupled Device

PSF – Point Spread Function

MTF –Modulation Transfer Function

LSF – Line Spread Function

1 INTRODUCTION

1.1 Motivation

Materials are the enablers for future nuclear technologies. Advanced materials with improved characteistics are needed for development of next generation of reactors, which will use new class of fuel material, cladding, and other critical components during their operation and pre/post processing activities. For example, fuel of compact high temperature reactors (CHTR), which are being developed worldwide as well as in India, is in the form of Tri Iso-coated (TRISO) particle with coatings of pyro carbon and silicon carbide on a seed of nuclear fuel as a kernel. Characterizing such a fuel is a big challenge, as conventional techniques do not work on such small coating layers of low z materials. Even for safe and uninterrupted operation of existing reactors, development of new methods of quality control are needed to characterize materials degradation which is the primary cause of unplanned outages in the nuclear industry. For example, growth of hydride blisters on Zr-alloy cladding is one of the main issues and requires new methods of study. Similarly, for study of safe transport of radioactive materials lead casks are used. For safe transportation of such casks, their behaviour

during accidental fire needs to be studied. Addressing such challenges in the development of advanced nuclear materials requires new means of high-resolution non-destructive testing (NDT) techniques, which can see not only the surface, but bulk of the specimen. Imaging with X-ray or Neutron is conventionally used for such applications. Over the years with increasing demand of high contrast and resolution in the X-ray and neutron images, there is a need to develop new techniques, sources, and detectors to meet such challenges. Imaging is no longer limited by the absorption contrast and a variety of advanced characterization tools including diffraction and phase contrast based imaging have recently been discovered. They allow measurements of microstructure and strain over a range of relevant time and length scales. There have been new developments in X-ray sources such as micro-focus sources or synchrotron sources to allow experiments on Phase contrast imaging (PCI), diffraction enhanced imaging (DEI) and holotomography, which can be used for meeting the challenges of developing advanced materials for next generation of reactors. Synchrotron radiation based imaging, in particular, offer new opportunities to advance the fundamental understanding of nuclear reactor materials, fuels, and engineering components with its capability of offering sub-micron resolution, high contrast, and exceptionally good signal to noise ratio. Many of these techniques, on a limited scale, can also be implemented using laboratory based microfocus sources and this opens up more widespread applications of these advanced techniques for material characterization. Even with neutrons, new techniques such as PCI, tomography, real-time imaging, have found widespread applications in material characterisation & NDT.

1.2 Highlights of the thesis

The objective of this thesis is to study of advanced X-ray & neutron micro-imaging techniques, develop improved methods and facilities for them, and use them to several new applications particularly nuclear materials. In this thesis, we have studied design concepts of micro-imaging systems and optimization strategies of experimental parameters for achieving high quality images in X-ray and neutron imaging. These concepts have been applied to develop state of the art micro-imaging facilities based on advanced synchrotron based X-ray source and reactor based neutron source. Specific design of these imaging facilities allows implementation of several advanced micro-imaging techniques in the same experimental station with a relatively low flux source. This thesis for the first time, reports on application of synchrotron X-ray imaging (using Indus-2 Synchrotron imaging Beamline), micro-focus X-ray imaging and neutron imaging (using CIRUS neutron imaging beamline) for characterization of fuel and components for advanced reactors such as CHTR where new kind of fuel and cladding are proposed to be developed & used, and conventional reactors such as pressurised heavy water reactor (PHWR) where material degradation and quality control of operational components are to be characterised.

We have applied synchrotron based micro imaging and tomography in the studies of several advanced materials such as carbon composites, polyurethane foam, Al-SiC metal matrix composites, and metal adsorbent polymer beads to find out their micro-structure and effect on them caused by various external factors [22]. Several types of carbon-carbon composites, which are the potential structural material for CHTR and

manufactured using different preparation processes have been characterised to study distribution and geometries of pores and carbon layers in epoxy matrix. Polyurethane foam being used as a packing material in the transportation of nuclear waste has been characterised for its porous microstructure and effect thereon due to different gamma irradiation dose. The microstructure variation is also shown to have correlation with the mechanical strength of the polyurethane foam. Polymer beads used as adsorbent materials for the extraction of metallic impurities from waste streams during processing of nuclear waste have also been characterised for its porous microstructure. A new technique of holotomography has been evaluated in the micro imaging of Al-SiC composite to study damages caused by external compressive load.

This thesis also examines use of Laboratory based X-ray μ-CT setup for examining nuclear fuel and other components for CHTR. The microfocus source has been uniquely used to study microstructure variations of thickness and porosity caused by reactant depletion during chemical vapour deposition process of oxidation protective SiC coating over the internal surface of bore in thick graphite tube sample, which is a prototype of several components of compact high temperature reactor (CHTR) [20,21]. Fuel tube of CHTR was studied to find bore area, inter-spacing, and their variation along the tube axis. Microstructure of TRISO coated fuel particles having layers of pyro-carbon, SiC over zirconia core were characterised to find their layer thickness, and uniformity using propagation based PCI.

Though neutrons have been used over the years for nuclear fuel characterization, we have demonstrated use of some recent techniques for nuclear material

characterization. This thesis reports on more advanced development and application of 3D neutron tomography for the detection of hydride blisters in the Zr-alloy made pressure tube of PHWR and study their shape, size, and distribution of hydride in the vicinity [23]. We have also applied neutron tomography images to calibrate hydride concentration to determine hydride concentration in unknown sample. Neutron imaging has also been applied for the non-destructive evaluation of fuel tubes of Pressurised Heavy Water Reactor (PHWR). Neutron dynamic imaging was used to study lead melting and solidification under external heating to study the effects of natural convection and heating rate on molten fraction and curvature of molten-solid interface[24,25]. The work reported in this thesis has been brought out in the form of several international publications.

1.3 Overview of micro-imaging techniques

When incident radiation (X-rays or neutrons) of certain intensity passes through the object, many interactions take place and intensity/phase of outgoing beam is modified depending on thickness, composition, and density distribution of the object. The objectcan be described by a complex transmission function T(x, y), which is modelled by projections of real and imaginary part of refractive index along the beam direction [Appendix-1]. The projection image show sample features with different clarity depending upon the contrast generation mechanism used such as attenuation, phase modulation, diffraction and scattering or their combination. Techniques such as absorption contrast imaging, PCI, DEI, dark field imaging, dual energy imaging etc. aim to extract distribution of variety of object’s physical properties such as absorption

coefficient, refractive index, scattering coefficient, atomic number etc. These imaging modes are implemented in three dimensions as well, and referred as tomography, phase contrast tomography etc. The imaging capabilities are also extended to real-time imaging to extract information about temporal variations in object and in-situ imaging to study object under various environmental conditions. Imaging, combined with fluorescence, diffraction, small angle scattering and absorption spectroscopy have also been proposed to enhance the extracted sample information. These techniques are able to image and distinguish small variations of various physical properties of materials with sub-micron resolution. A brief overview of micro-imaging techniques, their instrumental requirements, advantages and limitations, recent developments and potential applications is given here.

1.3.1 Absorption contrast imaging

Absorption contrast radiography is based on inhomogeneous attenuation of incident beam in the sample detected on an imaging plate or digital detector placed next to the sample. The two-dimensional images show distribution of negative exponential of integrated linear absorption coefficient along the beam propagation. It is still by far the most used imaging technique, mainly because of its experimental ease and versatility. It does not require specific characteristic of source, detectors etc. thus provide maximum accessibility for academia and industry. Recently with the availability of high intensity sources for X-rays and neutrons and high-resolution imaging detectors, it is possible to reach sub-micron resolution with sufficient signal to noise ratio. The technique is also extended for 3D tomographic imaging and real-time imaging with suitable instrumental

and computational inclusions. The drawback of this techniques is low sensitivity to small density variation and poor contrast for soft materials like biological tissues, polymers, composite etc. [15,26,27]. Absorption contrast X-ray and neutron imaging is used for non-destructive characterisation and quality control applications of nuclear industry.

1.3.2 Phase contrast imaging

Phase contrast imaging (PCI) offer superior contrast with reduced radiation exposure as compared to absorption contrast imaging. It is based on detection of phase modulations caused by the object to a coherent or partially coherent beam instead of attenuation. The increase in sensitivity is attributed to the fact that phase shift to incident wave is more prominent as compared to its attenuation. For neutron, it is useful for the visualization of material having very small absorption/incoherent scattering cross-section but relatively high coherent scattering cross-section. Imaging of objects containing these material in presence of highly absorbing subcomponents is quite challenging using absorption contrast whereas PCI provides improved visibility at the edges. For X-ray the probability of phase shift can be 1000 times larger than attenuation in the keV energy range, phase-contrast imaging permits visualization of soft tissues that have identical or similar attenuation characteristics hence not distinguishable by use of conventional attenuation-based imaging methods. Moreover, because the refractive index-based image contrast decreases less rapidly with increasing energy, phase-contrast imaging allow a reduction of the radiation dose delivered to the object when used at higher energies [15,18].

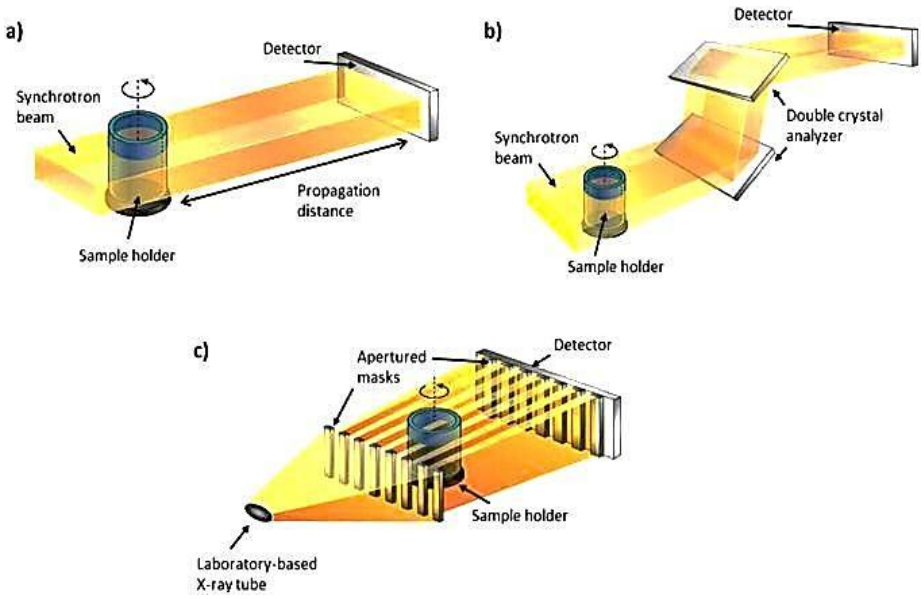

Figure 1.1 Schematic of different PCI techniques (a) PB-PCI (b) DEI (c) GI [30]

Phase modulation created by the sample in the incident beam cannot be directly detected with the currently available intensity sensitive imaging detector. In order to acquire phase contrast images, phase modulation are detected indirectly by creation of intensity modulation due to phase change through interference/diffraction. In the last few years, several techniques differing in their way to convert phase modulation into intensity modulations have been developed such as propagation-based PCI (PB-PCI), diffraction enhanced imaging (DEI) and grating interferometry (GI). These methods differ not only in the complexity of their experimental set-up and requirements of beam spatial and temporal coherence, but also in the nature and quality of images provided, object information encoded in the images formed, and the amount of radiation dose delivered to the sample. The final image contrast for them depends on several other factors, including the spatial resolution of the detector, the image formation mechanism, beam energy, divergence etc. [11].

a) Propagation based PCI (PB-PCI)

Propagation based technique is based on Fresnel diffraction and offers a unique advantage in terms of its simplicity, ease of implementation and efficient use of available flux. In this method, a spatially coherent incident wave traverses through the sample and the outgoing distorted wave front are allowed to propagate sufficiently far so that the small differences in phase propagation cause interference, and variations of intensity are observed in the image plane (Figure 1.1). Variations in thickness and refractive index of a sample lead to a change in the shape of wave front on passing through the sample. The technique is simplest in implementation and requires no optical instrument except a partially coherent source and moderate resolution detector. The images obtained are free from aberrations caused by optical lenses. The visual appearance of phase-contrast imaging is the edge enhancement at interfaces of the features with differing refractive indices. This feature is extremely useful in the detection of small cracks, enclosed particles, and studies of porosity or overall microstructure of nuclear materials due to their edge enhancement. The drawback of this method lies in its poor sensitivity to low frequency modulation in object properties and complexity of extracting pure phase information from the intensity image [31–34].

b) Diffraction enhanced imaging (DEI)

In Diffraction enhance imaging (also called analyser based imaging); a perfectly collimated monochromatic beam is refracted by the sample due to refractive index gradients present in the sample, which deflects its path by a small angle (Figure 1.1). The distribution of deflection angle, which is of the order of micro-radians, maps

distribution of refractive index in the sample thus electron density. This is converted into intensity distribution in the image with the help of analyser crystal between the object and detector using Bragg diffraction. The incident beam is also attenuated and scattered by the object resulting in its intensity modulation. The analyser crystals acting as a very efficient scattering rejecter due to very narrow angular acceptance also create a contrast called scatter rejection or extinction in the obtained images. Contribution of refraction, absorption, and extinction can be separated out using phase retrieval methods. The sensitivity of this technique to small density variations in nuclear materials is very high however; its implementation requires a very high energy-resolution crystal monochromator and identical crystals as beam refraction analyser. The technique also requires some crucial alignment of its optical components in vibration free environment [9,10].

c) Grating interferometry (GI)

Grating interferometry (GI), also known as differential phase-contrast imaging (DPC) is based on Talbot effect, which is explained as Fresnel diffraction in a periodic grating. In its implementation, the grooves of a phase grating produce periodic phase variations in the incident beam wave front behind the grating (Figure 1.1). Interference after a pure phase grating reproduces the phase pattern at multiples of the half Talbot distance, but intensity modulation is also observed at fractional distances. The phase shift is zero when there is no object in the beam. When an object is placed in front of or behind the phase grating, the wave front is deviated by refraction, and the intensity pattern is shifted. In the standard configuration, a suitable absorption grating is placed in front of

the detector, and the pattern is recorded by scanning the grating across the detector (phase stepping). Evidently, transverse coherence over a phase grating period is required. In phase stepping, three images are obtained: absorption, differential phase shift, and dark field. In other terms, the ‘differential phase shift image’ maps the refraction properties of the sample while the ‘dark field image’ maps the scattering properties. The phase-stepping method requires image recording at minimum of three positions of analyser grating scan and for that purpose, large precision and stability are needed. Slight rotation of the absorption grating and Fourier decomposition of the moiré pattern is also used to retrieve images of absorption, refraction and scattering without phase stepping[13,35,36].

1.3.3 Tomography

Tomography is a broad class of computational methods used to produce slice or volume images of a three dimensional (3D) object using its finite number of projection images [1]. The principle of tomography is illustrated schematically in Figure 1.2. Incident beam passes through a sample and produces a 2D projection image, which is recorded on a CCD detector set behind the sample. The sample is rotated about its axis and digitized signals in the form of 2D projection are collected for each angular step either in absorption or phase contrast modes [37,38]. A number of 2D projection images for different rotations of the sample are combined mathematically to make a sinogram. The slices of the object at different heights are reconstructed using backprojection methods [Appendix-2]. The technique overcomes the limitation of projection imaging caused due to inherent superposition of overlying structures thereby

reducing object contrast. In material science, two-dimensional imaging is suitable only for simple object. For the object having complex internal structure, overlying features are integrated along the beam propagation hence difficult to distinguish and identify in the image. Scope of extracting quantitative information regarding morphology, porosity, shape, size of features is limited from projection images. The slice images obtained provide local 2D object properties, which can be stacked to make three directional image to provide 3D distribution of the sample structure and density non-destructively without any need of sample preparation, staining or sectioning [2,3,5]. These images can be used for qualitative analysis of sample for example presence of various material phases and their local distribution, presence of cracks, voids, shape and size of enclosures, layered, composite and porous structure etc. 3D rendering software is used to re-create a 3D map of the object. Using image-processing tools like sectioning, segmentation, pseudo colouring etc., features in the 3D image can be enhanced, removed, or made transparent for improved visualization. Quantitatively analysing these tomography images, information related to structural and morphological parameters of the sample such as material distribution, inclusions, porosity, cracks dimension etc. can be measured. It is often necessary to make direct correlation between materials properties and their microstructure. Tomography images and measured quantitative parameters provide valuable inputs for design and modelling of advanced material. Some special cases of tomography having their specific applicability in material science to extract three dimensional object properties are discussed here.

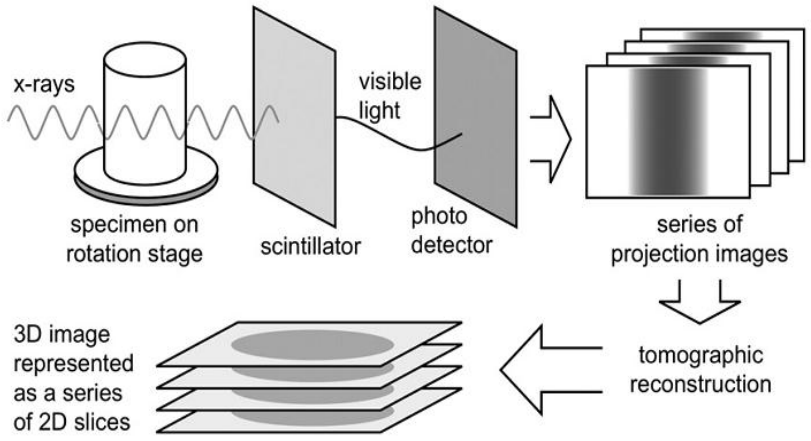

Figure 1.2 Sequence of operations in a typical tomography experiment[39]

a) Micro-tomography

Micro-computed tomography (µ-CT) is conventional CT implemented with a higher spatial resolution (~ few µm). It has numerous potential applications in various fields, mainly for the investigation of materials (alloys, porous media, composite materials), but also for biological or geological samples. Obtaining a high spatial resolution requires fine focus or parallel beam sources with high flux. For this purpose, the use of synchrotron radiation (SR) for X-rays and nuclear reactor with cold neutron beams for neutron are particularly attractive which allows the non-destructive acquisition of high resolution three-dimensional images with a cubic voxel size approaching less than 1 µm [2]. Sample placement and alignment over rotation stage becomes more important and challenging as voxel size reduces.

b) Laminography and tomosynthesis

Tomography reconstruction requires projection data collection for full angular span (180^0 for parallel beam or 360^0 for cone beam). Sometime it is necessary to acquire

tomographic scan in limited angular span instead of complete angular span due to objects laminar geometry, time limits in dynamic 3D imaging, to avoid sample obstruction by sample environment rig during in-situ imaging or to minimize object dose with reduced exposure. The limited angular span data does not map the sample completely in Fourier space hence special reconstruction methods based on algebraic reconstruction or modified filtered back projection are used. These reconstruction methods perform far better as compared to filtered backprojection algorithm and sometime applied in special acquisition geometries such as inclined rotation axis geometry, circular motion of source and detector etc.[40–42].

c) Phase contrast tomography and Holotomography

Tomography combined with PCI provides improved contrast in the visualization of material phases with small density difference. Edge enhancement of structural features helps in their easier segmentation and structural analysis. The technique requires acquisition of phase contrast projections at various angles and special filtered back projection methods for reconstruction. PCI combined with phase retrieval method and filtered back-projection is called holotomography allowing reconstruction of real part of refractive index, which provides improved visibility, and segmentation of materials having similar absorption characteristics. Combined absorption & phase tomography can be used for reconstruction of 3D distribution of complex refractive index[43,44].

1.4 Mechanism of contrast generation

As discussed earlier, PCI provides improved visibility of structural features and small density variation in the material due to edge enhancement effect. However, this

effect is dependent on variety of experimental parameters and characteristics of imaging system. Optimum phase contrast with high resolution is achieved in projection images and thereby in phase contrast tomography/ holotomography by virtue of designing suitable imaging system with coherent source and high-resolution detector along with optimization of numerous experimental parameters such as object to detector distance, beam energy and exposure time. There are two treatments commonly used to study mechanism of contrast formation in PB-PCI namely Transport of intensity (TIE) equation and contrast Transfer Function (CTF). Both the approaches explain the process of image contrast generation and give a quantitative relation between the image contrast and experimental parameters. TIE equation relate these variables with phase shift induced by a sample, through a differential equation while the CTF equation is based on solution of Fresnel propagation integral and relatively more complex [45,46]. The projected phase/attenuation map of the material can be obtained by solving these equations.

a) Transport of intensity equation

The transport-of-intensity (TIE) equation shows that phase shift introduced by a sample and the intensity recorded by the detector at sample-to-detector distance *z* are related by a second order differential equation.

$$I(x, y, z = z) = I(x, y, 0)\left[1 - \frac{z\lambda}{2\pi}\nabla_{\perp}^{2}\phi(x, y, 0)\right] \qquad (1.1)$$

This equation is referred as transport of intensity equation and relates the propagated intensity to incident intensity and object phase under the short propagation distance approximation [28,47]. The TIE describes how the intensity distribution of an

electromagnetic field changes as it propagates through space. In addition, by measuring the intensity and analysing how its distribution has changed with propagation, the phase of the field can in principle be deduced at object plane.

(b) Contrast transfer function

According to Fresnel theory, the beam interaction with object can be described by its optical transfer function and mathematically implemented by its multiplication to the wave function of incident wave [28,47]. This is further propagated through free space in PCI and formulated by convolution of wave function with Fresnel propagator. We consider that the beam propagates in the z direction and r = (x, y) is a two dimensional vector in the direction transverse to propagation direction. Considering the transmission of a monochromatic, coherent, plane wave of unit intensity ψ_0 through an object described by the distribution of complex refrective index. Under small angle approximation, the equation

$$\check{I}_z(u) = I_0[\delta(u;\lambda) - 2\check{\mu}(u;\lambda)\, cos(\pi\lambda z u^2) + 2\check{\varphi}(u;\lambda)\, sin(\pi\lambda z u^2)] \qquad (1.2)$$

called contrast transfer function relates the Fourier transform of the image intensity to the experimental parameters such as wave length, propagation distance and detector resolution or object features though object frequency (u) under Born-type approximation i.e. weak absorption and phase in object $\mu(r) \ll 1$, $\varphi(r) \ll 1$. The same equation can be derived under other approximations also such as (a) pure phase $\mu(r) = 0$ (b) slowly varying phase $|\varphi(r + \lambda zu/2) - \varphi(r - \lambda zu/2)| \ll 1$, (c) weak absorption and slowly varying phase approximations $\mu(r) \ll 1$, $|\varphi(r + \lambda zu/2) - \varphi(r - \lambda zu/2)| \ll 1$. More general cases consist of higher order terms in the eq. 1.2. Under the approximations of

small propagation distance (near field), the CTF can be reduced to TIE as obtained in eq. 1.1 [47]. As can be seen from CTF the intensity modulation created by the object depends on objects properties such as attenuation co-efficient $\mu(r;\lambda)$ distribution and $\varphi(r;\lambda)$ or experimental parameters such as propagation distance, sampling frequency on imaging detector and wavelength of incident beam radiation. Depending on values of these parameters through sine and cosine functions of $\sqrt{\pi\lambda z u^2}$, the intensity modulation may be dominated by absorption only or jointly on absorption and phase of the object. Figure 1.3 show the dependence of intensity on these experimental parameters [31].

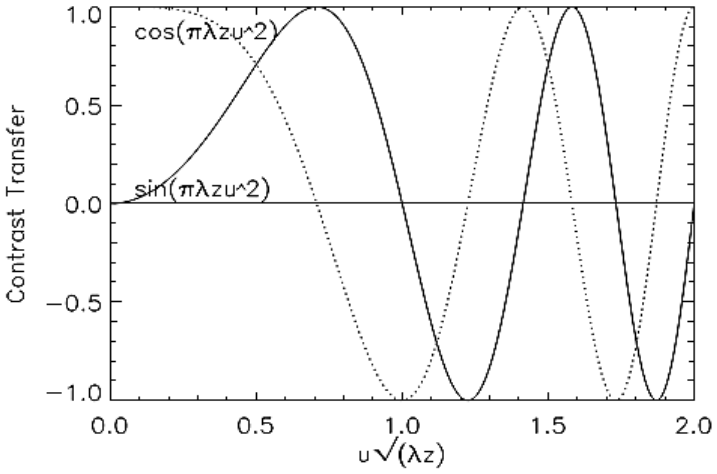

Figure 1.3 Contrast transfer variation with respect to distance and wavelength.[31]

In absorption contrast imaging, image contrast is entirely dependent on imaginary part of the complex refractive index i.e. second factor in Eq. 1.2. Such images do not show the contrast due to real part of refractive index i.e. phase contrast although present in principle. This is due to in-sufficient experimental conditions necessary for

enhancement of phase contrast in the acquired images. Phase contrast is mainly generated due to real part of refractive index i.e. third factor of Eq. 1.2. Incident wave that pass through materials of differing δ pick up different relative phases. The resulting phase shift is directly proportional to the projected electron density of the object.

1.5 Effects of experimental parameters on image quality

The contrast transfer function considered in section 1.4 describes variation of image intensity under ideal conditions of source, object composition, and detector i.e. parallel, monochromatic beam source, weak absorption and phase variations in the object and infinite resolution of imaging detector. In practical imaging system, such characteristics are not realized therefore the model of image formation is necessary to be reformulated in order to include practical conditions of experimental systems. Source characteristics such as focal spot dimensions, flux, coherence, collimation and bandwidth affect image unsharpness thus resolution and contrast, image statistics, scattered noise and acquisition time. Coherence of the beam is an important factor in PB-PCI, determining the sharpness of fringes at the phase gradient/interfaces. Detector characteristics such as efficiency, pixel size, geometrical and optical magnification, linearity, frame rate affect image resolution, contrast and frame capture frequency. Apart from this beam diffraction due to finite propagation, sample thickness and composition, beam energy and image integration time also affect image quality in different ways. Based on the contrast transfer function or transport of intensity equation, we can explicitly analyse the dependence of various experimental parameters on image quality in absorption and PCI [Appendix-3]. Pogany, Nestrestics, Olivo, Arfeli etc. have provided explicit

models of PCI under practical conditions [31,32,48–50] . If we consider I(r, λ, z) as the image pattern obtained under ideal conditions then the way in which different factors will affect the image are considered in this section.

i. Finite source size

In case of partially coherent point like source (spherical wave), the source is spread over a finite area instead of the ideal point source. Finite source size causes smearing of the sharp features in the image (unsharpness) specially at interfaces and mathematically realized through convoluting the ideal image pattern with source distribution J_s = I(r, λ, z) *S(r) where S(r) is the source distribution [51]. If 's' is the source spread function, the image PSF will be S(r) = R_2s/R_1, but when referred to the object this is reduced by M i.e., to R_2s/(R_1+R_2). For R_2 << R_1 this again reverts to the plane-wave case where θ, the angular width of the source at the object is identified as s/R_1. For R2 >> R1 the PSF tends to s; thus, resolution will be limited to the source size [31]. This, with the associated problem of intensity is the greatest limitation of point source systems for achieving high resolution.

ii. Spherical wave case

If the object is illuminated with a spherical wave instead of parallel wave, it is equivalent to putting an additional phase term to the wave function immediately after the object. If $\psi(r) = \psi_0 exp\big(i\varphi(r) - \mu(r)\big) = \psi_0 q(r)$ is the field after the object in case of parallel beam, then for a spherical beam emitted by a point source located at distance z_1 from the object, the field is

$$\psi_{sph}(r) = \psi(r) exp\left[-\frac{ik}{2z_1}(x^2 + y^2)\right] \quad (1.3)$$

Where a parabolic approximation have been made for the spherical wave front incident on the plane z = 0. After some simplifications and using this as a factor in Fresnel equation, and propagation of outgoing wave to a distance z_2, the effect can be summarised as follows [31]

$$\psi_{sph}(r;\, z_1, z_2, \lambda) = \frac{1}{M}\psi_{par}(r/M;\, z_{eff}, \lambda) \quad (1.4)$$

Where $z_{eff} = \frac{z_1 z_2}{z_1 + z_2}$ is the effective propagation distance and $M = \frac{z_1 + z_2}{z_1}$ is geometrical magnification. For $z_1 \sim \infty$ and $z_2 = 0$ the case become equivalent to parallel beam case.

iii. Coherence

A parallel beam or spherical beam from point source is considered perfectly coherent however, in practical cases; plane waves generally have an angular divergence and a spherical wave's source have a finite dimension making them partially coherent only.

iv. Parallel beam with divergence

If the incident beam is diverging instead of parallel, it represents a bundle of plane wave's incident on the object. Now, for off-axis incidence optical transfer function q(x) is modified by a factor exp(-ikx sin θ), where θ is the angle of incidence. It follows that for small θ, ψ(x) and I(x) are shifted to ψ(x- θz) and I(x- θz) respectively which is equivalent to convolution with a point spread function. So for partially coherent illumination, each image point is convoluted with a point-spread function (PSF) of width θz, whose exact shape depends on the distribution of illumination intensity with

angle. Equating this width with the inverse of spatial frequency optimally transferred at this z, i.e. $(2\lambda z)^{1/2}$, gives $\theta^2 z = 2\lambda$. This gives an estimate [θ/2λ] for the lowest spatial frequency, which can be observed with optimal contrast under these conditions. Higher spatial frequencies can always be brought into optimal contrast by decreasing z. The inverse of this, viz 2λ/θ, is called the ‘‘coherence width.’’ This coherence width is roughly the maximum distance between two object points for which interference effects will be observable. It is not necessary for the whole object or field of view to be coherently illuminated [31].

v. Beam polychromaticity

In order to see the effect of beam polychromaticity or temporal coherence on phase contrast image for both plane and spherical waves; the complete energy spread of beam is divided into sufficiently small but finite energy bins. The ideal pattern at mean energy of each bin is obtained using Fresnel equation for monochromatic beam (Eq. 1.2). Weighted sum of these individual patterns gives the final image pattern for polychromatic radiation [51]. Pogany suggested another approach in which the ideal pattern is convoluted with energy distribution of source spectrum. If the source has a normalized intensity distribution, w(λ) the effect can be formulated for a pure phase object as follows,

$$\psi_z(u; z, \lambda) = \psi_0[\delta(u; \lambda) - \int \breve{\varphi}(u; \lambda) \sin(\pi\lambda z u^2)\, w(\lambda) d\lambda] \qquad (1.5)$$

For example, if w(λ) has the Gaussian distribution, effect of this is the multiplication of an exponential damping function to ψ(u;λ,z). It follows that one could have a wavelength spread $\Delta\lambda = \lambda_0$without undue damping. This represents a large wavelength

spread and justifies suitability of polychromatic sources in PCI. However, there is a very rapid cut-off with increasing spatial frequency (u), due to its fourth power in the exponent, thus some monochromatization would be required for high resolution. The above results are essentially unchanged if absorption is included, although details of the correction terms differ due to the energy dependence of μ.

vi. Propagation distance

Effect of propagation distance, evaluated in terms of Fresnel number, is different in three different region namely near field, holographic region and far field. Fresnel number (a^2/λ) is a dimensionless physical quantity in diffraction theory where 'a' is the characteristic length in the object. The intermediate or Fresnel regime, when the radius of the first Fresnel zone $=\sqrt{\lambda z}$, can be compared to the characteristic dimension 'a' of the sample perpendicular to the beam direction, such that $z\lambda \approx a^2$ or $F \approx 1$. The image of the object is distorted here and varies rapidly with the propagation distance. In this regime, the information of the phase can be retrieved using combination of images recorded at different distances with a suitable algorithm. The "edge detection" or near Fresnel regime holds for small z values, such that $z\lambda \gg a^2$ or $F \gg 1$. Under these conditions, the object covers many Fresnel zones. The image has a close similarity with the object, and an immediate interpretation is possible. The image contrast depends linearly on the phase shift introduced by the object in to the transmitted wave. A boundary contrast appears because of interference of strongly scattered rays at the boundary due to refraction with the reference rays. Therefore, the phase gradient in the object becomes visible even for a purely transparent object. The far field regime holds

for larger z values, such that F $\ll$ 1. The image obtained in the far field has no resemblance to the sample. This corresponds precisely to the Fourier image of the object. In this region diffraction dominate over the imaging process.

vii. Detector pixel size

Finite pixel size of the detector also introduces smoothening effects to the fine features in the ideal image pattern resulting in reduction of the intensity of first minima and maxima. If P is the PSF of detector then modified pattern is given by $J_d = I*P$ where * is the convolution operator [48,51]. A smaller pixel size is preferable for high resolution but it also reduces signal to noise ratio unless used with higher beam flux.

viii. Incident beam energy

Higher incident beam energy helps in increased penetration in the object however reduces the possibility of interaction with thin or low density object features. The variation of absorption δ and phase β contribution with energy are also a subject to be taken care. At absorption edges, strong absorption/phase modulation by a given element is useful in spatial mapping of that component using dual energy imaging.

ix. Object composition and thickness

Intensity modulation of incident beam depends on attenuation (μ) and phase (φ) modulation due to object. Features visibility is affected by object composition. The object may consist of weakly/strongly absorbing materials with homogeneous /inhomogeneous distribution. Absorption characteristics of objects also depend on incident beam energy. The most general case of object composition is quite complex

hence different approximations are studied. Increasing thickness clearly reduces contrast thus sample of smaller thickness is preferable unless they create sufficient contrast.

x. Acquisition time/Integration time/frame rate

Integration time/ acquisition time per frame decides the collection of photon quanta in a given pixel thus signal to noise ratio in the image. Integration time should be sufficiently large to maximize signal to noise ratio however the saturation of integrating detector pixel need to be taken care. In case of visualizing time dependent features, integration is to be optimized with S/N and time varying scale in the object.

xi. Source flux

Source flux at object position is very important to maximize interaction with internal features and image statistics. At detector position, it is important for maximizing signal to noise ratio or reducing integration time. Filters for reducing the unwanted flux and focusing devised for increasing the flux are used as per the experimental requirements.

1.6 Optimization of image quality in experimental condition

The quality of images produced in PB-PCI is measured in terms of resolution, contrast, and signal to noise ratio and it is strongly correlated with the characteristics of imaging system. One major objective of this work is to study optimization of experimental parameters to achieve high quality in X-ray & neutron imaging. The resolution in PB-PCI depends on imaging camera resolution and unsharpness introduced in the image due to finite source size, beam divergence and energy spread of

the incident beam. For cone beam source, small source size, or high degree of collimation of the radiation source together with high detector resolution is essential for achieving high resolution with good contrast. For parallel beam with divergence, image resolution can be improved using high-resolution camera with large propagation distance and monochromatic beam source however; high beam flux would be required. Imaging camera resolution depends on scintillator thickness, optical magnification employed and pixel size of CCD detector. Selection of high resolution camera also requires a high flux source due to their low efficiency. The SNR depends on detectors electronic noise, statistical noise, source flux, detector pixel size, image acquisition time etc. and can be maximized using detectors with less electronic noise, applying appropriate cooling, employing high flux source and large acquisition time while avoiding detector pixels saturation. Phase contrast offers improved contrast sensitivity as compared to absorption contrast. In PB-PCI, image contrast is optimized with the appropriate choice of Fresnel propagation distance and beam energy. To maintain a good resemblance with the object features, the near field condition is required to be fulfilled. In this region, edge enhancement improves image contrast which increases with propagation distance z. The optimal choice of the distance should satisfy two competing requirements i.e. the sample-to-detector distance has to be large enough in order to convert the small angular variations to be visible with the detector spatial resolution but not so large that it induce blurring effects. Hence, contrast is related to image resolution. To achieve good contrast for low spatial frequency features, high lateral (spatial) coherence of the beam at the sample is required. Contrast is also

affected by sample thickness thus; beam energy should be employed to get sufficient transmission through it. The intensity of transmitted beam decreases with the thickness of the object, which also affects contrast and SNR

1.7 Literature review

Extensive review of literature related to individual problems addressed in this thesis is included in their respective discussions however; a broad historical development of micro-imaging concepts in X-ray and neutron imaging and their instrumental realization is presented here. X-ray & neutron imaging has a long history of applications in research and industry for non-destructive evaluation, security and medical diagnostic. With time, they were successfully implemented for imaging in higher dimension such as tomography, dynamic imaging etc. [52]. In last few years, a renewed interest in imaging research has resulted in large volume of high quality output, focused mainly on the invention of new contrast generation modes [53], their implementation to 3D imaging, dynamic imaging and in-situ modes[54,55],improving quality of images [33,50,56,57] etc. Several new and advanced applications in the diverse fields of research, industry, medicine have been discovered [58–62]. New modes of contrast based on scattering, diffraction, fluorescence are also being proposed and developed [39-42]. Imaging has become an active field of research in scientific community with the demands from wide range of users [57,64]. This was initiated with the introduction of the concept of phase contrast in optical images by Zernike [29,35,65–68]. Several modes of phase contrast implementation have been proposed such as crystal interferometer (CI) [69], diffraction enhanced imaging (DEI)[9,49],

propagation based phase contrast (PB-PCI) [12,33,63] and grating interferometers (GI) [35,70]. Neutrons phase contrast is also implemented in grating and propagation modes [71–73]. Due to improved contrast, phase contrast imaging has revolutionised field of imaging by allowing visualization of soft materials and tissues with small density variations, which were considered impossible earlier.

The phase contrast generated in X-ray and neutron images depends on object composition and several parameters of imaging system. Numerous theories have been proposed to explain mechanism of contrast generation in different PCI modes [46,74–77]. Extraction of quantitative phase at object plane also provide additional information about sample structure and density distribution not available in the acquired images however; this requires additional computational efforts. A large variety of algorithms have been proposed to allow extraction of quantitative phase map from the phase contrast images acquired using PB-PCI, DEI, and GI etc. In case of DEI and GI it is possible to extract quantitative phase, extinction, dark field, and absorption contrast images from acquired images [56,78–80]. PB-PCI specially requires complex computational methods for extracting quantitative phase due to complicated combination of contrasts in the image generated by attenuation and phase modulation by the object [14,34,63,80–84]. Limitations of projection imaging caused by inherent integration of overlying features along the beam propagation during image formation were surmounted after development of tomography and tomosynthesis techniques. In order to get images of local structures and density variations, concept of slice imaging was proposed. Hounsfield first proposed the computer reconstruction of 3D images out

of projection data which was previously being done manually or optically using shift and add method [40,42,52]. Further to this, computational concepts were proposed for slice reconstruction based on algebraic methods, filtered backprojection and Fourier methods [37,38,55,85,86]. Algorithms for reconstructing images from limited data, fast scan data, and region of interest data have also been proposed. Different algorithms within these domains have also been put forward for reconstructing slice images in number of experimental geometries[41]. Later efforts were put forward for improvements in reconstruction qualities via reducing image artifacts [55].

For the implementation of the absorption and phase contrast based micro-imaging techniques, several instrumental developments have taken place in X-ray and neutron imaging systems. State of the art imaging system are being developed with highly brilliant and coherent sources, sophisticated optics such as mirrors, monochromator and advanced imaging detectors. With the development of third generation synchrotron source, implementation of all PCI modes, μ-CT, phase contrast tomography and holotomography have been realized [87–90]. The techniques are now being combined with diffraction, fluorescence, and small angle scattering to extract wide range of sample information from the acquired images. Dedicated imaging beamlines have been developed at all major synchrotron facilities. These facilities are developing advanced coherent diffraction imaging and ptychography techniques to achieve resolution comparable to X-ray wavelength. Coherent diffraction imaging is implemented at PETRA-III, SPring-8, ESRF and APS among others and free electron lasers. With the help of advanced optics such as zone plates, mirrors and compund refrective lenses,

phase contrast microscopy has also been implemented with the resolution reaching up to 50 nm. Synchrotron based tomographic imaging technique has achieved several milestones in term of resolution, contrast. Further improvements of the image quality in terms of achievable resolution, lack of artefacts, reduced noise is being realized with the development of brighter sources, sophisticated optics and advanced detectors[15,91,92].

In most tomography work, the reconstruction of distribution of the imaginary part of refractive index in the object is obtained from intensity measurements based on absorption. In recent years, effort has been made to develop tomographic reconstructions based on phase information. The reconstruction of the full complex refractive index in a slice has been achieved by some groups from amplitude and phase reconstructions [93–96]. With the application of some advanced image segmentation and geometrical measurement algorithms, phase contrast tomography has also been applied to microstructure analysis studies on several material science and biomedical imaging related problems to optimize experimental parameters for their manufacturing, study of undergoing process and effect of various external effects, structure property co-relation and modelling of advanced materials[97–102].

2 SIMULATION STUDIES

While applying imaging techniques to practical applications, recorded images do not provide all the encoded information. Several post processing operations are needed to extract qualitative and quantitative information from the object image under study. Phase retrieval, tomography slice reconstruction, 3D volume rendering, feature segmentation and morphological quantification are a few examples of such post processing operations for which several methods and algorithms have been proposed and applied. In this chapter we have discussed some of these algorithms for phase retrieval and tomosynthesis through simulation studies and experimental validation.

2.1 Theory of phase retrieval

Purpose of phase retrieval is to determine 2D distribution of phase shifts introduced by the sample to the incident wave. The phase shift is related to scattering properties of an object and measured in terms of arguments of wave function at object plane i.e.[28]

$$[\Phi = arg(U_{out}) - arg(U_{in})e^{ikz_0} = -k\int_0^{z_0}\delta(z)dz] \qquad (2.1)$$

Since the measurements in imaging are always limited to intensity, which is proportional to amplitude square of the wave function thus direct measurement of

phase, is not possible yet. In various PCI techniques, phase contrast is enhanced through diffraction/interference but the images also combine contribution of absorption, scattering etc. Special techniques have been developed to extract phase of the outgoing wave either through optical instruments such as crystals, phase plate, gratings, coded aperture or computational algorithms or with their combinations. The simplest is for interferometry, which only requires unwrapping of the 2π phase shifts however it is difficult to implement experimentally whereas the PB-PCI is most demanding as it requires lot of computational work, however its also easiest to implement experimentally.

When applied to 3D imaging, PCI is quite useful even without phase retrieval because the contrast enhancement property of PCI improves visualization of the object structure any data processing. Applying the standard filtered back-projection CT reconstruction algorithm, qualitative analysis can be performed and the results are proportional to first or second derivative of refractive index distribution. For example, in case of PB-PCI, the quantity reconstructed is proportional to the Laplacian of the refractive index distribution and provides edge-enhancement. Such a reconstruction is called propagation phase contrast tomography (PPCT). The requirement of phase retrieval in micro-imaging applications is three fold. Diffraction fringes in the PB-PCI improves visibility of features having different refraction properties and enhances spatial resolution; but they may also lead to unpleasant artefacts in computerized tomography due to sharpness at the edges, and these can be reduced using phase retrieval. In addition to that, fringes in PB-PCI projections contain phase information

related to distribution of electron density of the object, which can be extracted by means of phase retrieval. Phase retrieval also helps in improving contrast sensitivity of PCI. Computational methods are used for extracting quantitative phase map at object plane from the projection images [63,84,103]. After phase retrieval, the projection images show integrated distribution of real part of complex refractive index, which is directly proportional to material electron density. Phase retrieved images are predominated by the real part of the refractive index without any edge effects. CT applied to these projections provides 3D distribution of refractive index of the material. In the qualitative CT analysis, this makes distinguishable various material phases with quite similar density. When applied for deducing quantitative micro-structure using image analysis methods, this enables feature segmentation, identification and measurement of porosity, shape, size, uniformity etc.

Several phase-retrieval algorithms have been proposed for PB-PCI. These algorithms may require multiple or single PCI projections to retrieve quantitative phase depending upon accuracy and experimental ease required. In general, at least two intensity measurements, taken at two different object to detector distances or wavelengths are required to retrieve the unique phase modulation introduced by the object. The algorithms which require more than one image are transport of intensity equation (TIE) method [24],the contrast transfer function (CTF) method [23], the mixed approach between the CTF and TIE method [25,26], iterative methods etc. Phase can also be retrieved using single image with a priori information about the sample composition using Born type approximation method [27], Paganin method,

Rytov approximation method, Wu method and Bronnikov algorithm etc. In this section, various phase retrieval methods based on multiple and single PB-PCI projection images are compared through simulation studies and experimental validation.

a) Multi distance algorithms

CTF (Eq. 1.2) is the most fundamental equation to discuss phase retrieval. It relates intensity modulation in the acquired image with the phase modulations introduced by the sample in the incident wave, propagation distance, and monochromatic beam wavelength through sine and cosine function hence can be used for phase retrieval by virtue of inversion. Because this expression is a result of an approximation, the final formula used to retrieve phase information is obtained by performing a least square minimization of the measured intensity and expression in the CTF equation. Images for least square minimization can be acquired at various propagation distances. We define a cost function in reciprocal space as[45,47,84]

$$S_z = \frac{1}{N}\sum_{m=1}^{N}\int df\left|\tilde{I}_{z_m}^{Exp}(f) - \tilde{I}_{z_m}^{Approx}(f)\right|^2 \qquad (2.2)$$

The summation is over N images acquired at different distances. From CTF equation

$$\check{I}_z(u) = I_0[\delta(u) - 2\check{\mu}(u)\,cos(\pi\lambda z u^2) + 2\check{\varphi}(u)\,sin(\pi\lambda z u^2) \qquad (2.3)$$

Minimization of this cost function $\partial S_z/\partial\phi = 0$ with respect to distances results in following expression for object phase and absorption

$$\tilde{\phi}(u) = \frac{1}{2\Delta+\alpha}\left[C\sum_z \tilde{I}_z^{Exp}\sin(\pi\lambda z u^2) - A\sum_z \tilde{I}_z^{Exp}\cos(\pi\lambda z u^2)\right] \qquad (2.4)$$

$$\tilde{B}(u) = \frac{1}{2\Delta+\alpha}\left[A\sum_z \tilde{I}_z^{Exp}\sin(\pi\lambda z u^2) - B\sum_z \tilde{I}_z^{Exp}\cos(\pi\lambda z u^2)\right] \qquad (2.5)$$

Where $A = \sum_z \sin(\pi\lambda z u^2)\cos(\pi\lambda z u^2)$ $B = \sum_z \sin^2(\pi\lambda z u^2)$ $C = \sum_z \cos^2(\pi\lambda z u^2)$ $\Delta = BC - A^2$ and α is a regularising term chosen to minimize the standard deviation outside the object image in tomographic data at one projection angle and then used for the whole tomographic data set.

b) Multi energy approach

Similar to multi-distance approach, the cost function can be minimized with respect to wavelength also. We have developed a new variable wavelength based phase retrieval method in CTF formulation. In this case, data is collected at multiple wavelengths, away from the absorption edges of the material present in a given object. The dependence of the real and imaginary parts of the complex refractive index on the wavelength of the incident radiation in the absence of absorption edges between λ and λ' for any elements present in the sample is assumed to follow the relation [104]

$$\beta(\mathbf{r},\lambda) = (\frac{\lambda}{\lambda'})^4 \beta(\mathbf{r},\lambda') \quad \delta(\mathbf{r},\lambda) = (\frac{\lambda}{\lambda'})^2 \delta(\mathbf{r},\lambda') \tag{2.6}$$

It may be noted that these relations hold good in the x-ray energy region where photoelectric effects dominate. When the above relations hold, the following relation exist between the absorption and phase at two different wavelengths

$$\phi(\mathbf{r},\lambda) = (\frac{\lambda}{\lambda'})\phi(\mathbf{r},\lambda') \; \mu(\mathbf{r},\lambda) = (\frac{\lambda}{\lambda'})^3 \mu(\mathbf{r},\lambda') \tag{2.7}$$

The cost function is defined as $S_\lambda = \frac{1}{N}\sum_{m=1}^{N} \int df \left| \tilde{I}_{\lambda_m}^{Exp}(f) - \tilde{I}_{\lambda_m}^{Approx}(f) \right|^2$ and minimized with respect to wavelength. Considering CTF equation is derived for different wavelengths and the data collected at the wavelength λ_1, having phase ϕ_1 and

absorption μ_1 is image I_{λ_1} and wavelength λ_2, having phase $\emptyset_2$ and absorption μ_2 is image I_{λ_2}

$$\check{I}_{\lambda_1}(u) = I_0[\delta(u) - 2\tilde{\mu}_1(u)\, cos(\pi\lambda z u^2) + 2\tilde{\varphi}_1(u)\, sin(\pi\lambda z u^2)$$

$$\check{I}_{\lambda_2}(u) = I_0[\delta(u) - 2\tilde{\mu}_2(u)\, cos(\pi\lambda z u^2) + 2\tilde{\varphi}_2(u)\, sin(\pi\lambda z u^2)$$

from equation (2.7) $\phi_2 = \alpha\phi_1\ and\ \mu_2 = \alpha^3\mu_1$ where $\alpha = {}^{\lambda_2}/_{\lambda_1}$

$$\check{I}_{\lambda_2}(u) = I_0[\delta(u) - 2\alpha^3\tilde{\mu}_1(u)\, cos(\pi\lambda z u^2) + 2\alpha\tilde{\varphi}_1(u)\, sin(\pi\lambda z u^2)$$

When placed in cost function and minimized using ${}^{\partial S_\lambda}/_{\partial\phi} = 0$, we get following expressions for object phase and absorption

$$\tilde{\phi}(u) = \frac{1}{2\Delta+\varsigma}\left[C\sum_\lambda \tilde{I}_\lambda^{Exp} \sin(\pi\lambda z u^2)\alpha - A\sum_\lambda \tilde{I}_\lambda^{Exp} \cos(\pi\lambda z u^2)\alpha^3\right] \quad (2.8)$$

$$\tilde{B}(u) = \frac{1}{2\Delta+\varsigma}\left[A\sum_\lambda \tilde{I}_\lambda^{Exp} \sin(\pi\lambda z u^2)\alpha - B\sum_\lambda \tilde{I}_\lambda^{Exp} \cos(\pi\lambda z u^2)\alpha^3\right] \quad (2.9)$$

$$A = \sum_\lambda \alpha^4 \sin(\pi\lambda z u^2)\cos(\pi\lambda z u^2)\ B = \sum_\lambda \alpha^2 \sin^2(\pi\lambda z u^2)\ C = \sum_\lambda \alpha^6 \cos^2(\pi\lambda z u^2)$$

$\Delta = BC - A^2$ and ς is a regularising term choosen to minimize the standard deviation outside the imaged object at one projection angle and then used for the whole tomographic data set. This equation is very similar to equation (2.4) except for wavelength-dependent weight factors. Equation (2.4) and (2.8) were used to simulate the extraction of projected phase map from PB-PCI images in the subsequent sections.

c) Single image algorithms

Instead of taking multiple images, if phase retrieval is tried from a single image, there could be infinite combination of absorption and phase distributions in the object that

would give rise to the registered intensity distribution. Therefore, the phase retrieved from only one image will not be unique. However, if the investigated samples are not completely unknown, a prior knowledge can be used to reduce the number of required images. Several phase-retrieval algorithms requiring only a single PB-PCI image has been proposed but they are applicable under very stringent conditions on sample composition and experimental parameters. The most common assumption on material properties is that the absorption is constant and thus can be neglected, or that absorption and phase coefficients β and δ are proportional to each other. The first condition is generally referred as pure phase object condition whereas the second condition is called phase-attenuation duality (PAD) condition. PAD condition states that if the imaging beam energy is higher than 30 keV, Compton scattering dominates in attenuation, so that both δ and β are proportional to the local density of the object, and their ratio is constant throughout the 'monomorphous' object.

$$\delta(r) = \varepsilon\beta(r) \tag{2.10}$$

Where ε is a constant. With the linearity property of Fournier transform, we can obtain

$$\tilde{\varphi}(u) = \varepsilon\tilde{\mu}(u) \tag{2.11}$$

In this section, we have reviewed some of the popular algorithms used for phase retrieval using single images and their validity conditions. Individual methods may come with their own additional conditions of validity [45,78,81,82,84,105,106].

i. Born Algorithm for pure phase Object:

CTF equation can be written in the following form after some rearrangement of terms

$$F\left[\left(\frac{I_z}{I_0}-1\right)/2\right] = \check{\mu}(u)\cos(\pi\lambda z u^2) + \check{\varphi}(u)\sin(\pi\lambda z u^2)$$

For the case of pure phase object $\mu = 0\ if\ I_0 = 1$; above equation can be solved for φ

$$\varphi = F^{-1}\left\{\frac{F[(I_z-1)/2]}{\sin(\pi\lambda z u^2)}\right\} \quad (2.12)$$

This equation can be used for retrieving phase map of a pure phase sample from a single propagation phase contrast image[105,107].

ii. Born algorithm under PAD condition

Since there is always a finite absorption in the object, the applicability condition of Born algorithm i.e. object being "pure phase object" is rarely satisfied. The residual absorption in the object corrupt the retrieved phase therefore using PAD property of low-Z object, the phase function in eq. (2.12) is re-formulated thereby the artefact can be removed. In the case of weakly absorbing sample, i.e. $I_0 \approx 1$ and substituting equation (2.11) into CTF equation and rearranging, we get

$$\varphi = F^{-1}\left\{\frac{F[(I_z-1)/2]}{\epsilon^{-1}\cos(\pi\lambda z u^2)+\sin(\pi\lambda z u^2)}\right\} \quad (2.13)$$

A priori knowledge of the sample in terms of δ and β can be obtained from x-ray database[105].

iii. Boronikov algorithm

Boronikov derived an equation relating projection intensity images in phase contrast mode collected at certain distance on various rotation angles of the sample and 3D distribution of object phase based on TIE and 3D Radon transform [108]

$$\delta(r) = \frac{1}{4\pi^2 z}\int_0^{\pi} q(r) **\ g_\theta(r)\, d\theta \quad (2.14)$$

Where $g_\theta(r) = \frac{I_{\theta,z}}{I_{\theta,0}} - 1$ and $q(r) = \frac{|y|}{x^2+y^2}$ is a filter. (2.15)

iv. Boronikov algorithm under PAD condition

Groso introduced an absorption correction factor (ACF: α) to modify the filter for weakly absorbing sample ($I_{\theta,0} \approx 1$). In Fourier space, the modified filter is

$$Q(u) = \frac{|\xi|}{\xi^2+\eta^2+\alpha} \quad (2.16)$$

With this filter the Boronikov algorithm is called Modified Boronikov Algorithm (MBA)[78,81,109,110].An appropriate α value is necessary for faithful reconstruction, which is determined using a semi empirical approach. A too small ACF value will result in blurring, while the filter will be eliminated with a too large value. Based on the PAD property of low-Z sample, an approximate value of ACF can be estimated using

$$\alpha = \frac{1}{\pi\epsilon\lambda z} \quad (2.17)$$

v. Rytov algorithm

According to Rytov type approximation the intensity at image plane is given by

$$F\left[ln\left(\frac{I_z}{I_0}\right)/2\right] = \check{\mu}(u)\,cos(\pi\lambda z u^2) + \check{\varphi}(u)\,sin(\pi\lambda z u^2) \quad (2.18)$$

If the object satisfies PAD and weakly absorbing conditions, this eq. can be solved for

$$\varphi = F^{-1}\left\{\frac{F\left[ln\left(\frac{I_z}{I_0}\right)/2\right]}{\epsilon^{-1}cos(\pi\lambda z u^2)+sin(\pi\lambda z u^2)}\right\} \quad (2.19)$$

vi. Paganin algorithm under PAD condition

Using TIE formulation, Paganin proposed a method to reconstruct the projected thickness t(x, y) of the homogeneous sample using a single defocused image [80,111].

Using this we can simultaneously extracts phase and amplitude information. The projected thickness of the object t(x, y) is given by:

$$t(x,y) = \frac{1}{\mu} ln\left[F^{-1}\left(\mu \frac{F\left[\left(\frac{I_Z}{I_0}\right)\right]}{4\pi^2 z\delta(\xi^2+\eta^2)+\mu}\right)\right] \quad (2.20)$$

For weakly absorbing materials and $I_{\theta,0} \approx 1$, considering PAD and substituting $k = \frac{2\pi}{\lambda}$, the object phase function can be defined as

$$\varphi = \frac{1}{2}\varepsilon ln\left[F^{-1}\left\{\frac{F[I_Z]}{1+\pi\epsilon\lambda z(\xi^2+\eta^2)}\right\}\right] \quad (2.21)$$

vii. Wu algorithm with PAD condition

Starting from either the paraxial Fresnel–Kirchhoff diffraction or the phase-space evolution of the Wigner distributions for x-ray wave fields, Wu proposed following phase retrieval method using a single phase-contrast image

$$\varphi = \frac{1}{2}\varepsilon \ln\left[F^{-1}\left\{\frac{F[I_Z]}{1+\pi\epsilon\lambda z(\xi^2+\eta^2)}\right\}\right] \quad (2.22)$$

Object phase function can be retrieved using above formula if PAD and weakly absorbing approximation are satisfied [112]. The final single SDD phase retrieval equations of Paganin and Wu algorithms are same, as shown in Eq. (2.21) and (2.22).

2.2 Simulation Studies on phase retrieval

The performance of different phase retrieval algorithms utilizing multiple or single PB-PCI images is evaluated using computer simulation on a mathematical phantom as shown in Figure 2.1. This phantom is representative of a weak phase object for which the maximum phase shift was restricted to [0, 1] rad and data was simulated to have a pixel pitch of 1 μm in a matrix of 256 x 256 pixels.

Figure 2.1 Mathematical phantom used for simulation studies on phase retrieval

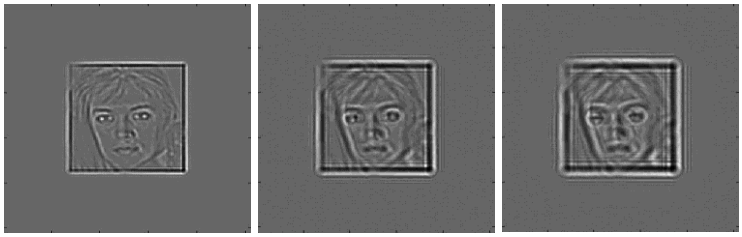

Figure 2.2 PB-PCI images of phantom at 2, 15, & 35 cm propagation distances

2.2.1 Multi-distance phase retrieval

We have carried out simulation studies for extraction of quantitative phase from simulated PB-PCI images of this phantom and later these results were confirmed on experimental data. Using computer simulation, PB-PCI images were obtained for the simulated phantom. Equation (1.2) was used for simulating the wave function in the near-field region at different object-to-detector distances. The Fresnel diffraction pattern was calculated at object-to-detector distances of z = 2, 15, and 35 cm. The raw data was convolved with a Gaussian function to simulate a realistic condition with finite detector resolution. For our calculation, the detector pixel size was taken as 5 μm. Figure 2.2 show the simulated intensity distributions i.e. PB-PCI images of the simulated phantom at different propagation distances. Retrieved phase map from these

projections using multi distance algorithms discussed in section 2.1 is shown in Figure 2.3. In this simulation Eq. (2.4) was used for retrieving the projected phase map.

Figure 2.3 Phase map retrieved at object plane using multi-distance method

Experimental application:

The sample considered for experimental studies is alumina microspheres coated with pyro carbon. The diameter of alumina micro-sphere is 500 μm while the thickness of the pyro-carbon coating is 40 μm. Table 1 shows the comparative values of δ and β at different energies for the alumina and pyro-carbon. The integrated values of phase shift for alumina and pyro-carbon at E=16 keV are 128 and 11.56 while integrated values of attenuation term for alumina and pyro-carbon at E=16 keV are 0.38 and 0.0039, respectively. The ratio of X-ray absorption term for alumina to that of pyro-carbon is quite high even though their respective values are too small for good X-ray radiography while the phase shift terms are comparable. Hence, these samples are most suited for characterization using the X-ray phase contrast technique. The PB-PCI images were acquired using SYRMEP beamline at the Synchrotron, Trieste (Italy) [113] for these studies. The beamline is characterized by a large source-to-sample distance of 22 m and a monochromatic laminar-section X-ray beam with a maximum area of 120 mm^2. The provision to vary sample-to-detector distances up to 1.8 m is

available for the PB-PCI experiments. A CCD detector and fiber-optic combination having an effective pixel pitch of 4.5 μm was used to collect high-resolution phase contrast images. Figure 2.4 shows experimental phase radiographs of alumina microsphere samples coated with pyro-carbon at different object to detector distances. The edge enhancement at the two different interfaces can be clearly seen. This technique, thus, can be easily used to identify the coating thickness and its uniformity in a non-destructive way. The experimentally measured thickness of pyro-carbon was calculated to be 40μm.

Table 2.1 Comparison of real and imaginary part of refractive index of alumina and carbon materials of phantom used in the experimental studies

E (keV)	**Al_2O_3 (δ) X 10^{-6}**	**Al_2O_3 (β)X 10^{-9}**	**C (δ)X 10^{-6}**	**C (β) X 10^{-9}**
16	3.159	9.485	1.78	0.586
18	2.456	5.785	1.41	0.350
20	1.980	3.802	1.142	0.222

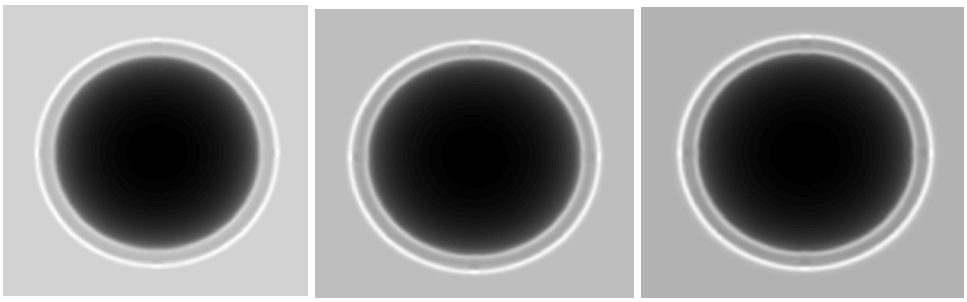

Figure 2.4 Experimental PB-PCI images of alumina particles at 15, 35 and 50 cm.

The phase map of the pyro-carbon coated alumina microsphere and its profile plot along the central row is shown in Figure 2.5.This figure shows the retrieved integrated

phase map of pyro-carbon using Eq. (2.4). The integrated phase data shows the irregular structure within the alumina kernel, i.e. lowering of alumina density as one moves towards edges, which are not easily visible in the simple phase radiograph. The phase profile in Figure 2.5 (b) indicate that experimentally evaluated phase shift values are in good agreement with sample data, thereby validating the CTF based method of phase retrieval. We have also tried to retrieve the thickness map of the object, treating it purely as a two-component system and using theoretical values of attenuation coefficients of alumina and pyro carbon [84,114]. The estimated thickness of alumina micro-sphere is found to be 490 µm and that of pyro-carbon matrix to be 42 µm in confirmation with their actual values (Figure 2.6).

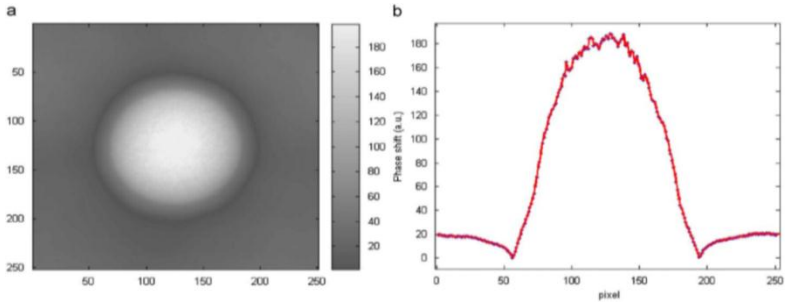

Figure 2.5 Phase map retrieved from the experimental images of alumina particle and its profile plot along the central row

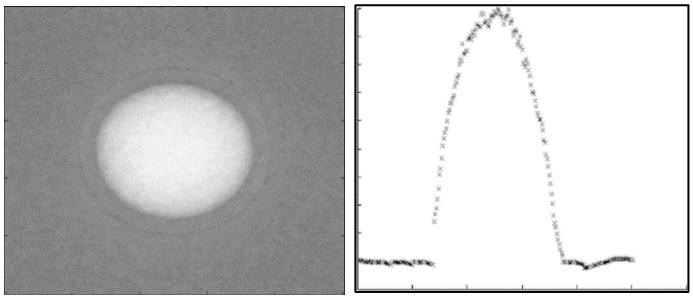

Figure 2.6 Thickness map of the alumina particle calculated from the phase retrieved

2.2.2 Multi energy phase retrieval

Similar to multi-distance algorithm, simulation studies on variable wavelength method were also carried out on a mathematical phantom (Figure 2.1) using equation (2.8) for retrieving the phase map from the simulated Fresnel diffraction. Keeping the object to detector distance fixed at 20 cm, the Fresnel diffraction patterns were simulated using equation (2.2) at three different energies, E= 16 keV, 18 keV and 20 keV (Figure 2.7) and the phase map was retrieved using the variable wavelength approach using eq. (2.8) is shown in Figure 2.8. It can be seen that the phase retrieved using the multi-wavelength approach is in agreement with the existing variable-distance approach.

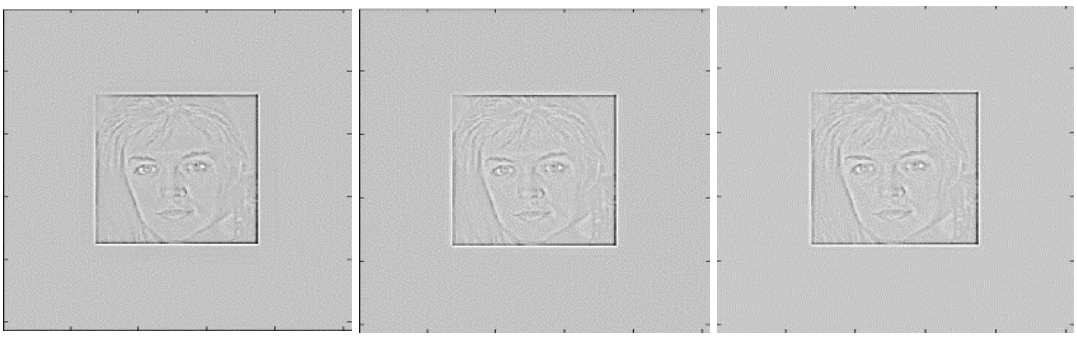

Figure 2.7 PB-PCI images of simulated phantom at beam energies 16, 18, 20 keV.

Figure 2.8 Phase retrieved using variable wavelength approach for simulated phantom

Experimental application

Experiments were carried out using SYRMEP beamline at Synchrotron Trieste (Italy) as described earlier. Silicon aerogel with fibrous structure was chosen as a low-absorption sample for application of the multi-wavelength formulation of phase retrieval. These aerogels have some very interesting properties such as low density, high strength etc. They are used to produce clean fuels, to insulate windows and even clothing, to study the percolation of oil through rock, and as drug-delivery systems. Figure 2.9 show phase radiographs of the sample at different energies. The object-to-detector distance was kept at z = 50 cm. It can be seen from these figures that, as the energy of the X-ray increases, the edge contrast decreases. This is in accordance with the fact that the phase shift decreases with increase in energy. Moreover, even with the flat-field correction, the effect of an inhomogeneous background owing to a beryllium window was not properly corrected. The noticeable variation in background across the image can be seen in these phase radiographs. The phase radiographs at three different energies (E= 16 keV, 18 keV and 20 keV) were used as input to equation (2.8). The retrieved projected phase map of the sample is shown in Figure 2.10. The quality of reconstruction critically depends upon the signal-to-noise ratio. In this experiment, we could not properly remove the effect of inhomogeneous absorption of the beryllium window, thereby achieving a poor signal-to-noise ratio, which resulted in an inhomogeneous variation of the background in the reconstructed image. However, the major features such as fiber structures can be easily recognized and located. This experiment shows that within the framework of the CTF-based approach one can

retrieve the projected phase map using the multi-wavelength-based formulation. This method can be used as an alternative approach to the existing method of distance based phase retrievals when variations with respect to different distances are difficult to perform, owing to constraints of the experimental set-up, and retrieval of the phase information is important.

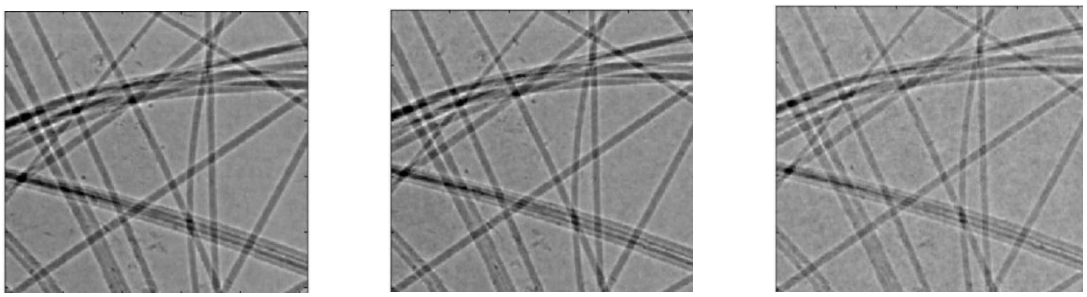

Figure 2.9 Experimental propagation phase contrast projection images of Silicon aerogel with fiberous structure with beam energies at 16, 18 and 20 keV.

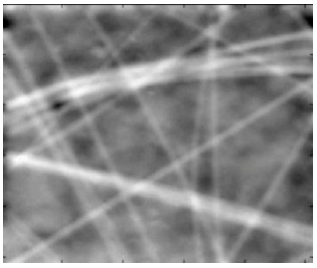

Figure 2.10 Phase Retrieved of silicon aerogel using variable wavelength algorithm

2.2.3 Single image phase retrieval

Single image phase retrieval algorithms are applicable strictly under the following validity conditions - The object consists of a single, homogeneous material or there lies a definite proportionality between real and imaginary part of the refractive index, monochromatic radiation is used and the distance between the object and detector

fulfils the near-field condition. Apart from these, some of the algorithms are applicable in the higher energy range only where Compton scattering dominates. In practical applications to material science fulfilment of all these conditions is rarely possible. The objects are in-homogeneous & introduce significant absorption to the incident beam. In practical application such as clinical diagnostics, utilization of monochromatic radiation is also not always possible and portable polychromatic sources are used. Sample may need to be placed at a finite distance due to experimental constraints such as in case of in-situ imaging where in-situ rigs causes a finite distance between object and detector. Thus, it is interesting to test the performance of certain single image phase retrieval algorithms when their validity conditions are not fulfilled. This will be very helpful in choosing suitable method for phase retrieval in practical applications. Several studies in past have been performed to compare phase retrieval algorithms, utilizing single and multi-image phase contrast projection data [45,78,81,82,84,105,106]. R.C. Chen et al have compared the performance of several single distance phase retrieval algorithms using simulation studies & fabricated phantoms of different composition [81,105,110]. Statistical and structural noise present in the images is shown to have significant effects on retrieved phases. The authors have also applied some of these algorithms for tomographic reconstruction. Wu et al. demonstrated that these kinds of algorithms can be applied for biological samples which are predominately composed of materials with a low atomic number ($Z< 10$) even when their validity conditions are not satisfied [115]. A few examples of applying single distance phase retrieval in practical application have also been reported. S.

mohammadi used mouse lung sample even in the presence of material with Z> 10 such as bone where samples do not fulfil the preconditions of a ‘homogeneous’ object. It has been found in these cases that the image quality is dramatically increased by single-distance phase retrieval and exceeds that of PBI [106]. This however has been pointed out that single-distance phase-retrieval algorithms cannot be used to calculate the δ value distribution of the refractive index in samples with a strong variance of δ/β ratios. In spite of these studies, the comprehensive comparison of performance of various single distance phase retrieval algorithms is not available yet on real experimental data of material samples when their validity conditions are not strictly satisfied. In order to find phase retrieval methods suitable for holotomography of materials of practical applications, we have compared the performance of various single image phase retrieval algorithms on real experimental data.

Materials

The samples chosen for our study represent two different cases of composition. The first sample is made of polyethersulphone (PES) having homogeneous but porous structure. The ratio of δ/β is uniform for the whole sample. The geometry of the sample is spherical and thickness varies from centre toward outside. The other sample is composed of several different materials with different densities and compositions. The sample also has layered structure with a spherical core in the centre. The thickness and density of different layers are given in Table 2.2. Thus, the samples considered cover a wide range of compositional and structural features such as low and high absorbing characteristics, random and porous or well-defined layered structures.

Experimental application

PITRE is an open source software providing application of several single image phase retrieval algorithms discussed in section 2.1 on PB-PCI images with the input parameter beam energy, propagation distance, ratio δ/β and regularisation parameter [116]. The performance of different single distance phase retrieval methods is compared using PITRE.

Table 2.2 Density and thickness of coating layers in TRISO coated fuel particle.

Coating Layer	Density (g/cm^3)	Coating thickness (μm)
Buffer	1.1	95
Inner PyC	1.9	40
SiC	3.18	35
Outer PyC	1.9	40

We have considered PAD Born Algorithm (PAD-BA), PAD Rytov Algorithm (PAD-RA), PAD Modified Bronnikov Algorithm (PAD-MBA), PAD Paganin algorithm (PAD-PA), and PAD Wu Algorithm (PAD-WA) and compared their performance for both the samples. The first sample (polymer bead) is a low absorbing homogeneous porous sample fulfilling condition of PAD. Hence, it is completely applicable for PAD-BA, PAD-RA, PAD-MBA, PAD-PA and PAD-WA however due to finite absorption, the sample cannot be considered as pure phase object hence does not satisfy validity condition of PO-BA and Bronikov. For the second sample condition of low absorption as well as PAD is violated. PB-PCI images were acquired for both the sample at beam

energies and propagation distance such that near field condition and monochromatic beam condition is satisfied (at 10 mm propagation distance and 10 keV beam energy for polymer bead and 15 mm propagation distance and 15 keV beam energy for TRISO particle). Different single image phase retrieval algorithms were applied to retrieve quantitative phase distribution at object plane and the resulting phase maps are compared in Figure 2.11.

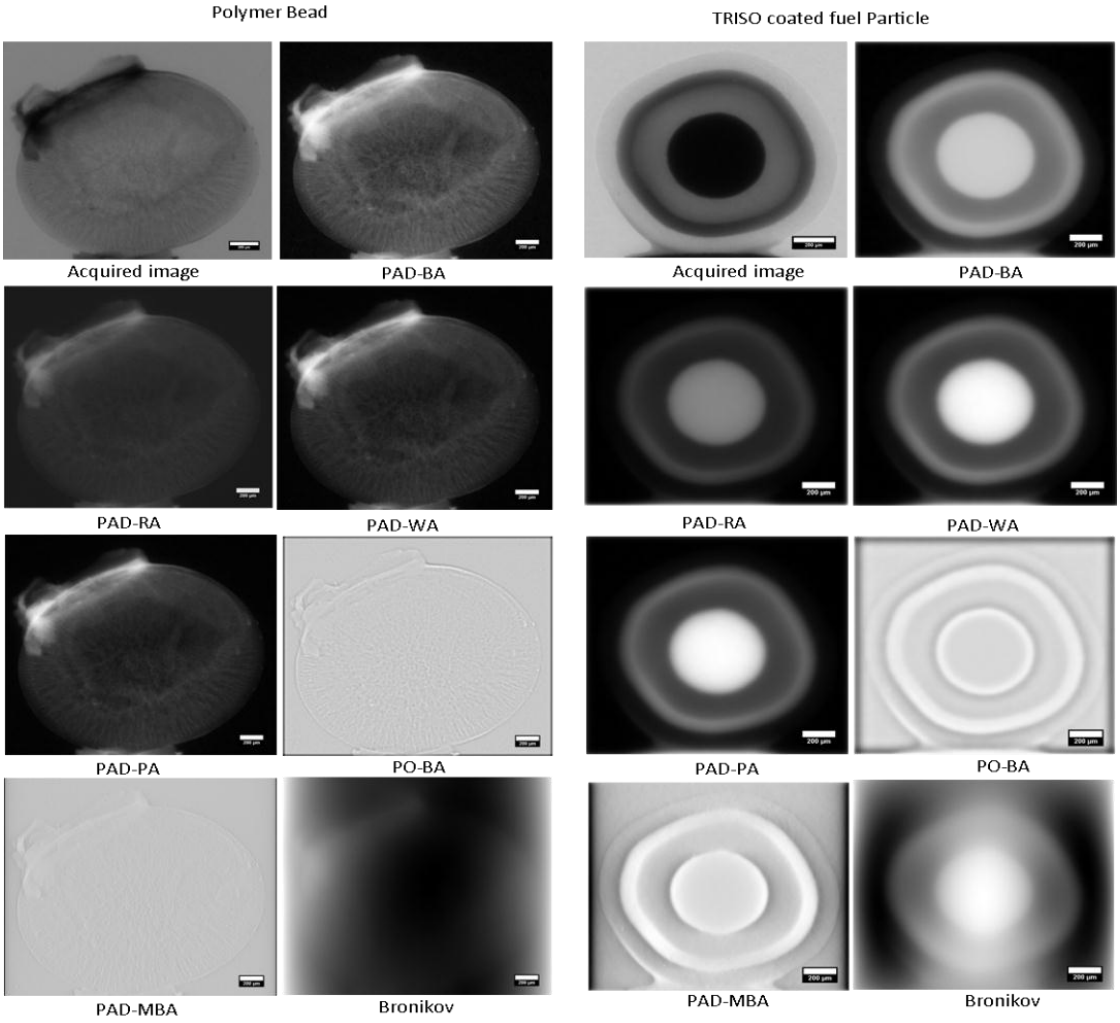

Figure 2.11 Comparison of various single image phase retrieval methods for Polymer Bead and TRISO coated fuel particle. [Scale bar = 200µm for all images]

As can be seen from these images, the performance for quantitative reconstruction of refractive index distribution is quite different for different single distance phase retrieval algorithms on the two samples. While some of the algorithms perform reasonably well, others fail miserably under violation of these validity conditions. For the low absorbing polymer bead sample, the performance of PAD-BA, PAD-PA/WA appears to be good as compared to other algorithms. The structural resemblance is good and does not get affected due to finite absorption in the sample. The contrast in these images is also improved and one can see the internal porous structure more clearly in the phase retrieved image as compared to the acquired PCI image. PAD-RA and PAD-MBA also reconstruct the quantitative phase and have good resemblance with the object features but the contrast between the structural features is poor as compared to PAD-BA and PAD-PA/WA. Other algorithms such as PO-BA and Boronikov do not show any similarity with the acquired image and found to be inapplicable. This is because the necessary conditions for these algorithms are not fulfilled. Similar results are seen for highly absorbing multi-layered TRISO coated fuel particle sample also though there are differences in the performance of PAD-RA/ PAD MBA, which have also shown good results in this case. Thus it can be concluded that if only the weakly absorbing condition is violated, the PAD-BA and PAD-PA/WA obtain better result than and PAD-RA/ PAD-MBA however they are acceptable whereas PO-BA and Boronikov fails in such condition. It can be however be noted that the performance of Boronikov algorithms is seen somewhat improved in TRISO sample as compared to Polymer bead. Thus, the application of single image phase

retrieval algorithms improves contrast and visibility of features of phase contrast images can be applied in tomography reconstruction to remove phase contrast artefacts.

Results and discussion

Simulation studies carried out on multi-image phase retrieval algorithms clearly show that the algorithms can quite successfully be used to reconstruct sample's phase map at object plane. The simulation results on standard phantom show that the performance of multi-distance and multi-energy algorithms are identical under the fulfilment of their respective validity conditions. When applied to experimental data, both the algorithms are able to accurately retrieve object phase map, which can also be used to reconstruct object thickness map if composition is already known. The phase retrieval also improves contrast sensitivity. Features not visible in acquired image start appearing in the retrieved phase map image as seen in the case of pyro-carbon coated alumina kernel particle. When combined to tomography, they can be used to reconstruct three-dimensional distribution of real part of X-ray complex refractive index of object. Due to their accuracy, these algorithms are the potential candidates for holotomography reconstruction. However, taking two or more images at different distances/energies at each rotation angle is difficult in tomography experiments where hundreds of images are required for slice reconstruction. This also causes extra step for alignment of acquired images due to imperfection in imaging system which results relative shifting of features in case of varying distance acquisition and variation of incident beam flux causing variation of noise in the image in case of varying wavelength. Multiple images also increases the total acquisition time per measurement thus reduces the possibility of

time dependent imaging and increases total dose delivered to the sample. On the other hand, for single image phase retrieval algorithms, the experimental studies carried out clearly show that if the validity conditions of these algorithms are satisfied they can fairly be used for reconstruct the quantitative phase map at object plane as seen in the case of polymer bead. This not only improves visibility of structural features in the image but also increases contrast sensitivity for lower density variation. The retrieved phase maps can also be used for tomography reconstruction with fair removal of phase contrast artefacts. However, when the validity conditions are not fulfilled, the application of these algorithms should be more careful as seen in the case of TRISO coated fuel particle. The improvement in contrast can still be seen for some of the algorithms while others may fail even to show any resemblance with object features.

Multi-image algorithms also have some restrictions on sample composition but they are quite relaxing as compared to single image algorithms. The disadvantage of multi-image algorithms lies in the complexity of their experimental data acquisition as discussed before but advantage lies in their more accuracy. Thus it can be concluded that the single image phase retrieval are easy and simple to use however valid under very stringent conditions and less accurate for quantitative extraction of real part of refractive index though can fairly be used for improved contrast and remove diffraction artefacts from phase contrast images. On the other hand multi image algorithms are more accurate and less stringent in their applicability conditions however more complex in their experimental data acquisition. Comparison of these algorithms for retrieval of quantitative phase and applicability to tomography for reconstruction of real

part of refractive index is being carried out. Comparison of noise sensitivity of these algorithms is the subject of our future studies.

2.3 Simulation studies on tomosynthesis

Tomosynthesis is a technique of producing slice images from a limited number of radiographic projections. Computed tomography (CT) discussed in the previous chapter is used quite successfully to provide 3D density distribution based on inverse radon transformation/filtered back projection however with the restriction of collecting projection images from all angle of incidence to the object while rotating about its axis. This restriction puts limitation on slice imaging of objects with laminar geometry or laterally extended objects such as printed circuit boards, plants leaves etc, where one dimension is significantly larger than the other one. This leads to inhomogeneous absorption of radiation within the object and only a limited number of projections collected at selected angles are of significance. Application of μ-CT methods results in inaccurate reconstruction with artefact in the slice images. To overcome this issue, alternative approaches called Tomosynthesis or computed laminography are developed for slice reconstruction from limited number of projections. The technique also finds potential applications in the imaging of objects having limited angular access due to sample environment rig used in in-situ imaging. It is also useful in reduced dose diagnostic imaging of biological specimens, fast tomography to study time dependent phenomena or reduced number of projections due to time constrains in case of scanning methods of imaging. As compared to CT and filtered back projection reconstruction method, tomosynthesis does not require complete 360^0 rotation of object about its axis.

Several approaches differing in scanning geometry or in reconstruction algorithms have been proposed such as shift and add method in iso-centric geometry, iterative reconstruction methods; tuned aperture CT, modified filtered back-projection, matrix inversion tomosynthesis and ectomography. These techniques have been extensively applied in the examination of circuit boards, weld crack examination, material microstructure and plant leaves [41,117–119]. A review of different limited angle reconstruction methods has been reported by Dobbins and Godfrey [40]. Recently limited angle reconstruction or laminography methods have found renewed interest due to potential applications in synchrotron imaging, fast tomography, reduced dose clinical imaging, and time dependent in-situ imaging. In this section we have discussed the simulation studies carried out on shift and add tomosynthesis based slice reconstruction for iso-centric rotational and translational data acquisition geometries.

2.3.1 Translational Geometry

In this geometry, projection images of object are collected using a cone beam source on an imaging area detector by stepwise translation of laminar object along two directions perpendicular to optical axis, equal to projection of detector pixel size on object plane as shown in Figure 2.12(b). In this scan various pixels of area detector successively record the information of a given volume element of the object under consecutively changing angles. The collected projection data is transformed by re-sorting the matrix of digital images in such a way that it represents a collection of parallel beam data for iso-centric motion of source and detector in opposite direction or swing motion of the object about the axis perpendicular to optical axis similar to iso-centric motion [Figure

2.12 (a)]. In this case, the angular scan range of iso-centric motion is equivalent to source cone angle [4, 5]. These projections contain the complete structure information of all object planes.

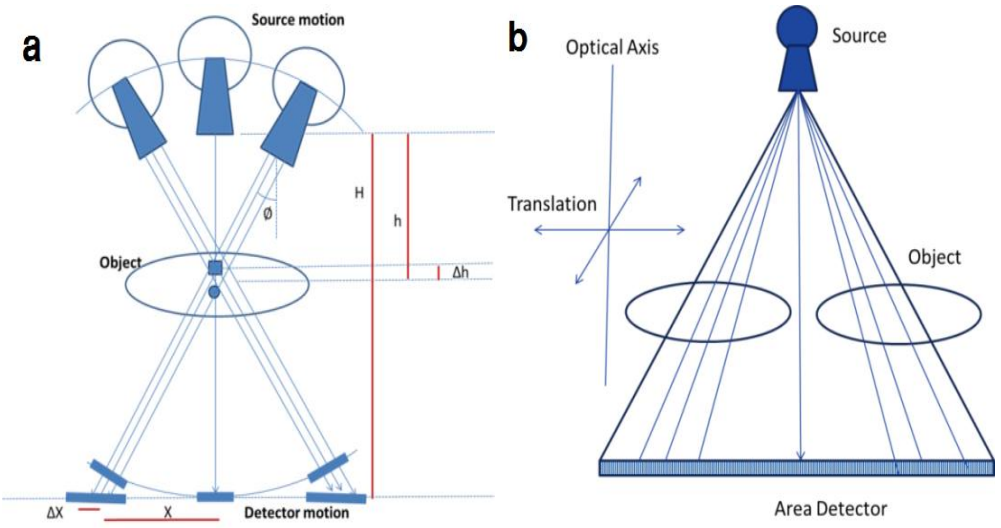

Figure 2.12 Data acquisition geometries considered for tomosynthesis simulation under limited angle projection (a) Iso-centric geometry (b) Translational geometry

2.3.2 Iso-centric Geometry

In this geometry the projection images are acquired while rotating the source and detector in opposite direction on a circular path with a stationary object at the centre of rotation or equivalently with swing motion of the sample about its axis while no source/detector motion as shown in Figure 2.12 (a). The projections can be collected using cone beam or parallel beam source. The radiographic images collected at different angles, project object features lying at different heights on different detector pixels depending upon angle of rotation, source to object and object to detector distances and location of the feature in the sample.

2.3.3 Shift and add method of Slice reconstruction

As discussed for both the geometries of data acquisition, the projection images can be obtained in the form of iso-centric motion projections. Several methods have been proposed for slice reconstruction at desired position but the most common is the so called 'Shift-And-Add' method first proposed by Grant. We have applied this method, which is based on analytical calculation of shift distance for various projections acquired at different angles followed by their pixel wise addition. The method is akin to (un-filtered) backprojection and based on the fact that objects at different heights above the detector will experience different degrees of parallax. As the tube moves, object features at different heights above the detector will project themselves at different location on the detector depending on the angle of beam incidence. When using linear geometry, the tube and detector move in synchrony in parallel planes so that the magnification of objects depends only on their height above the detector, not on the location of the tube or detector within these two planes. When these conditions are fulfilled, it is possible to shift and add the different images to bring a specific plane into focus[85]. During the first step, the images are shifted. The amount of shift, Δx, depends on the position of desired plane height above the detector. Considering the triangles created by the rays in Figure 2.12(a)**Error! Reference source not found.** and using equivalence of similar triangles, we can calculate exact length of shift as

$$\Delta s = \frac{H \times \Delta h. \times \tan\phi}{h} \qquad (2.23)$$

Where H is the focus-to-detector distance, h the distance from the tomographic plane (i.e.in-focus plane) and the tube, Δh the distance between the fulcrum and tomographic

plane (the plane to reconstruct) and 2φ is the tomographic angle. The projections are then added with the right amount of shift applied, so that the structures in plane of interest are all made to line up exactly and thus be in focus.

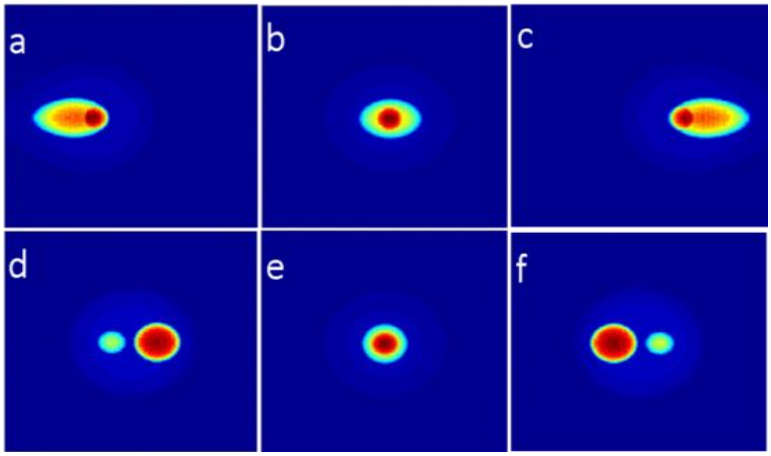

Figure 2.13. Simulated projection images in translational geometry keeping the object within the beam (a) The left most detector pixel (b) central pixel (c) right most detector pixel (d-f) Matching parallel beam projections after reshorting.

a) Simulated phantoms and projection data generation

Simulation studies were carried out for both the scan geometries on different mathematical phantom listed in Table 2.3 having different structures and composition. The first phantom is spherical phantom containing small spheres with various density, size, and location. The second one is Shep-logan phantom popular in clinical research for depicting breast lesions for mammography studies. It is suitable for studying features with different sizes and densities. Projection data for both the phantoms was generated for translation and iso-centric motion as shown in Figure 2.13. The cone

beam data in translational motion was converted to parallel beam projection data for iso-centric motion. Scan angle of 120 degree has been used in this case.

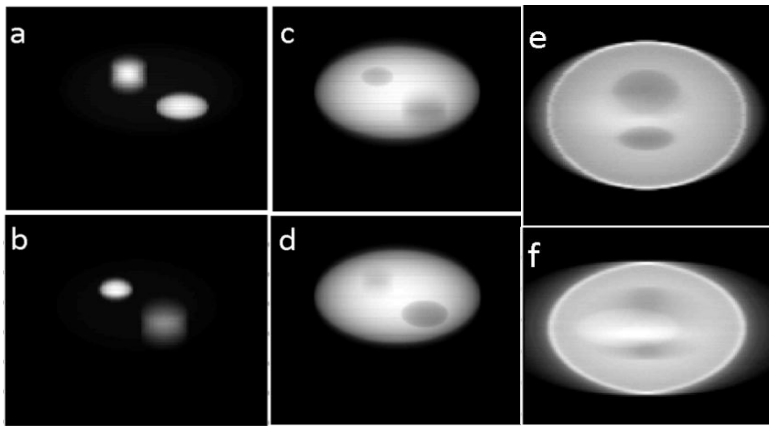

Figure 2.14 Tomosynthesis reconstruction (a, b) High density spheres in low density matrix (c, d) low density spheres in high density matrix (e, f) Shep-logan phantom

Table 2.3 Description of mathematical phantoms used in the simulation study

Case-1	**Small spheres of low density in high density matrix**
Case-2	Small spheres of high density in low density matrix
Case-3	Shep-logan phantom

b) Slice reconstruction using shift and add

For different cases, the reconstructed slices of these phantoms showing various planes are shown in Figure 2.14. The Figure show various features in the respective phantoms lying at different heights. The first column (a, b) show the reconstructed slice images of spherical phantom having high density small spheres embedded in low-density matrix. Figure 2.14 (a) show the top small sphere while bottom sphere is blurred whereas Figure 2.14 (b) show the bottom sphere where upper sphere is blurred. The blurring

introduced in particular plane reconstructed using tomosynthesis also depends on relative densities of features lying at other planes. Since the densities of the two small spheres is also different, the blurring in lower sphere is more caused by higher dense upper sphere whereas blurring in upper sphere is less due to lower dense lower sphere. Similarly the second column Figures 2.14 (c, d) show the reconstructed slice images of spherical phantom having smaller spheres of low density embedded in high-density matrix. The third column show reconstructed slice images of Shep-logan phantom. In the second phantom the densities of enclosed spheres was smaller as compared to matrix. It can be however noted that the shape and dimensions of features lying in the plane of interest is not distorted. Similar trend is seen in Shep-logan phantom in which the ellipsoid lying in the plane of interest is clearly visible while other features are blurred Figure 2.14 (e, f). All the results highlight the features in the desired plane whereas out of focus plane are blurred. Shapes, sizes and densities of features are also clearly distinguishable.

c) Results and discussion

The algorithms simulated are quite successful in retrieving the features in desired plane. The laminography methods discussed here although allow visualization of desired features in the respective plane but includes blurred contributions from out of plane structures. This limitation prevents the 3D visualization of sample volume unlike CT reconstructing pixel specific distribution of attenuation co-efficient. Recently a new geometry of reconstructing complete 3D volume without out of plane feature has been proposed and applied for microstructure analysis, which is the subject of future studies.

3 DEVELOPMENT OF ADVANCED MICRO-IMAGING FACILITIES

Design parameters of X-ray and neutron imaging system play an important role in determining its imaging capabilities and quality of images produced as discussed in chapter-1. Application of highly brilliant and coherent radiation sources, high resolution & high efficiency detectors and well-designed collimating and energy selective optics allows implementation of new imaging modes and improvement in resolution and contrast of the images. Keeping this in view, we have designed and developed two state of the art micro-imaging facilities based on synchrotron based X-ray and nuclear reactor based neutron sources to implement leading-edge micro-imaging techniques. These facilities are equipped with different type of optics and detectors to widen the utilization scope with the implementation of multiple imaging techniques in the same experimental station. In this chapter, we have discussed the design, specification, and important characteristics of micro-imaging facilities developed followed by their performance evaluation and first experimental results on various imaging techniques implemented.

3.1 Basic design of a micro-imaging system

The block diagram of a typical X-ray and neutron micro-imaging system is shown in Figure 3.1. The system typically consists of a beam-emanating source, beam processing optics, sample environments, sample holding and manipulation systems, detector manipulation system, imaging camera, image acquisition electronics, and image processing/analysis software etc. The performance of beam source is evaluated in terms of its beam emanating spot size, flux, collimation, bandwidth, emmitance, and coherence. In the last few decades, development of advanced beam sources such as third generation synchrotron sources, fission and spallation based neutron sources, and high power micro-focus X-ray tubes has raised the flux and coherence of incident beam by several orders of magnitude. To optimize the beam shape/size, flux, and bandwidth as per the experimental requirements, micro-imaging system may also use one or more optical instruments such as collimators, monochromator, mirrors, filters etc. A wide range of options is available for these optical components with multiple design options. For example, the energy selection for a synchrotron beam can be facilitated using different types of monochromators such as single or double crystal monochromators in Laue and Bragg geometries, multilayer monochromator, grating monochromators etc. Sophisticated sample holders and manipulators are used to place and align the sample in the beam with micron to submicron precision according to the data acquisition requirements of imaging technique. Imaging detectors are the integral part of imaging system. They are mostly CCD or CMOS based digital detectors whose performance is assessed in terms of pixel size, field of view, frame rate, quantum efficiency, and noise.

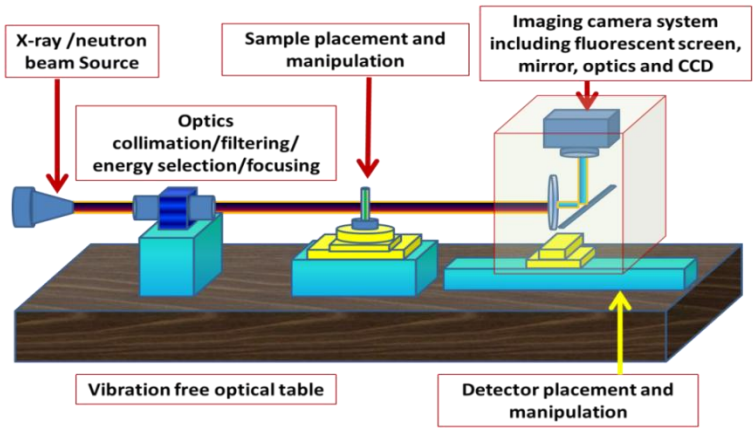

Figure 3.1 Schematic of X-ray or neutron micro-imaging system

Since quality of images obtained is strongly correlated with specification of these components, the choice of suitable parameters is extremely important. The implementation of several micro-imaging techniques in the same experimental station poses special challenge in design of imaging system due to large variation in the requirement of various imaging techniques in terms of sample handling; image detection and data analysis. Some of the techniques such as tomography, real time imaging, and in-situ imaging require additional instruments such as rotation stage, sample environment rig, and high frame rate camera. Apart from this, applications from various sectors in research and industry has placed specific requirements on imaging system in terms of sample geometry, structural resolution, time scale and dose induced thus imaging system is expected to have multiple options in its components and should be flexible to accommodate the required changes. In the forthcoming sections, we have discussed the design and specifications of two state of the art X-ray and neutron micro-imaging facilities developed at synchrotron and reactor based sources respectively along with their performance evaluation and feasibility experiments results.

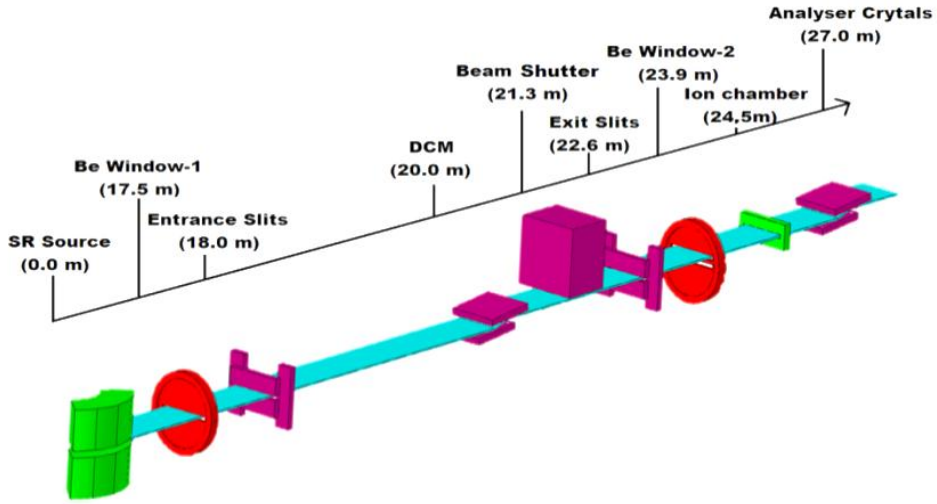

Figure 3.2 Optical layout of imaging beamline with component distances from source.

3.2 Development of synchrotron imaging beamline at Indus-2

In the last decade, development of third generation synchrotron sources has initiated revolutionary advances in X-ray imaging. With their high brilliance, coherence, and energy tunability, synchrotron sources allow faster image acquisition, better sensitivity, and higher resolution. Synchrotrons sources are ideally suitable for the implementation of phase-sensitive techniques such as PB-PCI, DEI etc. Moreover, even conventional techniques like X-ray absorption contrast imaging can benefit from the improved brilliance of synchrotron sources and allow dual energy imaging and studies of time dependent phenomena. We have designed, developed, installed and commissioned a full-field hard X-ray imaging beamline at 10º port of bending magnet (DP-2) of Indian third generation synchrotron source Indus-2[120]. Important parameters of beamline are summarized in Table 3.1. The beamline is operated in monochromatic and white beam mode. Micro-imaging techniques such as high-resolution radiography, PB-PCI

and DEI, absorption and phase contrast tomography, dual energy imaging, real-time imaging, large area imaging etc. are implemented. A list of experimental techniques implemented at imaging beamline is given in Table 3.2. The optical layout of the beamline and the distances of its major components from the tangent point are shown in the Figure 3.2. The beamline consists of four hutches i.e. front-end, optics hutch, experimental station, and control room. The front-end design of all the bending magnet beamlines in Indus-2 complex is identical [121]. All components up-to the exit beryllium (Be) window are included in the optics hutch and operated in ultra-high vacuum (10^{-9} mbar). Optics hutch is designed to perform specific tasks of beam preparation such as beam filtering, collimation and energy selection as per the experimental requirements. All components of the optics hutch downstream of the DCM are designed to allow monochromatic as well as white beam mode operation of the beamline. Instrumentation required for beam diagnostics and safety system are also included in the optics hutch. Major components of the beamline are water-cooled and their temperatures are measured continuously via thermocouples installed in the respective devices. The data is used as feedback for the equipment protection system (EPS) of the beamline to operate its components in safe condition and avoid any possibility of excess heating or contamination. The experimental station shown in Figure 3.3 consists of all the instruments required to perform sample holding, manipulation and alignment, imaging detectors, data acquisition electronics, beam analysis, vibration free optical tables etc. The beamline serves as a national facility and routinely used for X-ray micro-imaging in material and bio-medical applications.

Table 3.1 Beamline Characteristics

Parameters	Typical values
Source	Bending magnet, 1.5 T dipole
Operational modes	White and monochromatic
Monochromator	Si(111) Double crystal monochromator (DCM)
Energy range	8-35 keV
Energy resolution	(3.2×10^{-4} @ 12keV) in monochromatic mode
Beamline acceptance	5.5 mrad (H) X 0.5 mrad (V)
Photon flux	~ 1.74×10^{8} photons/s /mm^2/120mA at 12keV monochromatic energy and 25 m from the tangent point
Sample stage	Five axis (2D translation + rotation +2D tilt)
Detectors	CCD detector, Flat panel detector, X-ray microscope, Imaging Plate, Photo diode etc.
Detectors stage	3 axis manipulator for detectors (X-Y-Z)

Table 3.2 Different experimental techniques at imaging beamline

Hard X-ray imaging techniques	**Mono beam**	**White beam**
Absorption contrast micro-imaging	✓	✓
In line PCI	✓	✓
Diffraction enhanced imaging	✓	☒
X-ray μCT (absorption & phase contrast)	✓	✓
Laminography	✓	✓
Dual energy imaging	✓	☒
Real-time imaging	✓	✓

3.2.1 Indus-2 Synchrotron source

Indus-2 is a 2.5 GeV, 300 mA third-generation synchrotron source at RRCAT, Indore, India, with a critical wavelength of 2 Å [120,122]. It is being operated at energy 2.5 GeV and 150 mA current. It comprises of a double-bend-achromatic lattice with zero dispersion function along the straight sections. This yields a low-emmitance and high-brightness photon source for the bending magnets. The estimated photon source size (FWHM) for the bending magnets is 234 μm (H) X 237 μm (V).

3.2.2 Beamline optics

a) Filters:

Beryllium (Be) windows of dimensions 105 mm X 15mm X 0.4 mm is the first optical component of the beamline installed at 17.5 m from the tangent point. It acts as a high pass energy filter allowing passage of all the energies higher than 4 keV. It also acts as heat load remover because lower energies of synchrotron radiation carrying most of the heat load are absorbed here. Be window is diffusion bonded to water-cooled copper body and designed to withstand 180W heat load. To make it especially suitable for imaging experiments, the beryllium foil (99.8% pure) has a surface roughness of 0.1μm RMS that minimizes scattering of the incident beam. The beryllium window also separates the front end of the beamline from the optical elements and isolates their vacuum. Similar to this, at the end of the optics hutch, a pair of beryllium windows is used with dimensions 140mm x 15mm x 0.4mm separated by 25 mm to allow monochromatic and white beam exit. Both exit Be-windows are coated with aluminium to prevent the oxidation of beryllium during white beam operation.

b) Slits:

A pair of entrance slits made of tungsten carbide blades is used for shaping the white beam before falling on first crystal of DCM and further reduces its heat load after Be window. Apart from this, exit slits installed after DCM having tungsten carbide blades are used for selecting beam size of monochromatic or white beam as per the experimental requirements. Both the monochromatic and white beam slits allow systematic opening of the beam aperture up to 140 mm (H) and 60 mm (V) and can select beam size as small as 0.1 mm both in horizontal and vertical direction.

c) Monochromator:

The beamline uses a double crystal monochromator (DCM) with a pair of Si (111) crystals for selecting the desired energy of monochromatic beam in the energy range (8-35 keV). In order to implement diffraction enhanced imaging, the monochromator chosen is DCM instead of multilayer monochromator. The first crystal having an optical area of 140 mm x 100 mm and 10 mm depth is indirectly rear cooled with water. The second crystal with an optical area 160 mm x 140 mm and 20 mm depth does not have any cooling attachment. The diffracting face of both the crystals is polished and strain free with orientation accuracy ~ +/- 0.05°. The big crystals allow acceptance of the full fan of incident beam at all Bragg angles in the entire energy range. Optical flatness is within 2 µrad to give a FWHM of rocking curve within 5% of theoretical value for the range of 8-35 keV. The desired energy is selected by rotating the crystal, thereby varying the Bragg angle. The beam bounces off the diffracting face of the second crystal and leaves the monochromator parallel to the input beam with an

upward offset of 25 mm. The use of perpendicular and parallel translation stages allows retaining the fixed exit capability of the beam. A provision to lower the first crystal is designed in the monochromator to allow passage of the white beam.

d) Beam Diagnostics

For beam diagnostics, beamline uses a blade beam position monitor installed after first beryllium (Be) window to measure beam position and stability. It consists of two pairs of photosensitive pyro-carbon blades placed across the beam to allow measurement of generated photoelectron current and trace beam movement as small as 1 µm. In order to image the footprint of the beam and monitor its shape and size online, the blades of monochromatic and white beam slits are coated with 100 µm thick X-ray fluorescent material (Y_2O_3). For the online measurement of intensity of monochromatic beam, an ionization chamber is installed next to the exit beryllium windows. The beam intensity profile can also be measured with the help of ion chamber current variation due to scanning of thin slit opening. The ion chamber filled with nitrogen or argon between 50 mm long electrode, 140 mm x 15 mm aperture size and 18mm electrode separation is operated at potential up to 1.7 kV and pressure range 0.7 to 1.3 bars absolute.

e) Shielding and safety instrumentation

The beamline is enclosed in a radiation shielding of 3mm thick lead sandwiched between MS plates of thickness 1.4 mm. To shield directly scattered bremsstrahlung and SR beam, a local shield of 100 thick lead is used at 20 m. To reduce noise from BR accompanying SR beam, lead collimators have been installed with entrance slit, before DCM and near exit slit. A safety shutter with tungsten block of dimensions 180 mm x

80 mm and 200 mm thickness is used as beam shutter for both synchrotron and bremsstrahlung radiation. The fast shutter installed for controlled irradiation of live samples, has a maximum speed of 2500 rpm and opening/closing time of 20 ms hence a minimum controlled exposure of duration ~50 ms can be achieved. A beam dump of 300 mm thick lead is used to dump bremsstrahlung and SR beam at the end of beamline. Radiation in experimental hutch and control room is continuously monitored using radiation dosimeter. To measure ozone in the experimental station during white beam mode operation, ozone monitor is installed. All monitors generate alarm beyond a defined limit and interfaced with beam and hutch access.

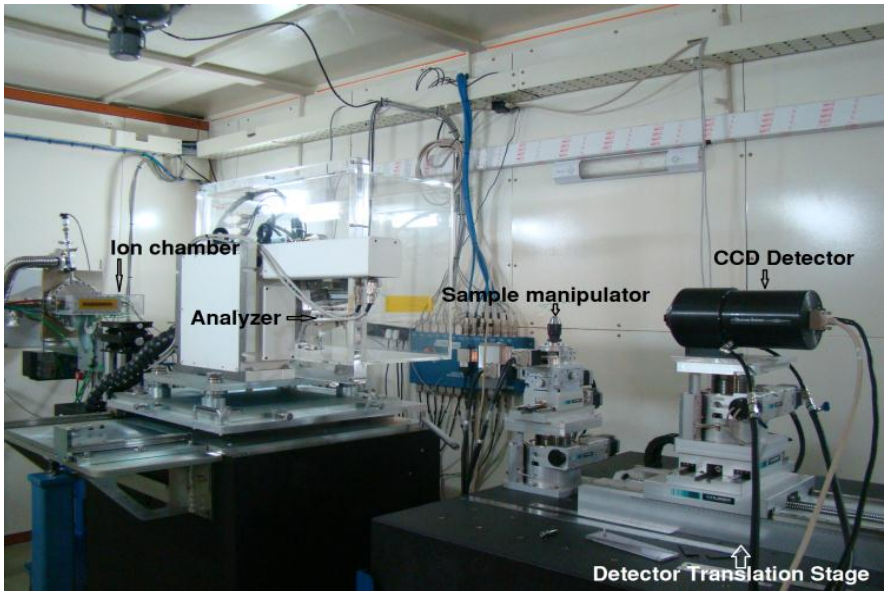

Figure 3.3 Experimental station of imaging beamline Indus-2 at RRCAT India

3.2.3 Experimental Station

Experimental station of imaging beamline consists of all the components such as sample manipulators, detectors, sample environments required for the implementation

of various advanced X-ray micro-imaging techniques in the same experimental station. Imaging techniques such as high-resolution absorption contrast imaging, PB-PCI, DEI, and dual energy imaging are implemented at the developed beamline. Some of these techniques are also applicable in white beam mode whereas others can be used in monochromatic mode. Table-3.2 list various techniques implemented and their applicability in respective beam operation modes.

a) Detectors

The beamline utilizes three different detectors namely fiber optic coupled CCD, X-ray microscope and flat panel detector for varied experimental requirements. These detectors have different characteristics such as pixel size, field of view, efficiency, frame rate, linearity and noise characteristics as discussed here and offer wide range of options to imaging applications.

i. Flat panel detector

In order to image samples of larger dimensions, a flat panel detector (Hamamatsu C7942CA-22) having imaging area 120mm x120mm with pixel size ~50 µm is used. The detector can acquire 14-bit digital images with frame rate up-to 9 frames/s.

ii. Fiber optic coupled CCD

This is a Photonic Science VHR-11 CCD camera consisting of a 1:2 Fiber-optics plate, coated with Gadox scintillator and high resolution CCD (Pixels 4007 X 2678, pixel size 4.5 µm and field of view 18 mm x 12 mm). The performance of the camera is linear in the energy range 5-50 keV. The full frame images can be captured in a shutter less

operation with a readout time ~ 600 ms, which can be reduced further through selecting sub-area and binning. The detector is suitable for high-resolution radiography, phase imaging, tomography, and dynamic imaging.

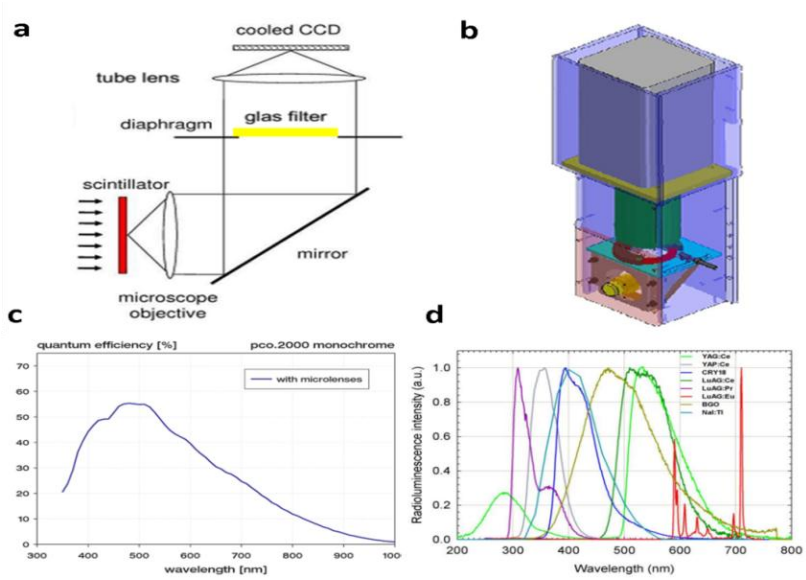

Figure 3.4 (a, b) Lens coupled X-ray imaging microscope. (c) Quantum efficiently of (PCO2000) CCD with wavelength (d) Photo-luminescence of various scintillators

iii. X-ray micro-scope

Two separate modules of lens coupled X-ray imaging microscopes are used for monochromatic and white beam imaging respectively. Monochromatic camera system uses YAG: Ce scintillators with 5-300 µm thicknesses, objectives lenses of 1.25X to 20X magnifications and a PCO-2000 camera. Various objectives are used for optimizing resolution (800nm to 12 µm) and field of view (0.7 mm to 12 mm) of the system as per the experimental requirement. The design and important characteristic of monochromatic microscope are shown in Figure 3.4. Efficiency of the camera depends on incident beam energy and the scintillator being used. Achievable resolution and

maximum field of view for the monochromatic microscope with different objective lenses and PCO-2000 camera are listed in Table 3. For white beam imaging, the microscope uses tungsten shield for objective lens protection and a thicker scintillator for heat load compatibility. The absorption efficiency of YAG: Ce scintillator decreases with energy and increases with thickness. The spectrum of the incident white beam at sample position is shown in Figure 3.5 (a). The energy ranges from 5 to 40 keV and peaks at nearly 10 keV. The sensitivity of white beam detector is optimized using a 300 μm thick scintillator, which has approximately 99.5% absorption efficiency at 10keV. Objectives 2X, 5X and 10X are used.

Table 3.3 Resolution and field of view of X-ray microscope with different objective lenses used with PCO-2000 Camera

Micro-scope objective	Optical resolution (μ)	Resolution with scintillators (μ)	Maximum field of view (mm x mm)
1.25X	12	15	12.1x12.1
2X	7.8	10	7.6x7.6
4X	3.5	3	3.8x3.8
10X	1.5	1.8	1.5x1.5
20X	0.78	0.8	0.76x0.76

b) Sample and detector manipulation

Five-axis sample manipulator system is used to position and align the sample. It consists of one full circle rotation stage (360° travel range and 0.001° resolution), two

dimensional tilt stage (+/- 20° travel range and 1" resolution) and high precision translation stages to move the sample perpendicular to beam propagation (travel range 100mm, accuracy 0.1 μm). Detectors can also be moved in two-direction perpendicular to beam propagation. It is mounted on a long linear stage of 1500 mm travel range and 100μm accuracy for varying sample to detector distance required for PB-PCI.

c) Beam analyser

In order to implement the DEI, the beamline utilizes a pair of analyser Si (111) crystals for analysing diffracted beam. The analyser is designed for energies 8-35 keV with a Si (111) crystals with an offset of 25 mm upwards. It acts as a very narrow angular slit, reflecting only the rays that make the correct Bragg angle with the atomic planes of the crystal. It converts the angular distribution in the transmitted beam into intensity variation in the image and removes all scattered photons. DEI images can be acquired by adjusting the analyser crystal at various positions on its rocking curve. By using two crystals instead of one, there is no need to have the scanning of the sample or positioning the detector in opposite directions as there is no net beam inversion.

d) Data acquisition and analysis

Beamline control system allows operational control and parameter setting of the optics, motion stages, detectors, and beam diagnostics components. It also consists of data acquisition system, equipment protection system (EPS) and personal safety system (PSS). EPS is designed to operate beamline components in safe conditions and circumvents accidental heating, vacuum failure or contamination whereas PSS is designed for personal protection against exposure to radiation, hazardous gases and

high voltage. The beamline uses a GPU based multicore computing facility with various software packages for tomography reconstruction, visualization, and analysis.

3.2.4 Characterisation of imaging beamline

Intrinsic characteristics of micro-imaging system such energy dependent variation of beam size, divergence, flux density, beam uniformity, bandwidth of synchrotron beam, energy resolution (ΔE/E) of DCM, spatial resolution and uniformity of various imaging detectors are strongly co-related to the image quality, a prior knowledge of system parameters is necessary before the planning of imaging experiments. These parameters were measured experimentally and compared with their theoretical calculations using XOP in order to evaluate the performance of imaging beamline[123].

a) Beam divergence and flux

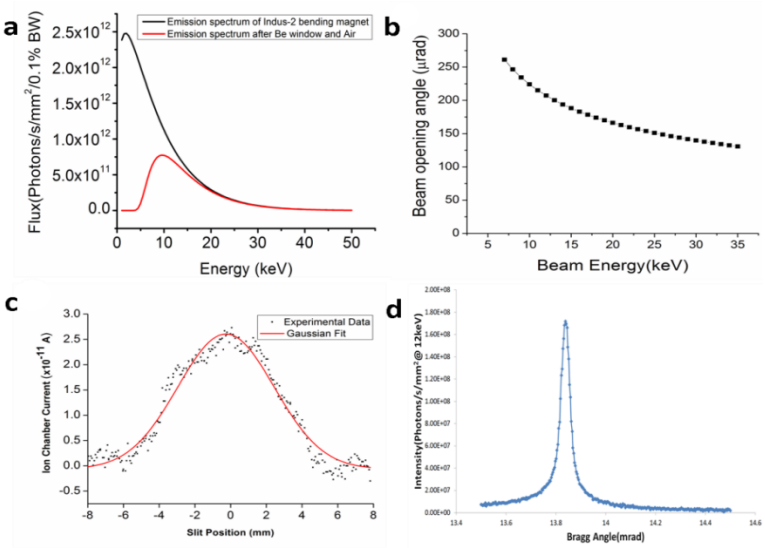

Figure 3.5 Characteristics of White beam at imaging beamline (a) Calculated spectra of synchrotron white beam (b) Beam divergence (FWHM) with energy (c) Beam profile at 18 m (FWHM 4.5 mm) (d) Rocking curve of DCM at 12 keV(FWHM 53.53 µrad).

i. White beam mode:

In case of white beam mode, the integrated beam flux is calculated to be 1.7 x 10^{16} photons/seconds using XOP[124]. Figure 3.5 (a) compares the emission spectrum (energy range 1-50 keV) of synchrotron radiation from a banding magnet source and its modification due to absorption losses in beryllium windows and air path in experimental station. Beam opening angle variation is shown in Figure 3.5 (b). Beam profile is measured using scanning of small vertical aperture (300μm) in entrance slit against ion chamber current as shown in Figure 3.5 (c). The beam size was measured to be 4.5 mm (FWHM) at 18 m from the source point, which is in accordance with the theoretical value.

b) Beam monochromaticity

The energy resolution of DCM is measured using its rocking curve as shown in Figure 3.5 (d). The FWHM of the rocking curve is 53.5 μrad at 12 keV; hence, energy resolution (ΔE/E) at this energy is measured to be $3.2x10^{-4}$. The intrinsic energy resolution (ΔE/E) of Silicon<111> is $1.2x10^{-4}$ for a perfectly collimated beam. The difference in intrinsic and measured energy resolution is attributed to the beam divergence [125]. As shown in Figure 3.5 (b) the beam divergence is decreasing with increasing photon energy. This improves the energy resolution at higher energies.

ii. Monochromatic beam mode:

The peak flux and angular divergence of monochromatic beam decrease with increasing photon energies. Experimental measurement of vertical beam size is carried

out at 18 m from the source using slit aperture scanning against ion chamber current and calculating the FWHM of Gaussian profile. The beam sizes are in good agreement with theoretical data as shown in Figure 3.6 (a). The peak flux density at all energies was measured at 25 m from the source using a calibrated silicon photodiode AXUV100 (IRD, USA). Figure 3.6 (b) also shows the comparison of calculated and experimental flux density at various energies. The calculated flux at 12 keV is 4.98 x 10^8 ph/s/mm^2/120 mA whereas the measured flux is 1.74 x 10^8 ph/s/mm^2/120 mA. Difference in measured and calculated flux is attributed to the attenuation and scattering losses in the beamline optical components such as beryllium windows, DCM crystals, ion chamber, and air in the propagation path of the beam from its source to the experimental station. Transmission of a 12 keV beam through 2 x 0.4 mm of beryllium is 93%; through 10 cm argon (ion chamber) is 37%. Therefore, the calculated flux x 0.93 x 0.37 = 1.71 x 10^8ph/s/mm^2/120mA is quite comparable to the measured flux.

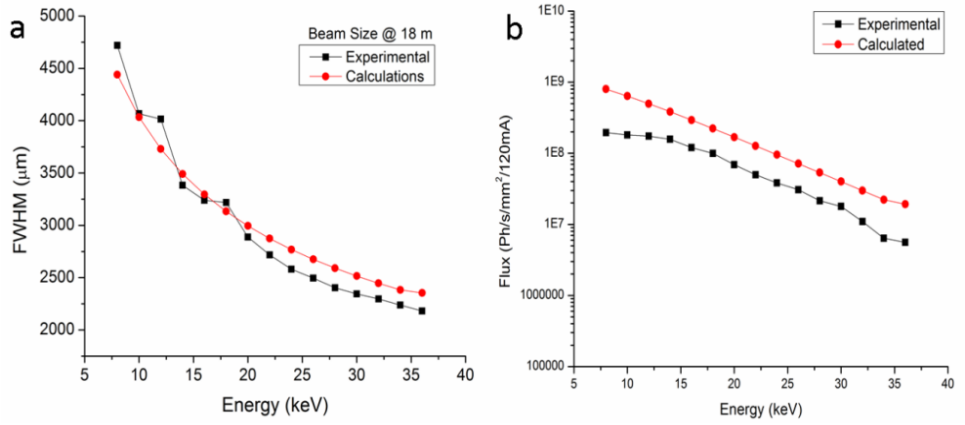

Figure 3.6 Characteristics of Monochromatic beam (a) Beam size (FWHM) variation with energy) (b) Beam flux variation with energy

c) Beam uniformity

A direct beam image acquired at 12 keV using high-resolution CCD detector is shown in Figure 3.7(a). The variation of intensity along the horizontal and vertical directions is shown in the figure along with its histogram to show beam uniformity. There seems to be some variations in the image gray values (FWHM ~14.7%) which are attributed to the fiber-optic structure in the CCD image and non-linear response of various pixels. For imaging application, a flat field correction is applied to correct these effects. Figure 3.7 (b) shows the flat-field corrected image along with its horizontal and vertical profiles and histogram. The beam uniformity is significantly improved after flat field correction (FWHM ~4%).

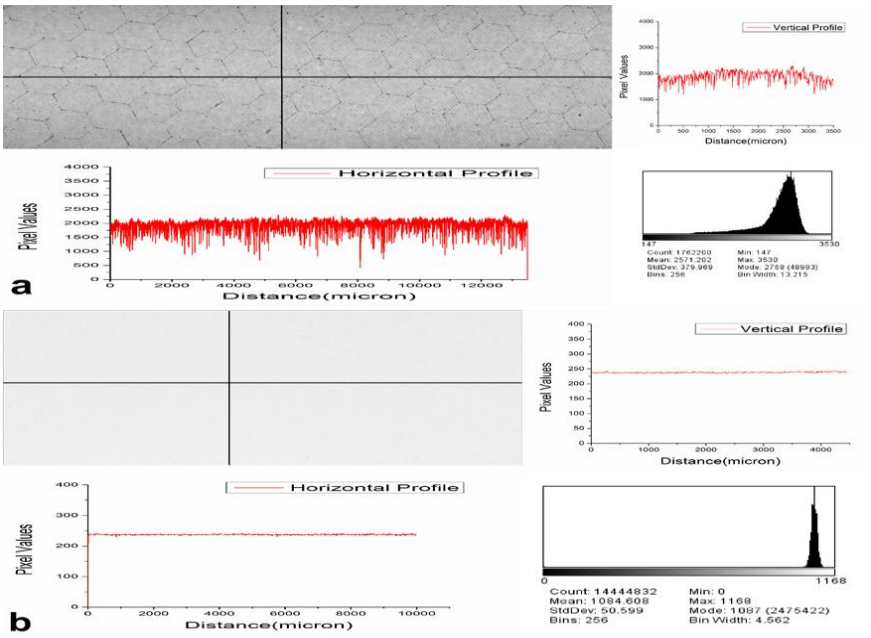

Figure 3.7 Measurement of beam uniformity (a) Flat image of synchrotron beam at 12 keV acquired using CCD detector. The figure also shows horizontal and vertical profile plots and its histogram. (b) Image (a) after flat field correction

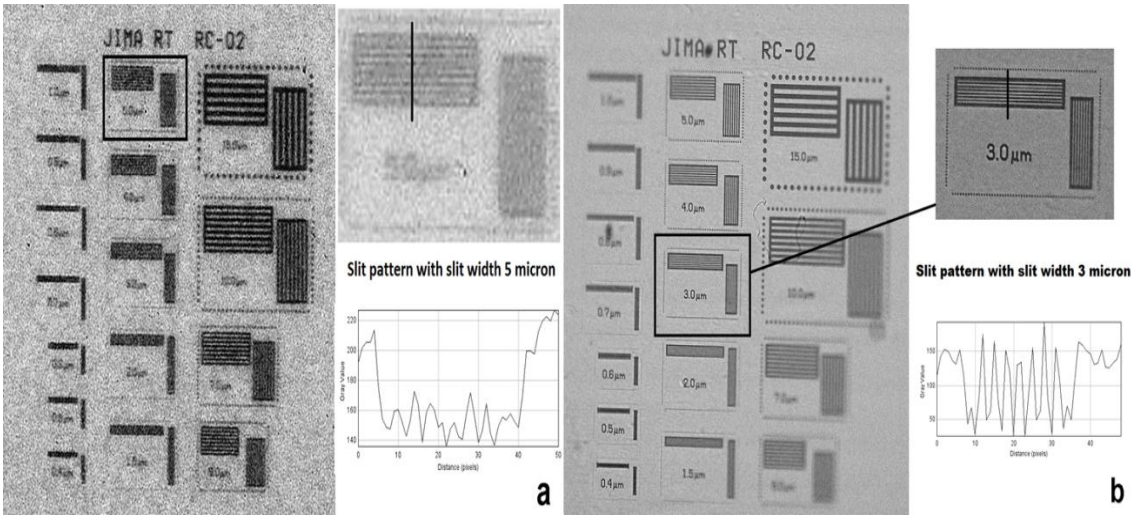

Figure 3.8 Spatial resolution measurement using JIMA pattern (a) Fiber optic coupled CCD detector (b) Lens coupled CCD detector.

d) Detector resolution

The spatial resolution of two most popularly used detectors at imaging beamline is measured using JIMA resolution pattern RC RT02B (http://www.jima.jp). For the fiber optic coupled CCD camera, the resolution was measured to be 5 µm with 8% contrast. Line segments up to 5 µm intervals can be visualized clearly in the image acquired using 15 keV monochromatic beam and 800 ms exposure time as shown in the Figure 3.8 (a) which is in line with the intrinsic resolution of the camera with pixel size 4.5µm and 2X magnification. Similarly, the resolution of lens coupled high-resolution X-ray microscope was also measured with 50µm thick YAG scintillator and 4 X objectives. The image was acquired at 15keV with an exposure time of 120 seconds. Line segments of 3 µm are visible with 20% contrast hence the resolution of the system with this combination is ~3µm as shown in Figure 3.8 (b).

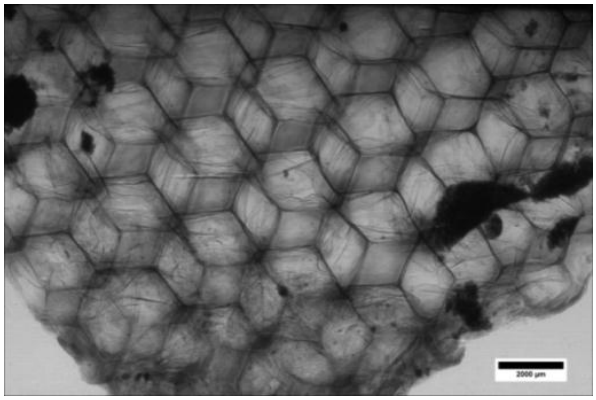

Figure 3.9 Full field high-resolution absorption contrast image of beehive.

3.2.5 Feasibility experiments

Implementation of various micro-imaging techniques is confirmed through their respective feasibility experiments. Samples from material science and bio-medical science are used to show their structural and density variation using various micro-imaging techniques[15].

a) Absorption contrast micro-imaging

Absorption contrast imaging is used to obtain the distribution of the attenuation coefficients for strongly absorbing materials. A high-resolution full-field absorption contrast projection image of Indian bee's beehive is shown in Figure 3.9. The image is acquired with fiber optic coupled CCD camera using monochromatic beam at 12 keV and 600 ms exposure time. The resolution of image is 4.5μmand field of view (FOV) is 18mm x 10mm. The image shows hexagonal microstructure of natural fibres in beehive and entrapped honey within it. The technique can potentially be used for studying internal structure of natural beehives, design and optimization of the structure of artificial beehives.

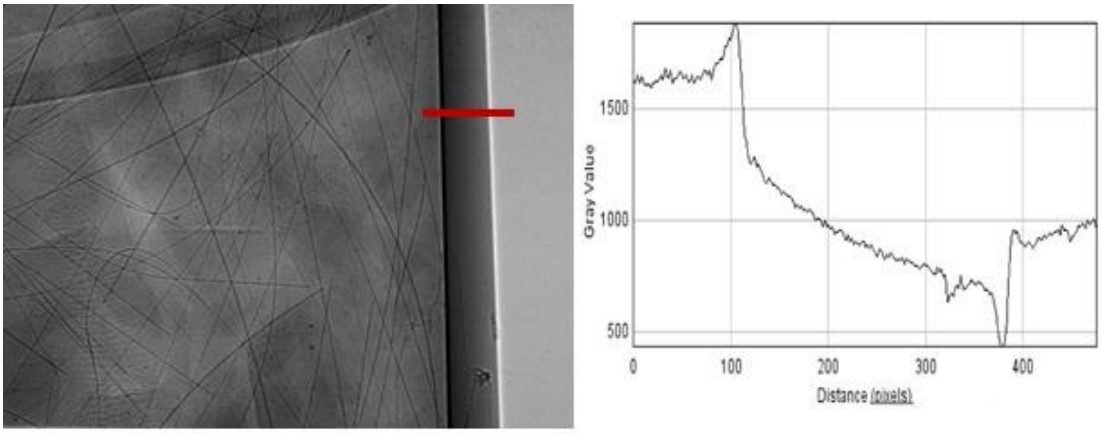

Figure 3.10 (a) PB-PCI image of silicon aerogel (b) Profile plot along the red line

b) Propagation based PCI

Propagation based PCI is useful for retrieving the refractive index distribution in weakly absorbing materials with improved contrast in structural and material features. It provides improved visibility of the interfaces at small density gradients [12,31,50]. We have tested its feasibility on wall of thin plastic bottle containing aerogel sample made from silica gel. The material is of extremely low density with high mechanical strength and low thermal conductivity. Phase contrast image in figure 3.10 clearly show the embedded fibres and gel matrix. The phase contrast can also be seen in the profile plot drawn across the wall of the plastic bottle.

c) High resolution phase contrast micro-imaging using X-ray microscope

The lens coupled X-ray imaging camera allows a wide range of image resolution through the choice of magnification and scintillators thickness due to its modular structure[15]. Using a thin scintillator of 20µm thickness and an objective of 4 X magnification, we have successfully tested a resolution of 2 µm in the absorption and

PCI. We have successfully applied it for the microstructure study of flowers and stems of an endangered plant *Byttneriaherbacea* as shown in *Figure*.

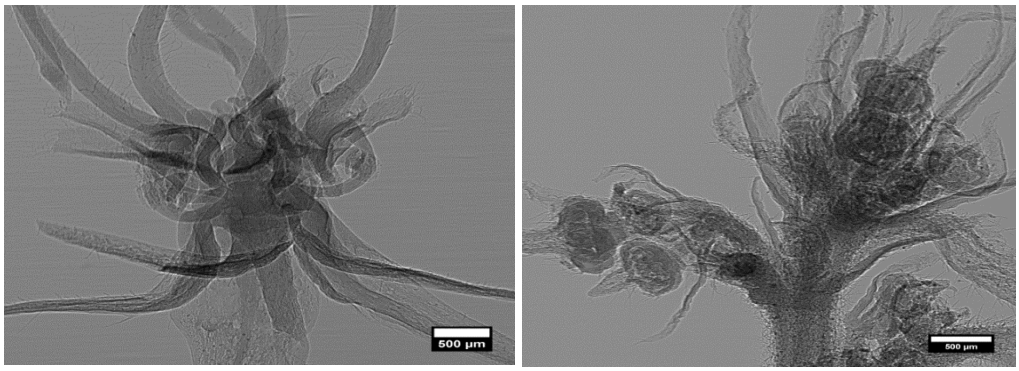

Figure 3.11 High-resolution PB-PCI using X-ray microscope of (a) Flower (b) Anther

d) Phase contrast µ-CT

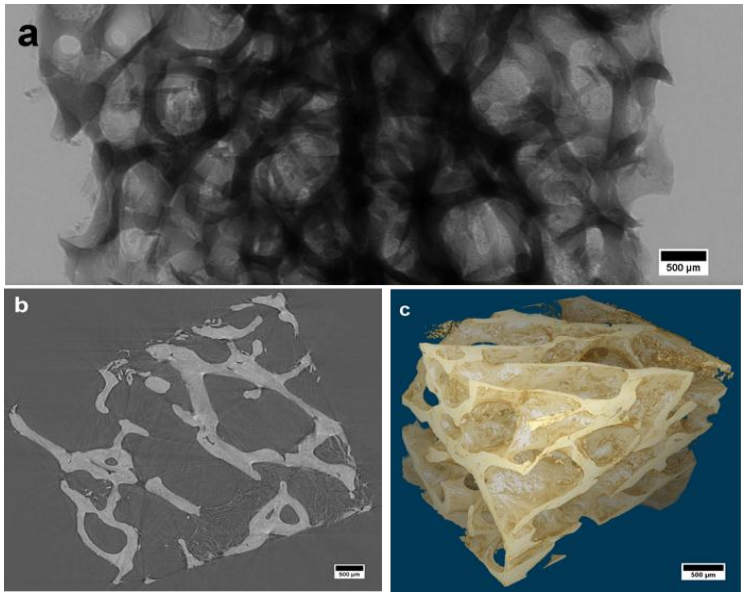

Figure 3.12 (a) PB-PCI projection image (b) µ-CT slice image (c) 3D image of bone.

Tomography is used for 3D imaging of objects in absorption and phase contrast modes to determine the 3D distribution of the linear attenuation coefficient or the refractive index, respectively [126,127]. X-ray µ-CT experiments were carried out on a cartilage

bone sample to study its porous microstructure and density distribution to find out the feasibility of osteoporosis. The experiment is performed in phase contrast enhanced projection imaging mode. The data is acquired for 180-degree rotation of the sample with 0.2-degree rotation step in parallel beam geometry of tomography scan. Total 901 such projections are collected apart from reference and background images. The data is pre-processed for image noise correction, and then back projected using filtered back projection algorithm. The projection image of the sample and its 3Dvolume reconstructed using DRISTI is shown in Figure 3.12[128]. While projection images hardly identify the shape and size of porous microstructure, tomography reconstructed slice images and 3D image clearly shows the microstructure as well as enclosed low-density fibrous material.

e) Diffraction enhanced imaging (DEI)

Diffraction enhanced X-ray imaging is highly sensitive to small density and thickness gradients in the sample due to its extreme sensitivity to refraction contrast created by the sample which is still unmatched by any other PCI method[9,10]. The techniques allow simultaneous retrieval of refraction, scattering and apparent absorption contrast X-ray images with a simple image analysis. In this technique, a perfectly collimated monochromatic beam is refracted by the sample due to refractive index gradients present, which deflects its path by a small angle. The distribution of deflection angle is of the order of micro-radians given by

$$\Delta\theta = {}^{1}/_{k}\,{}^{\partial\emptyset(x)}/_{\partial x}$$

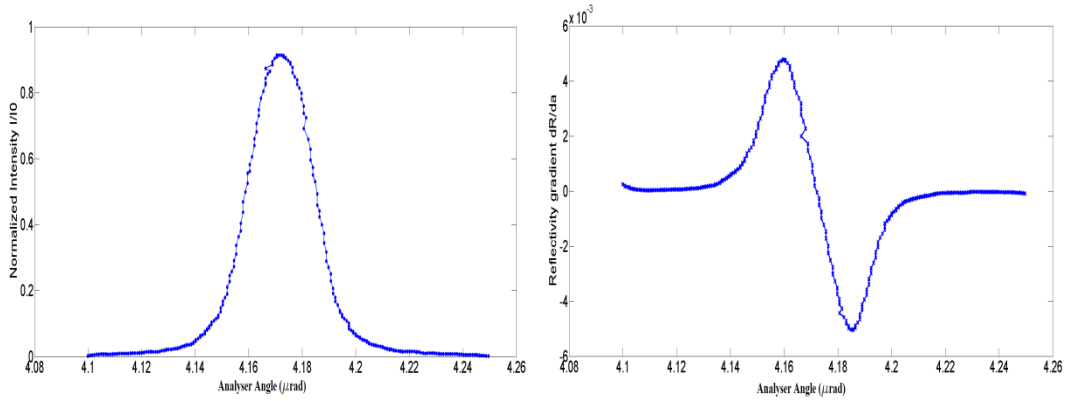

Figure 3.13 Characteristics of analyser crystal used in diffraction enhanced imaging (a) Rocking curve (b) Gradient of rocking curve

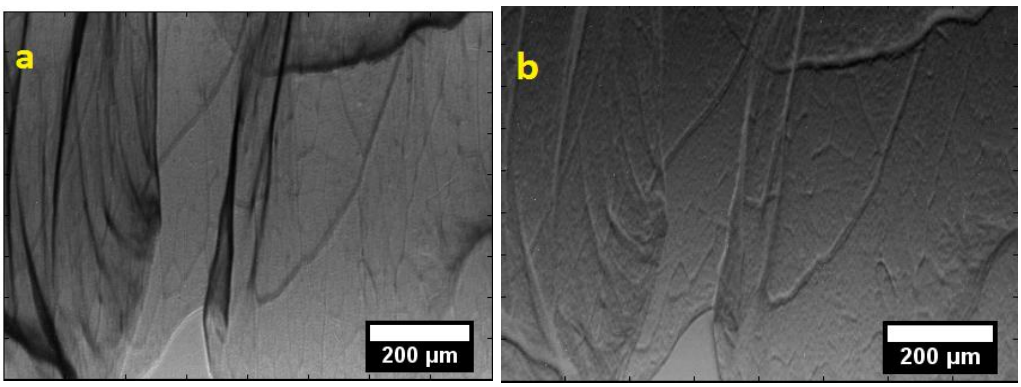

Figure 3.14 DEI of Rose petals. (a) Apparent absorption image (b) Refraction image.

The phase change Φ in incident beam is related to the real part (δ) of complex refractive index n = (1- δ + iβ) thus electron density of material through Φ = k δ z. Thus $\Delta\theta$maps distribution of refractive index in the sample. The incident beam is also attenuated and scattered by the object resulting in its intensity modulation. Distribution of deflection angle is converted into intensity distribution in the image with the help of Bragg diffraction in analyser crystal between the object and detector. The diffraction characteristics of a crystal are interpreted by its rocking curve as shown in Figure 3.13

(a-b). X-rays striking at slightly different angles than Bragg angle are less strongly reflected by the crystal depending upon angle of incidence. When images are acquired at different angular positions of rocking curve, the analyser converts the gradient of incidence angle present in the incident beam in to intensity gradient. The sensitivity of analyser to incidence angle is very high because of high gradient in its rocking curve. The analyser crystals also acts as a very efficient scattering rejecter due to very narrow angular acceptance and create a contrast called scatter rejection or extinction in the obtained images. Using suitable mechanism of image acquisition and analysis, each contribution of refraction, absorption, and extinction can be separated out. we have done experiments on various soft materials to study the feasibility and applications of the technique at imaging beamline. At beam energy 12 keV and acquisition time of 10 sec, DEI images of rose petals were acquired at different point of the rocking curve and after using quantitative analysis, refraction and absorption contributions to the projection image were separated out. Figure 3.14(a-b) shows the extracted phase images of rose petals. The small thickness variations in these samples are clearly visualized which are not visible in the projection image.

f) Dual energy imaging

Dual energy imaging is very useful for elemental mapping with in the sample. Very high-energy resolution at imaging beamline due to crystal monochromator and high X-ray beam flux, dual energy imaging can be used in absorption and phase contrast modes. With the acquisition of projection images at incident beam energies below and above the absorption edges of the desired element in the sample followed by

subtraction of logarithmic flat field corrected images provides the spatial distribution of the desired element or compound in the sample[129]. The technique can also be used in tomography mode and very useful in localized imaging of variation elements. We have applied this technique to find out distribution of Arsenic impurity in Rice samples caused due to its presence in the soil. The images were acquired below (11.5 keV) and above (12 keV) the absorption edge of Arsenic (As) that is at 11.87 keV. The resulting subtraction image in Figure 3.15 show the distribution of As in Rice sample.

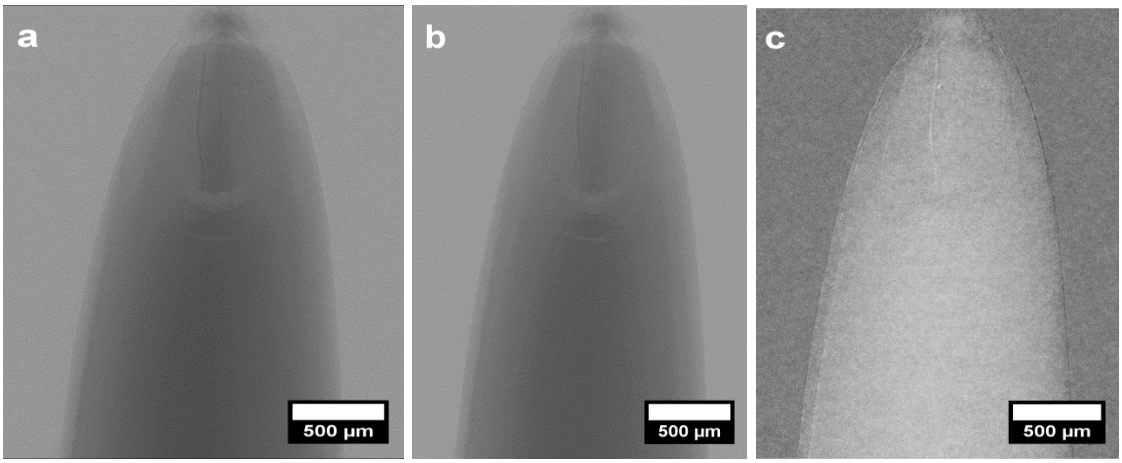

Figure 3.15 Dual energy imaging of Arsenic (As) [Absorption edge 11.87 keV] in Rice using X-ray CCD Projection image acquired at (a) 11.5 keV (b) 12.0 keV (c) difference of logarithmic images(a and b) to visualize distribution of As.

g) High resolution large FOV imaging

The high-resolution imaging of large samples in a single frame is not possible due to limitation placed by finite field of view (FOV) of the available imaging detectors. In order to image large samples with high resolution, several images of the sample covering different region of interest are collected while translating it across the beam in

a stepwise manner. The images are computationally stitched together to make a single high-resolution large FOV image[130]. The application of stitching algorithms requires a certain overlap in the acquired images in both the directions. We have acquired the large area image of a Zebra fish of dimension 35 mm x 18 mm after stitching of 6 images acquired in a matrix of 3 rows and 2 columns. The resulting image is shown in Figure 3.16. The step-wise acquisition of the images is obtained through CCD camera, which is interfaced with translation stages. The sample is being considered for osteoporosis studies.

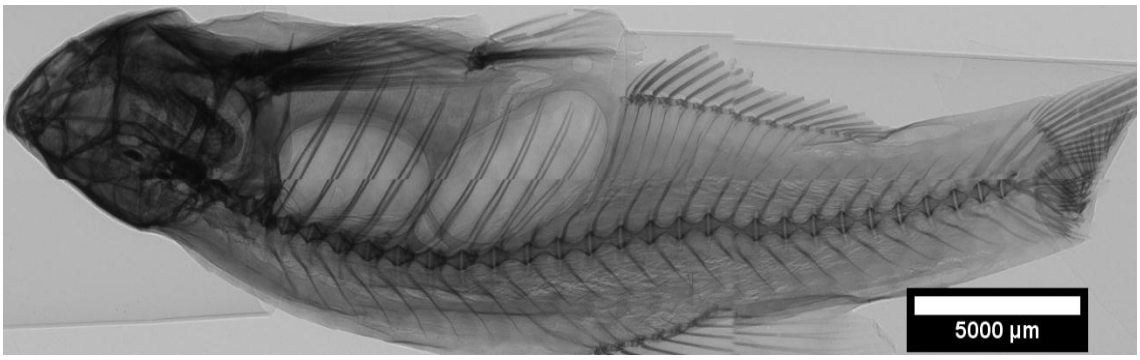

Figure 3.16 High-resolution large FOV imaging of Zebra fish

3.3 Development of neutron imaging beamline at CIRUS reactor

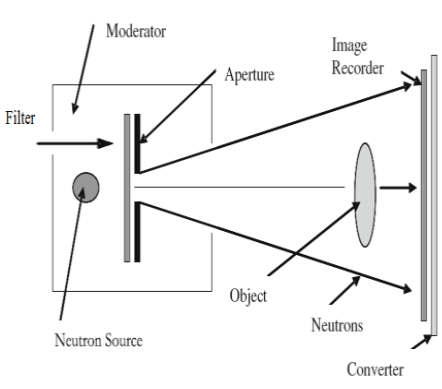

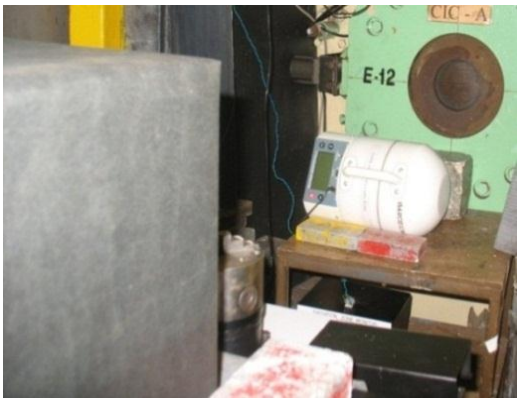

Figure 3.17 Neutron imaging beamline at CIRUS reactor, INDIA

Neutron imaging is a powerful non-destructive imaging technique that produces two or three dimensional attenuation maps of objects being examined. Because of its unique attenuation characteristics, neutrons based techniques are often considered complimentary to the X-ray based techniques. In order to realize high quality absorption and phase contrast projection imaging and tomography, data should be free from scattered noise and possess good statistics. The beam quality needs to be optimized with a high flux neutron source with good collimation and high-resolution high efficiency detector. Implementation of PCI requires a coherent or partially coherent source. Though the technique is quite successfully used for X-rays, for neutrons, it is slowly gaining importance with the advent of new ideas to improve coherence of the available neutron sources. The technique is particularly important for metallic objects which are opaque for X-rays but quite transparent for neutron and hence cannot be imaged using conventional attenuation based techniques[36,131–133].

We have designed and developed a state of art neutron micro-imaging beam line at CIRUS reactor, India to implement digital neutron radiography, tomography, and PCI in the same experimental station (Figure 3.17). A dual mode special collimator was used to allow high flux for absorption contrast radiography and tomography. With a minor modification in the same collimator housing, the coherence of the incident beam was also achieved for PCI. The imaging camera was designed and used consisting of a high sensitivity scintillator and high-resolution CCD camera configured in an ‘off-axis’ design. This imaging system in combination with data acquisition and image analysis software was used for neutron radiography, neutron 3D tomography. Neutron sensitive

imaging plate was used as detector for neutron PCI. The shielding of the beam line is designed using Monte Carlo calculations on different shielding materials and fabricated using borated polyethylene blocks in combination with lead blocks. The beamline is characterised in terms of thermal neutron flux, thermal to fast neutron ratio and gamma flux in the experimental station[134–136].

3.3.1 Neutron source: CIRUS reactor

The beamline was designed and developed at the tangential beam port of CIRUS reactor India E-12which have 4inch diameter circular opening. CIRUS was a 40MW research reactor having natural uranium as fuel and heavy water as moderator. The reactor consists of heavy water moderated core with graphite reflector and cast iron annular shielding zones. The core is surrounded by a 9-inch thick graphite layer followed by another 24-inch thick layer of graphite. This in turn is surrounded by the two 6 inch thick layers of cast iron separated by air gap. Thus, the flux from the CIRUS reactor has very good thermal neutron flux (0.025 eV).

3.3.2 Collimator

A collimator in an imaging beamline helps in defining shape and size of the beam and reduces scatter-induced degradation of the image produced. The angular spread of the emerging beam depends upon the ratio of the collimator tube length (L) to its aperture diameter (D), referred to as the L/D ratio[137]. A higher L/D results in a narrower beam spread and lower image un-sharpness at the expense of a lower neutron flux, which in turn requires longer exposure time at the sample. Thus, high resolution and large flux at object plane are contradictory to each other and a compromise on one or

the other is therefore necessary. Based on these concepts, a dual cone aluminium collimator of length 1921mm made of 1S grade aluminium (Fig 3.18) was designed to allow high flux and a provision for inserting another collimator to improve coherence of the beam as and when required for PCI.

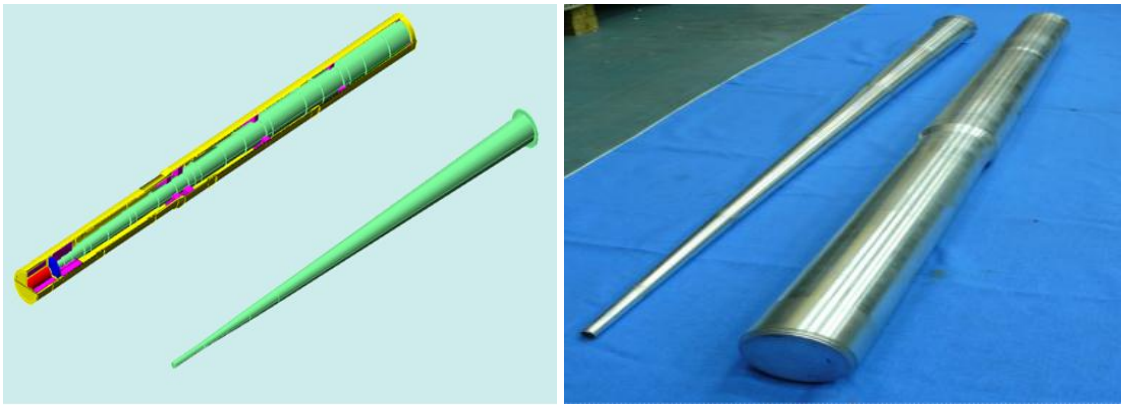

Figure 3.18 Design (left) and photograph (right) of main collimator for neutron imaging and tomography and the conical insert for neutron PCI

For the main collimator, a double layer conical aluminium tube was used and borated carbon was filled between the two aluminium tubes to prevent streaming of scattered neutrons in the experimental station. A 100 mm diameter single crystal bismuth plug was used to avoid direct view of fast neutrons and gamma rays from the core. The inner aperture of the tube was defined byB_4C annular disk and gadolinium disk so as to give effective source size of 16mm and L/D of 125 at the exit of the beam port. Using this collimator, the neutrons flux at the exit of beam port and sample location was measured to be ~ 9.0×10^6 n/cm^2/s and 1.0×10^6 n/cm^2/s respectively with a cadmium ratio of ~10 and beam divergence of 1^0 approximately. These parameters are good enough for absorption contrast imaging and tomography. For PCI experiments requiring high

spatial coherence and reasonably good neutron flux, a source size of 0.5mm and object–to-detector distance of 2000mm was chosen. A separate conical shaped aluminium collimator was designed and fabricated as an insert to the main collimator. This gave a coherence length ($\lambda L/D$) of ~0.8 mm. The dimensions of collimator insert were chosen to fit it completely within the empty space of the preceding collimator. The inner part of the collimator was lined with 0.2mm of cadmium to prevent the streaming of scattered neutrons down the experimental station. A cadmium pinhole of 0.5mm diameter and thickness 0.5mm was fitted at entrance of the collimator towards the reactor core, which was followed by another pinhole of 5 mm diameter in 0.6mm thick gadolinium foil so as prevent any further streaming of high-energy neutrons and limit the divergence of neutron beam. Besides these neutron pinhole assemblies, conical shaped lead inserts were placed inside the aluminium structure so as to minimize the gamma contamination of the beam. The assembly was aligned using He-Ne laser for any possible blockage of neutrons.

3.3.3 Shielding hutch

To protect personnels working at the beamline against radiation exposure, a shielding hutch was designed and developed around the E-12 beam port of imaging beam line based on Monte Carlo simulations. The experimental station has a working area 4000mm x 3000mm surrounded by shielding walls from two sides and a shielded motorized door which also serves as a beam dump in the front. The shielding walls were fabricated using borated polythene blocks of 400 mm thickness followed by 188 mm lead blocks sandwiched between 6mm of MS on either side. Borated polythene

blocks with total thickness 600mm followed by 188 mm lead blocks sandwiched between 6mm of MS on either side were used for fabrication of door which can be moved on rails. The roof of the experimental hutch was fabricated using 16mm MS sheets, 25mm of borated polythene (1% boron concentration) sheets, borated rubber (20% boron concentration) sheets and 1.5mm thick cadmium sheets.

3.3.4 Experimental station

The experimental station consists of a sample manipulation stage, neutron sensitive shielded imaging camera with CCD detector, image plate holding platform, remote viewing camera etc. It is located at distance of 1500 mm from the biological shield of the reactor. The sample manipulator consists of two translational motion stages to allow sample movement in perpendicular direction of beam propagation, sample holders for placing the sample at the suitable position in front of the beam and a rotation stage capable of rotating sample with a precision of 0.25^0or more. The detector was kept on an adjustable stand of dimensions 600 (L) mm x 600mm (W)x 1000 mm(H) and shielded from all sides by lead and borated polythene to minimize the scattered noise. A neutron imaging camera, designed, and developed in house was used for image acquisition. Figure 3.19 shows the schematic of this camera which consists of neutron scintillator (LiF-ZnS) coupled to the CCD camera (Andor cooled, model DW432N) through front coated (aluminium) reflecting mirror and focusing lens. The light, proportional to the incident neutron flux, generated at the output of the scintillator was recorded using a high-resolution CCD camera, which was thermoelectrically cooled to -40^0C for minimizing the detector noise. It has 1250 x 1050 pixels with a pixel pitch of

22 micron and the achieved resolution was measured ~200µm with 16-bit dynamical range. It was surrounded from all the sides by 100mm thick lead to shield the scattered neutron and gamma. High-resolution neutron image plates were used for carrying out phase sensitive experiments, which can be read with up-to 25µm pixel pitch. Both the detectors can be easily accommodated on the same detector platform. The CCD camera is connected to a remote PC. The rotations of sample are synchronized with image acquisition and controlled through in-house developed software. The data from CCD camera is readout with 1 micro-sec/pixel using frame grabber. Operation and control of sample manipulator, neutron detector can be carried out remotely from a separate control cabin. Two different monitoring camera units were installed within the experimental hutch to monitor the remotely controlled opening and closing of neutron beam ports and movement of translation stages for sample alignment.

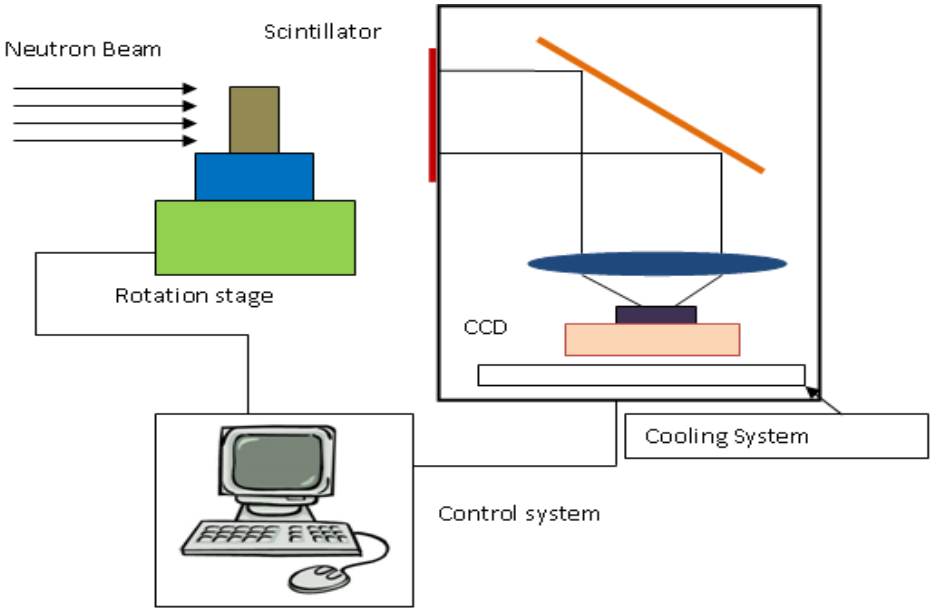

Figure 3.19 Schematic of imaging camera used for neutron tomography experiment.

3.3.5 Neutron beam characterisation

The neutron flux at different points of the beam line was measured using bare gold foil and cadmium covered gold foils, and results are presented in Table-3.4. An average neutron flux of the order of ~10^6 n/s was measured at both sample and detector location. The cadmium ratio was measured to be ~10 at the sample location. The CIRUS reactor consists of heavy water moderated core with graphite reflector and cast iron annular shielding zones as a result about 70% of the emerging neutrons are thermalized.

Table 3.4 Neutron flux measurement

	Exit Beam Hole	**Sample Location**	**Detector Location**	**Neutrons due to scattering**
Reaction Rate Au^{197} (n, γ)Bare	9.87e-16 (±3.23%)	2.83e-16 (±3.30%)	1.16e-16 (±3.27%)	1.39e-18 (±14.07%)
Reaction Rate Au^{197}(n, γ)+Cd	9.68e-17 (±3.31%)	1.88e-17 (±4.40%)	1.51e-17 (±4.71%)	No count
Thermal Neutron Flux	8.91e+6	2.64e+6	1.01e+6	~1.39e+4

a) Calculation of resolution and contrast

The image resolution with CCD camera was measured using two methods first using sharp edge radiograph and measurement of Modulation Transfer Function (MTF), which was found to be 1.64 lp/mm at 10% contrast, and second using recorded image of the test pattern, which also show approximately 1.6 lp/mm at 10% contrast. The

MTF plot is shown in Figure 3.20. Radiography image contrast variation with object diameter and thickness measured using standard radiography phantom is shown in Figure 3.21. The contrast is seen to be decreasing very rapidly with object thickness whereas the effect of object diameter is less prominent [138,139].

b) Phase contrast variation as a function of aperture dimension

Phase contrast variation as a function of neutron aperture dimension was measured using aperture dimension from 0.5 mm, 1 mm, 5 mm, respectively. The Table 3.5 shows that the contrast decreases with the increase in the aperture dimension.

Table 3.5 Measurement of contrast as a function of neutron aperture

S. No.	Neutron aperture dimension(mm)	Contrast (%)
1	0.5	4.7
2	1.0	1.9
3	5.0	Not measurable

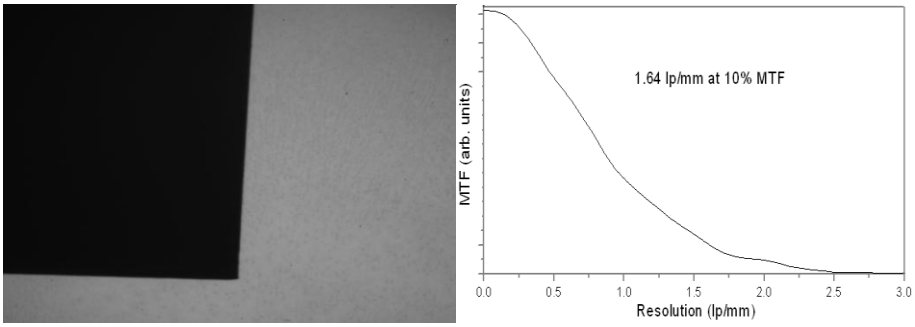

Figure 3.20 Sharp edge image and plot of Modulation transfer function (MTF) for CCD

3.4 Feasibility Experiments

a) Neutron micro-radiography

Neutron radiography has long been used in various scientific investigations and industrial applications. This non-intrusive method is based on principle of radiation

attenuation passing through matter. Because different materials have different attenuation behaviour, the neutron beam passing through a sample carries information about the composition and structure of the sample [18]. Neutron being a subatomic particle with no net charge, coulomb attraction has no effect on it. This fact makes it more useful for imaging applications of thick and high-density material. The implementation of technique requires only a well-collimated neutron source and a high-resolution detector. Feasibility of neutron radiography for non-destructive applications has been tested on the developed experimental set-up using various samples as shown in Figure 3.22.

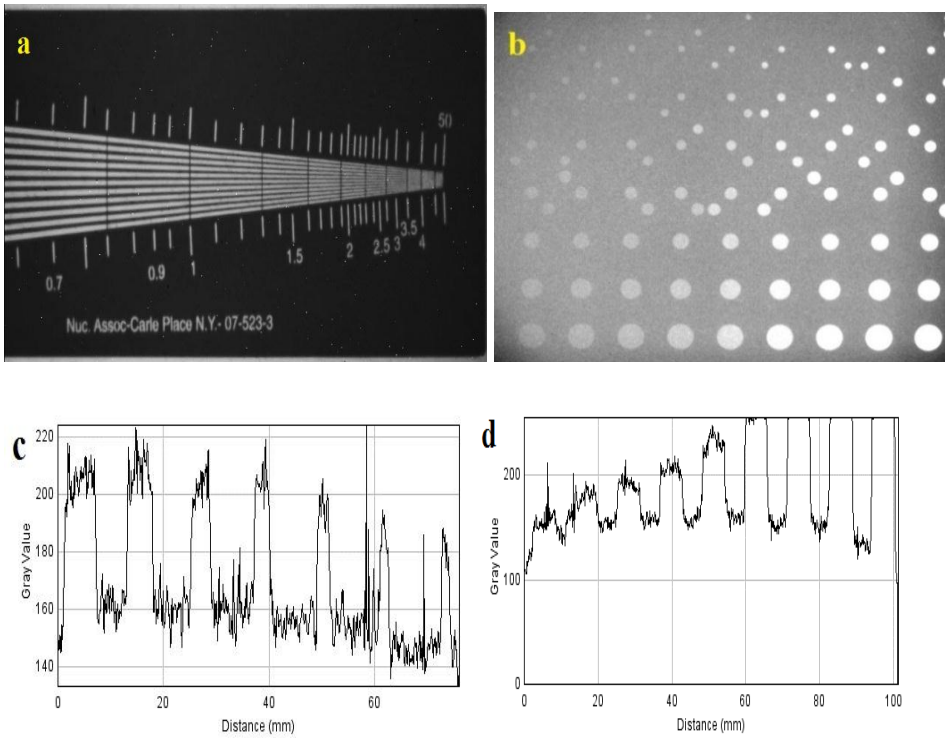

Figure 3.21 (a) Measurement of resolution using test pattern (b) contrast variation in with object disc thickness (Horizontal) and diameter (vertical). (c) and (d) show the profile plot for (b) along right most vertical and bottom most horizontal series of disks

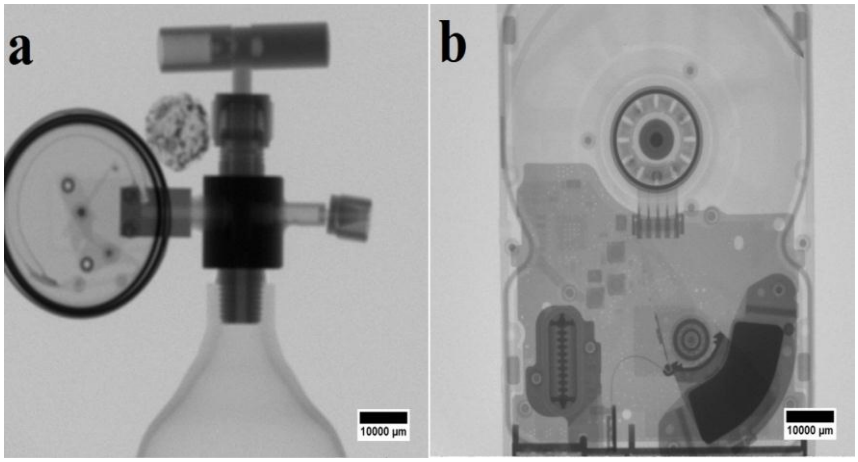

Figure 3.22 Neutron Radiography images acquired at neutron imaging beamline at CIRUS (a) nozzle of a gas cylinder (b) Hard disk

b) Neutron PCI

Most of the current facilities where neutron PCI is being performed are located at high intensity neutron sources with source fluxes reaching 4 x 10^{14} n/cm^2/s. We have developed propagation based neutron PCI facility at medium flux research reactor and demonstrated its usefulness in neutron imaging due to its improved contrast for low absorbing materials. The 40-MWth CIRUS reactor represents a medium flux (10^{13} n/cm^2/s) facility with a neutron flux one order of magnitude lower than commonly used sources. All the beam ports at this facility are radial in nature, which increases gamma noise in the acquired images and hence it makes the development of such an experimental set-up even more challenging. The implementation is based on the use of dual-purpose collimator discussed earlier so that both conventional neutron imaging and PCI can be performed without any substantial modification of the experimental set-up. The switchable phase contrast installations have been standard at the HZB reactor

Berlin, the FRM II reactor Munich and the SINQ spallation source at PSI, Villigen for many years. Our approach is innovative in so far as the collimator insert moves the phase contrast diaphragm as close to the reactor core and moderator as possible, while the aforementioned installations have it at the outside of the biological shielding. This approach helps not only in meeting the coherence requirements for phase contrast experiments but also in minimizing the flux loss thereby achieving good signal-to-noise ratio for neutron phase contrast images and reduction in data collection time for facilities at medium flux reactors such as CIRUS. A number of samples were studied to demonstrate the phase contrast technique using neutrons; one of them is shown in Figure 3.23. The exposure time for both of these experiments was 35 min.

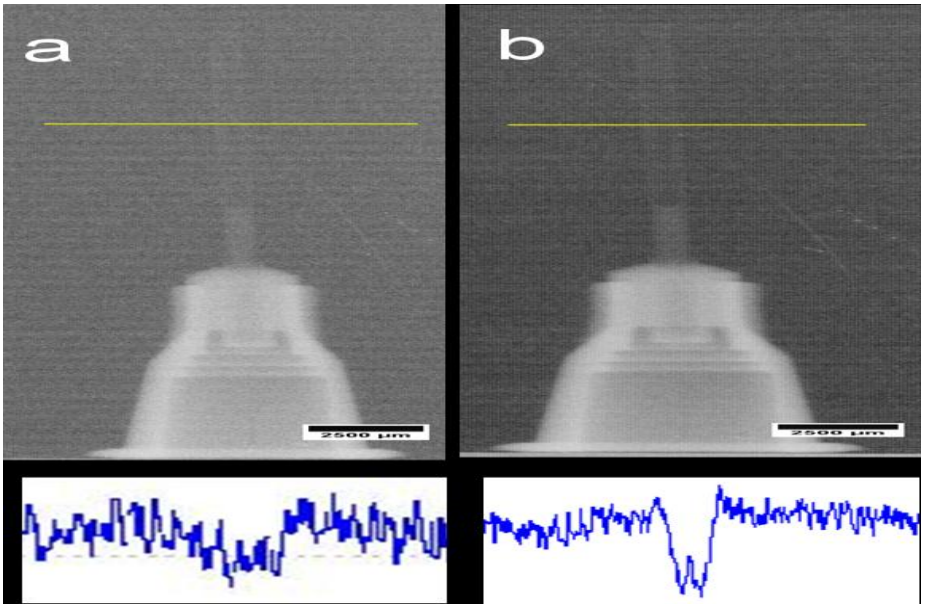

Figure 3.23 Comparison of (a) neutron absorption and (b) PCI of syringe and their profile plots along the line shown.

4 APPLICATION OF MICRO-FOCUS BASED IMAGING SYSTEM

Micro focus based X-ray imaging system provide most affordable and accessible micro-imaging solutions thus widely used worldwide. We have used this system for the micro-structure characterisation of nuclear materials especially those used in Compar high temperature reactor (CHTR). Visualization of internal geometries and quantification of micro-structure was carried out for various components of CHTR. Area and interspacing of fuel tube bores, porosity, morphology and thickness uniformity of SiC coating over their internal surface, thickness and uniformity of coatings in multi-layered TRISO coated fuel particles was measured using quantitative image analysis of micro-CT images. This chapter discusses details of experimental system, image analysis methodology, and results of micro-structural characterisation of various components of CHTR using laboratory scale X-ray imaging system.

4.1 Micro-imaging requirements in CHTR

Figure 4.1 shows the schematic diagram of CHTR core and its subcomponents. It consists of nineteen prismatic beryllium oxide (BeO) moderator blocks [140]. These 19

blocks contains centrally located graphite fuel tubes. Each fuel tube carries fuel inside 12 equispaced longitudinal bores made in the wall. The fuel tube also consists of a central bore, which serves as coolant channel for liquid metal/salt based coolant. The internal surfaces of these bores are coated from SiC, which protects graphite from corrosion and abrasion. The fuel for this reactor is based on TRISO coated particle fuels, which can withstand very high temperatures ~ 2000K and provide very high burn up. Eighteen blocks of beryllium oxide reflector surround the moderator blocks. These are surrounded by graphite reflector blocks. Reactor core is contained in a shell of materials resistant to corrosion against lead bismuth eutectic alloy coolant and suitable for high temperature applications. Top and bottom plates of similar material close this reactor shell. Components of CHTR are required to survive under extreme environmental conditions such as high neutron flux leading to irradiation damages in the materials, high temperatures causing thermal gradient and stress in the material, which may further lead to material fractures and corrosive environment of liquid metal/salt coolant. Design optimization and initial development is under progress for fuel tube, down-comer tube, fuel pellet, fuel particles etc. TRISO coated fuel particles has a specific layered structure which requires optimization of coating thickness, uniformity, and integrity. Fuel pebbles containing thousands of these fuel particles in graphite matrix requires optimization of number density of fuel particles in the matrix without damaging the coatings of fuel elements. Fuel tube which has one central bore and 12 equispaced peripheral bores requires dimensional characterization of bore diameter and interspacing uniformity throughout the tube and micro-imperfections in

the bulk of sample. For efficient oxidation and corrosion resistance, SiC coating over the internal surface of fuel tube bore requires non-destructive characterization of coating thickness, large-scale uniformity, porosity, and morphology. Non-destructive evaluation of sub-components geometry, distribution of various material phases and densities and quantitative measurement of internal microstructure using a suitable technique is important in order to optimize manufacturing parameters, minimize imperfections, and enhance dimensional accuracy.

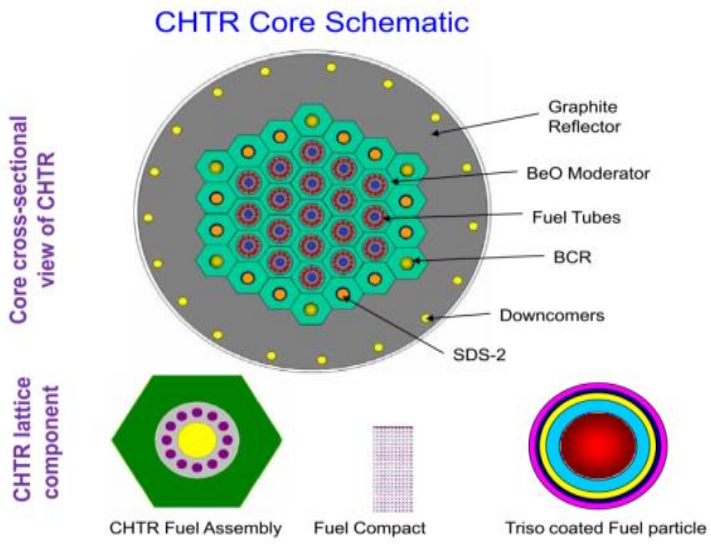

Figure 4.1 Schematic of CHTR core to show lattice subcomponents of the reactor

Most of these components are proposed to be manufactured from graphite, pyro-carbons, carbon-carbon composites and other carbon based material because of their exceptional properties at high temperatures [140,141]. In view of the routine requirement of micro-structural characterisation for these components, application of tabletop X-ray imaging is considered due to its easy accessibility instead of synchrotron micro-imaging. Some of the micro imaging techniques such as high-resolution

absorption contrast imaging and tomography, PB-PCI, and phase tomography techniques can easily be implemented using micro-focus X-ray tube. Due to small source size, the unsharpness introduced in the image is quite less as compared to macro-focus source and high-resolution images can be obtained with suitable choice of imaging detector. PB-PCI can also be achieved to enhance edge contrast for improved visualization of interfaces with the optimization of a suitable source to object and object to detector distance. Enhanced resolution and contrast in the X-ray images provides extra ease in visualization and segmentation of structure and material phases. With use of some image analysis tools, features can be quantified for improved understanding.

4.2 Micro-structure of SiC coatings

Graphite components of high temperature reactors such as fuel tube, down comer tube etc. are operated in corrosive and oxidative environment of liquid metal salt based coolant. Protection of the internal surfaces of fuel and coolant channels against oxidative degradation is necessary in view of their long-term performance [140,141]. SiC coatings are most commonly used for this purpose because of its unique combination of physico-chemical and mechanical properties [142,143]. Operational performance of the coating depends on its microstructure such as porosity, thickness, uniformity and integrity to the substrate, which in turn depend on the coating deposition technique and its process variables [143–145]. The microstructural properties of SiC coating are affected by a wide range of variables related to CVD such as temperature regime, coating kinetics, diluents gases, residence time etc. [146–148].

In order to find suitable deposition technique and optimize its process variables to deposit SiC coating with desired microstructure, it is important to find a suitable non-destructive quality evaluation method allowing characterization on real samples.

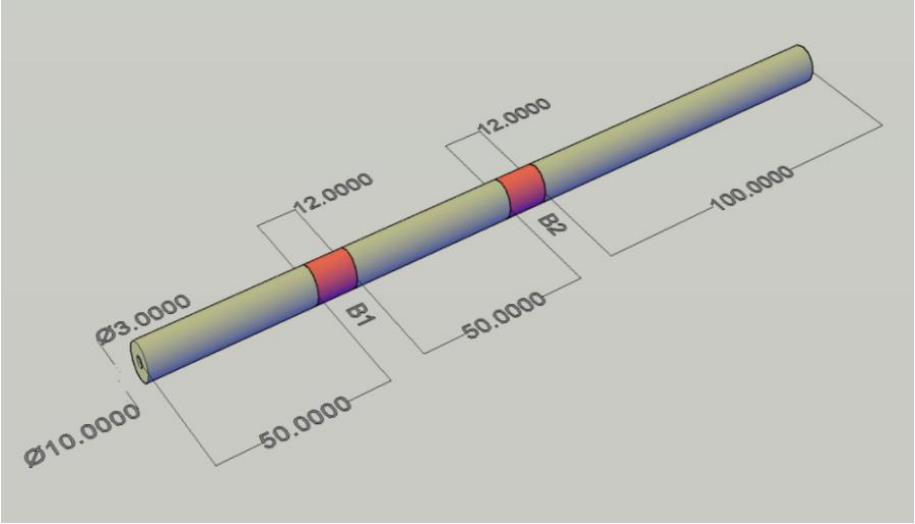

Figure 4.2 Schematic of Prototype fuel tube with SiC coating over its internal surface of the central bore. B1 and B2 are the tube domains for microstructure characterization.

In this study, we have used micro-focus based X-ray µ-CT for the micro-structural characterization of SiC coating. The coating is deposited over the internal surface of pipe structured graphite fuel tube of diameter 10 mm, which is a prototype of potential components of compact high temperature reactor (CHTR). Atmospheric pressure chemical vapour deposition (APCVD) was used for coating deposition and properties such as morphology, porosity, thickness variation are evaluated. Micro-structural differences in the coating caused by substrate distance from precursor inlet in a CVD reactor were also studied. The study establishes µ-CT as a potential tool for characterization of SiC coating during its future course of engineering. We showed that

depletion of reactants at larger distances causes development of larger pores in the coating, which affects its morphology, density, and thickness.

X-ray µ-CT provide three-dimensional structure of an object non-destructively owing to the high penetration of X-ray [39,127,149]. It has been popularly applied to several applications of micro-structural characterization of bulk materials such as foam, composites, bones etc. [150,151]. Application of X-ray µ-CT for the analysis of coating layers is a relatively new method, which has only been the topic of a few publications so far. The first investigation of coating layers with µ-CT was performed by Perfetti who determined characteristics of the coating layer such as porosity and layer thickness [152]. Recently structural analysis of coatings on tablets and granules has also been reported using an in-house X-ray generator [8,153]. Sondej et. al. has applied this technique for investigation of thickness and morphology of coating on porous particles [154]. Bulcke et al. have applied X-ray µ-CT apart from other technique to study structure of coatings on wood [155]. High quality X-ray µ-CT analysis on sub-mm specimens has also become possible with sub micrometer spatial resolution with the application of synchrotron X-ray sources which is extremely bright and highly parallel and has a tuneable energy [156]. This is the first attempt of applying µ-CT in such geometry, possibly due to cylindrical symmetry of the sample. Most of the previous studies are carried out on spherical samples where coating is deposited over the outer surface [152,154]. It is also shown that simple image analysis methods applied to tomographic slice images provide valuable information regarding the porosity, presence of cracks, morphology, and thickness variation of the

coating. The 2D image analysis, applied using open-source image analysis tools ImageJ, is able to provide quantitative micro-structural insight of SiC coatings [157].

Table 4.1 Process parameters of Sic coating deposition using APCVD

Coating Temperature	**1350^{o}C**
Pressure	Atmospheric
Argon flow rate	5 lpm
Hydrogen flow rate	5 lpm
MTS flow rate	2ml/min
reaction time:	18 min
Coating rate	5μm/min

c) Sample preparation

The prototype of actual fuel tube was prepared in the form of graphite cylinder of length 235 mm and diameter 10 mm. An internal bore of diameter 3 mm was created at the centre of this sample. APCVD (Atmospheric pressure chemical vapour deposition) was then used to deposit SiC coating over the internal surface of the bore [158,159]. The CVD was carried out using electrically heated vertical high temperature graphite reactor at 1623 K, which defines the rate-limiting step of the CVD process to be diffusion controlled. MTS (Methyl-tri-chloro-silane) was used as precursor of SiC along with the argon-hydrogen gas mixture as carrier gas. The MTS flow-rate to evaporator at 473 K was controlled by peristaltic pump and the resulting vapour is swept into CVD reactor by argon-hydrogen gas mixture. The argon-hydrogen flow-rate

is controlled by Mass flow controller. The schematic of the graphite tube on which SiC coating was grown is shown in Figure 4.2. The process parameters used in coating deposition are summarized in Table 4.1.

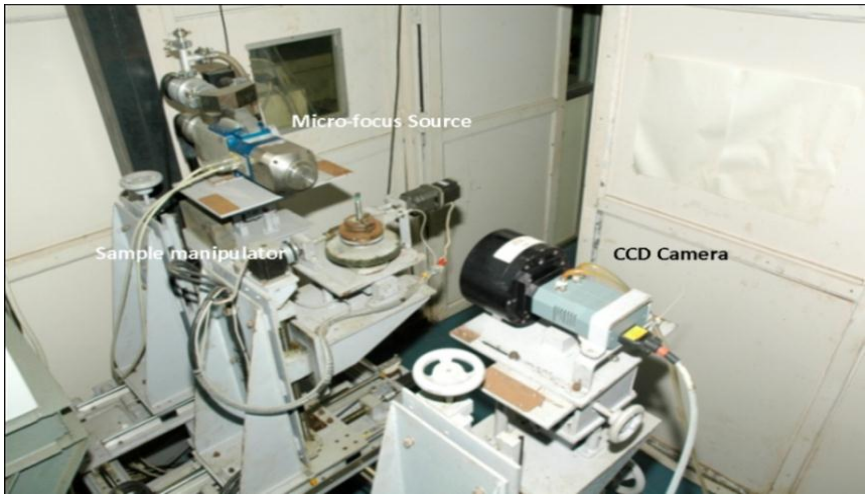

Figure 4.3 Micro-focus based imaging system used in this study

d) Experimental

Laboratory based X-ray μ-CT system used in this study consists of three major components namely source, sample handler and detector (Figure 4.3). The X-ray source is a Fainfocus micro-focus tube (160 kV, 1mA, 10 W, ~ 5μm focal spot). The sample handler is an in-douse designed and developed 4-axis sample manipulator system (x, y, z and θ). The detector is an Andor make front illuminated CCD camera having 100μ thick Gd_2O_2S: Tb phosphor layer coating over the front face of 70 mm diameter coupled fiber-optic [160]. The sample was placed on the rotation stage and projection images were acquired at 40kV tube voltage, 300μA tube current, 20 seconds exposure time, 60 mm source to object distance and 240 mm object to detector distance. This

allows imaging of full 10 mm diameter of prototype fuel tube in the field of view of CCD with optimum contrast and 4X geometrical magnification to enable effective pixel size of ~10μm. A single μ-CT scan covers 12 mm length of the sample, which covers approximately 85 mm^2 of internal surface of the tube with SiC coating. In order to evaluate the effect of substrate distance from the precursor inlet, μ-CT experiments were carried out for two different domains of the tube B1 and B2 as shown in the Figure 4.2. Regions B1 and B2 were chosen during the experiment by moving the sample in vertical direction. The distances to the centre of the two domains from the gas inlet are 56 mm, 118 mm respectively. Tomography projection data was collected for each domain with sample rotating about its axis for 360 degrees at an angular step 0.45 degree. Total 800 projections were collected for each domain. μ-CT reconstruction was carried out using in-house developed software based on filtered back-projection algorithm for cone beam reconstruction using FDK method [161]. The reconstructed slice images obtained for each domain data were stacked to form 3D image of the sample which after segmentation, virtual sectioning and color-coding according to gray values of respective materials, show distribution of various sub-components, their geometries and micro-structure.

e) Results and Discussion

i. Qualitative analysis

Visual inspection and qualitative analysis of μ-CT images provide information regarding the morphology, uniformity, and porosity of the coating. Several studies have

been reported based on two-dimensional characterization of coating [162,163]. Figure 4.4shows various images of X-ray µ-CT reconstruction from a typical tube domain B2.

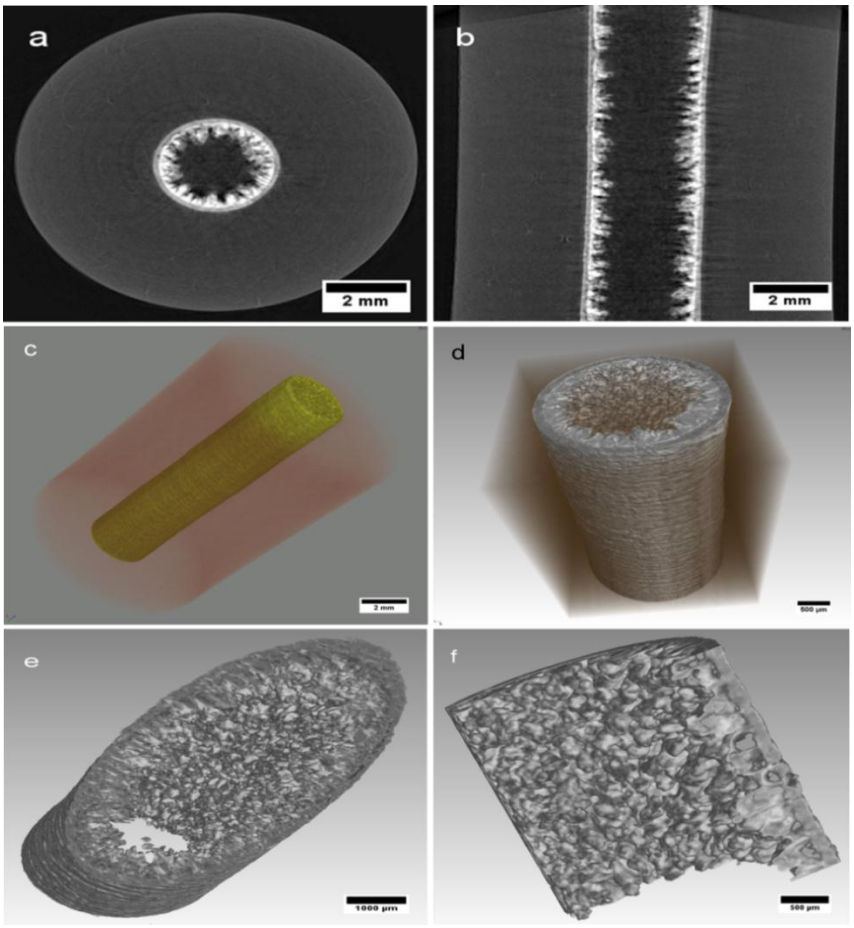

Figure 4.4 Horizontal (a) and vertical (b) slice images of µ-CT reconstructed graphite tube domain B2 (c) 3D micro-graph of coated fuel tube section B2 (d) 3D cropped view to show substrate coating interface (e) 3D segmented view of coating only showing granular morphology (f) a close view of (e)

Qualitative observation of horizontal and vertical slice images shown in Figure 4.4(a-b) depict the full cross section of graphite fuel tube, internal bore and its surface, SiC coating deposited throughout the internal surface of the bore and some dendrite

structures over its surface. Gray region is the cylindrical graphite fuel tube whereas central region show bore of 3 mm diameter. Graphite tube is not of much interest for the present study except its central bore acts as substrate for SiC coating and it will not be shown in further images. The white region in the image is SiC coating. It is seen to have a base coating of certain thickness attached to the substrate over which granular shaped dendrite structures are attached. The fact is more clearly visible in the 3D images presented in Figure 4.4(c, d). The volume rendered 3D images of typical tube domain is presented with different color-coding for substrate graphite, SiC coating and air in the hollow region. Figure 4.4(a-d) presents a clear view of major structural properties of the coating i.e. morphology, thickness, uniformity over a large region of interest. The interface of the coating with graphite substrate can also be visualized which show apparent detachments at certain radial and axial locations.

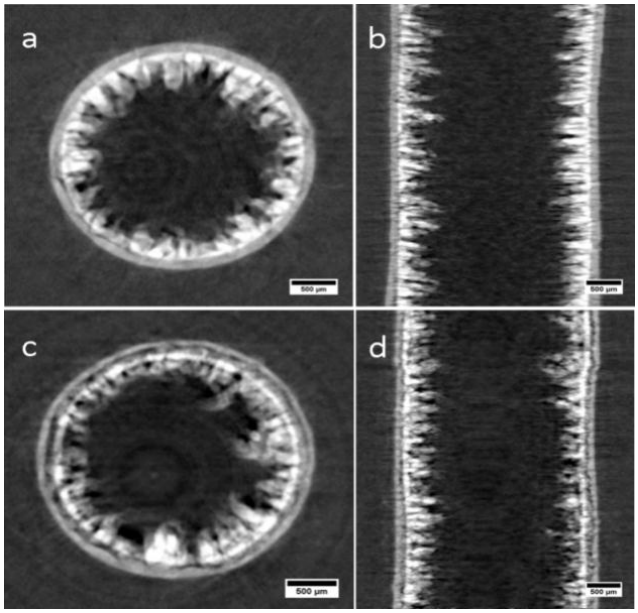

Figure 4.5 Comparison of horizontal and vertical region of interests in slice images of SiC coating of domains B1 (a, b) and B2 (c, d)

The reason for loosing adherence at certain places is due to bridging of dendrite structures with the formation of inadequately adherent coating caused by reduced reactant concentration. Some closer views of the coatings obtained from virtual sectioning of 3D volume are shown Figure 4.4 (e, f). For clarity of visualizing coating morphology, the graphite tube is completely removed through volume rendering. Morphology of the coating is seen to be granular having some dendrite structure over its surface. The shape and size of the dendrite structure can be seen to be varying randomly. This is because, in the beginning of CVD process as the reactants pass through the substrate surface, the nucleation occurs homogeneously and growth is controlled by chemical kinetics at the solid-gas interface, which leads to the formation of initial coated region with uniform thickness and density. Later, when the crystals of reactive species start to grow, concentration gradient formed above the interface causes the growth to be controlled by mass transport process, which is the reason for the formation of dendrite structure and deposition of SiC granules [164].

Figure 4.5 compares the microstructure and morphology of SiC coating in the two tube domains B1 and B2. The region of interest presented here show only the SiC coating whereas graphite substrate is removed for improved visibility. Both the regions of tube i.e. B1 & B2 consist of the base coating over which the dendrite structures are attached. The thickness of base coating appears to be less in B2 as compared to B1. As we see from Figure 4.5, the coating thickness appears to have short range (with-in the domain) and long range (across the domains) variation in B1 and B2 along the tube axis. The base coating and dendrite structure appears to be decreasing as we go from B1 to B2

whereas porosity and detachments from substrate are increasing. Both the regions B1 and B2 consist of some micro-pores in the deposited coating however frequency and size of micro-pores is more in B2 as compared to B1. Through qualitative comparison of the two images, B1 is seen bonded more strongly with the substrate and having less number of voids and cracks at the interface. The dendrite structures in B2 are also smaller and attached poorly to the base coating. Such trend is observed because the CVD coating was carried out in mass transfer controlled domain, which usually occurs at high temperature. CVD being predominantly a boundary layer phenomena, high temperature leads to increased kinetics thereby the reactant species are consumed at faster rate than they are replenished, hence decreasing coating thickness along the axial direction was observed. The situation may be overcome by the reversing the gas flow direction periodically [165]. The tomography reconstructed slice images represent two-dimensional distribution of gray values, which for a given chemical compound such as SiC is proportional to its absorption coefficient. Comparing average gray values in reconstructed slice images of SiC coatings of different domains namely B1 and B2, B1 appears to have larger and uniform gray values distribution as compared to B2.

i. Quantitative analysis

Quantitative analysis of tomography images provides estimates of structural and morphological differences of the sample regions B1 and B2. In this study, we have applied simple 2D image analysis to show the additional benefits of μ-CT for measurement of porosity and thickness uniformity [150,152,154]. Image analysis methods are chosen based on their open source availability and applications for coating

characterisation in the current literature. 2D image analysis is preferred here instead of 3D in order to focus more on axial variation of structural properties caused by reactant depletion in the tube during the coating deposition instead of exclusive analysis of porous shapes and geometries. The simple image analysis methods adopted here quite clearly show the quantitative comparison for the microstructure of the coating. Two major properties porosity and uniformity of the coating were analysed quantitatively using simple 2D image analysis on reconstructed slice images. Tomography reconstructed slice images were subjected to a sequence of morphological image processing operations followed by geometrical analysis of micro-structural features.

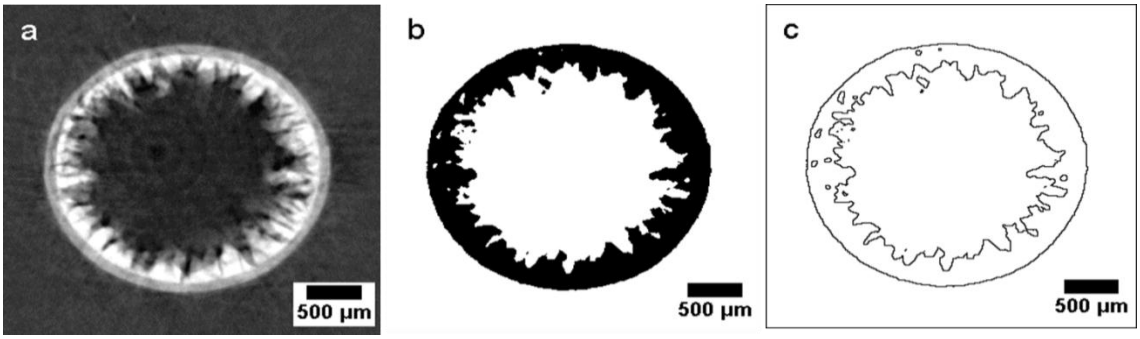

Figure 4.6 Sequence of image processing operations for quantitative analysis of slice images (a) Reconstructed raw (b) Threshold (c) segmented and outlined.

Porosity

Porosity or formation of cracks in the coating plays a crucial role in its operational performance as they lead to penetration of oxygen to the substrate at specific sites [143,144,166]. Porosity also affects its hardness, young modulus, fracture toughness etc. that ultimately influence the wear-resistance, crack propagation and stress-strain behaviour [167]. Coating adherence to the substrate is also affected by pores, voids,

cracks at the coating-substrate interface, which may lead to detachment and peeling-off phenomena in the long-term operation. Figure 4.6 depicts the sequence of image processing operations applied on slice images of the coating in B1 and B2 for their quantitative microstructure analysis. The gray scale images are segmented to select SiC coating using threshold and converted into binary. The value of threshold was chosen based on visual inspection of coating interface. In the binary image, micro-structural features such as pores, cracks, and coating surface are identified, outlined, and labelled with a unique identifier based on their binary scale. Using this image analysis, enclosed area and circularity of micro-pores in the coating of the two tube domains are also measured and compared. Table 4.2 lists the mean values and standard deviations of these measurements. Analysis of these features is based on measurement of number of pixels enclosed by them in the segmented image and fitting with optimum ellipse in its area. In this study, "particle analysis" tool of ImageJ has been employed for geometrical analysis of pores in the slice images. Pore size distribution, porosity (porous area/coated area) and their variation along the tube axis was measured compared for the two domains B1 and B2 to study effect of substrate distance from the precursor on the coating properties [164]. Figure 4.7(a) shows the histograms of Pore frequency distribution in the two tube domains B1 and B2 whereas the variation of pore frequency per slice along the tube axis is shown in Figure 4.7(b). It is clear from the plots that B2 consists of more pores as compared to B1. Pore frequency per slice varies randomly along the tube axis in a given domain however, the average number of pores per slice increases as we go from B1 to B2. Figure 4.8(a) shows the histogram of

integrated pore area per slice for B1 and B2 whereas Figure 4.8(b) shows its variation along the tube axis. It is evident from the plots that the integrated porous area per slice for all the pores increases in B2 as compared to B1 whereas within the domain it varies randomly. Figure 4.9 (a) shows average pore size distribution B1 and B2. It is evident from this plots that the pore size in B2 is larger as compared to B1. Some of the pores of very large size also present in B2. The ratio between B2 and B1 keeps increasing as pore size increases (at a size of 100 µm, there are only about 25% more pores in B2 than B1, at 200µm, there are twice as many, and past 400 µm there are no more in B1..

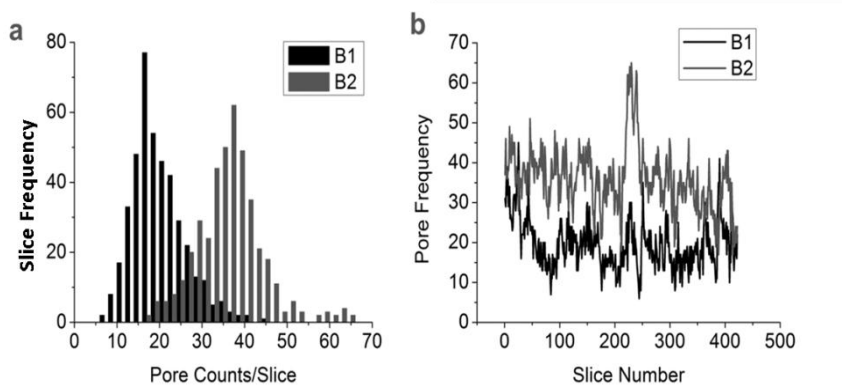

Figure 4.7(a) Pore frequency distribution for domains B1 and B2 (b) Pore frequency variation along the tube axis

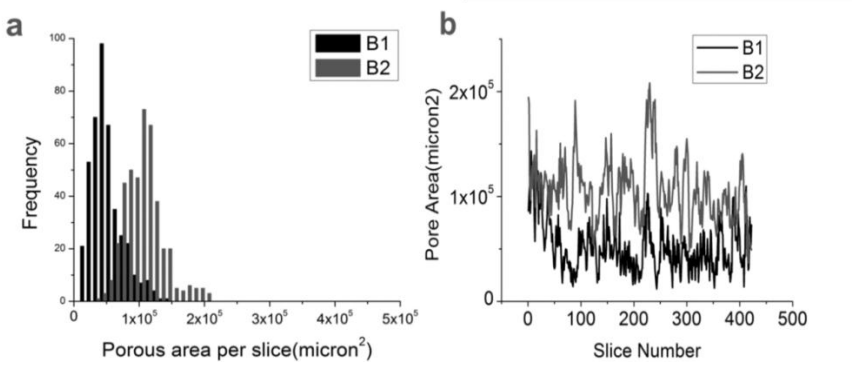

Figure 4.8 (a) Pore area distribution for B1 and B2 (b) its variation along the tube axis

This clearly shows that not only are there more pores in B2, but also larger in diameter as well. Measuring the contour of curved surface cause by dendrite structures and multiplied by the slice thickness, the surface area of the SiC coating per slice is calculated. It is shown in Figure 4.9 (b) that coating surface area is comparable in B1 and B2. Hence, even when the surface area of the coating is similar in the two domains; the coating is comparatively more porous in B2 as compared to B1.

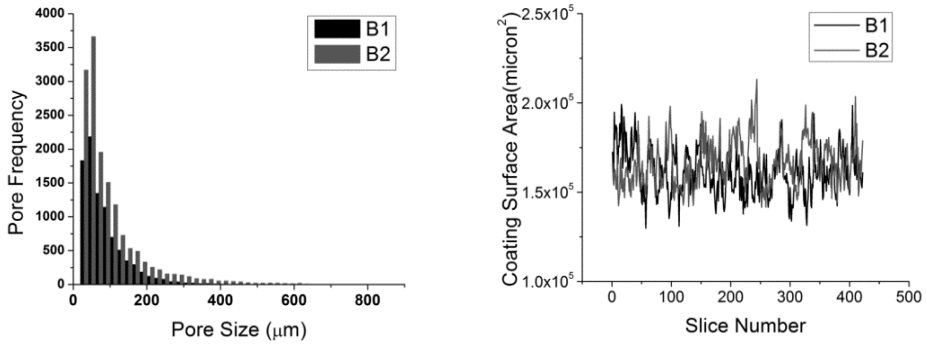

Figure 4.9 (a) Pore Size distribution (b) Surface area of the coating in B1 and B2

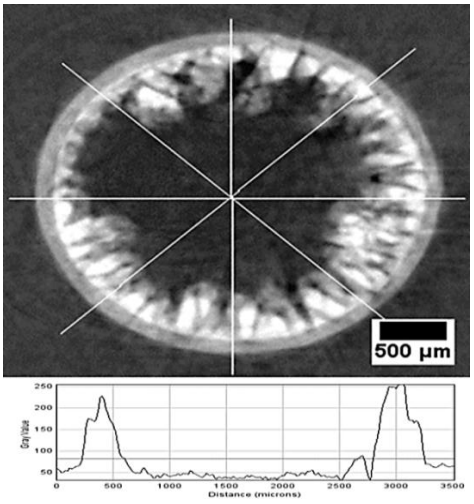

Figure 4.10 Slice image to show method of coating thickness measurement using grid lines and their profile plots. One profile plot along the vertical line is shown.

Coating thickness and uniformity

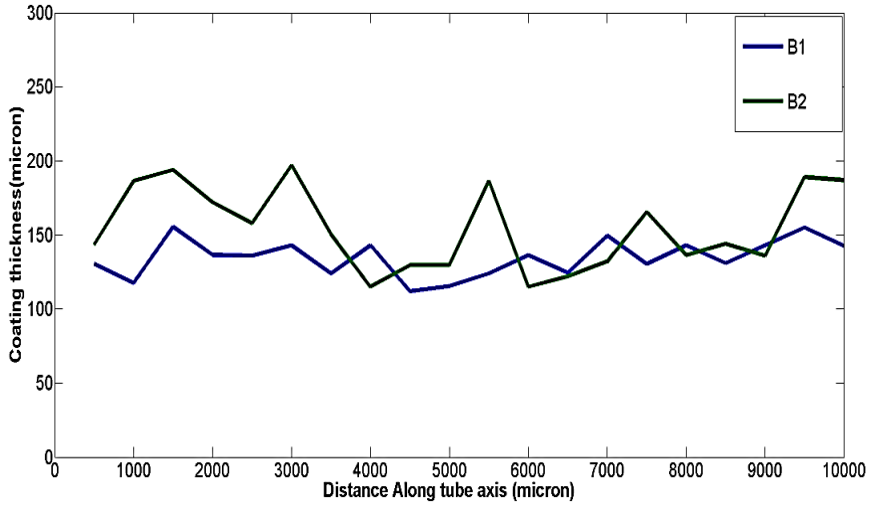

Figure 4.11 Coating thickness variation along axial direction for B1 and B2

As stated earlier, SiC coating has a base coating attached to the graphite substrate covered by dendrite structures. Finding distinction between base coating and dendrite structure is difficult at all the places of the two regions hence thickness calculation of SiC coating is carried out taking dendrite structures also into account. Figure 4.5 shows segmented images of only coating portions i.e. the coating base and dendrite structures. The thickness measurements are carried out on these images using the method explained in Figure 4.10. For coating thickness measurement, profile plots along the grid line were drawn and values of intercepted length over the line of fixed gray value is measured at both the ends. The mean value of these measurements is taken as coating thickness considered slice. This process was repeated for all the slice of region B1 and B2. The coating thickness variation along the axial direction of tube for the two domains B1 and B2 is shown in the Figure 4.11. The mean coating thickness and

standard deviation are tabled in Table 4.2 for the two domains. As explained earlier, due to bridging of dendrite structures with the inadequately adherent coating, the coating appears to be detached from the substrate at certain locations. These detachments have contributed in the increased porosity of the coating at larger distance. Increased thickness is due to the larger pores in the coating covered by dendrite structures.

Table 4.2 Comparison of microstructure measurements on SiC coating on B1 and B2

Structural Properties of coating	B1		B2	
	Mean	Standard Deviation	Mean	Standard Deviation
Coating thickness (μm)	134.65	12.50	154.45	28.04
CT number	151.73	13.90	154.94	22.53
Pore counts	19.51	6.18	35.91	7.95
Average area of pores (μm^2)	2590	740	2970	591
Total porous area (μm^2)	51405	2380	106850	2935
Pores circularity	0.80	0.20	0.76	0.24
Pore dimension (μm)	83.82	60.67	100.33	89.91
Curved perimeter (μm)	16120	1264	16633	1298

4.3 Graphite fuel-tube of CHTR

Fuel tube of compact high temperature reactor is made of either high-density nuclear grade isotropic graphite or carbon-carbon composites. It is a 1430 mm long tube having a central bore with 35 mm inner diameter and 75 mm outer diameter which serves as flow channel for liquid metal/salt based coolant. Fuel tube also houses 12 nos. of 10 mm diameter and 1180 mm long peripheral fuel channels made in the thickness; out of

this 1050 mm is used to accommodate fuel compacts. The fuel tube is designed to withstand high temperature gradients caused by low temperature central region caused by coolant flow and high temperature peripheral region due to fission energy in the high burn-up fuel [140,141]. It requires dimensional characterization of fuel and coolant channels i.e. their cross sectional area, inter-spacing and longitudinal uniformity throughout its length [168]. Since the internal surface of the tube is coated with oxidation resistant material such as SiC and the coating micro-structure is affected by substrate structure and uniformity; characterization of micro-imperfections and surface non-uniformity of the graphite substrate is necessary. Micro-imperfections in graphite matrix are also important to be evaluated to ensure long term failure free performance of the fuel tube under operation at high temperature [169,170]

Traditionally non-destructive dimensional characterization of fuel tube is based on radiographic projection imaging. Micro-structure and surface morphology is evaluated using techniques of electron microscopy such as SEM/TEM etc. [171]. While radiography provides limited insight about internal structure because of inherent superposition of overlying features, electron microscopy allows surface specific micro-structure visualization with limited field of view. The later one is also destructive in nature as it requires contrast agents; elaborate sample preparation, and serial sectioning. For the non-destructive dimensional characterization of full CHTR fuel tube, we used high resolution X-ray CT followed by 2D image analysis to measure cross sectional area and inter-spacing of the fuel/coolant channels, micro-imperfections of graphite matrix and surface non-uniformity of the bores.

f) Sample preparation

To study the feasibility of X-ray CT for non-destructive analysis, a simulant fuel tube has been fabricated with low grade graphite. A schematic and actual photograph of the fuel tube used in this study is shown in Figure 4.12. The peripheral bores of equal diameters and a central bore with uniform inter-bore spacing along the longitudinal direction were created. The dimensions and inter-spacing of the bores was not controlled very precisely. In actual design, internal surface of these bores are coated with oxidation protective SiC coatings. However, in this study the fuel tube with un-coated bores has been taken so as to focus on dimensional characterization of bores and their inter-spacing.

g) Experimental procedure

The resolution, depth of penetration and field of view of X-ray CT system depends upon source size (focal spot size) in combination with detector pixel size, power of X-ray tube and geometrical magnification of the system respectively. Two different experimental systems have been used in this study to incorporate suitable resolution, field of view and depth of penetration in the sample to image required details at two different resolution scales. A higher resolution is required to image the surface roughness and sub-surface imperfections in the fuel tube material. A 160 kV X-ray tube with (~ 400 μm) focal spot size and a detector, which consists of a CCD, based X-ray imaging camera having a Gd_2O_2S: Tb phosphor layer coating and a de-magnifying optics so as to enable a field of view of 120 mm has been used to study a small section of the large fuel tube. The tomographic resolution of the system has been

measured to be ~ 200 µm. The sample has been mounted on a rotation stage for collecting radiographic projections while rotating the sample about its axis for 360 degrees at an angular step 0.45 degree. The experiments have been carried out at X-ray tube voltage 110 kV and 1 mA current.

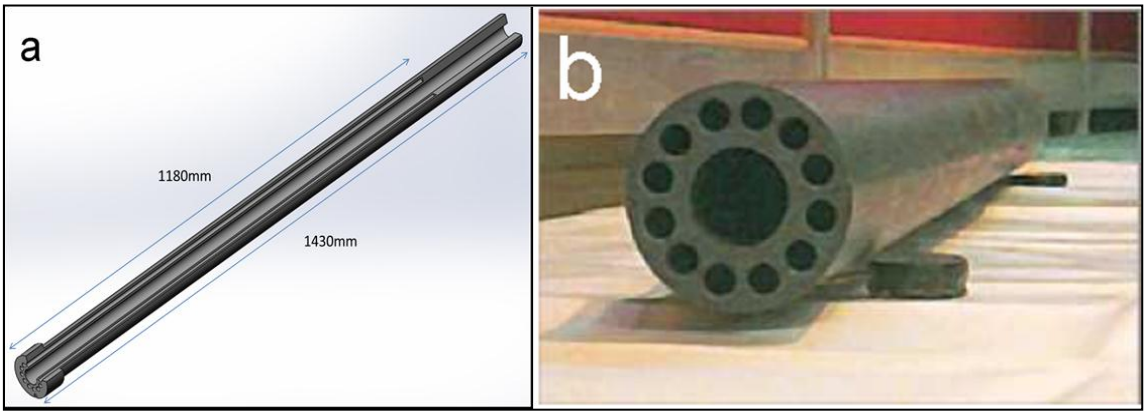

Figure 4.12 Schematic of the samples fuel tube studied (a) and its actual photograph (b)

h) Image reconstruction and analysis

Cross sectional area and inter-spacing of fuel/coolant channels have been measured using image based quantitative analysis on reconstructed slice images obtained from high-resolution CT. The study has also been used to detect and measure micro-imperfections in the graphite matrix and surface non-uniformity of the fuel tube bores. Acquired data obtained from different scanning processes have been used in computational reconstruction of tomography slice images using filtered back-projection [37,161]. 3D images have been produced by stacking sectioning, color-coding of these slice images using ImageJ [157]. Tomography slice images show distribution of material attenuation co-efficient in various sample planes. Image processing and image analysis tools have been used to measure various structural features of fuel tube.

Sequence of various operations for quantitative analysis of tomography slice images have been shown in Figure 4.13. Features related to a single material was selected using threshold operation and binary images are obtained.

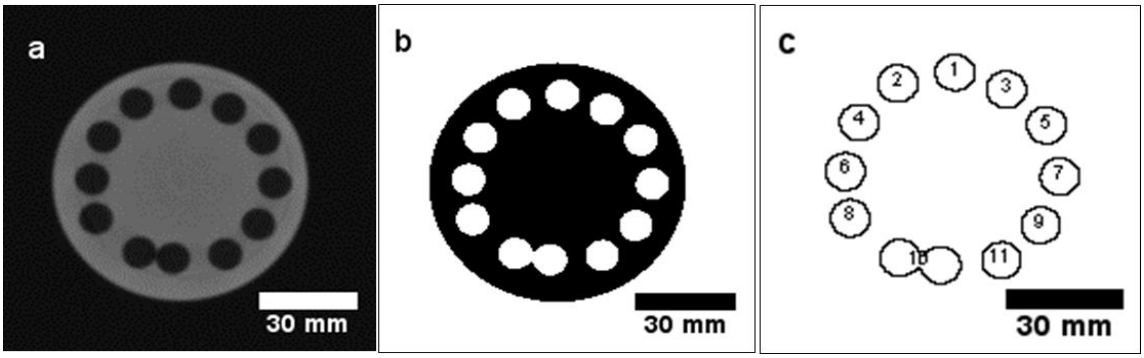

Figure 4.13 Sequence of digital image processing operations to carry out structural and morphological analysis of X-ray CT data.

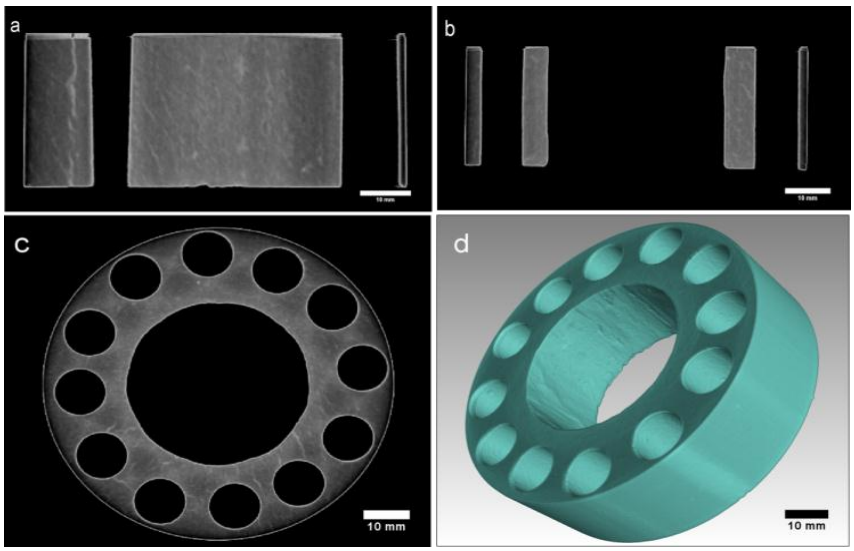

Figure 4.14 Section of fuel tube (a) XZ slice (b) shows the YZ slice (c) XY slice (d) 3D image of fuel tube section show surface roughness.

The quantitative measurement of structural features is based on their segmentation in the image by various morphological operations such as opening, closing, dilation,

erosion etc. Each individual feature in the segmented image is outlined and labelled with unique identifier. In the scaled images, counting the pixels and fitting of most appropriate geometry in the labelled feature identified as particles provide measurement of various geometrical and morphological parameters [5,152,154]. Particle counting module in open source image analysis tool, ImageJ has been used. In this study, segmented features are fitted with ellipse and their area and centre of mass co-ordinates has been calculated for each bore in all the slices. The distance between the centres of mass of consecutive bores has been taken as bore inter-spacing.

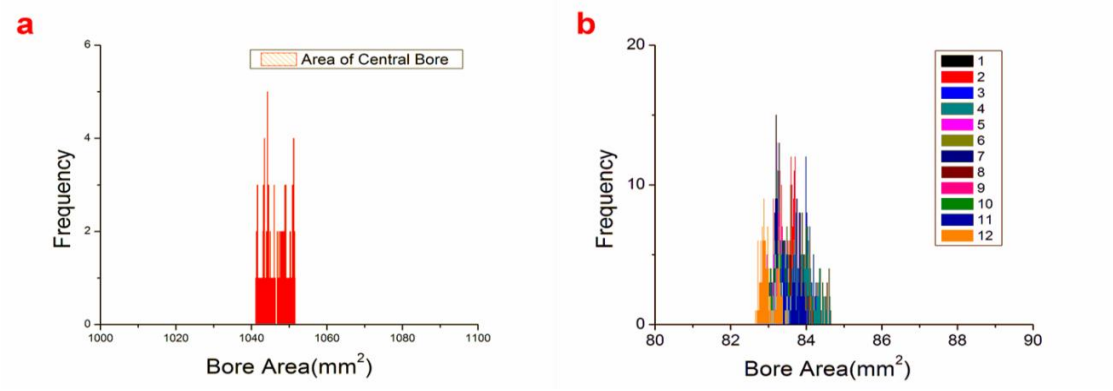

Figure 4.15 Histogram of bore area (a) central (b) peripheral

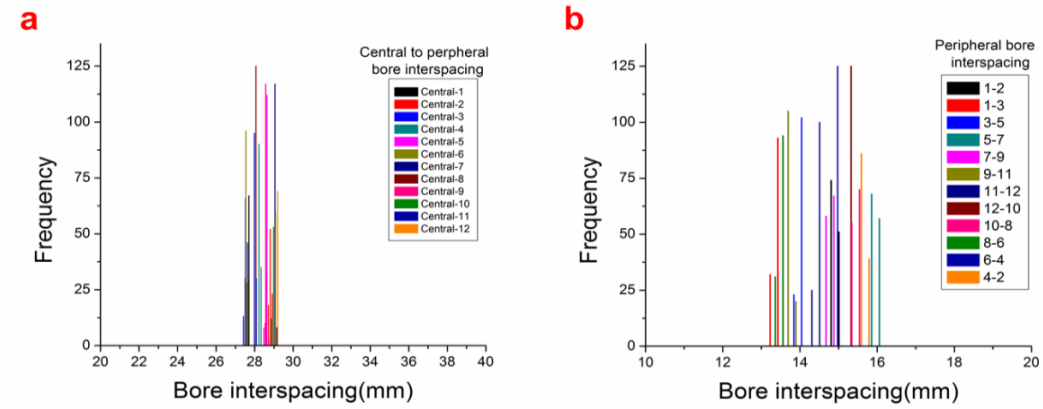

Figure 4.16 Histogram of bore inter-spacing (a) central (b) peripheral

i) Results and discussion

High-resolution tomography reconstructed orthonormal slice images of a fuel tube section of dimension100mm x 100mm x 30mm and its 3D volume image is shown in Figure 4.14. Qualitative observation of XY slice show apparently uniform bore cross sectional area and interspacing however, YZ and XZ slice indicate some variation in bore interspacing along the longitudinal direction. These images also show some small imperfections in the graphite matrix. The 3D images shown in the figure also show some surface non-uniformity over the central bore.

Table 4.3 Measured parameters of fuel tube for high-resolution tomography system

	Bore area (mm^2)		**Bore Inter-spacing (mm)**		**imperfections size**		**Bore circularity**	
	Central bore	Peripheral bores	Central to peripheral	Between Peripheral bores	Major axis (μm)	Minor axis (μm)	Central bore	Peripheral bores
Mean	1046.6	83.51	28.35	14.66	976.7	577.6	0.89	0.90
Standard deviation	3.23	0.05	0.02	0.01	368.4	112.75	0.003	0.001

i. Dimensional characterization of Fuel tube channels

Following image based quantitative analysis of tomography slice images, as discussed in the previous section, variation of bore cross sectional area and inter-spacing has been measured and shown in Figure 4.15 and Figure 4.16 respectively. Histograms of bore

area for central and peripheral bores have been shown in Figure 4.15 (a, b). Histogram distributions of interspacing between peripheral bores and their spacing with central bore are shown in Figure 4.16 (a, b). The mean and standard deviation of these measurements has been listed in Table 4.3. As can be seen, there is a very small (<0.2%) variation in bore area and interspacing at this resolution and the bores can be considered reasonably uniform.

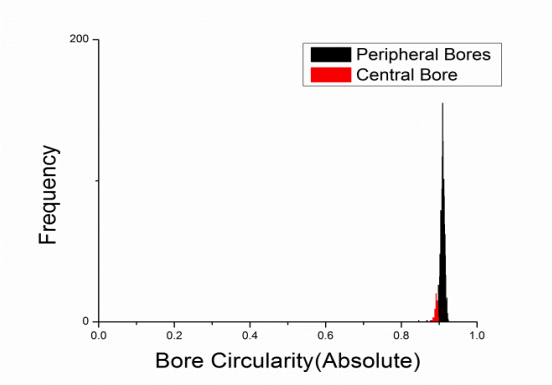

Figure 4.17 Histogram of bore circularity of peripheral and central bore

ii. Micro structure of graphite

The slice images of fuel tube as shown in Figure 4.14 show some micro-cracks being initiated in the material region. These micro-cracks may lead to imperfections and in-homogeneity in the oxidation protective coatings over its surface, which ultimately affect its performance in environment of liquid metal/salt, based coolant during operation [20]. Image analysis has been used to measure circularity of the bores and size distribution of micro-cracks. Figure 4.17 shows the circularity of the bores which is also a measure of its surface roughness. The micro-cracks of the matrix are of random shapes hence their size has been measured in terms of major and minor axis of

ellipse fitted in their segmented area and shown in Figure 4.18. The mean and standard distribution of these measurements has also been listed in Table 4.3.

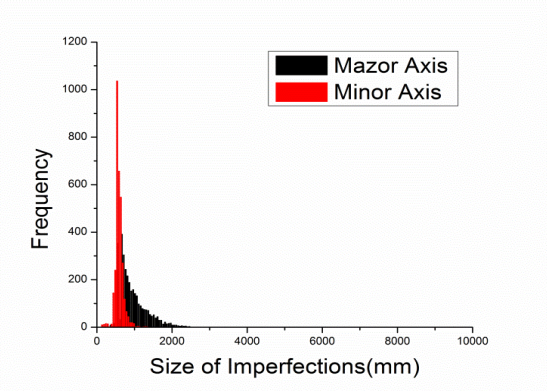

Figure 4.18 Histogram of length of major and minor axis of ellipse fitted in the micro-imperfection of the graphite matrix

4.4 TRISO coated fuel particles

TRISO (Tri-structural Isotropic) coated fuel particles are the most fundamental element of the reactor core. Figure 4.19 shows its basic design which consists of a kernel ~ 500µ diameter comprising of fissile, fertile, and burnable poison materials. This core is coated with four layers of pyro-carbon (PyC) and SiC with specific thicknesses and densities in a particular order. Each layer in the TRISO coated fuel particle performs their specific functions when used as a fuel of high temperature reactors.

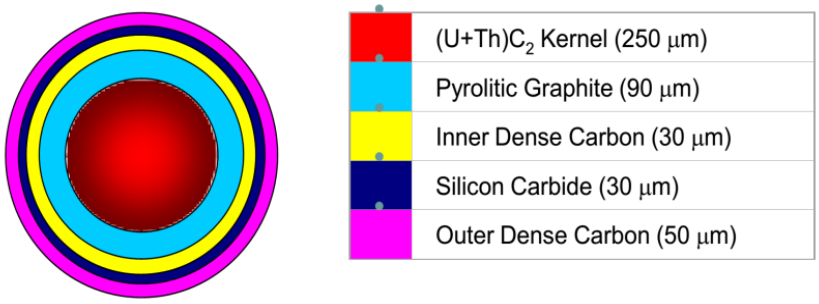

Figure 4.19 TRISO coated fuel particles showing core radius and thickness of layers

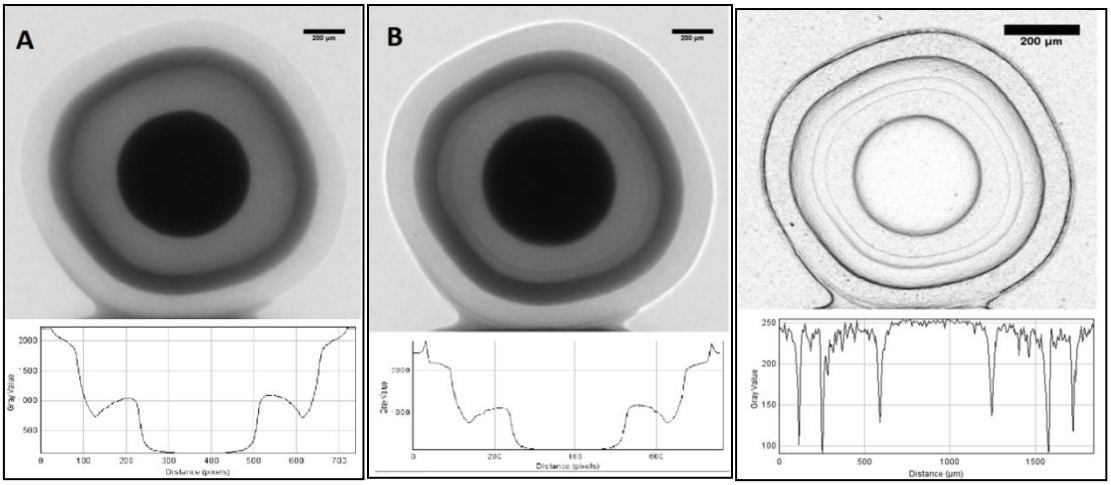

Figure 4.20 Comparison of absorption and phase contrast images of TRISO coated fuel particles showing different layers (a) Absorption contrast image (b) Propagation phase contrast image (c) The edge enhanced image clearly showing all the interfaces. [Scale bar = 200µm for all images]

The densities of pyro-carbon coatings are very close, hence traditional absorption contrast imaging has been found to be incapable of distinguishing different layers. Instead PB-PCI offers improved visibility of the layered interfaces at small density gradients [25]. Figure 4.20 (a and b) shows absorption contrast image (a) taken at 5mm and PB-PCI images (b) taken at 500 mm distance of the sample from the detector. The small density difference between inner PyC and buffer layer not resolved in absorption contrast image is clearly visible in PB-PCI image due to increased coherence in the parallel monochromatic beam. Since very large number of TRISO particles (about 13.5 millions) comprise the core, manufacturing of fuel kernels, deposition of multi-layered coatings on the particles, and characterization of the coated particles pose special challenges. We have successfully applied PCI for the optimization of process

parameters during the development of coating layers over a simulated fuel element with ZrO_2 and Al_2O_3 kernels. In the process of design and optimization of technique for the fabrication of Fuel elements, several experiments have been carried out with 2 layers, 3 layers, and four layers fuel particles with different manufacturing parameters and characterized using X-ray PCI [160,172,173].

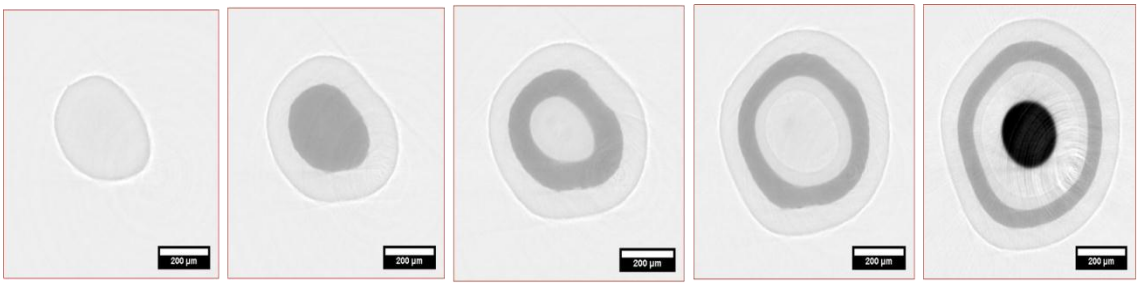

Figure 4.21 X-ray µ-CT slice images of TRISO coated fuel particle at different planes of elevation. [Scale bar = 200µm for all images]

After optimization of manufacturing process issues related to optimization of structure and density of these particles need to be dealt with the application of suitable non-destructive imaging technique. One of the important characteristic is the measurement of coated layers thickness and uniformity. Applying X-ray PCI and some basic image analysis, we have measured coating layers thickness Figure 4.20(c). The thickness of different layers was measured using intensity plot profile of scaled image and taking average for various directions. The thickness of various coating layers was measured as follows - Low-density pyrolitic carbon (PyC) buffer layer 99 µm; Inner high-density PyC layer 53µm; Silicon carbide (SiC) interlayer 69µm; Outer high-density PyC layer 95µm. Using image gradient different, interfaces of different layers in the fuel particle can be distinguished more clearly. Acquiring such images over several angles of

rotation, we also visualized the azimuthal non-uniformity of the coating thickness of various layers.

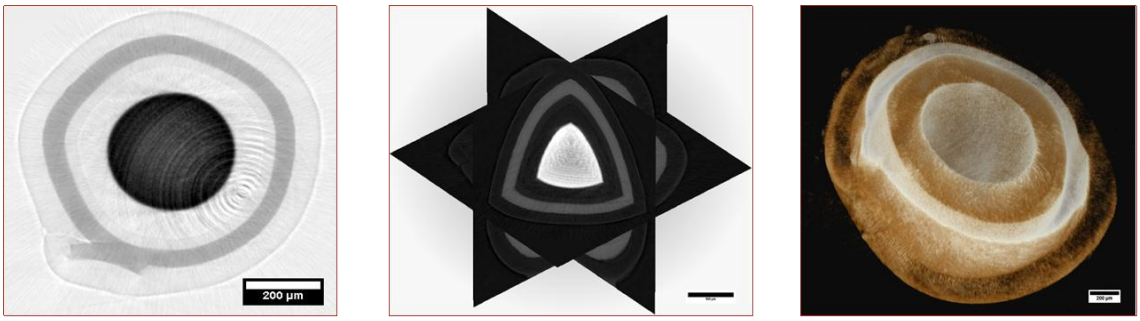

Figure 4.22 Different view of phase contrast µ-CT of TRISO coated fuel particle (a) Slice image (b) Orthonormal view (c) 3D volume rendered view. [Scale bar = 200µm for all images]

Further to this X-ray phase contrast µ-CT has been applied to visualize the coating layers in 3 dimensions and measure their thickness at various orientations. µ-CT also deteµs the size, shape, and integrity of the microspheres in addition to the measurement of coating thickness. The technique involves taking phase contrast enhanced projection images of the microspheres on high-resolution X-ray detector using micro-focus X-ray source at 40 kV and 300 µA. The projection data is processed for flat field correction, noise removal. µ-CT reconstruction was carried out using filtered backprojection algorithm and reconstructed slice images at various elevations showing anisotropy of the shape and deviation from spherical geometry are shown in Figure 4.21. The variation of thickness of different layers at different planes is also visible in these images. The three dimensional view of the TRISO coated fuel particle is shown in Figure 4.22.

5 APPLICATION OF SYNCHROTRON IMAGING BEAMLINE

In this chapter we have discussed the applications of synchrotron X-ray μ-CT for the micro-structural characterisation of advanced materials such as extracant impregnated polymer beads (EIPBs), polyurethane foam, Al-SiC metal matrix composites and carbon composites. For extracting quantitative structural information from reconstructed μ-CT slice images, image processing and image analysis algorithms are applied.

5.1 Polymeric beads

The principal aim of radioactive waste treatment in nuclear industry is to minimize the volume of the secondary waste via optimized treatment processes, leading to generation of effluents, free from radioactive contaminants, for their final disposal. Therefore, the waste streams needs to be efficiently treated to bring down the radio toxicity to permissible levels or to level of zero discharge. The process of radioactive waste mnagement is also useful in recovery of some useful isotopes and actinides from a variety of waste streams employed in nuclear industry using aqueous radiochemical

separations[174–180]. The currently available technologies for separation and recovery of metal ions are solvent extraction, ion exchange, chemical precipitation, membrane based technologies and sorption on solid matrix using natural and synthetic adsorbents. Even though they are popular and efficient for bulk separations, these methods do have marked limitations that force the separation scientists to look for more efficient and technically feasible alternatives. The macro porous polymeric beads, impregnated with metal-specific extractants, show excellent extraction capability under column operation. They represent second generation of extraction system and offer distinct advantages due to possibility of high extracant loading resulting in enlarged metal uptake capacity. PES is well known for its application in preparation of polymer supported extraction systems, like membranes, beads due to its outstanding oxidative, thermal and hydrolytic stabilities, as well as good mechanical and film-forming properties [175,176,181,182].

a) Micro-structure of beads

The performance of Extracant impregnated polymeric beads is strongly correlated with its porous structure. The morphology of the PES bead is an important physical characteristic, which determines its usability and stability for metal ion separation from aqueous media. Ideally, for metal ion sorption, an extractant impregnated polymeric beads should have a hollow cavity at its core, surrounded by a porous polymeric matrix structure. The central hollow core enables it to encapsulate organic solvent and the pores on the matrix provide channels for the interfacial contact of aqueous and organic phases essential for metal ion transfer [175,181]. Ideally, a radial variation of pore size

distribution from periphery towards the centre of the bead is desired. The inner portion of the bead matrix should have high porosity with relatively bigger pore size for better mass transfer of aqueous and organic phases, while the outermost part of the bead should have a thin layer of nano-porous but relatively dense matrix, which prevents the loss of organic extractants. During the solidification of polymeric mixture drop to bead, additive's solubility in the antisolvent (water) determines the porosity and overall distribution of polymer inside the bead. The PES based extracant impregnated polymeric beads (EIPBs) have been therefore investigated for their micro-structure using synchrotron based X-ray μ-CT followed by quantitative image analysis.

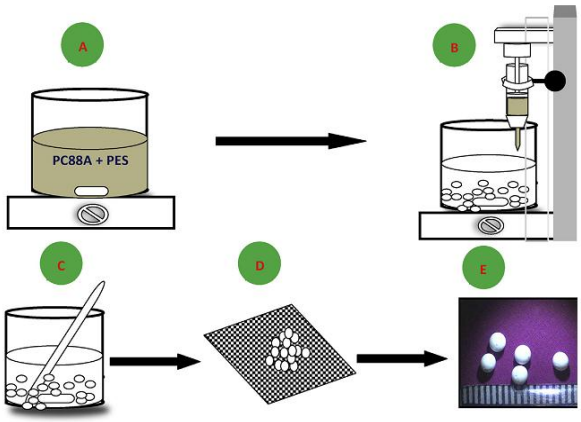

Figure 5.1 Preparation of extractant impregnated porous PES beads (EIPBs) [182]

b) Sample preparation

Extracant impregnated porous PES beads (EIPBs) with DTDGA extractants were prepared, using phase inversion technique. Laboratory reagent (LR) grade 1-methyl 2-pyrrolidone (NMP)[C_5H_9NO], polyethersulphone (PES) [$C12_2H_8O_3S]_n$ and poly vinyl alcohol (PVA) $[C_2H_4O]_n$ were procured from local market. PES powder was dissolved in 1-methyl-2-pyrollidone (NMP), to obtain the PES solution of required

viscosity. Aqueous solutions were prepared, using water purified by Millipore-Q water purification system, having conductivity of 0.6mS/cm, or lower. DTDGA and polymer solution-DTDGA was synthesized by the condensation reaction of potassium salt of ethane-1, 2-dithiol with N,N-bis-(2-ethylhexyl)-2-chloroacetamide [176,182]. The purity of the product was 99% and the yield of the reaction was 95%. A known amount of DTDGA was added to the PES solution and the mixture was added drop wise into a suitable aqueous bath, using a syringe with needle of appropriate diameter. A dilute aqueous PVA solution (~0.1%), under continuous stirring by a mechanical stirrer was used as a suitable phase inversion medium. Within a few minutes of stirring, soft beads were obtained which were filtered and repeatedly washed with DI water. The beads were then incubated in water, for 24 h, for complete curing. A flow-chart, presenting the sequence of operations during sample preparation is given in Figure 5.1.

c) Data acquisition and experimental details

Phase contrast X-ray μ-CT of as prepared polymer bead sample was carried out using synchrotron imaging beamline at Indus-2 synchrotron source RRCAT Indore described in chapter-3 [18]. A PES bead sample of diameter 2.4 mm was placed on rotation stage with the help of suitable sample holder. The experiment was carried out at 10 keV monochromatic beam energy. This selection of beam energy is based on sample composition and thickness to ensure sufficient transmission of beam through the sample and interaction within it to generate good contrast and S/N in the phase contrast projection image. The propagation distance of 150 mm from sample to detector was optimized to allow development of phase contrast edge enhancement and improve

visualization of material-air interfaces and pore volume. The acquisition time was 600 ms for each image and total 900 projections were collected over 180^{o} rotation of the sample about its axis along with reference and background images which were used for flat field correction of the acquired projection images. The experiments were carried out using Photonic science make VHR CCD detector due to its high efficiency and at the same time high resolution. The PSF for imaging system with this detector of pixel size of 4.5 X 4.5 µm is measured to be 15 µm.

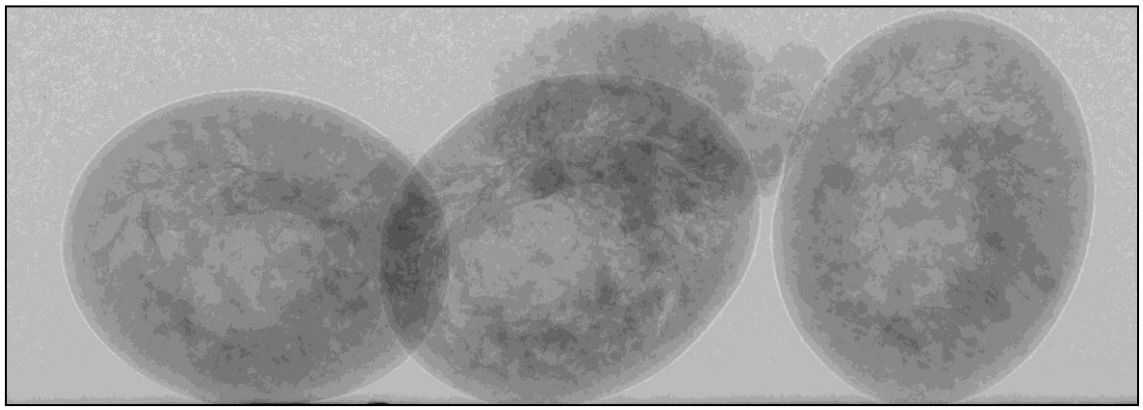

Figure 5.2 PB-PCI projection image of some PES polymeric beads.

d) Results and discussion

Polymeric beads have relatively thin outer polymeric layer and 'shell within shell' type of internal structure due to uneven distribution of polymer suggesting its highly porous central region and comparatively less porous peripheral region. In order to visualize the local microstructure at various planes, we have carried out X-ray µ-CT reconstruction using filtered backprojection technique and slice images of the sample were obtained at different elevation planes. Before tomography reconstruction, each projection image was flat field corrected, normalized, and adjusted for any rotational shift. Figure 5.2

show a typical phase contrast enhanced projection image of polymer beads samples suggesting their highly porous central and comparatively less porous peripheral region.

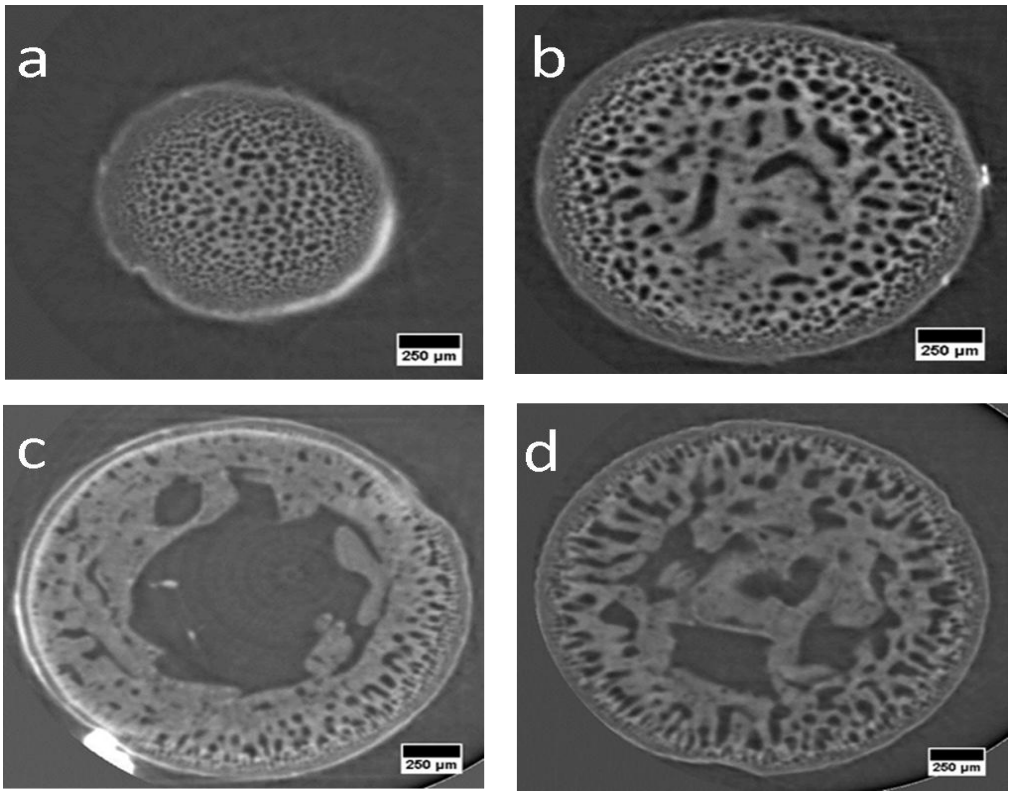

Figure 5.3 SRμ-CT reconstructed slice images at various planes of polymeric bead showing porous architecture and its variation at different sectional planes

Figure 5.3 show reconstructed slices images at different cross sectional planes of the polymer bead sample. The slice images at different plane elevation are showing porosity of the sample and its variation within the sample volume. These images suggest that the bead is almost spherical in shape and microstructure show a wide range of pores varying in shape and sizes. The sample has a coconut type of internal structure with a large central void (volume 10 mm^3) which is filled with organic extractant during application. The porosity is also not uniform throughout the sample and it

appears that the pores in the bulk are of larger size as compared to pores in the outer regions. The central pores of bead are quite large while the other pores at the peripheral region are quite small and generally formed within the solid material making a closed cell. The pore size keeps on decreasing from central region towards outermost surface of the bead where only micro to nano pores are present. 3D visualization of porous structure of polymer bead is shown in Figure 5.4. The figure show a 3D volume rendered image of complete sample where violet colour is showing the porous region and yellow colour is showing the polymeric material of bead. A close look of this 3D image is also shown in the Figure 5.4 showing the large pore cell and enclosed small pores in the wall of large pores. For the quantitative analysis of porosity, we used quantitative image analysis tools to the reconstructed slice images. After segmentation of individual pores, the quantitative measurement of different structural parameters related to pore structure of polymer bead was carried out using 3D particle analysis tool in the open source software ImageJ. The results of various quantitative measurements are shown in Figure 5.5. Measurement of these parameters of pores is based on fitting of ellipsoid of maximum dimension accommodated with in the pore volume and measurement of various characteristic of ellipsoid such as major and minor axis length, angle which the major axis make with horizontal and surface area. sphericity is the measures of the shape, which is found to be varying randomly suggesting the pores having quite large distortions from spherical shapes however; a small number of spherical pores are also confirmed through these measurements possibly lying in the peripheral region with small size.

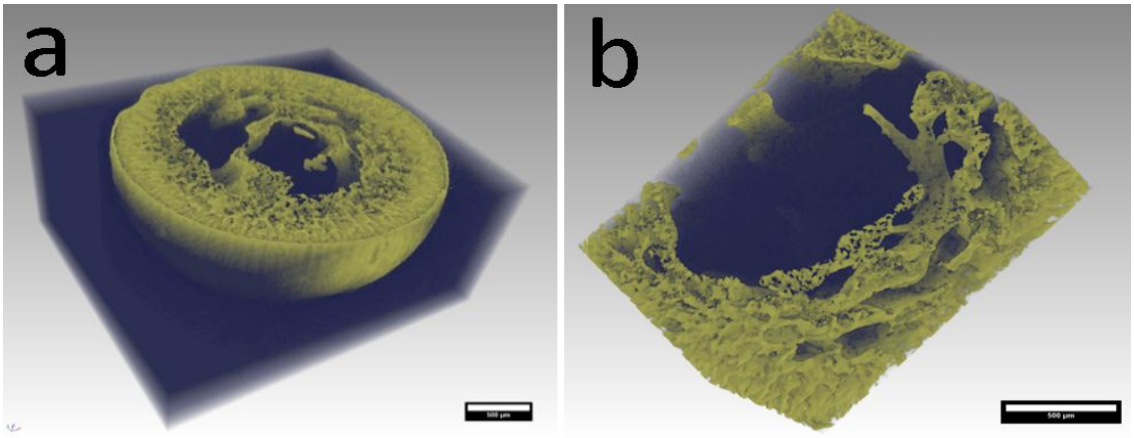

Figure 5.4 3D volume rendered images of Polymeric bead showing its internal microstructure (left) and a close view in the central region (right). [Scale bar = 500µm]

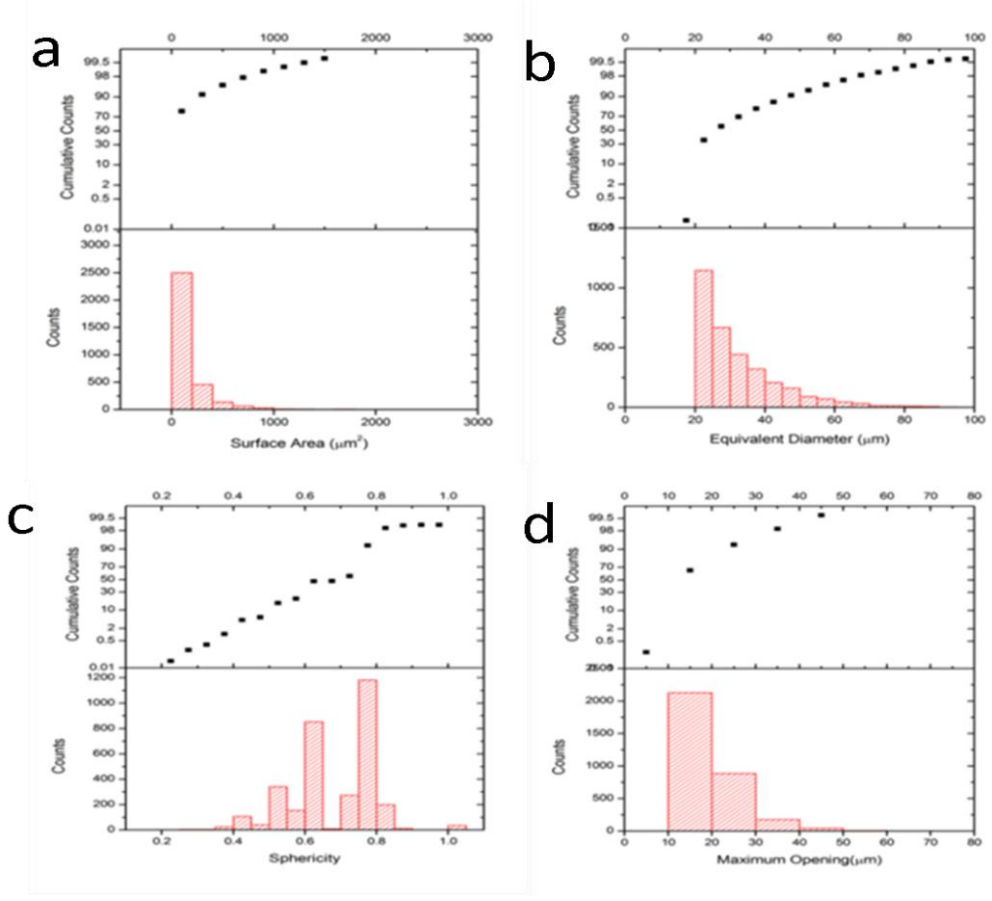

Figure 5.5 Quantitative measurement of various micro-structural properties of bead

Equivalent diameter is the diameter of sphere equivalent to the volume of pore, which provides a measurement of pore size. Histogram distribution of surface area of pores show that frequency of smaller pores lying in the range of 200 μm^2 is large whereas number of larger pores is small. There are very few pores of size larger than 1000μm^2. Maximum opening is the diameter of largest inclibed sphere also a measure of pore size. Future studies will focus on the effect of various experimental parameters on the porosity, morphology and architecture of polymer beads and their optimization to achieve the desired porous nature of the product.

5.2 Polyurethane foam

Polymers are part of everyday life and used in the form of natural polymers such as amber, silk, wool, wood, rubber etc. or synthetic polymers devised using various processes such as rubber, backelite, neoprene, polyvinyl chloride (PVC), polystyrene, polyethylene etc. These polymers are manufactured and used in various structural forms such as foams, solids, membranes, composites etc. Polyurethane foam (PUF) is one particular polymer with porous structure which is quite popularly used in household applications as packing materials, for insulation in construction & industrial processes, life preservers, and marine equipment [183,184].The PUF used in this study is flame retardant PUF, specially designed to use as protective enclosure for radioactive material transport package against accidental mechanical shock and fire.

a) Micro-structure of polyurethane foam

PUF show some unique physical properties such as low thermal conductivity, low density, excellent dimensional stability, high strength-to-weight ratio, low moisture

permeability and low water absorption. The application of polymer foams for various applications depends on these physico-mechanical properties, which have very strong co-relation with its cellular microstructure and morphology. These cellular structures can be varied within limits by choice of raw materials, density, blowing agent and other process parameters in foaming process. Non-destructive microstructure characterization and optimization through variation of process parameters and ingredients during sample preparation is extremely important to find the suitable product with optimum properties. Establishing structure property co-relation based on finite element modelling further help in this process [184,185]. In the quest of finding a suitable microstructural characterisation technique, we studied flame retardant polyurethane foam (PUF) using micro-focus as well as synchrotron based X-ray μ-CT and compared their performances for qualitative & quantitative analysis.

b) Sample preparation

For the preparation of fire retardant PUF, the polymeric methane diphenyldiisocyanate (PMDI, Suprasec 5005) and sucrose-based polyetherpolyol (Daltolac R 180) were procured. Distilled water was used as a chemical-blowing agent. N,N,N,N,N-pentamethyldiethylenetriamine (PMDETA) was used as a catalyst. Poly-ether dimethyl siloxane was used as a surfactant [184,185]. All these raw materials, except PMDI, were first well mixed in a plastic beaker. Then PMDI was added into the beaker with vigorous stirring for10 s. The amount of PMDI required for the reaction with polyether polyol and distilled water was calculated from their equivalent weights. The resulting mixture was immediately poured into an open paper mold (50 x 50x 50 cm^3) to produce

free rise foams. The foam blocks were developed in well-designed mould enclosures to achieve high density by arresting free rise. After the preparation, the foams were kept in an oven at 708^0C for 24 h to complete the polymerization reaction. Different test samples of specific shapes were cut from the cured foam. Dimensional finishing was achieved through rubbing with fine emery paper.

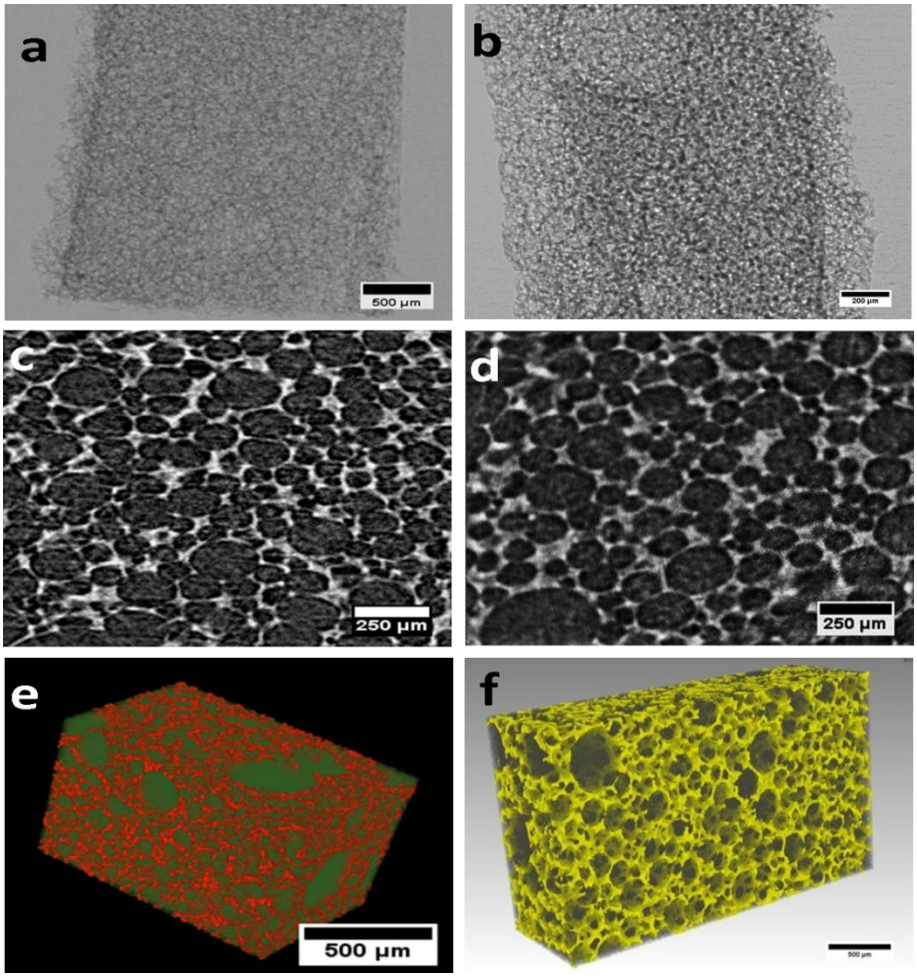

Figure 5.6 Comparison of micro-focus and synchrotron based X-ray µ-CT imaging. (a, c, e) show phase contrast projection image, tomography reconstructed slice image and 3D volume rendered image of micro-focus experiment and (b, d, f) show the corresponding images from synchrotron based experiment.

c) Data acquisition and experimental details

In order to compare the performance of laboratory and synchrotron based X-ray µ-CT systems for the charecterisation of polyurethane foam, we have conducted phase contrast µ-CT experiments using both the experimental systems. The samples were placed on the rotation stage with help of suitable sample holder. Using variation of experimental parameters, first the phase contrast in the projection image was optimized. For laboratory-based system, the source voltage, current, acquisition time, source to object and object to detector distance were adjusted whereas for synchrotron imaging, beam energy, acquisition time and objet to detector distance was optimized. The sample size chosen for both the system was 3 mm x 3 mm x 10 mm.

In laboratory based imaging, the projection images over full 360 rotations were collected while rotating the sample about its axis as required for cone beam acquisition. Angular step of 0.45 degree was chosen to acquire total 800 projections apart from reference and background images. For synchrotron imaging system, the 900 projections over only 180 degree of rotation with rotation step of 0.2 degree are needed because of parallel nature of beam. The smaller step in laboratory-based imaging was not possible because of lower flux thus much higher acquisition time per image and variation of source current with time. The total scan with laboratory-based imaging took approximately 4 hours whereas the synchrotron scan was completed in 15 minutes. The laboratory-based experiment was conducted at 40 KV, 300 µA source parameters with source to object distance 60 mm, object to detector distance 240 mm, and acquisition time of 20 sec. The synchrotron imaging was conducted at 10 keV beam energy, 150

mA current, 600 ms acquisition time, and object to detector distance of 300 mm. Since the imaging detectors used in the two systems are different, the ultimate resolution was different in the two systems. The MTF for synchrotron imaging was ~ 15 µm whereas for laboratory-based system with magnification, it was approximately ~ 20 µm.

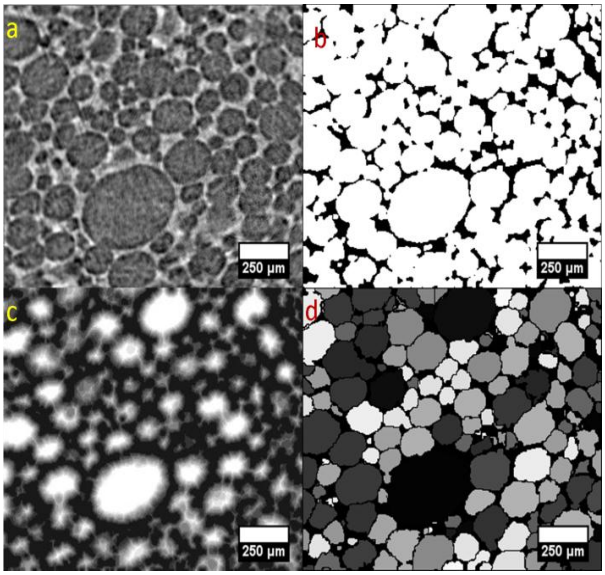

Figure 5.7 Sequence of morphological image analysis f polymer foam µ-CT data (a) Reconstructed slice image (b) threshold image (c) distance transformation (d) labelled.

d) Results and discussion

The data acquired from both the imaging systems was used for tomography slice reconstruction using their respective cone beam filtered back projection (FDK method) and parallel beam filtered back projection algorithms respectively. An in-house developed tomography reconstruction code was used for this purpose. Different slice images and 3D rendered volume images were visualized using ImageJ, an open source 3D visualization software. Figure 5.6 compares high-resolution projection and µ-CT

images of PUF sample obtained from laboratory based and synchrotron based µ-CT experiments respectively. The projection images shown in this figure shows random structures of pores in the bulk of PUF however, the contrast at interfaces and signal to noise ratio is better in synchrotron image as compared to laboratory-based system. This is due to improved coherence and lower acquisition time facilitated by high flux of synchrotron beam. Comparing reconstructed slice images of PUF from the two system, the shapes of the cells appears to be approximately spherical in both the images however the boundaries of cell is well defined in synchrotron reconstructed image due to high resolution and high contrast. The thin wall connections between different pores and thin pore boundaries are hardly visible in laboratory-based image whereas these features of cellular structure are quite clearly visible in synchrotron image.

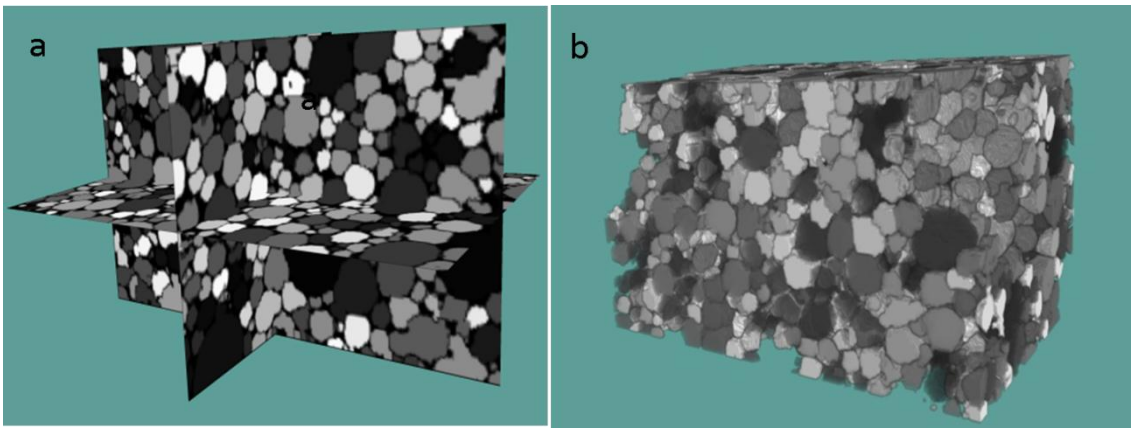

Figure 5.8 (a) Orthonormal slice view and (b) 3D volume rendered image of segmented cells in polyurethane foam using synchrotron µ-CT

This improved image contrast and resolution in synchrotron imaging is useful in improved 3D visualization and structural segmentation of various cells in the microstructure of PUF. Comparison of volume rendered 3D images reconstructed from

the two-tomography experiments show that, though both the systems are capable of visualizing 3D cellular structure, the quality of images is much improved in synchrotron imaging. The difference of resolution and contrast in these images is clearly visible.

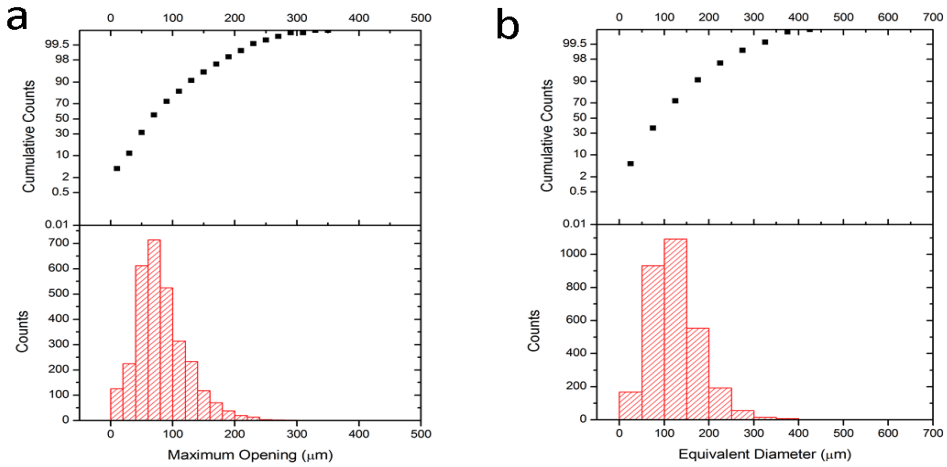

Figure 5.9 Quantitative measurement of pore size distribution in polyurethane foam using SR μ-CT. Maximum opening is diameter of largest inscribed sphere and equivalent diameter is the diameter of sphere with equal volume

Quantititative analysis of μ-CT slice images was conducted to measure cell architecture in terms of cell size, shape, and orientations. The image analysis requires segmentation of cells in the microstructure using image thresholding followed by distance transformation and watershed segmentation. A typical sequence of operation used for quantitative analysis of cellular structure is shown in Figure 5.7. The segmentation of images in laboratory-based system is quite difficult as compared to synchrotron-reconstructed images due to their poor resolution, contrast, and SNR. The shapes of cell are quite comparable to the actual shapes in synchrotron tomography data

as compared to laboratory imaging. This is primarily caused by in-visibility of partitioning walls of cell in laboratory data as compared to synchrotron imaging. The 3D structure of segmented cell in the synchrotron data is shown in Figure 5.8. Quantitative size distribution in terms of maximum opening and equivalent diameter is shown Figure 5.9. Histogram distributions of other micro-structural properties of pore such as surface area, volume, orientation angle and sphericity are shown in Figure 5.10

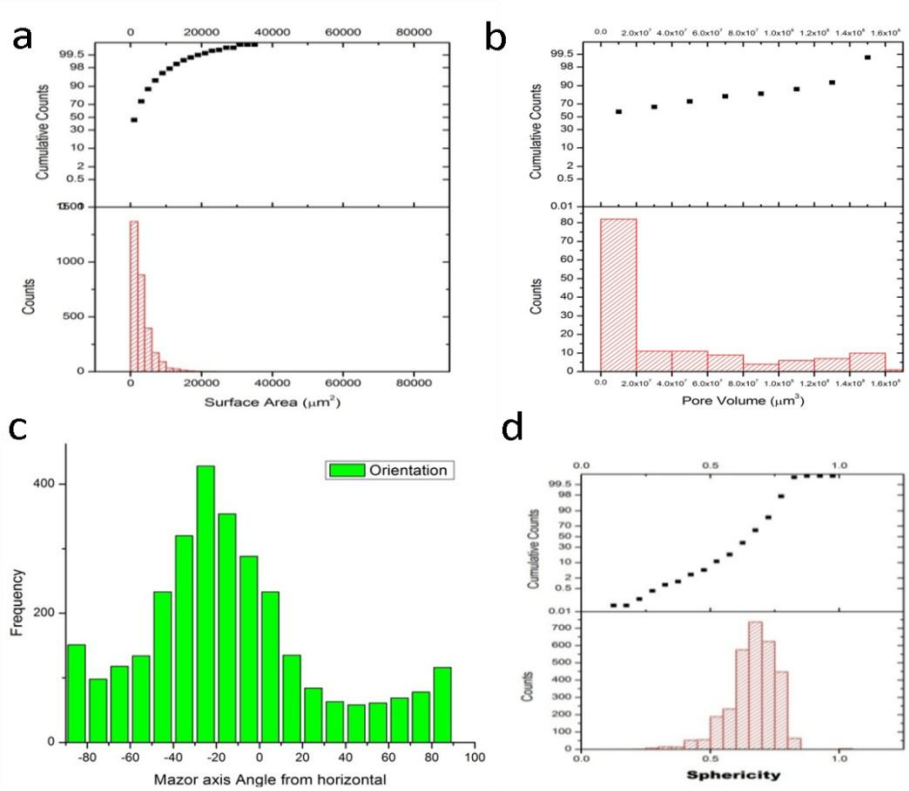

Figure 5.10 Quantitative measurement (a) surface area (b) volume (c) orientation angle and (d) sphericity of pore in polyurethane foam using SR µ-CT

Measurement of pore size (pore area in 2D and surface area in 3D distribution from both laboratory and synchrotron analysis is suggesting that the pore area is less than 5 x $10^4 \mu m^2$. This gives an average size of pores 210µm. This is also confirmed

from the measurement of ferret diameter (maximum distance between two points lying at the boundary of the shape) in 2D and equivalent diameter in 3D (diameter of enclosing sphere). The maximum Ferret diameter/equivalent diameter is measured to be 400 µm but the average value lies 210 µm. The shape of the pores is measured in terms of shape descriptors such as circularity, sphericity, and aspect ratio. These measurements are based on fitting of most appropriate ellipse within the pore area. Aspect ratio is the ratio of major and minor axis of the ellipse whereas circularity is a measure of deviation from perfect circle, expressed in terms of pore area and perimeter as $4\pi(\text{area}/\text{perimetre}^2)$.

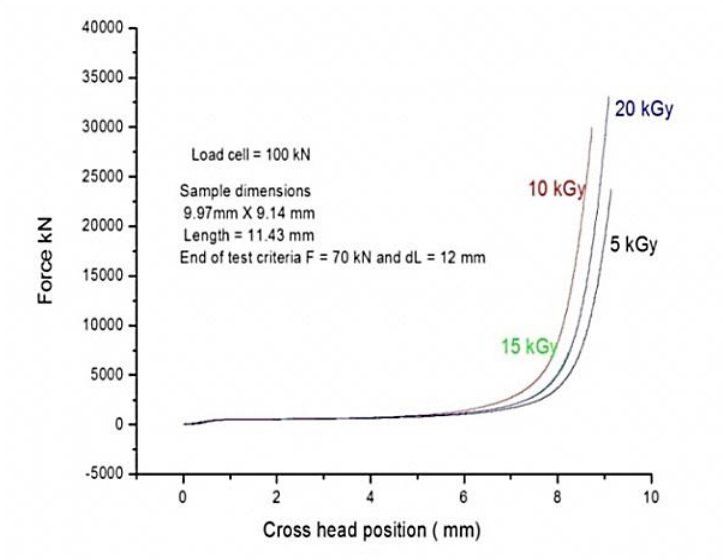

Figure 5.11 Compressibility test on polyurethane foam samples exposed with different gamma doses of 5, 10, 15, 20 kgray.

e) Effect of gamma irradiation on polymer foam

Polymers are quite susceptible to incident radiation and their microstructure is affected by high radiation dose due to breaking in polymeric chains of macromolecules and

crosslinking induced by radiation [186–188]. In order to see the effect of radiation dose on cellular microstructure of polyurethane foam, the sample prepared with the method discussed in the previous section were subjected to γ doses of 5,10,15,20 kGy using irradiator. Effect of γ irradiation on three-dimensional microstructures in the bulk of these samples was studied using synchrotron based phase contrast X-rays tomography and their mechanical strength was measured via compressibility test using micro hardness tester. Measurement of hardness was based on pressing a standardized indenter with a standard force into the material to be tested to allow the deformation to take place. This deformation is measured in terms of the deformation produced beyond the elastic limits. Figure 5.11 shows the compression curves obtained for the γ-irradiated foam. Effect of gamma irradiation on elastic properties is not altered significantly up to a force of 900 Newton.

The foam is within the elastic limits so long as the applied force was below 900 Newton with a reversible deformation of 5 mm. However, beyond this limiting force, it is reduced upon irradiation of a dose of 10 kGy due to γ induced cross-linking of the polymeric chains leading to increased hardness. This results in reduced deformation to the extent of 10% as seen in the figure. Compressibility curves of samples with dose of 15 and 20 kGy show increased deformation again. This is indicative of the chain session of already strained cross-linked polymeric chains. Since the cellular microstructure of polymeric foam is strongly correlated with the mechanical properties we have applied synchrotron based phase contrast μ-CT to see the effect of radiation dose on cellular microstructure and tried to correlate this with the results of

compressibility test on polyurethane foam. Phase contrast µ-CT experiments were carried out on PUF samples irradiated with 5, 10, 15, 20 Kgray with experimental parameters similar to those discussed in the previous section and reconstructed slice images of various samples were obtained and compared as shown in the

Figure 5.12.

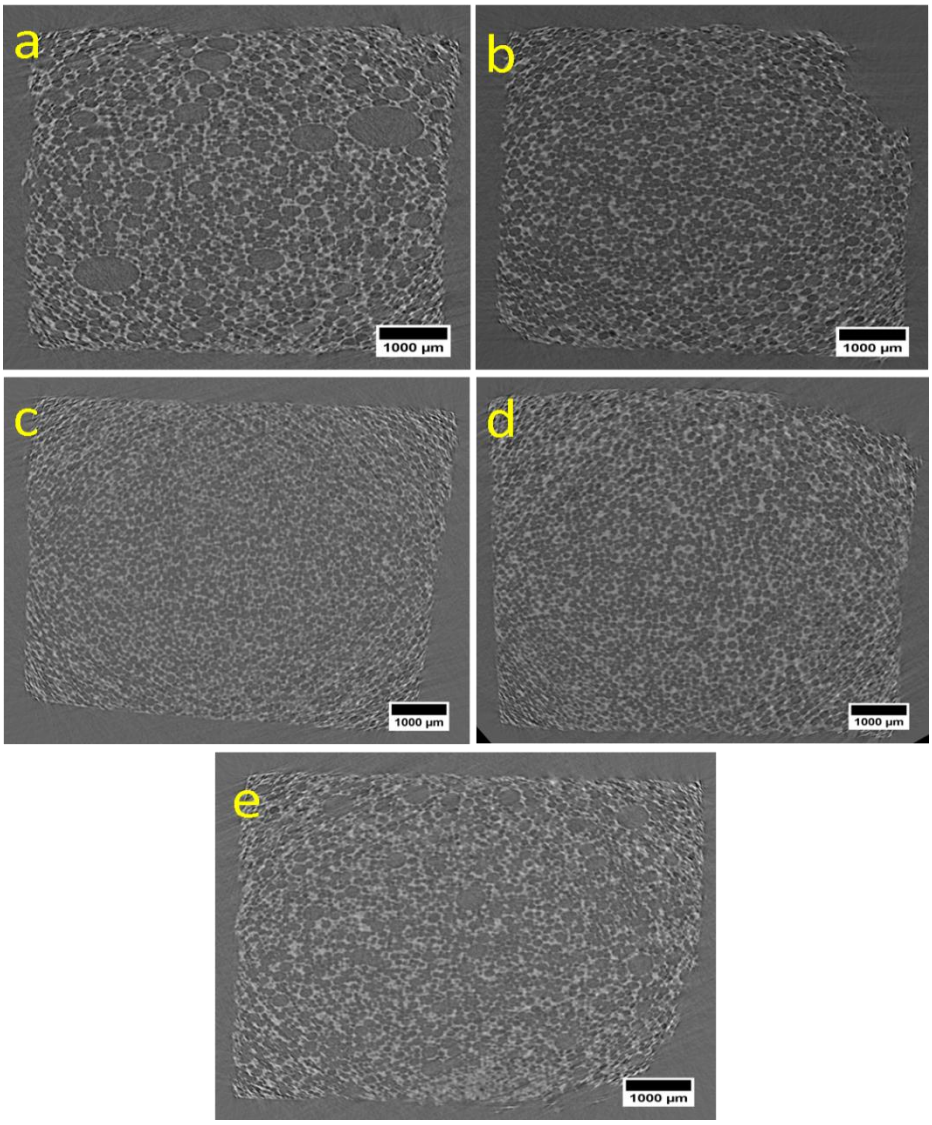

Figure 5.12 SRµ-CT images showing the effect of gamma dose on microstructure of polyurethane foam exposed with different gamma doses of 0,5, 10, 15, 20 kgray.

It is clearly seen that the γ dose quite strongly affect the microstructure of polyurethane foam. We can see that when the samples are irradiated with 0 to 10 kGray of gamma dose, the irradiation of the foam results in cross-linking leading to increased wall thickness and shrinkage of cellular structure. This leads to increased strain around the foam bubble and increased hardness is also observed in the compressibility test. Further increased exposure to gamma doses lead to rupture at the cellular boundaries connecting the bubble structure leading to decreased mechanical strength and finally leading to increase in deformation seen in the 15 and 20 kGy samples. Thus, we find that the cellular structure of foam is modified by irradiated gamma dose in terms of average cell size, average wall thickness, fractured cell content, total porosity etc. Using compressibility test based on micro hardness tester, we have also found that porosity and other cellular properties are strongly co-related with macroscopic behaviour of foam. Thus, we have found correlation between gamma dose, cellular structure, and mechanical properties of polyurethane foam.

5.3 Metal Matrix Composite

Metal matrix composites (MMCs) have ceramic particle reinforced in the metal matrix. This specific micro-structure of MMCs enables its exceptional properties such as high strength, high stiffness, and low density [189–191]. Study of damage mechanism in (MMCs) is carried out using traditional mechanical testing, microstructural characterization, and post-experiment fractographic analysis. It is generally agreed that damage in extruded ceramic particle reinforced MMCs takes place by a combination of particle fracture and matrix void growth. An understanding of the precise nature of

these damage mechanisms is limited by examinations of the two-dimensional fracture surface or polished cross-section of the material [191,192]. X-ray tomography is an excellent technique for non-destructive visualization and quantifying damage that eliminates need of destructive cross sectioning, and allows superior resolution and image quality with minimal sample preparation. It is important to note that, while 3D techniques such as X-ray tomography enable the acquisition of large data sets representative of the microstructure of the material, it is often the image analysis methodologies that are the rate-limiting step in such analyses. It is common to acquire data in a short time, but spend a fair amount of time in segmentation, reconstruction, and statistical analysis of the relevant microstructural features.

In this study, we have applied synchrotron based X-ray μ-CT for the cohesion damage visualization in Al-SiC metal matrix composites (MMC). In these materials, one major problems with X-ray μ-CT analysis is that the densities of Al and SiC are quite similar. Thus, the contrast between the two phases is extremely poor. This poses a big challenge on the imaging technique to produce sufficient contrast in the image between different structures and densities so as to allow their clear visualization and segmentation. The segmentation of different structures and density features in the image depends on the quality of image measured in terms of resolution, contrast and signal to noise ratio [191,193–195]. Synchrotron X-ray μ-CT with its unique characteristic of coherence, high flux, collimation, and monochromaticity improves image contrast and signal to noise ratio significantly in hard X-ray imaging. In addition to this, the inclusion of phase contrast significantly improves the visualization of

interfaces of materials with different refractive index. In this work, we have carried out a comparative study of three different synchrotron based 3D micro-imaging techniques namely absorption contrast μ-CT, phase contrast μ-CT and holotomography to find out their application in the visualization of damage behaviour in Al-SiC MMC [196].

f) Sample preparation

Aluminium metal matrix composite consisting of 20% vol SiC (P) in the extruded form was prepared and tested in compression to a true strain of ~ 0.9 – 1.0 over a range of temperatures and strain rates. Small coupons of about 500 μm thickness were extracted from multiple locations of a set of tested samples and subjected to μ-CT scans.

g) Data acquisition and experimental details

Absorption contrast μ-CT and propagation based phase contrast μ-CT experiments were carried out at synchrotron imaging beamline discussed in chapter 3. The principles of absorption and phase contrast tomography are also discussed in chapter-1. For holotomography, different single distance phase retrieval techniques discussed in chapter-2 were tried and it was found that Paganin algorithm and modified Boronikov algorithm under PAD conditions perform well as compared to other methods. For absorption contrast tomography, experiment were carried out placing detector in contact to the object (5 mm distance only) whereas for propagation based phase contrast tomography the detector was placed at 180 mm from the object. For both these cases, apart from reference and background images, 900 projections were collected and flat field corrections was done before reconstruction. For Holotomography, the projection images acquired in phase contrast mode after flat field correction were used

for phase map retrieval and modified Boronikov algorithm used. All the tomography scans were carried out using a monochromatic beam of energy 20 keV, at an incident flux of the order of 10^8 photons/sec on the sample. The illuminated volume of the sample was obtained in the form of reconstructed slices dataset for absorption, phase tomography and holotomography data, which were subsequently visualized in 3D to reveal the nature of, decohesion damage in terms of its location, morphology, relative content and spatial distribution. The slice images and 3D images of Al-SiC sample were compared for different modes of μCT. Relationship of damage with the SiC particles shape, size & spatial distribution along with other properties of MMC are being explored.

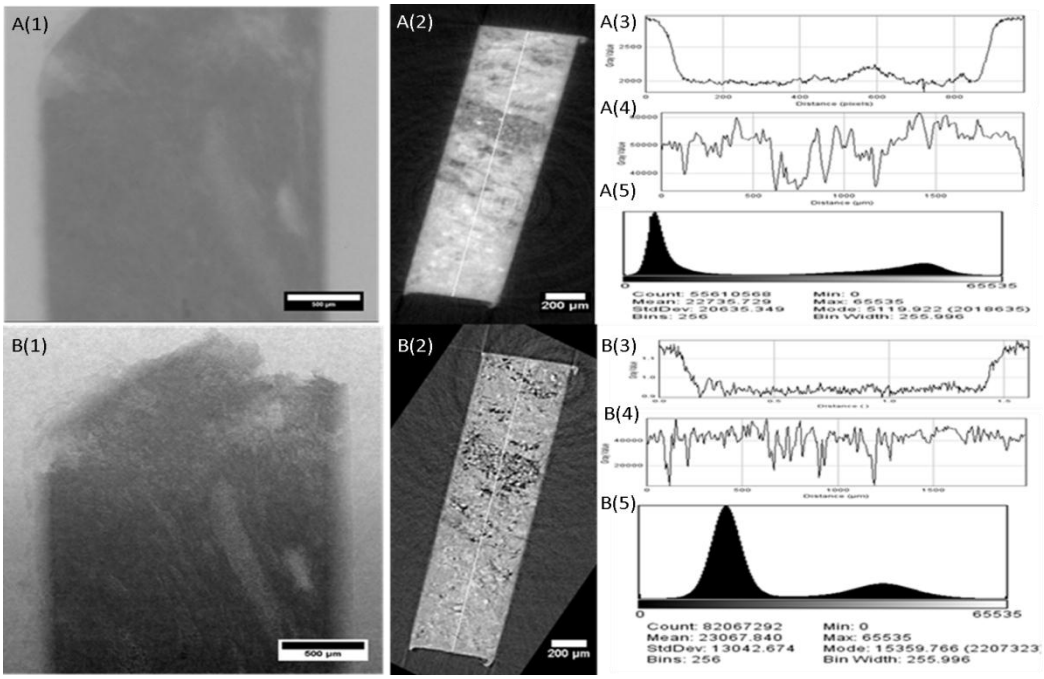

Figure 5.13 Comparison of absorption and phase contrast imaging - projection images, reconstructed slices of the same plane, plot profiles of projection (along the central row) and reconstructed slices (along the line shown) and histograms of slice

h) Results and discussion:

i. Comparison of absorption contrast and phase contrast tomography

Figure 5.13 show the radiographic projection image and a typical tomography reconstructed slice image in absorption contrast and phase contrast projection modes in the same elevation plane. The profile plots for projection image along its central row and profile plot along the depicted line for the reconstructed slice is shown in Fig 5.13. The figure also shows histogram distribution of respective reconstructed slices. The comparative analysis of the figures suggest that absorption contrast reconstructed slice image show poor contrast between the structural features and fine features are smoothened resulting in poor visibility of damaged regions whereas phase contrast image more accurately resolve the fine structures as evident from the profile plots. This feature is especially useful in distinguishing small damages, openings, and cracks generated in the matrix volume of the MMC. However, the reconstructed slices from absorption contrast images also show some white regions not visible in PCI image. These features suggest the existence of some highly absorbing but small particles embedded in the matrix. These may be the iron or similar heavy element. These features are not visible in the phase contrast image due to intensity re-distribution in the propagated image caused by diffraction at the edges and possible merger with the other features. Therefore, the absorption contrast imaging offers improved visualization of embedded high atomic number particles whereas phase contrast slices images provide better visualization of internal damages in the Al metal matrix (Figure 5.14). In spite of visibility of these features, the SiC particles embedded in the matrix of Al metal are

still not visible. This is because, the absorption as well as phase contrast generated in the image is not sufficient to distinguish the small density difference between Al and SiC. In order to resolve this problem we have applied holotomography reconstruction after retrieving quantitative phase from the phase contrast projections.

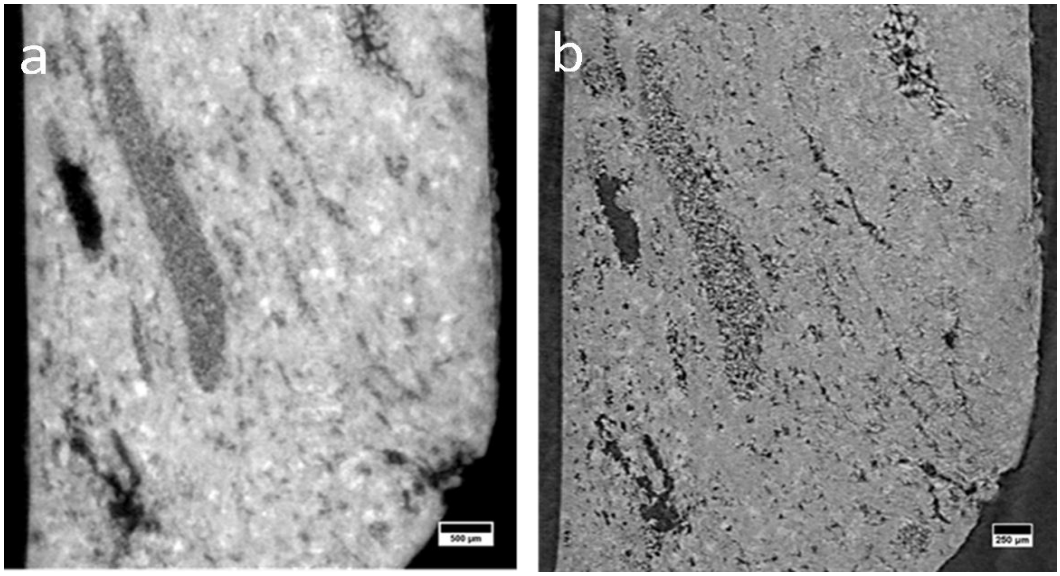

Figure 5.14 Comparison of reconstructed slice images of absorption contrast tomography (left) and phase contrast tomography (right). [Scale bar = 500µm]

i) Comparison of phase contrast tomography and holotomography

The intensity distribution I(x, y) measured at a single known distance Z between the object and the detector plane can be used to retrieve the projected thickness t(x, y) of the object, which is equivalent to the projected phase shift of the X-ray wave-front and thus we get a better contrast in the image. In this study, we have used modified Boronikov algorithms for phase retrieval before tomography reconstruction. The algorithm is strictly valid only if the following experimental conditions are fulfilled.

The object imaged consists of a single, homogeneous materialand Monochromatic radiation is used. The distance z between the object and the detector plane fulfils the near-field condition. Although all the validity conditions for this algorithms are not strictly satisfied for Al-SiC sample due to its mixed composition consisting Al, Si and C, the method is still considered for the study as difference in ö/β ratio for these elements is not large [105,110]. The result after applying this phase-retrieval algorithm is shown in Figure 5.15.

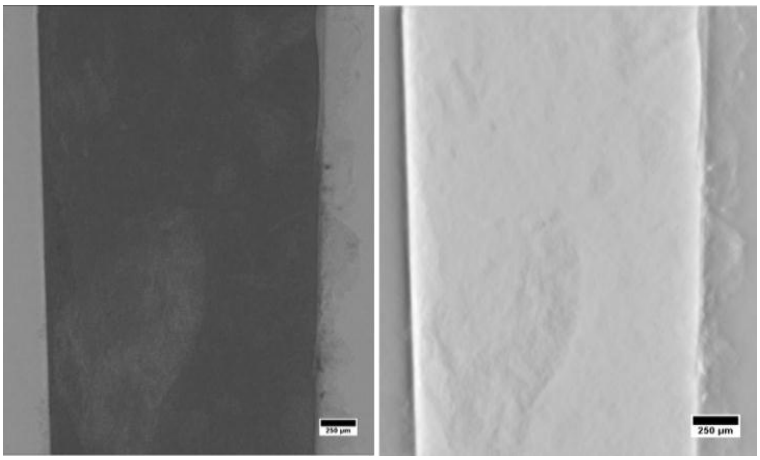

Figure 5.15 Comparison of flat field corrected phase contrast image and phase map retrieved using PAD-MBA at object plane for Al-SiC composite

It depicts the phase maps at object plane retrieved from phase contrast projection at 0 degree. The retrieved phase is directly proportional to the projected electron density in the sample therefore expected to provide improved visibility of SiC particles in Al matrix. These maps were retrieved for all the projection images and reconstructed using a standard reconstruction algorithm to obtain CT slices. The slice reconstructed using holotomography is compared with phase contrast tomography image in Figure 5.16.

The SiC particles present in the matrix has been reported in the literature to be visible in the holotomography slice images when the more sophisticated and computationally complex phase retrieval algorithms requiring multiple projection data are used. In our case some of the embedded particle are seen however their boundaries are still not clearly visible possibly due to in-sufficient contrast generated in the image.

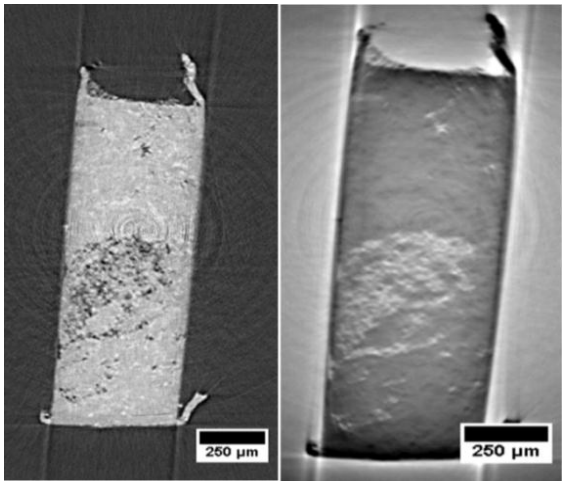

Figure 5.16 Comparison of µ-CT slice images of Al-SiC composite without phase retrieval (Phase contrast CT) and with phase retrieval [PAD-MBA] (Holotomography)

The possible reasons for this is the application of single distance phase retrieval algorithm under the conditions of its non-validity, availability of comparatively poor coherence at synchrotron imaging beamline and poor resolution of the system measured to be 15µm MTF. Future experiments are being planned with higher resolution detector and improved algorithm of phase retrieval applicable to conditions that are more general. The phase retrieval applied is not sufficient to resolve and segment the embedded particles and therefore the quantitative analysis of data sets is not carried out. It has been however observed that the strong edge enhancement, caused by the

phase effects provide improved visibility of sharp features such as cracks voids, opening in the matrix and whereas absorption contrast for embedded high atomic number particles. This information can fairly be used to quantify damage mechanism in the metal matrix of Al-SiC MMC. The percentage of damaged region/cracks can be quantified out of their total volume based on three dimensional image analysis.

5.4 Carbon-carbon composites

Carbon-carbon composites are a generic class of carbon materials consisting of carbon fibres reinforced in a carbon matrix. The special property of fibre-reinforced composites is their inherent anisotropy, a characteristic dictated by the spatial arrangement of the constituent phases. Indeed, the microscopic arrangement of the complex fibrous structure and matrix plays a major role in the determination of the macroscopic properties of the material such as light weight, high thermal shock resistance; high sublimation temperature, high thermal conductivity, low coefficient of thermal expansion, strength retention at higher temperatures, high impact resistance, high stiffness etc. These special properties make them a good choice in the fusion reactors, where they are expected to endure severe environment including high-heat fluxes, high armour, surface temperature, and eddy-current induced stresses during plasma disruption. The quest for improving the physical properties for high temperature, high pressure applications provided the impetus for research on these materials, which mainly includes improvements in properties of the constituent materials, i.e., carbon fibres and carbon matrix precursors and design optimization by an intelligent combination of two different constituents. The fibres possess a very high

modulus and classified either based on the type of precursor used for their manufacture or the final properties they attain. Among the various precursors only three precursor namely–rayon, polyacrylonitrile (PAN) and pitch are considered for commercial processes depending on the end application. After selection of fibres, next crucial job is the design and fabrication of a suitable preform that forms the starting material for manufacturing the composite. Also referred as fiber architecture, the preform not only imparts rigidity to the composite, but also in combination with fiber properties, it determines the properties of the composite. The matrix serves to protect the fibres from damage due to the environment and also it plays a very important role of stress transfer, which helps in attaining excellent properties finally. In carbon/carbon composites, the matrix is also made up of pure carbon, which can be developed, from various precursors with their specific characteristics that determine the final CC composite properties. Matrix precursor is decided depending on final application. The various sources of matrix precursors are Pure hydrocarbons, Oxygen and Nitrogen containing hydrocarbons, Sulphur and halogen-containing compounds etc. [145,169].

a) Micro-structure of carbon-carbon composite

The carbon/carbon (C/C) composites can be tailor made according to the requirement. As C/C composites are infinitely variable family of materials, the processing and design parameters such as (a) architecture, i.e., 1D, 2D, 3D or random fiber distribution; (b) fiber precursor, i.e., pitch, polyacrylonitrile (PAN) or vapour grown; (c) matrix, i.e., liquid impregnation (pitch or resin) or CVI and (d) final graphitization temperature will influence the properties and behaviour of C-C composites. In order to

estimate bulk properties of designed carbon-carbon composites, a whole range of numerical methods such as those based on Finite Elements Models are used provided the characteristics of constituent phases and their spatial arrangement are known. Among the structural characteristics that influence the properties of the material are those regarding the fibres, such as the distribution of lengths and orientations, waviness, curvature, and volume fraction, and similar quantities for the matrix and void phases. Manufacturing techniques are fine-tuned to control these characteristics, but the tuning process usually requires repeated cycles of fabrication and comparison with characterized samples. Moreover, no matter how much fine-tuning, there is no such a thing as the perfect manufacturing process and, therefore, different factors in the fabrication chain introduce in the real microstructure of the product deviations from the theoretical design, which affect the predicted performance of the material. Manual methods for the characterization of fibrous composites are expensive, limited & error-prone [197–201]. In this study, we have investigated the feasibility of use of X-ray µ-CT for the non-destructive charecterisation of C/C composites manufactured using different techniques and having different architecture and spatial arrangement of fibres in the carbon matrix. µ-CT produces accurate images of 3D volumes by reconstruction from multiple X-ray projections, allowing the direct characterization of the 3D microstructure of samples with significant thickness. C/C composites pose a significant challenge to X-ray imaging systems due to the close densities of inclusions and matrix, yielding very poor contrast among the constituent phases. Sensitivity is increased for composites made up of materials with neighbouring densities such as C-C composites

by using coherent X-rays from a synchrotron source using phase contrast tomography where interfaces between constituent phases are detected through the interference patterns arising from the out of phase waves propagated through materials with different refraction indices. Qualitative comparison of different characteristic of C-C composites microstructure such as porosity, volume fraction, lengths, orientations, waviness, curvature of fibres, and the matrix is done in their respective tomography slice images. In the following, we have shown 3D microstructure of several C/C fibrous composite using phase contrast X-ray µ-CT and advanced image analysis [197,198].

b) Preparation of samples

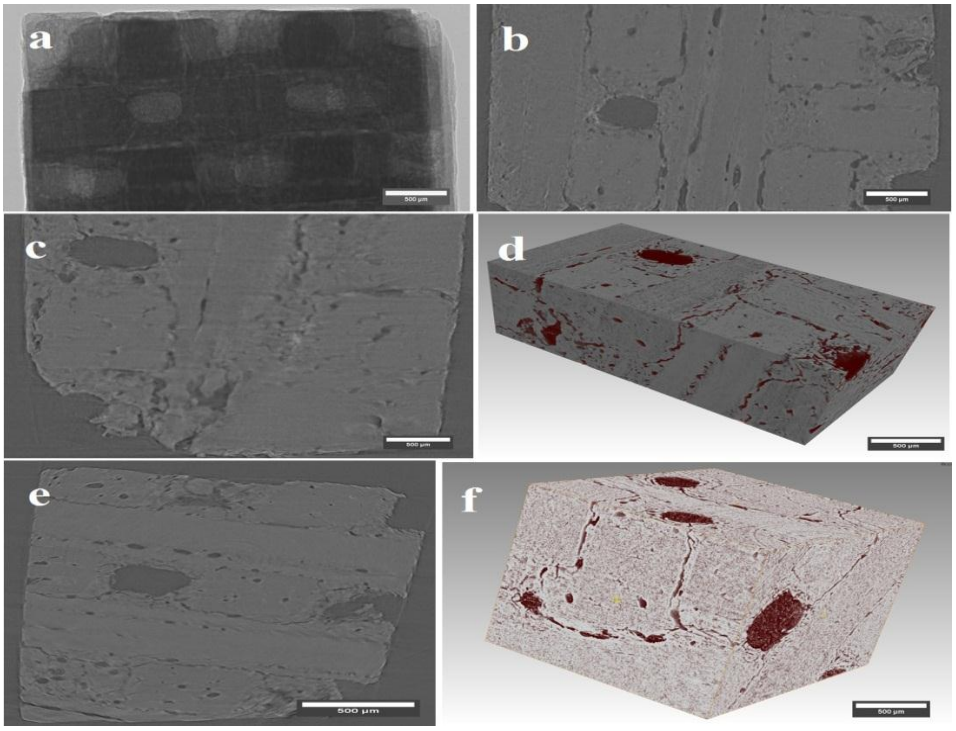

Figure 5.17 µ-CT of C-C composite-I (a) Phase contrast projection image (b-d) reconstructed tomographic slice images in YZ, XZ and XY orientation (e-f) 3D volume images. [Scale bar = 500µm for all images]

i. Sample-1 (C-C Composite I)

In this sample, carbon preforms were made using polyacrylonitrile (PAN) carbon fibres. These fibres were matted and stacked to a 2-D preform using phenol formaldehyde resin. Rectangular green preforms were cut into 1´´x 1´´ x 0.4´´ size and carbonized at a slow heating rate at 1000°C. They were further densified using impregnation with liquid phenol formaldehyde resin at pressures of 50 bar for 10 hrs. The impregnated samples were then carbonized at 1000^0C under inert atmosphere with a heating rate of 6°C/h. The entire cycle was repeated for the second time.

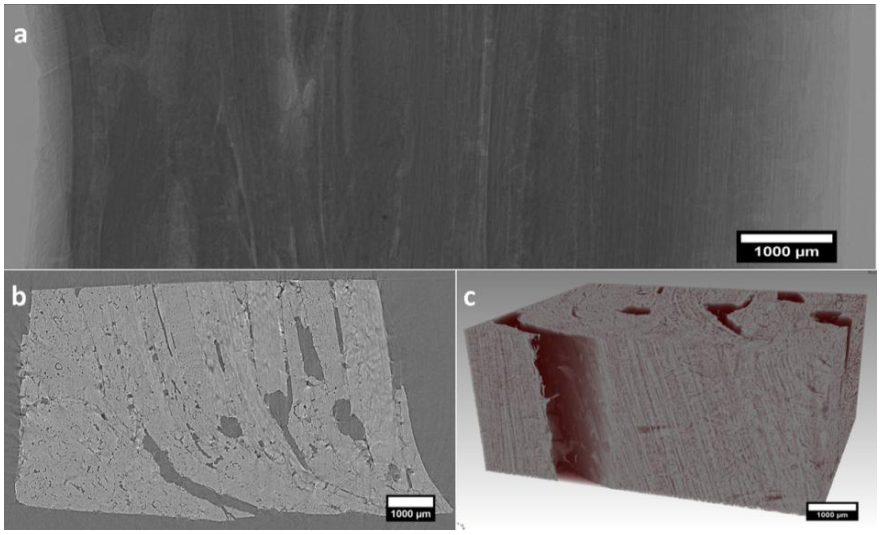

Figure 5.18 µ-CT of CC-9 carbon-carbon composite (a) Phase contrast projection image (b) reconstructed tomographic slice image (c) 3D volume image

ii. Sample -2 (C-C Composite II)

These high density C-C composite have been fabricated by using 3D woven carbon PAN fiber based preform. The preform was densified by a few number of cycles of resin impregnation and hot isostatic pressing to achieve a density of 1.75 g/cc.

iii. Sample -3 SiC coated composite sample:

The SiC coating was developed on 2D C/C composites (3.5 cm × 3.5 cm × 0.5 cm) using CVD. A high temperature vertical graphite reactor of 400 mm length and 60 mm diameter was used for the coating studies. SiC coating was carried out using MTS as source for silicon carbide, hydrogen argon mixture was used as the carrier gas. During growth, the furnace was operated at 1673 K under normal atmospheric pressure. A controlled MTS flow rate was achieved using a peristaltic pump. MTS was pumped with a particular rate to the feed line connected to the vertical furnace, which was preheated to a temperature of 473 K. Hydrogen along with argon was used as carrier gas to sweep the MTS vapor into the reactor.

c) Data acquisition and experimental details

The phase contrast μ-CT experiments on all the C/C composites were carried out at synchrotron imaging beamline BL-4 Indus-2 RRCAT, Indore, India as discussed in chapter-3. The samples sizes chosen were 3 mm x 4 mm x 8 mm for C/C I, 3 mm x 3 mm x 10 mm for C/C II and 4 mm x 2 mm x 10 mm for SiC sample. All the experiments were carried out at 15 keV monochromatic beam energy with an exposure time of 800 ms per projection image. One by one, the samples were placed over the tomography rotation stage with the help of suitable sample holder and tomographic projections were collected for all the rotational positions in a step of 0.2 degree for total 180-degree rotation. Total 900 projections were collected for each sample along with reference and background image required for flat field correction. The tomography slice reconstruction was carried out for all the samples using filtered backprojection

algorithm for parallel beam using an in-house developed reconstruction code. The visualization of reconstructed slice image and 3D volume rendering of various samples were carried out using ImageJ and VG-studioMax.

d) Results and discussion

Figure 5.17, Figure 5.18 and Figure 5.19 show the results of μ-CT experiments carried out on different C/C composites samples. The X-ray projection images itself show the distinct microstructure of these samples however clear identification of architecture and any quantitative measurement is nearly impossible from these images. The 3D reconstructed slices shown in these figures show their respective microstructure clearly in all the orientations. The woven architecture of fibrous tube in relatively lesser dense matrix is seen with a large volume of pores in C/C-I composite. The slice image also show a few pores of very large size but nearly same dimension and shape running through the volume in various directions. The architecture of fibres in the matrix is seen to be well woven in all three directions with some distortions at the boundaries. As compared to this, the C-C II sample show the individual fibres reinforced in the resin matrix with a well-defined architecture in one direction. All the fibres are oriented in the same direction with some pores varying in size and shape along the fibres. The microstructure of SiC coated CC composite is completely different from the other two sample having large pores in the central region with relatively smaller pores towards boundaries. The fibres are evenly distributed in the resin matrix however; large pores of similar size to that of resin bundles are generated in the bulk. The pores size is also

varying in large range. Further quantitative analysis of these micro-structural properties is being carried out.

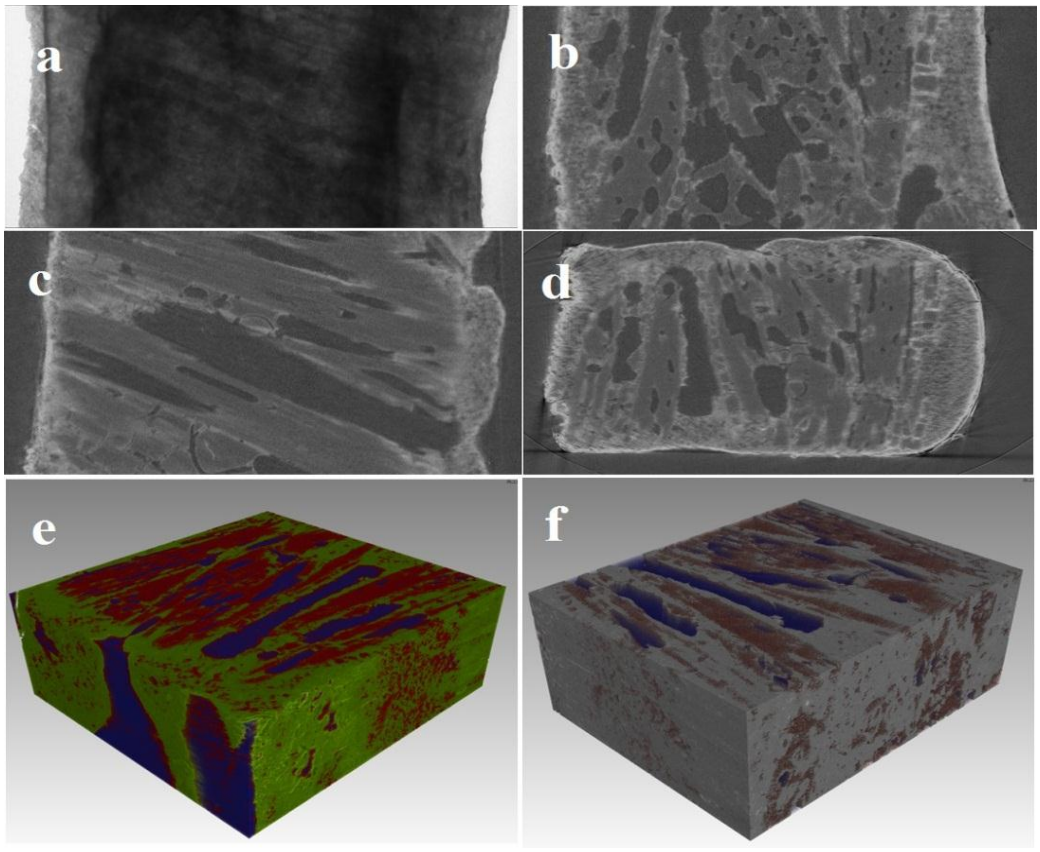

Figure 5.19 µ-CT of SiC coated CC composite (a) Phase contrast projection image (b-d) reconstructed tomographic slice images in YZ, XZ and XY orientation (e-f) 3D volume images

6 APPLICATIONS OF NEUTRON IMAGING BEAMLINE

In this chapter, we have illustrated the applications of neutron imaging to some unique problems of material science and engineering related to microstructure determination and imaging. Details of experimental system used, data analysis strategy adopted and results of various experimental studies carried out using neutron imaging are discussed here. The neutron tomography is applied to study the process of hydride blister formation in the Zr-alloy pressure tube and non-destructive evaluation of fuel tubes of pressurized heavy water reactor (PHWR). Dynamic neutron radiography is applied to study the effect of natural convection and heating rate to the melting and solidification of lead enclosed in SS cuboid.

6.1 Study of hydride blisters formation using neutron tomography

Formation of hydride blisters in Zr-alloy pressure tubes of pressurized heavy water reactor (PHWR) is a major life-limiting factor, which hinders the safe and uninterrupted operation of the reactor. Non-destructive detection and evaluation of

location, shape and size of these blisters along with study of hydride concentration distribution in the heavy metal matrix surrounding them is essential for damage quantification and studying the process of blister formation in the pressure tube. While early detection of blisters in pressure tube will extend its residual life, the knowledge of its formation process will be helpful in designing the reactor system, which is less prone to blister formation. We have for the first time explored the application of neutron tomography as a tool for non-destructive investigation of blister formation process in the pressure tubes of pressurized heavy water reactors (PHWRs). Neutron tomography is successfully used to visualize and analyse shape, size, and concentration distribution of hydride in the volume of blister and its surrounding. In the neighbourhood of detected blisters, a region with much less hydride concentration as compared to the bulk is observed indicating the depletion of hydride from these regions to form the blister. Further to this, calibration of hydride concentration in Zr-alloy (Zr-2.5Nb) with respect to gray values in neutron tomography images is carried out to find the minimum detectable difference of hydride concentration. The technique is also capable of detecting the in-homogeneity in spatial distribution of hydride concentration with such a low concentration distribution. The linear relation between ‘Mode’ of grey values histogram distribution and hydride concentration is established which can be used to predict the unknown concentration of hydride from the reconstructed image. This study establishes neutron tomography as a potential non-destructive evaluation tool for the estimation of the severity of damage in the pressure tubes and provides valuable information about kinetics of blister formation.

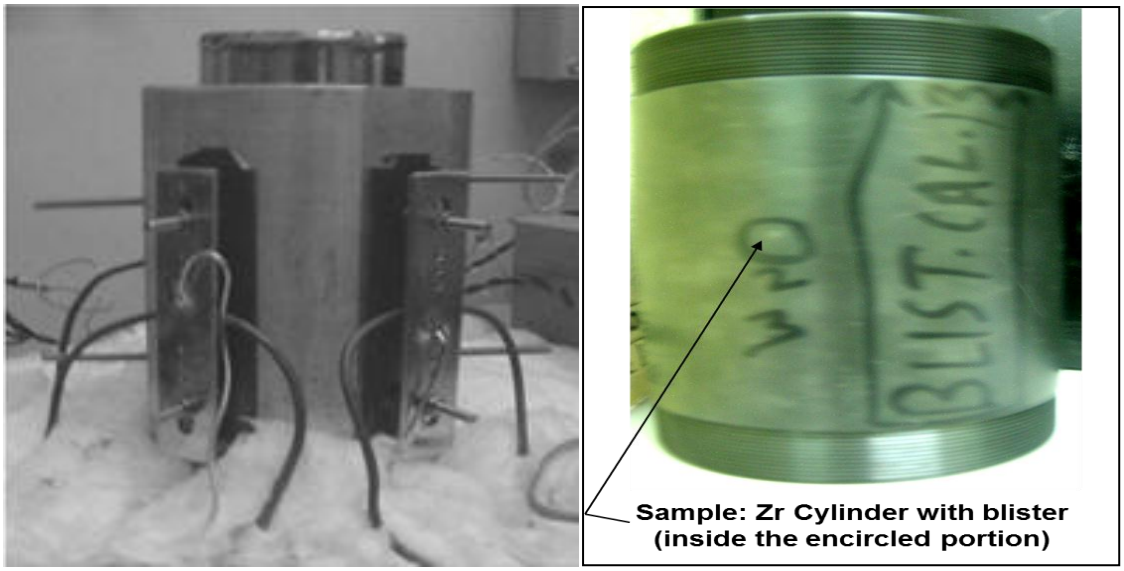

Figure 6.1 Experimental set-up for hydride blisters preparation in pressure tube and picture of sample prepared.

6.1.1 Detection of hydride blister in a matrix of zirconium pressure tube

Zr-alloy is used as a fabrication material for pressure tube in pressurized heavy water reactor (PHWR). In PHWR, the pressure tubes are maintained at 253-293°C and are surrounded by concentrically located cooler calandria tube. Garter springs are provided at regular interval in the annulus space to prevent contact between hot pressure tube and cooler calandria tube. However, either due to segregation of garter springs during installation or due to its movement during operation, large span of pressure tube remains unsupported, which can make contact with cooler calandria tube and thereby setting up temperature gradient. Hydride is known to migrate down the thermal gradient and once the solid solubility is exceeded at the cold spot, low-density hydride phase precipitates out. The hydride thus formed at the cold spot has blistery appearance and is called hydride blister. Though an individual blister is unlikely to defy

leak before break criteria of pressure tube design, an array of blisters joined together by delayed hydride cracking (DHC) may form a crack larger than the critical crack length, which can cause catastrophic failure of the pressure tube. Since pressure tube is the primary containment for the hot pressurized coolant, catastrophic failure of pressure tube will result in complete loss of coolant, which if unabated for long period may eventually leads to release of activity.

In view of this, it is important to study and examine the blister formation process in pressure tubes and quantification of the hydride concentration in it so that the severity of the problem can be identified. Various techniques such as optical imaging, ultrasonic imaging, X-ray and neutron radiography etc have been used for this purpose . While optical imaging provides quite a good resolution for feature observation, it is destructive technique and most of the information regarding shape, size, concentration etc. is lost or altered during sample preparation. Moreover due to its destructive nature, the sample cannot be reutilized hence this technique is not suitable for onsite investigation [202,203]. The sensitivity of ultrasonic detection is limited to concentration difference of several thousands of wppm and it is blind about the shape and size of the blister [204]. Since neutrons possess high scattering for Hydrogen (H), neutron imaging is the most suitable probe for investigating materials containing H and other low-atomic-weight materials. Recently neutron radiography using neutron sensitive imaging plate is reported to be used for quantitative characterization of hydride concentration in Zr-alloy tubes from pressurized heavy water reactor. Although neutron radiography is quite versatile technique, the information extracted is limited

because of inherent integration of the structure and density information in the object along the beam path. For this reason, localized information cannot be achieved using neutron radiography [205,206]. We have, for the first time; used neutron tomography to characterize the hydride blisters formed in Zr-alloy PHWR pressure tubes. Three-dimensional images of blisters formed are obtained through neutron tomography [207]. Shape, size, concentration of hydride, spatial in-homogeneity of concentration distribution near blisters is determined. A region with much lesser hydride concentration showing depletion of hydride to form the blister is observed.

a) Preparation of sample: simulated blisters in Zr-alloy pressure tube:

Hydride blisters were grown under controlled thermal boundary condition in Zr-alloy (Zr-2.5Nb) pressure tube spools of length 200 mm (Figure 6.1). The pressure tube section was gaseously charged with 100 wppm of hydrogen and three hydride blisters 120 ° apart from each other were grown on the outer circumference of tube sections using a fixture as shown in the figure. The hydrogen charged tube section was first heated to a temperature of 300°C. The tube section was then soaked for two hours to attain thermal equilibrium. Subsequently, water-cooled conical copper fingers were brought in contact with the tube surface to impose thermal gradient, which was maintained for three months. The imposition of thermal gradient resulted in migration of hydrogen towards the cold spot [202,203]. Since at the cold spot the solid solubility of hydrogen is very little, the hydrogen arriving at the cold spot as a result of thermal migration precipitates out as hydride, which due its low density bulges out of surface

resulting in blistery appearance. Size of blisters formed was measured to be approximately 2 mm.

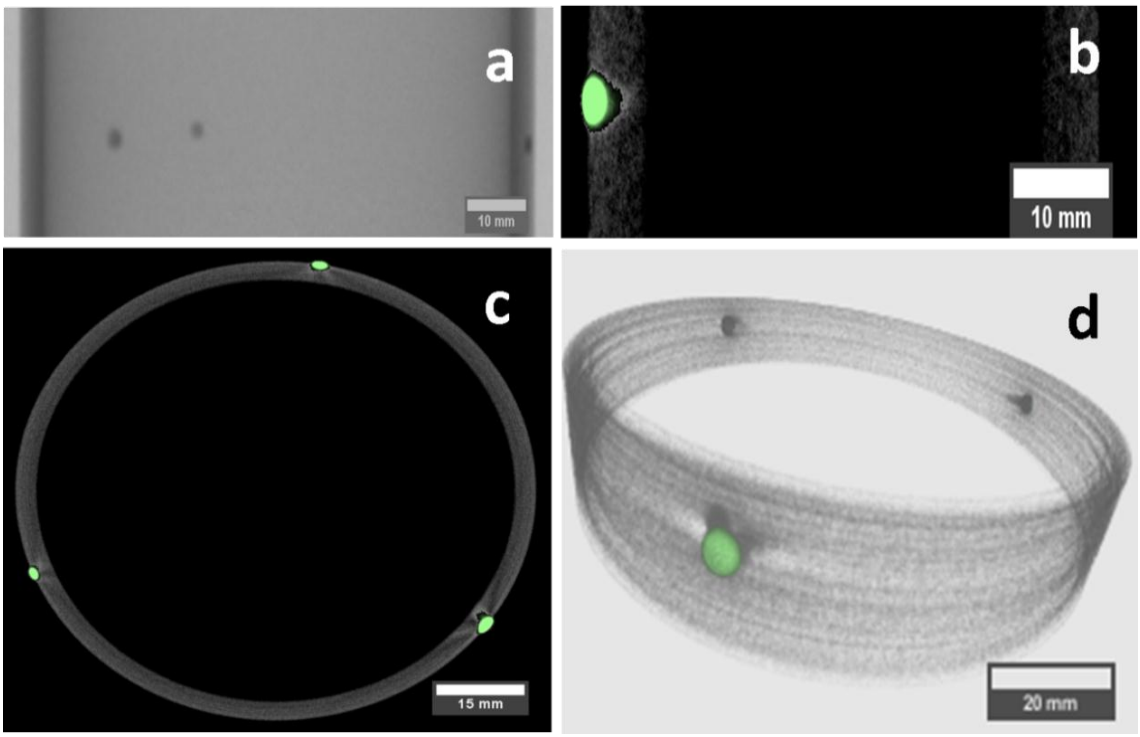

Figure 6.2 Neutron tomography of Zr-alloy pressure tube to detect hydride blisters (a) Flat field corrected radiograph (b) Vertical slice showing cross section of the detected blister (c) Horizontal slice showing relative location of three blisters (d) 3D image showing hydride blisters and their nearby regions with low hydride concentration caused by migration.

b) Data acquisition and reconstruction

Neutron tomography of as prepared pressure tube sample was carried out using the experimental setup described in chapter 3. The sample was placed over a rotational stage and rotated with an angular step 0.25^0. Radiographic projections were collected

for 20 sec at each rotational position. The rotations are synchronized with the image acquisition software. All the tomographic projection data are transferred to a PC and stored. A typical radiographic image of such sample with the blisters formed has been shown in Figure 6.2 (a). The three hydride blisters are clearly identified along with their relative location and size. For tomography, total 1440 projection were collected along with reference and background images. A full tomographic scan took around 8 hours. All projections were normalized using reference and background images and the reconstruction was carried out using in-house developed reconstruction software based in FDK algorithm of filtered back projection [207]. As shown in figure 6.2 (b-d), the 3D volume of the object was obtained using VGstudioMax showing spatial distribution of neutron attenuation coefficients of the materials present in the object.

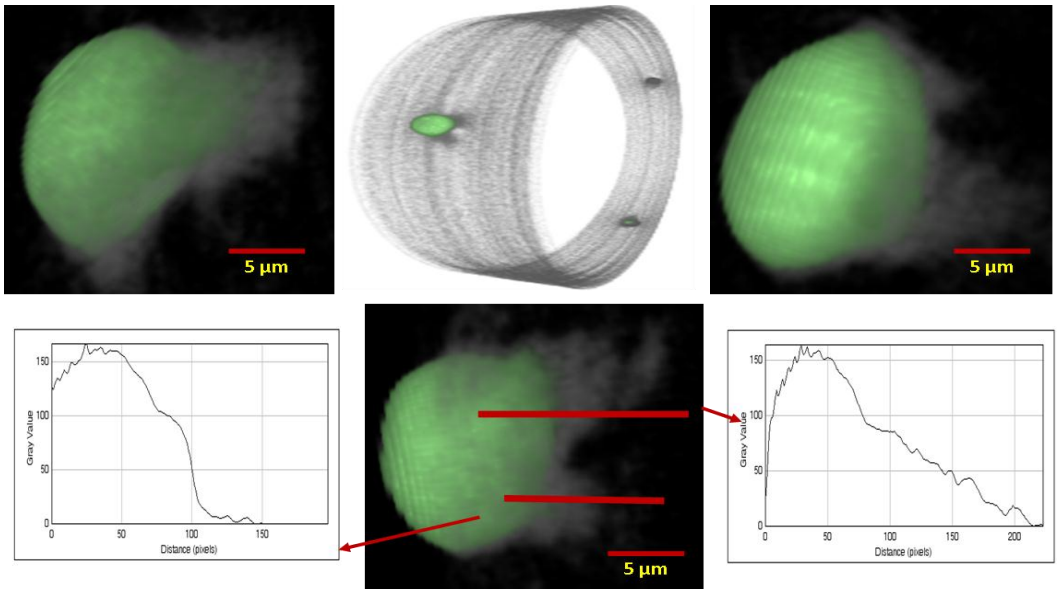

Figure 6.3 Enlarged vies of hydride blisters formed in Zr-alloy pressure tube. The figure also shows the intensity profile plots of one of the blisters to confirm the inhomogeneity of hydride concentration in the nearby region of the blister.

c) Results and discussion

i. Detection and 3D visualization of hydride blisters

Figure 6.3 shows reconstructed volume of the object. The three hydride blisters in the sample containing hydride concentration of 16000 wppm can be clearly seen in the reconstructed volume. The image grey values represent the neutron attenuation coefficient of the materials. The images have been pseudo coloured in green for hydride blister and grey for Zr-alloy. The three blisters detected are also shown in their enlarged view. Due to presence of excess hydride concentration, blisters formed in the pressure tube attenuate and scatter larger number of neutron as compared to its surrounding. The relative concentration of these blisters can also be distinguished from the reconstructed slice image Figure 6.2 (b-c).

ii. Measurement of shape and size of blisters

Information about shape, size, and depth of blister, the presence of cracks inside it and orientation of crack with respect to hoop stress are required for safety assessment of the pressure tubes. The 3D images in Figure 6.3 clearly show the shape and size of the blisters formed. It is found and shown in enlarged image of blister that the blister has a shape of an elongated ellipsoid while its size is measured to be approximately 2 mm. Since the shape and size of the blisters formed depends upon shape and size of the contact tip, thermal boundary conditions and tube section dimensions, varying these, the dependence over various parameters can be calibrated for their effect on the shape and size of the blister. It is important to note that the catastrophic failure of the pressure tube in the event of delayed hydride cracking (DHC) in which an array of such blisters

join together and form a crack larger than the critical crack length, will strongly depend upon the shape and sizes of the blisters formed.

iii. Non-uniformity of hydride concentration in the vicinity of blisters

As can be seen from the images and plot profile in Figure 6.3, grey values appears to be decreasing near the blister. Also from the enlarged image of the blister, it is seen that the hydride distribution is anisotropic in region surrounding the blister. The plot profile near the blister at two different regions clearly shows the non-uniformity in the hydride depletion in this region. As it is known that before blister formation the sample consists of a uniform spatial distribution of hydride, the lack of hydride in these areas clearly show that hydride from these regions has migrated to the region where blister is formed. The information regarding distribution of hydride concentration in this depleted region is useful in the study of kinetics of the hydride migration in the sample under various thermal boundary conditions.

iv. Study of hydride migration towards blister

Continuing our effort with the study of hydride blister formation, we have carried out neutron tomography experiments to examine the migration of hydride towards blister formation region. A sample was prepared with the method described previously for blister formation however; the sample was removed prematurely from the set-up so that a complete blister could not form at the cooling tip. Neutron tomography of this sample was carried at neutron imaging beam-line using the same experimental procedure as described earlier. Various images shown in Figure 6.4 clearly depict the typical concentration distribution of hydride during blister formation. The hydride

concentration is seen as a whirl having blister at its centre and hydride migrating towards it along its spokes. In this way, concentration keeps on increasing at the centre while decreasing in the vicinity as was observed in the final form of blister in the previous experiment. This migration of hydride occurs because of thermal boundary conditions applied during sample preparation, which are similar to the thermal gradient caused by accidental contact of pressure tube with coolant calandria tube.

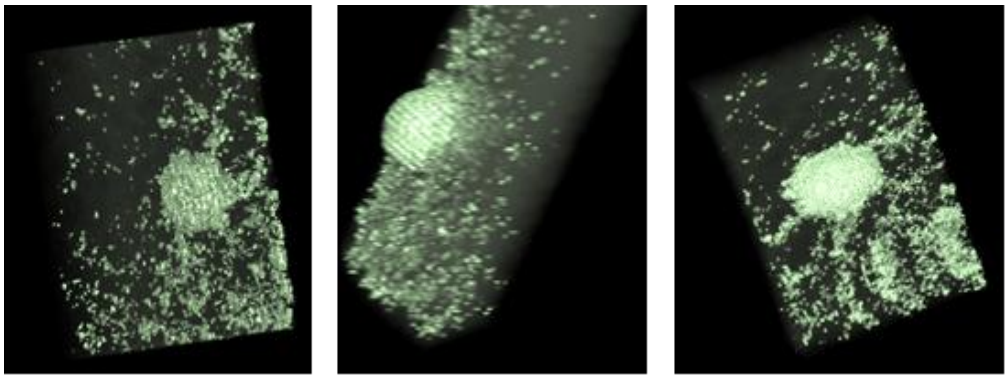

Figure 6.4 3D images near blister showing hydride migration towards blister formation

6.1.2 Quantitative analysis of hydride concentration:

Quantitative values of hydride distribution in the sample may provide additional information regarding blister formation like its sensitivity for catastrophic failure through DHC, its dependence over thermal boundary condition, spatial distribution of hydride in near about region and its depletion mechanism. In order to get quantitative hydride concentration distribution inside the blister as well as its surrounding regions, we have carried out calibration of hydride concentration with respect to image gray values in the neutron tomography reconstructed slice images of Zr-alloy samples having various concentrations of hydride. Since hydride has a large scattering co-

efficient for neutron, its small presence in Zr-alloy affects the resulting grey values in the image significantly. Calibration has been performed with respect to gray values in the reconstructed images and sensitivity of our imaging system for detecting low-level hydride concentration was analysed. It has been found that this technique can detect concentration difference of hydride as low as 25 wppm. An in-homogeneity in spatial distribution of hydride with such a low concentration has also been detected.

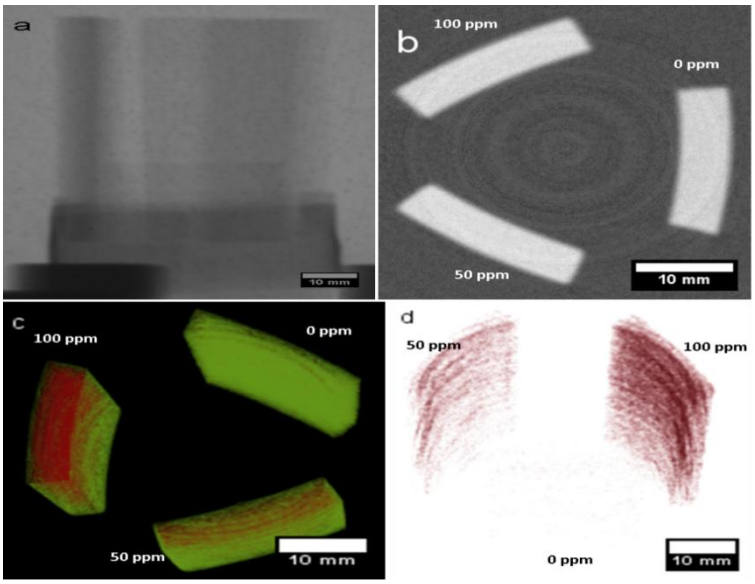

Figure 6.5 Neutron tomography of Zr-alloy coupons charged with hydride concentration 0, 50, 100 wppm. (a) Projection image (b) reconstructed slice (c) 3D image showing hydride in red and Zr-alloy in green colour (d) 3D image showing only hydride concentration.

a) Preparation of sample: Zr-alloy coupons with different hydride concentration

Zr-alloy (Zr2.5Nb) samples charged with different concentration of hydride (0 wppm, 25wppm, 50wppm, 75wppm, 100wppm) were prepared and investigated using neutron tomography. The samples were sealed in Pyrex glass capsules at 75 torr of Helium.

These capsules were loaded in a resistance-heated furnace maintained at 400°C and soaked for 24 hours followed by furnace cooling. The temperature of 400° C was chosen to dissolve all the hydrides. During furnace, cooling hydrides precipitate out uniformly in the sample.

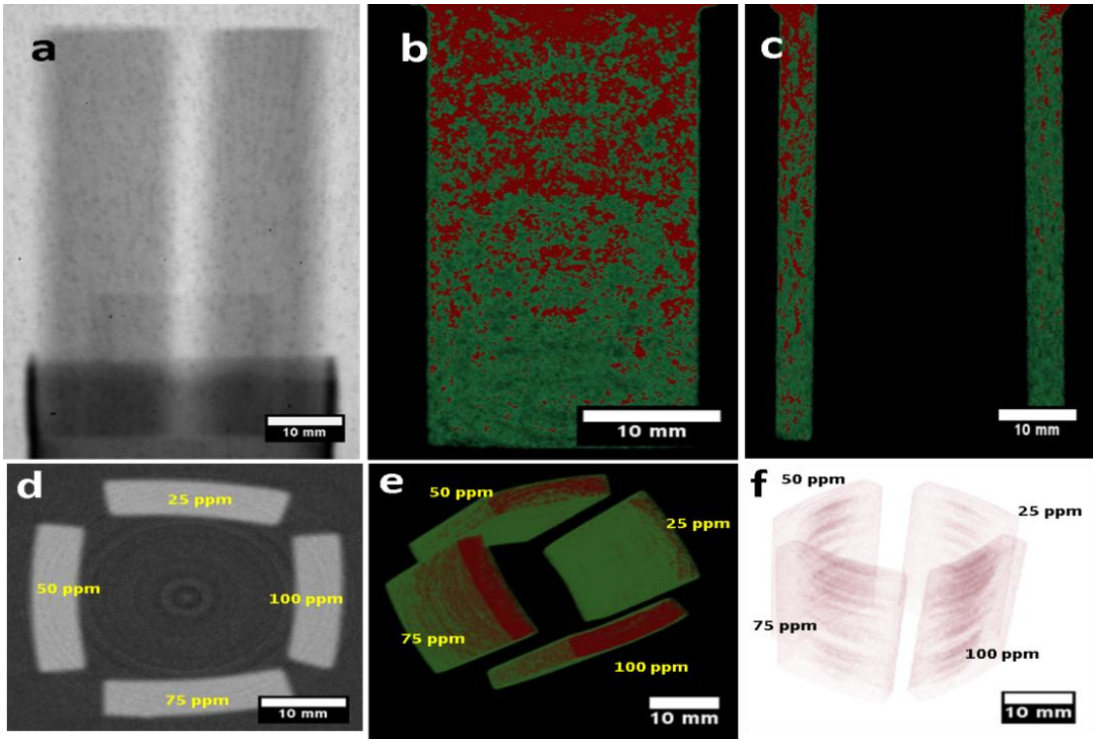

Figure 6.6 Neutron tomography of Zr-alloy coupons charged with 25, 50, 75, 100 wppm of hydride concentration. (a) Projection image (b) YZ slice (c) XZ slice (d) XY slice (e) 3D image showing hydride in red colour and Zr-alloy in green (f) 3D image showing only hydride concentration.

b) Experimental results and discussion:

Two Neutron tomography experiments were carried out on these coupons of Zr-alloy charged with hydrogen. The first experiment was performed for coupons charged in the range of 0-100 ppm in steps of 50 wppm which was further refined for the range of 25-

100 wppm in steps of 25 wppm. The samples with different hydride concentration were mounted on the rotational stage and a total 720 projections were acquired in each case while rotating the sample with angular step 0.5^0. After flat field correction, the slice images of the coupons were reconstructed using filtered backprojection algorithm and its 3D rendered volume images were obtained using VGStudioMax as shown in Figures 6.5 and 6.6. The slice images as well as 3D volume images clearly identify the concentration difference of hydride distribution in these coupons. Orthogonal slice images showing XY, YZ, XZ planes of the reconstructed volume are also shown in Figure 6.6, which show a certain degree of in-homogeneity in hydride distribution in the sample and confirm the capability of neutron tomography for detection of such in-homogeneity in concentration distribution of hydride in Zr-alloy. It is observed that the concentration difference of 25 wppm can be clearly distinguished in the reconstructed 3D images. The frequency of larger gray values in the reconstructed slice images and 3D images (red region in Figure 6.6) increases with the increase in hydride concentration as evident from the histogram distribution of the gray values shown in Figure 6.7(a).

c) Calibration

To calibrate the concentration of hydride in the samples against the image intensities (grey values) in the reconstructed image, histogram of the 3D volume image of all the samples were calculated separately. Equal area was selected in the reconstructed image of each sample. Figure 6.7 (a) shows the plot of histograms of each sample. It is seen from the histograms that the most probable grey value (Mode of

the distribution) in the reconstructed images keeps on increasing with the increment of hydride concentration in the volume. This is because with more and more hydride in the sample, larger number of voxel in the image possesses higher grey values hence the mode of the histogram distribution shifts towards higher values. A variation on peak heights in the histogram is attributed to the non-uniform distribution of hydride in the sample as described in the previous section. A graph showing the variation of hydride concentration value with respect to mode of the distribution has been plotted in Figure 6.7(b), which is linearly fitted to show the direct proportionality between the two quantities. The linear relation between Mode of histogram distribution of gray values and hydride concentration is established which can be used to predict the unknown concentration of hydride from the reconstructed image.

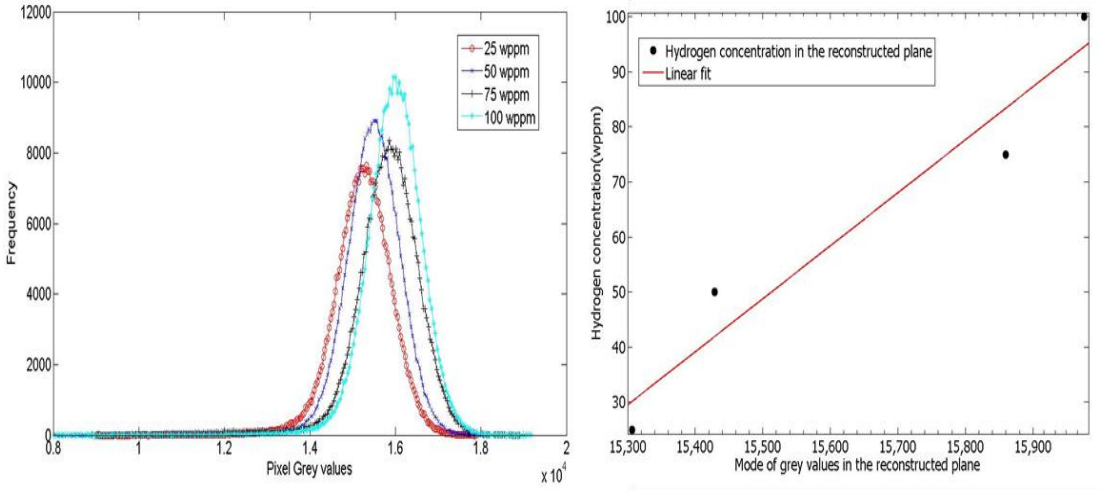

Figure 6.7 Calibration of hydride concentration against gray values (a) Histogram distribution of gray values for Zr-alloy coupons charged with different hydride concentrations (b) Linear fit of mode of gray values and hydride concentration

6.2 Non-destructive evaluation of PHWR Fuel Rod

Pressurized heavy water reactor (PHWR) consists of a fuel bundle with large number of fuel elements each of which is hermetically sealed by two end caps welded to cladding tube by pressure resistance welding Figure 6.8. Quality of end-cap welding is very crucial, as several cases have been witnessed of its failures. A defect/failure of a single end cap weld needs removal of 8-12 fuel bundles from the channel. It is essential to have highly reliable end cap welding which guarantees integrity of the fuel pin. In the neutron tomography experiments, the sample was placed over the rotational stage described in chapter 3 and rotated with an angular step 0.5^0. Radiographic projections were collected for acquisition time 20 sec at each rotational position and total 720 projections were collected while rotating the sample in 360 degree.

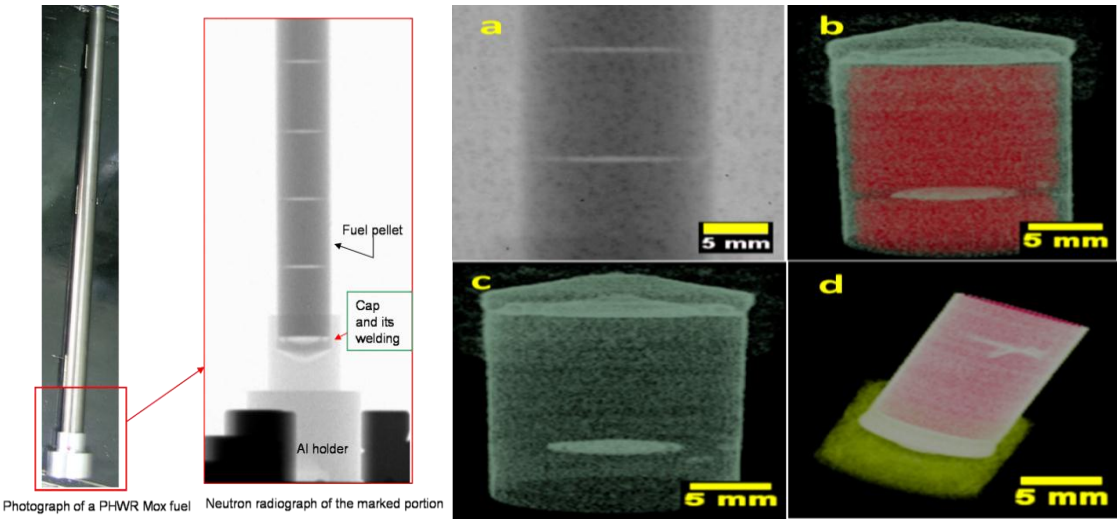

Figure 6.8 Fuel rod sample of PHWR and its projection image. Images in right show (a) region of interest (b) 3D image showing Zr-alloy cladding and end-cap in green and fuel pellet in red. (c) Segmented image of Zr-alloy cladding and end-cap (d) 3D image showing the defective fuel pellet.

A full tomographic scan took 4 hours. Image acquisition was followed by tomography reconstruction and 3D visualization. The non-destructive examination of the quality of this weld using neutron tomography has been carried out which provides high-resolution 3D images of the inspected volume of the sample. Defects and imperfections can be clearly visualized in the welded zone of the end cap Figure 6.8 (b, c). In the same experiment, the quality of fuel pellet in the fuel pin was also examined. In the 3D images of several pellets, one pellet was found having some crack as shown in Figure 6.8 (d). The crack may propagate during operation of the reactor and cause serious problems to safety related issues.

6.3 Study of lead melting and solidification

Dynamic neutron imaging is very useful in the visualization of time dependent variation of density and structure of materials. Such variations may be natural or instigated by external factors such as variation of temperature, pressure, chemical environment etc. We have applied neutron imaging for in-situ visualization of melting and solidification of lead to see the effects of variation heat flux and natural convection and measured in terms of variation of molten fraction, curvature and movement of interface of solid-liquid phases with time.

a) Importance of study and past studies

The transportation packages carrying radioactive material are designed using lead as a shielding material. In order to minimize the damage to public during transportation, these packages need to qualify the performance standards specified by IAEA/AERB. Thermal testing is one such performance standard for simulating fire

during transportation. It specifies the package to be exposed for a period of 30 min to a thermal environment which provides a heat flux of at least equivalent to that of a hydrocarbon fuel/air fire with an average temperature of at least 800^0C [208]. Under these test conditions, lead usually starts melting. The solid-liquid interface, wall temperature, and molten fraction variation with time for a prescribed thermal boundary condition are important engineering parameters for evaluating the package performance. Hence, it is very important to generate the accurate mapping of solid-liquid interface using nonintrusive methods. Previously several studies for studying melting and solidification of various metals under different boundary conditions have been reported. Gau and Viskanta [209] conducted experimental investigations on the melting of gallium in a rectangular enclosure in which a single vertical wall was heated at constant wall temperature boundary condition. Gau and Viskanta [210] also studied influence of natural convection on the solid-liquid interface motion during melting and solidification of Lipowitz metal in a rectangular cavity using pour out method where heating was carried out on the top and bottom wall of the rectangular enclosure. Wang and Fautrella [211] tracked the solid-liquid interface during the solidification of pure tin influenced by thermally driven natural convection using thermocouples. Szekely and Chhabra [212] used thermocouples to study the effect of natural convection on the controlled solidification of lead under conditions of nearly unidirectional heat flow within the system. The application of X-ray and neutron imaging technique is also reported for understanding the melting phenomenon. Phase change from solid to liquid causes a change of density typically ~ 2%, which results in a change of transmitted

intensity of X-ray or neutron beam. The review of literature suggests that solid liquid interface data is available only for constant wall temperature boundary condition. In addition, role of natural convection in the melting and solidification is not studied extensively based on non-destructive methods. In this study, we have applied non-destructive dynamic neutron radiography for the time dependent visualization of solid-liquid interface. The molten fraction and curvature of the interface is calculated using application of appropriate image analysis methods.

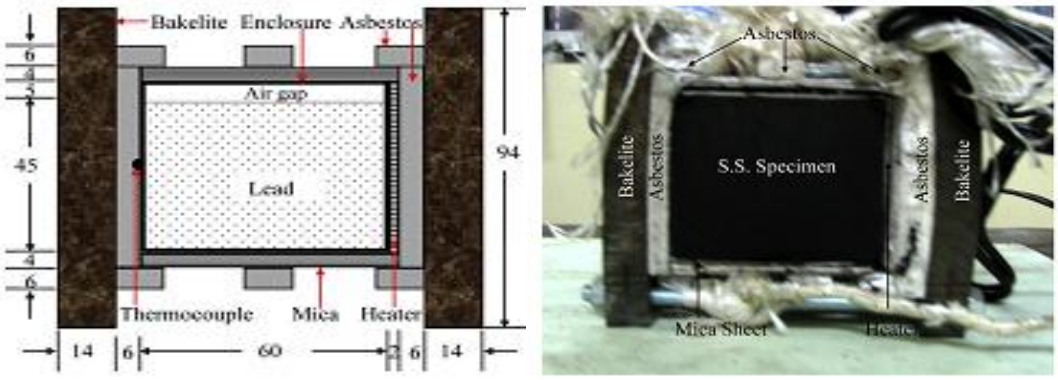

Figure 6.9 (a) Schematic diagram showing the lead sample, heating arrangement and other components used (b) Photograph of the sample used.

b) Experimental details

The experimental investigation of melting or solidification of lead contained in a stainless steel cuboid was carried out at beamline E12 in CIRUS reactor in BARC using digital neutron radiography. The method involves dynamic capture of the progress of solid liquid interface under the effects of natural convection in a non-intrusive manner. To see the effect of natural convection in the molten metal under various conditions, the heating from different surfaces of cuboid was applied however,

constant heating rate was maintained. Visualisation of solid-liquid interface movement was observed online during melting/solidification of lead in the CCD detector. Time taken for initiation of melting, completion of melting was noted down. Variation of molten fraction with time was computed using image analysis methods on experimental data and compared for various cases. The experimental data serves as a benchmark for analytical/numerical studies of lead melting and solidification under various conditions of natural convection. These tests also highlight the importance of natural convection during melting. Image acquisition was carried out using CCD camera with a readout rate 1 ms/pixel. The minimum acquisition time required to generate sufficient contrast between solid and molten lead (~15%) was found to be 10 s. Apart from this, time of 1.7 s for readout and data transfer and 2.1 s for further saving of image file is required making total 13.8 s between successively acquired images. During the experimentation, the camera chip was kept cooled at -40^0C to minimize the thermionic noise. Test section set up as shown in Figure 6.9 consist of a cuboidal enclosure made of stainless steel sheet of thickness 1 mm. The size of the specimen is 50 x 50 x 60 mm^3. Lead is filled in specimen. Air gap of 5 mm is kept above the lead to accommodate the volumetric expansion of lead during melting. This air gap also acts as a good heat insulator. Aspect ratio (Height to width) of the test section is 0.75. The front size of the test section is designed according to the limit of size of the scintillator screen (150 mm x 100 mm). Plate heater is attached on different walls of the cuboid as per the experimental requirements. Plate heater is made of nichrome strip of 0.1 mm thickness and 5 mm width placed on mica sheet. This is sandwiched between two mica sheets as

shown in Figure 6.9. Asbestos sheet of thickness 6 mm and glass wool is used as insulation to minimize the heat loss at the heated side and the opposite side. Bakelite sheet of thickness of 14 mm is used to hold the insulating material and the heater. This Bakelite also acts as an insulating material. Asbestos strip is placed on the other walls for the sake of insulation. The front and backward facing walls are open to atmosphere so that the neutron beam faces no hindrance in its path. The actual photograph of test section is shown in Figure 6.9 (b). K-type thermocouples and thermal camera is used to measure the temperature of the wall opposite to the heated surface. Controlled electric supply is applied using 0-240 V variable AC. During the experiment, the heater is put on. The supply of power is kept constant during the experiment

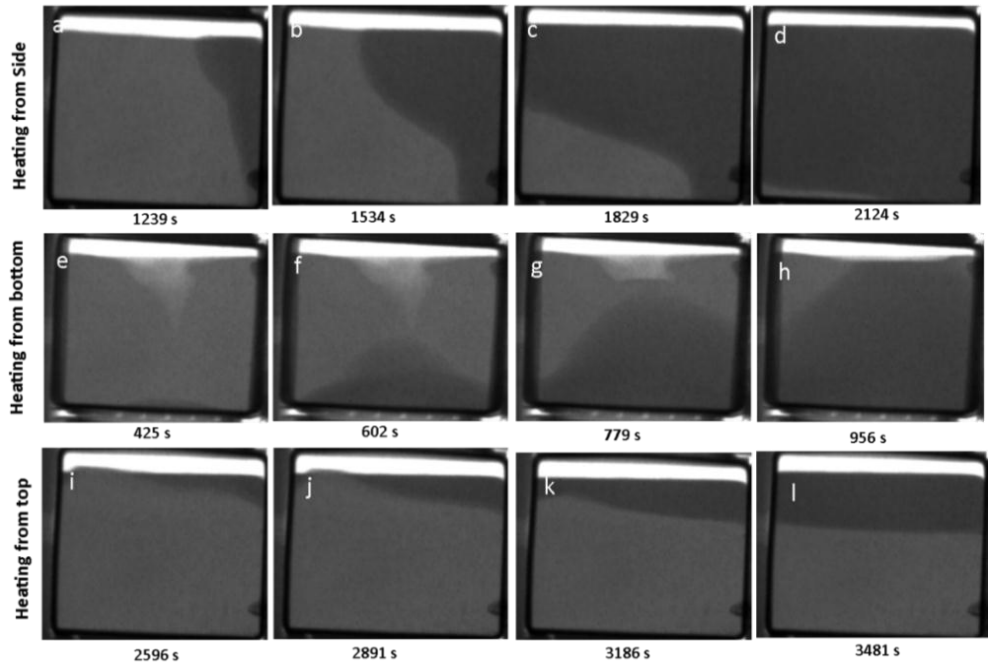

Figure 6.10 Lead melting: Neutron radiography images acquired at different time after initiation of heating. Images show movement of solid-liquid interface for heating from different surfaces.

c) Results and discussion

i. Effect of natural convection

In these experiments, a constant heat flux at 16.3 kW/m^2 is maintained on various surfaces of the cuboid namely side, bottom, and top surfaces one by one and effect of natural convection is studied through finding variations in the movement of solid-liquid interface, time required for melting initiation, time required for complete melting etc. (Figure 6.10). When lead is heated from different sides of the cuboid, a temperature gradient is created between heated wall and the opposite wall of the test specimen because the other sides of the cuboid are insulated. Effect of natural convection will be different for all these cases due to effect of gravity. In case of heating from the side, solid-liquid interface is not straight which moves faster nearer the top surface compared to that at the bottom surface because of high melting rate at the top. This is because of the dominance of natural convection at the top in the nearby region of air-gap which is not there at the bottom. Similar observations are reported by Gau and Viskanta [3]. When heated from bottom, the role of convection is similar from the two side surfaces. The heat transfer to the solid is dominated by conduction from the bottom surface however slowly convection of liquid also starts playing a major role.

When heated from top, due to air gap initially there is no contact of heated surface to the lead specimen hence heat transfer occurs due to radiative mode or through convection in the air column between heated surface and lead specimen. Therefore, the melting rate is very slow initially, which picks up after some melting due to increased

natural convection in the liquid. However, in absence of substantial conductive heating the complete melting of lead block was not observed.

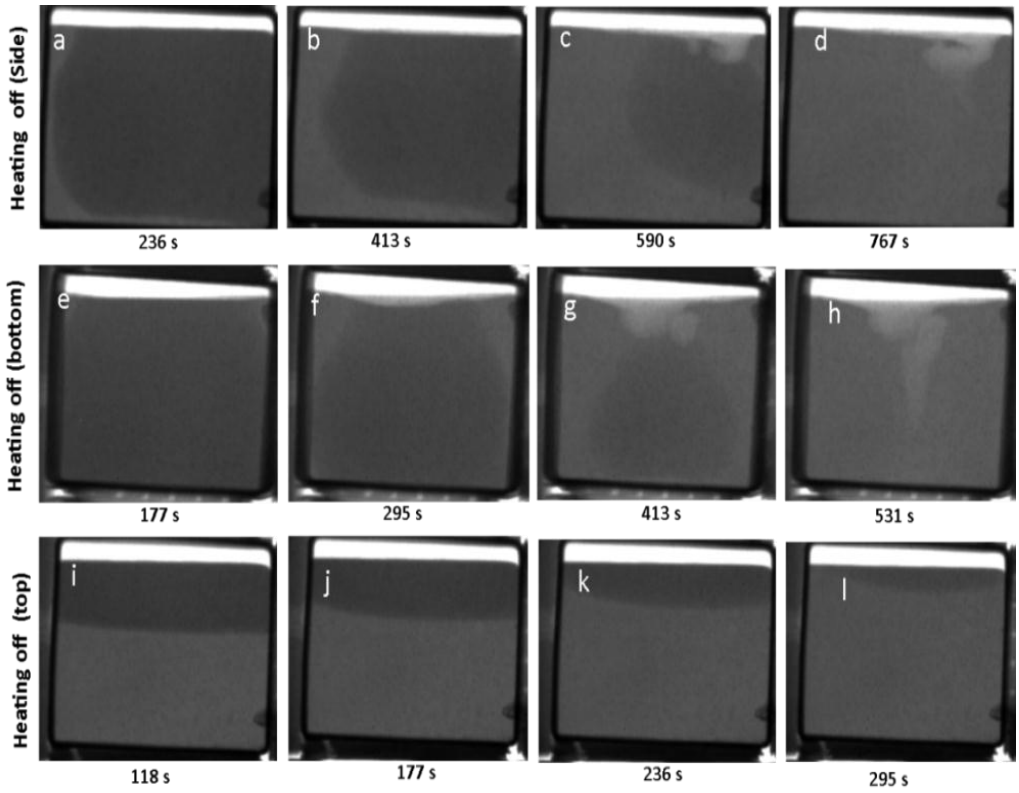

Figure 6.9 Lead solidification: Neutron radiography images acquired at different time after initiation of cooling. Images show movement of solid-liquid interface after heating from different surfaces was put-off.

In case of solidification, when heating was stopped, the molten lead starts to solidify under the given boundary conditions. Since the hot surface is still present, its effect on solidification was also observed on solidification time and solid-liquid interface. Due to effects of natural convection, the contours of interface are different in different cases of solidification as shown in Fig-6.11. Figure 6.12 shows the movement of solid-liquid interface with time in case of melting and solidification whereas Figure

6.13 shows variation of molten fraction with time. The parameters of melting and solidifications are compared in Table-6.1.These observations are being further studied through fluid dynamics simulations under given boundary conditions.

Table 6.1 Comparison of transient behaviours of lead melting and solidification under various cases of natural convection

	Melting		**Solidification**	
	Time to start(s)	Time to melt (s)	Time to start(s)	Time to solidify(s)
Bottom	378	684	79	460
Top	2407	1109	24	236
Side	979	1192	59	271

ii. Effect of heating rate

In order to study effect of heating rate, the cuboid was heated from one side with different heating power. Three cases were studied with heating rate maintained at 16.3, 22.7 and 35.1 kW/m^2. Depending upon the heating rate, the time taken for initiation of melting was different which was started eventually. The rate of melting was also different as can be seen in Figure 6.14. The figure compares the solid-liquid interface after a fixed time from heating initiation for lead melting and after fixed time after stopping of heating for solidification. As can be seen from these images, due to different heating rate, the molten fraction and contour of solid-liquid interface is different for melting. After 1027 seconds, for heating rate 16.3 kW/m^2 the melting is just started while for 35.1 kW/m^2 the melting is complete in the same time. Simulation

studies on heat transfer rate and fluid dynamics for different cases and measurement of different useful parameters has been carried out using fluent code.

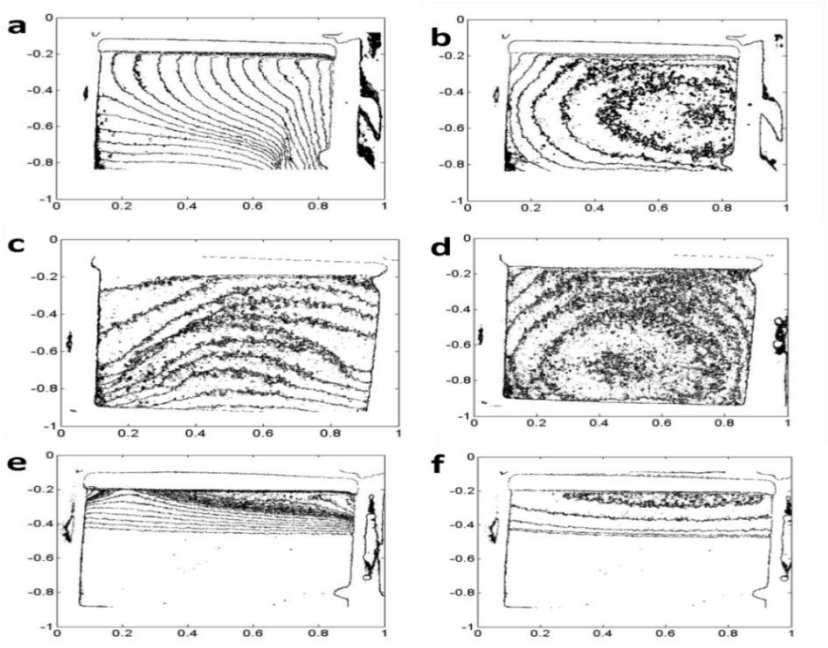

Figure 6.10 Contours showing the movement of solid-liquid interface with time for different cases of heating and solidification (a,b) side (c,d) bottom (e,f) top

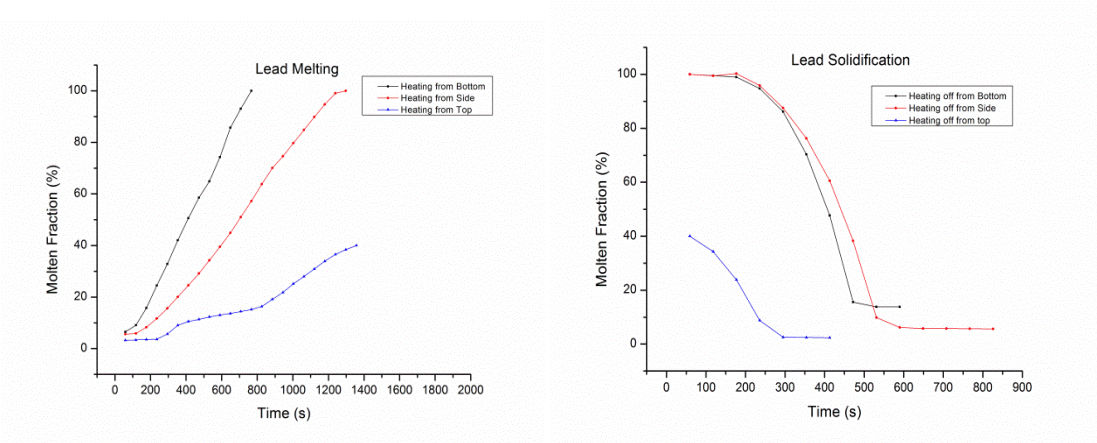

Figure 6.11 Molten fraction vs. time in different cases of lead melting and solidification

Table 6.2 Comparison of transient behaviour of lead melting and solidification caused by different heating rates

Heating rate (Heating from Side)	**Melting**		**Solidification**	
	Time to start(s)	Time to melt(s)	Time to start(s)	Time to solidify(s)
16.3 kW/m^2	861	1204	118	507
22.7kW/m^2	401	861	130	472
35.1kW/m^2	342	696	106	507

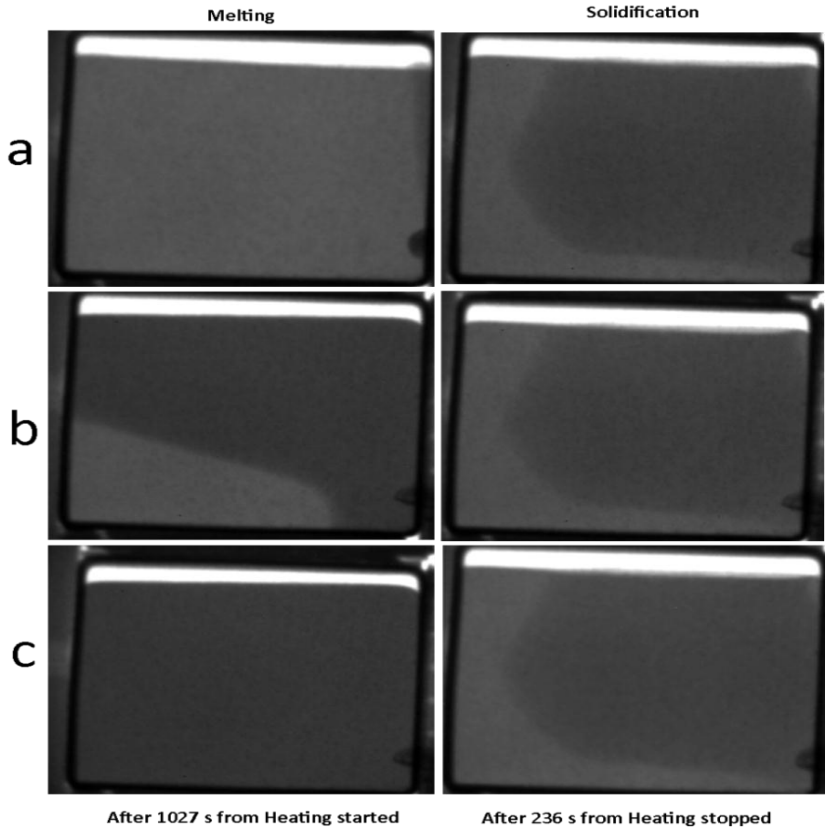

Figure 6.12 Effect of heating rate on lead melting & solidification though images acquired after fixed time of heating & cooling initiation (a)16.3 (b) 22.7 (c)35.1 kW/m^2

7 CONCLUSIONS

New materials are the pivot of future developments in nuclear technologies. Fabrication of fuel, cladding or other components of nuclear reactor requires materials with advanced physio-mechanical properties to ensure their compatibility in adverse operational environments of high temperature, high pressure and radiation. The properties of materials depend on their composition, density and internal structure threfore non-destructive 3D visualization and measurement of micro-structural features requires imaging techniques with high sensitivity and high penetration in the sample to allow surface as well as bulk information. Imaging is also useful in non-destructive assessment of degradation of reactor components to ensure their un-interrupted long term operation. Advances in X-ray and neutron sources, experimental techniques such as phase imaging and phase retrieval, tomography and much improved instrumentation bring out new opportunities for in-depth understanding of mechanical behaviour in a broad spectrum of materials in general and nuclear materials in particular.

This thesis studies several advanced modalities of X-rays and neutron micro-imaging such as PCI, diffraction enhanced imaging, phase retrieval, μ-CT and holotomography, and examines their applications in the image based characterisation of

nuclear materials in particular those used in CHTR and PHWR. First we have reviewed different advanced modes of X-ray and neutron imaging which are useful in the studies of nuclear materials. Design concepts for their implementation in micro-imaging systems and strategies for optimization of experimental parameters to achieve high quality images are discussed.

In order to further improve contrast sensitivity using computational methods, the thesis work also includes simulation studies on phase retrieval methods utilizing single or multiple phase contrast images to extract object's quantitative phase map. Various algorithm available in the littrature are compared for their performance along with experimental validation to find out their applicability in practical applications of material science. Two cases of multi-image algorithms based on CTF formulation are compared namely multi-distance algorithms and multi-wave-length algorithm and it has been found that both the algorithms can quite successfully used to reconstruct sample's phase/thickness map at object plane however data acquisition for multi-wavelength algorithm is easy due to no alignment related restrictions. Single image algorithms are generally applicable under some stringent condition of validity regarding sample composition and near field condition. We have investigated their performance under the conditions where their validity is not strictly followed. It has been found that these single image algorithms quite successfully remove the phase contrast artefact from the phase contrast images, and improve visibility of features at interfaces. However, to retrieve quantitative phase thus real part of refractive index, they should be employed under the conditions of their strict validity. Simulation studies on shift and add

algorithm of tomosynthesis reconstruction of slice images of a 3D object from its limited angle projection data is also carried out in two different acquisition geometries and found that the algorithms are capable of highlighting desired features of the selected plane and blur all the out of plane features. The simulation results are tested on mathematical phantoms representing three different sample compositions.

In order to implement new modalities of X-ray and neutron imaging, we have developed two state of the art micro-imaging facilities utilizing synchrotron based X-ray source and nuclear reactor based neutron source. The synchrotron based imaging beamline is developed to work in monochromatic and white beam mode. It implements high-resolution micro-radiography and tomography; propagation based and diffraction enhanced PCI and holotomography, dual energy imaging and real-time imaging. The neutron imaging facility is developed with a dual-purpose collimator for the implementation of high-resolution digital neutron radiography, tomography and PB-PCI in the same experimental hutch. System charecterisation & feasibility experiments have been carried out on these facilities to measure their important characteristics and establish implementation of various advanced micro-imaging techniques.

In the application domain, X-ray & neutron micro-imaging and tomography have been applied to a variety of material science problems specifically nuclear materials to determine their microstructure and density distribution, non-destructive evaluation and see effects of various external factors. Micro-focus based X-ray micro imaging in absorption and phase contrast mode has been applied to the applications, which have thicker samples and ultimately require X-ray μ-CT as a routine quality assessment tool.

X-ray μ-CT has been applied on microstructure studies of various components of compact high temperature reactor. TRISO coated fuel particles having layers of pyro-carbon, SiC has been studied to find layer thickness, and uniformity using PB-PCI and image analysis. Oxidation protective coatings on graphite fuel tube components have been studied to find out variation in coating properties in the axial direction of the tube to see the effect of reactant depletion. X-ray μ-CT has also been used for non-destructive analysis CHTR fuel tube to find bore area, inter-spacing and their variation along the tube axis.

Synchrotron based micro imaging and tomography has been applied to the materials of relatively low density, small size and composed of mostly low atomic number materials due to the available energy range of 8-35 keV at the developed imaging beamline. We have characterised microstructure of several materials such as carbon composites, polyurethane foam, Al-SiC composites, metal adsorbent polymer beads etc. For extraction of quantitative structural information from reconstructed tomography slice images, several image processing and image analysis algorithms have been applied. Porous microstructure and its spatial inhomogeneities have been deduced for polymer beads. Comparative study of micro-focus based and synchrotron-based tomography for microstructure determination of polyurethane foam signifies the merit of synchrotron based micro-imaging. Effect of irradiation dose on microstructure of polyurethane foam and its correlation with mechanical strength is established using X-ray μ-CT and image analysis. Several types of carbon-carbon composites, the potential structural material for high temperature reactor, have also been imaged to study

distribution of carbon layers in epoxy matrix and their geometries caused by their different method of manufacturing.

Neutron imaging is uniquely applied for micro-imaging application of detecting distribution of small quantity of low atomic number element such as hydride in the heavy metallic matrix of Zr-alloy. In the Zr-alloy pressure tube, hydride blister is detected successfully and its shape, size and in-homogeneity in the neighbourhood is also characterised. Small quantity of hydride as low as 25 wppm is shown to be detected in the Zr-alloy matrix. Neutron imaging is also applied for non-destructive 3D visualization of PHWR fuel rod and study of lead melting/ solidification. Study of lead melting shows the effect of natural convection, heating rate and gravity on melting rate and curvature of solid-liquid interface. Molten fraction variation and movement of solid-liquid interface with time is quantified using image analysis.

Future scope of this thesis work in methodological domain lies in the development and simulation of new algorithms of phase retrieval suitable for tomography and applicable in most general conditions. Significant efforts are required to be made to improve accuracy of single image phase retrieval methods to apply them in practical applications. Slice reconstruction algorithms for special cases of tomography such as reduced dose, flat object, fast acquisition, limited projections, region of interest imaging are also being considered for our future studies. In the instrumentation domain, the scope of micro-imaging will be further enhanced with the installation of focusing device leading to X-ray imaging combined with fluorescence/absorption and micro diffraction to identify material phases and crystal grains boundries with sub-micrometer

spatial resolution and element specific imaging. To improve resolution and reduce data acquisition time of neutron imaging system, further options will be explored in collimator design, detector design and cold neutron beam source. New application of X-ray and neutron micro-imaging will be explored in a field of bio-medical imaging, material science, agriculture, archaeology, geoscience, engineering and NDT. The application of these advanced X-ray and neutron micro-imaging techniques, in combination with theoretical simulations and numerical modelling, will help in the development of new materials with advanced mechanical and transport properties in the near future.

8 REFERENCES

[1] S.R. Stock, MicroComputed Tomography: Methodology and Applications, 2008. doi:doi:10.1201/9781420058772.fmatt.

[2] A. Madra, N. El, M. Benzeggagh, X-ray microtomography applications for quantitative and qualitative analysis of porosity in woven glass fiber reinforced thermoplastic, Compos. Sci. Technol. 95 (2014) 50–58. doi:10.1016/j.compscitech.2014.02.009.

[3] M. Salamon, R. Hanke, P. Krüger, N. Uhlmann, V. Voland, Realization of a computed tomography setup to achieve resolutions below 1 μm, Nucl. Instruments Methods Phys. Res. Sect. A Accel. Spectrometers, Detect. Assoc. Equip. 591 (2008) 50–53. doi:10.1016/j.nima.2008.03.024.

[4] S.H. Lau, H. Huang, B. Metscher, H. Chang, W. Yun, E. Lundgren, Imaging biological , polymer and low Z materials in 3D to submicron spatial resolution , with a novel MicroCT, (2008) 34–35.

[5] G.F.D.U. Labate, F. Pennella, F. Consolo, P. Gentile, U. Morbiducci, S.H. Lau, P.D.I. Torino, Porosity and Computational Flow Analysis for Collagen-membrane and Cross-Linked Gelatin Scaffolds using a high contrast MicroCT with submicron resolution, 61 (2009) 73781.

[6] E. Boller, P. Cloetens, J. Baruchel, P. Tafforeau, O. Rozenbaum, J. Pourchez, Synchrotron X-Ray microtomography: a high resolution, fast and quantitative tool for rock characterization, Road Mater. Pavement Des. X (2001) 1–9.

[7] J.D. Yeager, S.N. Luo, B.J. Jensen, K. Fezzaa, D.S. Montgomery, D.E. Hooks, High-speed synchrotron X-ray phase contrast imaging for analysis of low-Z composite microstructure, Compos. Part A Appl. Sci. Manuf. 43 (2012) 885–892. doi:10.1016/j.compositesa.2012.01.013.

[8] H. Li, X. Yin, J. Ji, L. Sun, Q. Shao, P. York, T. Xiao, Y. He, J. Zhang, Microstructural investigation to the controlled release kinetics of monolith osmotic pump tablets via synchrotron radiation X-ray microtomography., Int. J. Pharm. 427 (2012) 270–5. doi:10.1016/j.ijpharm.2012.02.017.

[9] D. Chapman, W. Thomlinson, F. Arfelli, N. Gmür, Z. Zhong, R. Menk, R.E. Johnson, D. Washburn, E. Pisano, D. Sayers, Mammography imaging studies using a Laue crystal analyzer, Rev. Sci. Instrum. 67 (1996) 3360. doi:10.1063/1.1147502.

[10] Z. Zhong, W. Thomlinson, D. Chapman, D. Sayers, Implementation of diffraction-enhanced imaging experiments: at the NSLS and APS, Nucl. Instruments Methods Phys. Res. Sect. A Accel. Spectrometers, Detect. Assoc. Equip. 450 (2000) 556–567. doi:10.1016/S0168-9002(00)00308-9.

[11] S.A. Zhou, A. Brahme, Development of phase-contrast X-ray imaging techniques and potential medical applications, Phys. Medica. 24 (2008) 129–148. doi:10.1016/j.ejmp.2008.05.006.

[12] S.W. Wilkins, Y.I. Nesterets, T.E. Gureyev, S.C. Mayo, A. Pogany, A.W. Stevenson, On the evolution and relative merits of hard x-ray phase-contrast imaging methods., Philos. Trans. A. Math. Phys. Eng. Sci. 372 (2014) 20130021. doi:10.1098/rsta.2013.0021.

[13] T. Weitkamp, A. Diaz, C. David, F. Pfeiffer, M. Stampanoni, P. Cloetens, E. Ziegler, X-ray phase imaging with a grating interferometer., Opt. Express. 13 (2005) 6296–6304. doi:10.1364/OPEX.13.006296.

[14] M. Langer, Y. Liu, F. Tortelli, P. Cloetens, R. Cancedda, F. Peyrin, Regularized phase tomography enables study of mineralized and unmineralized tissue in porous bone scaffold, J. Microsc. 238 (2010) 230–239. doi:10.1111/j.1365-2818.2009.03345.x.

[15] A. Rack, S. Zabler, B.R. M??ller, H. Riesemeier, G. Weidemann, A. Lange, J. Goebbels, M. Hentschel, W. G??rner, High resolution synchrotron-based radiography and tomography using hard X-rays at the BAMline (BESSY II), Nucl. Instruments Methods Phys. Res. Sect. A Accel. Spectrometers, Detect. Assoc. Equip. 586 (2008) 327–344. doi:10.1016/j.nima.2007.11.020.

[16] Y.S. Kashyap, A. Agrawal, P.S. Sarkar, M. Shukla, T. Roy, A. Sinha, A variable-wavelength-based approach of phase retrieval for contrast transfer function based methods, J. Synchrotron Radiat. 17 (2010) 799–803. doi:10.1107/S0909049510028311.

[17] Y.S. Kashyap, A. Agrawal, P.S. Sarkar, M. Shukla, T. Roy, A. Sinha, Study of

pyro-carbon coated alumina kernel using mixed contrast transfer based X-ray phase retrieval technique, NDT E Int. 44 (2011) 41–46. doi:http://dx.doi.org/10.1016/j.ndteint.2010.09.004.

[18] A.K. Agrawal, B. Singh, Y.S. Kashyap, M. Shukla, P.S. Sarkar, A. Sinha, Design, development and first experiments on the X-ray imaging beamline at Indus-2 synchrotron source RRCAT, India, J. Synchrotron Radiat. 22 (n.d.) 1531–1539.

[19] Y.S. Kashyap, A. Agrawal, M. Shukla, T. Roy, A. Sinha, Development of Neutron Phase Contrast Imaging Technique At Cirus Reactor , India, (2011) 10–13.

[20] A.K. Agrawal, P.S. Sarkar, B. Singh, Y.S. Kashyap, P.T. Rao, A. Sinha, Application of X-ray micro-CT for micro-structural characterization of APCVD deposited SiC coatings on graphite conduit, Appl. Radiat. Isot. 108 (2016) 133–142. doi:10.1016/j.apradiso.2015.12.040.

[21] P.T. Rao, U. Jain, P.K. Mollick, A. Agarwal, J.K. Chakravartty, S. Kumar, Application of atmospheric CVD for internal surface coating of graphite conduit by silicon carbide, J. Nucl. Mater. 456 (2015) 200–205. doi:10.1016/j.jnucmat.2014.09.049.

[22] A. Agrawal, B. Singh, Y. Kashyap, P.S. Sarkar, M. Shukla, A. Sinha, Micro-structural characterization of materials using synchrotron hard X-ray imaging techniques, SOLID STATE Phys. Proc. 59th DAE Solid State Phys. Symp. 2014. 1665 (2015) 60020. doi:10.1063/1.4917855.

[23] A. Agrawal, Y. Kashyap, P.S. Sarkar, A.N. Behra, M. Shukla, R.N. Singh, A. Sinha, J.K. Chakravartty, Study of hydride blisters in Zr-alloy using neutron tomography, J. Nucl. Mater. 421 (2012) 47–53. doi:10.1016/j.jnucmat.2011.10.047.

[24] P. Sarkar, A. Agrawal, Y. Kashyap, M. Shukla, A. Sinha, L. Kumar, Visualization of Lead Melting and Solidification Using Neutron Radiography, 3 (2013) 7–14.

[25] L. Kumar, B.S. Manjunath, R.J. Patel, S.G. Markandeya, R.G. Agrawal, A. Agrawal, Y. Kashyap, P.S. Sarkar, A. Sinha, K.N. Iyer, S. V. Prabhu, Experimental investigations on melting of lead in a cuboid with constant heat flux boundary condition using thermal neutron radiography, Int. J. Therm. Sci. 61 (2012) 15–27. doi:10.1016/j.ijthermalsci.2012.06.014.

[26] J.C. Domanus, Neutron Radiography , Techniques and Applications, 1987.

[27] B.C. Masschaele, V. Cnudde, M. Dierick, P. Jacobs, L. Van Hoorebeke, J.

Vlassenbroeck, UGCT: New X-ray radiography and tomography facility, Nucl. Instruments Methods Phys. Res. Sect. A Accel. Spectrometers, Detect. Assoc. Equip. 580 (2007) 266–269. doi:10.1016/j.nima.2007.05.099.

[28] D. Paganin, Coherent X-Ray Optics, OUP Oxford, 2006.

[29] F. Zernike, How I discovered phase contrast., Science. 121 (1955) 345–349. doi:10.1126/science.121.3141.345.

[30] C.K. Hagen, P. Maghsoudlou, G. Totonelli, P.C. Diemoz, M. Endrizzi, L. Rigon, R.-H. Menk, F. Arfelli, D. Dreossi, E. Brun, P. Coan, A. Bravin, P. De Coppi, A. Olivo, High contrast microstructural visualization of natural acellular matrices by means of phase-based x-ray tomography., Sci. Rep. 5 (2015) 18156. doi:10.1038/srep18156.

[31] a Pogany, D. Gao, S.W. Wilkins, Contrast and resolution in imaging with a microfocus x-ray source, Rev. Sci. Instrum. 68 (1997) 2774–2782. doi:10.1063/1.1148194.

[32] T.E. Gureyev, Y.I. Nesterets, A.W. Stevenson, P.R. Miller, A. Pogany, S.W. Wilkins, Some simple rules for contrast, signal-to-noise and resolution in in-line x-ray phase-contrast imaging., Opt. Express. 16 (2008) 3223–3241. doi:10.1364/OE.16.003223.

[33] X. Wu, H. Liu, Clinical implementation of x-ray phase-contrast imaging: theoretical foundations and design considerations., Med. Phys. 30 (2003) 2169–2179. doi:10.1118/1.1593836.

[34] P.C. Diemoz, F.A. Vittoria, C.K. Hagen, M. Endrizzi, P. Coan, E. Brun, U.H. Wagner, C. Rau, I.K. Robinson, A. Bravin, A. Olivo, Single-image phase retrieval using an edge illumination X-ray phase-contrast imaging setup, J. Synchrotron Radiat. 22 (2015) 1072–1077. doi:10.1107/S1600577515008978.

[35] A. Momose, S. Kawamoto, I. Koyama, Y. Hamaishi, K. Takai, Y. Suzuki, Demonstration of x-ray Talbot interferometry, Japanese J. Appl. Physics, Part 2 Lett. 42 (2003) 866–868. doi:10.1143/JJAP.42.L866.

[36] F. Pfeiffer, O. Bunk, I. Johnson, X. Donath, C. Grünzweig, C. David, G. Frei, G. Kühne, P. Vontobel, E. Lehmann, Neutron Phase Imaging using a Grating Interferometer Neutron Phase Imaging using, Imaging. (2006).

[37] S. Valton, F. Peyrin, D. Sappey-Marinier, A FDK-based reconstruction method for off-centered circular trajectory cone beam tomography, IEEE Trans. Nucl. Sci. 53 (2006) 2736–2745. doi:10.1109/TNS.2006.880977.

[38] H. Gao, Direct filtered-backprojection-type reconstruction from a straight-line

trajectory, Opt. Eng. 46 (2007) 57003. doi:10.1117/1.2739624.

[39] E.N. Landis, D.T. Keane, X-ray microtomography, Mater. Charact. 61 (2010) 1305–1316. doi:10.1016/j.matchar.2010.09.012.

[40] I. Dobbins, James T., D.D.J. Godfrey, Digital x-ray tomosynthesis: current state of the art and clinical potential., Phys. Med. Biol. 48 (2003) R65-106.

[41] L. Helfen, T. Baumbach, P. Cloetens, J. Baruchel, Phase-contrast and holographic computed laminography, Appl. Phys. Lett. 94 (2009) 3–5. doi:10.1063/1.3089237.

[42] D.G. Grant, Tomosynthesis: a three-dimensional radiographic imaging technique., IEEE Trans. Biomed. Eng. 19 (1972) 20–28. doi:10.1109/TBME.1972.324154.

[43] P. Cloetens, W. Ludwig, J. Baruchel, D. Van Dyck, J. Van Landuyt, J.P. Guigay, M. Schlenker, Holotomography: Quantitative phase tomography with micrometer resolution using hard synchrotron radiation x rays, Appl. Phys. Lett. 75 (1999) 2912. doi:10.1063/1.125225.

[44] D.W. Sweeney, C.M. Vest, Reconstruction of three-dimensional refractive index fields from multidirectional interferometric data., Appl. Opt. 12 (1973) 2649–2664. doi:10.1364/AO.12.002649.

[45] M. Langer, P. Cloetens, J.P.-P. Guigay, S. Valton, F. Peyrin, Quantitative evaluation of phase retrieval algorithms in propagation based phase tomography, Biomed. Imaging From Nano to Macro, 2007. ISBI 2007. 4th IEEE Int. Symp. (2007) 552–555. doi:10.1109/ISBI.2007.356911.

[46] F.N. Chukhovskii, J.P. Guigay, Towards a rigorous treatment of the wave-field propagation according to the statistical theory of dynamical diffraction, J. Phys. D. Appl. Phys. 26 (1993) A53–A56. doi:10.1088/0022-3727/26/4A/012.

[47] J.P. Guigay, M. Langer, R. Boistel, P. Cloetens, Mixed transfer function and transport of intensity approach for phase retrieval in the Fresnel region, Opt. Lett. 32 (2007) 1617. doi:10.1364/OL.32.001617.

[48] A. Olivo, Towards the exploitation of phase effects in clinical synchrotron radiation radiology, Nucl. Instruments Methods Phys. Res. Sect. A Accel. Spectrometers, Detect. Assoc. Equip. 548 (2005) 194–199. doi:10.1016/j.nima.2005.03.089.

[49] F. Arfelli, M. Assante, V. Bonvicini, A. Bravin, G. Cantatore, E. Castelli, L. Dalla Palma, M. Di Michiel, R. Longo, A. Olivo, S. Pani, D. Pontoni, P. Poropat, M. Prest, A. Rashevsky, G. Tromba, A. Vacchi, E. Vallazza, F. Zanconati, D.

Dontoni, P. Poropat, M. Prest, A. Rashevsky, G. Tromba, A. Vacchi, E. Vallazza, F. Zanconati, D. Pontoni, P. Poropat, M. Prest, A. Rashevsky, G. Tromba, E. Castelli, L. Dalla Palma, M. Di Michiel, R. Longo, A. Olivo, S. Pani, D. Pontoni, P. Poropat, M. Prest, A. Rashevsky, G. Tromba, A. Vacchi, E. Vallazza, F. Zanconati, Low-dose phase contrast x-ray medical imaging, Phys. Med. Biol. 43 (1998) 2845–2852. doi:10.1088/0031-9155/43/10/013.

[50] Y.I. Nesterets, S.W. Wilkins, T.E. Gureyev, A. Pogany, A.W. Stevenson, On the optimization of experimental parameters for x-ray in-line phase-contrast imaging, Rev. Sci. Instrum. 76 (2005) 1–16. doi:10.1063/1.2038107.

[51] a Olivo, R. Speller, Experimental validation of a simple model capable of predicting the phase contrast imaging capabilities of any x-ray imaging system., Phys. Med. Biol. 51 (2006) 3015–3030. doi:10.1088/0031-9155/51/12/001.

[52] Godfrey N. Hounsfield - Biographical, (n.d.).

[53] A. Momose, Recent Advances in X-ray Phase Imaging, Jpn. J. Appl. Phys. 44 (2005) 6355–6367. doi:10.1143/JJAP.44.6355.

[54] G.W. J. Goebbels, B. Illerhaus, Y. Onel, H. Riesemeier, 3D-COMPUTED TOMOGRAPHY OVER FOUR ORDERS OF MAGNITUDE OF X-RAY ENERGIES J. Goebbels, B. Illerhaus, Y. Onel, H. Riesemeier, G. Weidemann Federal Institute for Materials Research and Testing (BAM), Berlin, Germany, (n.d.).

[55] T. dos S. Rolo, A. Ershov, T. van de Kamp, T. Baumbach, In vivo X-ray cine-tomography for tracking morphological dynamics, Proc. Natl. Acad. Sci. 111 (2014) 3921–3926. doi:10.1073/pnas.1308650111.

[56] G.R. Myers, D.M. Paganin, T.E. Gureyev, S.C. Mayo, Phase-contrast tomography of single-material objects from few projections., Opt. Express. 16 (2008) 908–919. doi:10.1364/OE.16.000908.

[57] P.C. Diemoz, M. Endrizzi, C.K. Hagen, T.P. Millard, F.A. Vittoria, A. Olivo, Angular sensitivity and spatial resolution in edge illumination X-ray phase-contrast imaging, Nucl. Instruments Methods Phys. Res. Sect. A Accel. Spectrometers, Detect. Assoc. Equip. 784 (2015) 538–541. doi:10.1016/j.nima.2014.12.027.

[58] M. Haghgoo, E. Plougonven, A.A. Yousefi, J.P. Pirard, A. Léonard, N. Job, Use of X-ray microtomography to study the homogeneity of carbon nanotube aqueous suspensions and carbon nanotube/polymer composites, Carbon N. Y. 50 (2012) 1703–1706. doi:10.1016/j.carbon.2011.11.031.

[59] P. Tafforeau, R. Boistel, E. Boller, A. Bravin, M. Brunet, Y. Chaimanee, P.

Cloetens, M. Feist, J. Hoszowska, J.J. Jaeger, R.F. Kay, V. Lazzari, L. Marivaux, A. Nel, C. Nemoz, X. Thibault, P. Vignaud, S. Zabler, Applications of X-ray synchrotron microtomography for non-destructive 3D studies of paleontological specimens, Appl. Phys. A Mater. Sci. Process. 83 (2006) 195–202. doi:10.1007/s00339-006-3507-2.

[60] A.M. Trater, S. Alavi, S.S.H. Rizvi, Use of non-invasive X-ray microtomography for characterizing microstructure of extruded biopolymer foams, Food Res. Int. 38 (2005) 709–719. doi:10.1016/j.foodres.2005.01.006.

[61] F. Mees, R. Swennen, M. Van Geet, P. Jacobs, Applications of X-ray computed tomography in the geosciences, Geol. Soc. London, Spec. Publ. 215 (2003) 1–6. doi:10.1144/GSL.SP.2003.215.01.01.

[62] M. Van Geet, R. Swennen, M. Wevers, Towards 3-D petrography: Application of microfocus computer tomography in geological science, Comput. Geosci. 27 (2001) 1091–1099. doi:10.1016/S0098-3004(00)00154-0.

[63] P. Cloetens, W. Ludwig, J. Baruchel, J.-P. Guigay, P. Pernot-Rej anko, M. Salo e-Pateyron, M. Schlenker, J.-Y. Buffì ere, E. Maire, G. Peix, Hard x-ray phase imaging using simple propagation of a coherent synchrotron radiation beam, J. Phys. D Appl. Phys. J. Phys. D Appl. Phys. 32 (1999) 145–151. http://iopscience.iop.org/0022-3727/32/10A/330.

[64] E.F. Donnelly, K.G. Lewis, K.M. Wolske, D.R. Pickens, R.R. Price, Characterization of the phase-contrast radiography edge-enhancement effect in a cabinet x-ray system., Phys. Med. Biol. 51 (2006) 21–30. doi:10.1088/0031-9155/51/1/002.

[65] T.E. Gureyev, D.M. Paganin, G.R. Myers, Y.I. Nesterets, S.W. Wilkins, Phase-and-amplitude computer tomography, Appl. Phys. Lett. 89 (2006) 2006–2009. doi:10.1063/1.2226794.

[66] H.N. Chapman, S. Bajt, A. Barty, W.H. Benner, M.J. Bogan, M. Frank, R.A. London, S. Marchesini, E. Spiller, A. Szöke, B.W. Woods, J. Hajdu, M. Bergh, F. Burmeister, C. Caleman, G. Huldt, F.R.N.C. Maia, M.M. Seibert, D. Van Der Spoel, U. Uppsala, S.- Uppsala, S. Boutet, K.O. Hodgson, M. Park, D.A. Shapiro, U.C. Davis, Ultrafast Coherent Diffraction Imaging With X-Ray Free-Electron Lasers*, (2006) 1–7. papers2://publication/uuid/1FF3BD44-0F76-4B85-ACFF-9E2D2ACC0C46.

[67] F. Arfelli, R.H. Menk, H.J. Besch, L. Rigon, H. Plothow-Besch, Contrast improvement with diffraction enhanced imaging for scattering materials, Proc. - Int. Symp. Biomed. Imaging. 2002–Janua (2002) 133–136. doi:10.1109/ISBI.2002.1029211.

[68] J. Miao, D. Sayre, H.N. Chapman, Phase retrieval from the magnitude of the Fourier transforms of nonperiodic objects, J. Opt. Soc. Am. A. 15 (1997) 1662. doi:10.1364/JOSAA.15.001662.

[69] A. Momose, Phase-sensitive imaging and phase tomography using X-ray interferometers., Opt. Express. 11 (2003) 2303–2314. doi:10.1364/OE.11.002303.

[70] F. Pfeiffer, C. David, O. Bunk, T. Donath, M. Bech, G. Le Duc, A. Bravin, P. Cloetens, Region-of-interest tomography for grating-based X-ray differential phase-contrast imaging, Phys. Rev. Lett. 101 (2008) 1–4. doi:10.1103/PhysRevLett.101.168101.

[71] N. Kardjilov, Absorption and phase contrast neutron imaging (overview), Hand. (n.d.).

[72] E.H. Lehmann, W. Wagner, Neutron imaging at PSI: a promising tool in materials science and technology, Appl. Phys. A. 99 (2010) 627–634. doi:10.1007/s00339-010-5606-3.

[73] M. Strobl, C. Gr??nzweig, A. Hilger, I. Manke, N. Kardjilov, C. David, F. Pfeiffer, Neutron dark-field tomography, Phys. Rev. Lett. 101 (2008) 1–4. doi:10.1103/PhysRevLett.101.123902.

[74] J. a Koch, O.L. Landen, L.J. Suter, L.P. Masse, Simple solution to the Fresnel-Kirchoff diffraction integral for application to refraction-enhanced radiography., J. Opt. Soc. Am. A. Opt. Image Sci. Vis. 30 (2013) 1460–3. doi:10.1364/JOSAA.30.001460.

[75] H. Yu, S.S. Han, W.J. Peng, Ieee, Simulation on In-Line Fresnel Diffractive Phase-contrast Imaging with Partially Coherent Hard X-ray, 2008 Ieee Nucl. Sci. Symp. Med. Imaging Conf. (2009) 5476–5478. doi:10.1109/NSSMIC.2008.4775240.

[76] X.Z. Wu, H. Liu, Phase-space evolution of x-ray coherence in phase-sensitive imaging, Appl. Opt. 47 (2008) E44–E52. doi:10.1364/AO.47.000E44.

[77] a Snigirev, I. Snigireva, V. Kohn, S. Kuznetsov, I. Schelokov, On the possibilities of x-ray phase contrast imaging by coherent high-energy synchrtron radiation, Rev. Sci. Inst. 66 (1995) 5486–5492. doi:10.1063/1.1146073.

[78] A. Burvall, U. Lundström, P. a C. Takman, D.H. Larsson, H.M. Hertz, Phase retrieval in X-ray phase-contrast imaging suitable for tomography., Opt. Express. 19 (2011) 10359–10376. doi:10.1364/OE.19.010359.

[79] F. Meng, H. Liu, X. Wu, An iterative phase retrieval algorithm for in-line x-ray

phase imaging, Opt. Express. 15 (2007) 8383–8390. doi:10.1364/OE.15.008383.

[80] D. Paganin, T.E. Gureyev, K.M. Pavlov, R.A. Lewis, M. Kitchen, Phase retrieval using coherent imaging systems with linear transfer functions, Opt. Commun. 234 (2004) 87–105. doi:10.1016/j.optcom.2004.02.015.

[81] R.C. Chen, L. Rigon, R. Longo, Quantitative 3D refractive index decrement reconstruction using single-distance phase-contrast tomography data, J. Phys. D. 44 (2011) 495401. doi:10.1088/0022-3727/44/49/495401.

[82] M.N. Boone, W. Devulder, M. Dierick, L. Brabant, Comparison of two single-image phase-retrieval algorithms for in-line x-ray phase-contrast imaging, 29 (2012) 2667–2672.

[83] T.E. Gureyev, D. Paganin, D.J. Parry, A. Pogany, A.W. Stevenson, Quantitative X-ray projection microscopy : phase-contrast and multi-spectral imaging, 207 (2002) 79–96.

[84] M. Langer, P. Cloetens, J. Guigay, F. Peyrin, Quantitative comparison of direct phase retrieval algorithms in in-line phase tomography, Med. Phys. 35 (2008) 4556–4566. doi:10.1118/1.2975224.

[85] W. Chlewicki, 3D Simultaneous Algebraic Reconstruction Technique for Cone-Beam Projections, Master's Thesis, Univ. Patras. (2001). http://bme.med.upatras.gr/bit/WChlewicki/msc.pdf.

[86] D.J. Gentle, N.M. Spyrou, Region of interest tomography in industrial applications, Nucl. Inst. Methods Phys. Res. A. 299 (1990) 534–537. doi:10.1016/0168-9002(90)90838-W.

[87] K. Balewski, W. Brefeld, W. Decking, H. Franz, E. Weckert, PETRA III : A Low Emittance Synchrotron Radiation Source Technical Design Report, (2004).

[88] R. Barrett, X-ray Optics for Synchrotron Radiation Beamlines X-ray Optics for Synchrotron Radiation Beamlines Introduction to X-ray Optics for SR ¾ Introduction ¾ General X-ray optics ¾ High heat-load optics ¾Zone plates ¾Refractive lenses ¾ Summary, Source. (n.d.).

[89] L. Berman, Synchrotron Beamline X-Ray Optics, (2010).

[90] D.H. Bilderback, P. Elleaume, E. Weckert, Review of third and next generation synchrotron light sources, J. Phys. B At. Mol. Opt. Phys. 38 (2005) S773. doi:10.1088/0953-4075/38/9/022.

[91] J. Baruchel, P. Bleuet, A. Bravin, P. Coan, E. Lima, A. Madsen, W. Ludwig, P. Pernot, J. Susini, Advances in synchrotron hard X-ray based imaging, Comptes

Rendus Phys. 9 (2008) 624–641. doi:10.1016/j.crhy.2007.08.003.

[92] E. Busetto, Optical components for hard x-ray beamlines., (2006).

[93] A. V. Bronnikov, Phase-contrast CT: Fundamental theorem and fast image reconstruction algorithms, J. Opt. Soc. Am. 19 (2002) 472–80. doi:10.1117/12.679389.

[94] A. Ruhlandt, M. Krenkel, M. Bartels, T. Salditt, Three-dimensional phase retrieval in propagation-based phase-contrast imaging, Phys. Rev. A - At. Mol. Opt. Phys. 89 (2014) 1–8. doi:10.1103/PhysRevA.89.033847.

[95] M. Langer, P. Cloetens, A. Pacureanu, F. Peyrin, X-ray in-line phase tomography of multimaterial objects, Opt. Lett. 37 (2012) 2151. doi:10.1364/OL.37.002151.

[96] J. Hagemann, A.L. Robisch, D.R. Luke, C. Homann, T. Hohage, P. Cloetens, H. Suhonen, T. Salditt, Reconstruction of wave front and object for inline holography from a set of detection planes, Opt. Express. 22 (2014) 11552–11569. doi:10.1364/OE.22.011552.

[97] K. Schladitz, C. Redenbach, T. Sych, M. Godehardt, Microstructural characterisation of open foams using 3d images, 148 (2008).

[98] G. Van Dalen, M.W. Koster, 3D imaging of aerated emulsions using X-ray microtomography, (n.d.).

[99] D. Wildenschild, Application of x-ray microtomography to environmental fluid flow problems, Proc. SPIE. (2004) 432–441. doi:10.1117/12.559056.

[100] A. Kaestner, E. Lehmann, M. Stampanoni, Imaging and image processing in porous media research, Adv. Water Resour. 31 (2008) 1174–1187. doi:10.1016/j.advwatres.2008.01.022.

[101] X. Fu, J.A. Elliott, A.C. Bentham, B.C. Hancock, R.E. Cameron, Application of X-ray microtomography and image processing to the investigation of a compacted granular system, Part. Part. Syst. Charact. 23 (2006) 229–236. doi:10.1002/ppsc.200601054.

[102] R.A. Ketcham, Computational methods for quantitative analysis of three-dimensional features in geological specimens, Geosphere. 1 (2005) 32–41. doi:10.1130/GES00001.1.

[103] S. Zabler, P. Cloetens, J.P. Guigay, J. Baruchel, M. Schlenker, Optimization of phase contrast imaging using hard x rays, Rev. Sci. Instrum. 76 (2005). doi:10.1063/1.1960797.

[104] Single Crystal Diffractometry - Cambridge University Press, (n.d.).

[105] R.C. Chen, L. Rigon, R. Longo, Comparison of single distance phase retrieval algorithms by considering different object composition and the effect of statistical and structural noise., Opt. Express. 21 (2013) 7384–99. doi:10.1364/OE.21.007384.

[106] S. Mohammadi, E. Larsson, F. Alves, S. Dal Monego, S. Biffi, C. Garrovo, A. Lorenzon, G. Tromba, C. Dullin, Quantitative evaluation of a single-distance phase-retrieval method applied on in-line phase-contrast images of a mouse lung, J. Synchrotron Radiat. 21 (2014) 784–789. doi:10.1107/S1600577514009333.

[107] T.E. Gureyev, T.J. Davis, A. Pogany, S.C. Mayo, S.W. Wilkins, Optical phase retrieval by use of First Born- and Rytov-type approximations, Appl. Opt. 43 (2004) 2418–2430. doi:10.1364/AO.43.002418.

[108] Y. De Witte, M. Boone, J. Vlassenbroeck, M. Dierick, The Bronnikov Aided Correction for X-ray Computed Tomography, 710 (2007) 239–244.

[109] a Groso, R. Abela, M. Stampanoni, Implementation of a fast method for high resolution phase contrast tomography., Opt. Express. 14 (2006) 8103–10. doi:10.1364/OE.14.008103.

[110] R.C. Chen, H.L. Xie, L. Rigon, R. Longo, E. Castelli, T.Q. Xiao, Phase retrieval in quantitative x-ray microtomography with a single sample-to-detector distance., Opt. Lett. 36 (2011) 1719–1721. doi:10.1364/OL.36.001719.

[111] T. Weitkamp, D. Haas, D. Wegrzynek, A. Rack, ANKAphase: Software for single-distance phase retrieval from inline X-ray phase-contrast radiographs, J. Synchrotron Radiat. 18 (2011) 617–629. doi:10.1107/S0909049511002895.

[112] X. Wu, H. Liu, X-Ray cone-beam phase tomography formulas based on phase-attenuation duality., Opt. Express. 13 (2005) 6000–6014. doi:10.1364/OPEX.13.006000.

[113] K. Nugent, T. Gureyev, D. Cookson, D. Paganin, Z. Barnea, Quantitative Phase Imaging Using Hard X Rays, Phys. Rev. Lett. 77 (1996) 2961–2964. doi:10.1103/PhysRevLett.77.2961.

[114] T.E. Gureyev, A.W. Stevenson, D.M. Paganin, Quantitative analysis of two-component samples using in-line hard X-ray images research papers, Imaging. (2002) 148–153.

[115] X. Wu, H. Liu, A. Yan, X-ray phase-attenuation duality and phase retrieval., Opt. Lett. 30 (2005) 379–381. doi:10.1364/OL.30.000379.

[116] D. Dreossi, L. Mancini, R. Menk, L. Rigon, T.Q. Xiao, R. Longo, Manual (2013.04), 19 (2013) 836–845.

[117] J. Moosmann, V. Altapova, L. Helfen, from single-distance radiographs applied to developmental stages of Xenopus laevis, (n.d.).

[118] K. Krug, L. Porra, P. Coan, A. Wallert, J. Dik, A. Coerdt, A. Bravin, M. Elyyan, P. Reischig, L. Helfen, T. Baumbach, Relics in medieval altarpieces? Combining X-ray tomographic, laminographic and phase-contrast imaging to visualize thin organic objects in paintings, J. Synchrotron Radiat. 15 (2007) 55–61. doi:10.1107/S0909049507045438.

[119] A.J. Moffat, P. Wright, L. Helfen, T. Baumbach, G. Johnson, S.M. Spearing, I. Sinclair, In situ synchrotron computed laminography of damage in carbon fibre-epoxy [90/0]s laminates, Scr. Mater. 62 (2010) 97–100. doi:10.1016/j.scriptamat.2009.09.027.

[120] V.C. Sahni, S.-P. Chia, K. Ratnavelu, M.R. Muhamad, Status of The Indian SRS Indus-2, in: AIP Conf. Proc., AIP, 2009: pp. 180–187. doi:10.1063/1.3192234.

[121] V.K. Raghuvanshi, V.P. Dhamgaye, A.K. Singh, R. V. Nandedkar, Design and Development of Front-end components of Indus-2 Bending Magnet Beamlines, in: AIP Conf. Proc., AIP, 2007: pp. 631–634. doi:10.1063/1.2436140.

[122] M.K. Tiwari, P. Gupta, A.K. Sinha, S.R. Kane, A.K. Singh, S.R. Garg, C.K. Garg, G.S. Lodha, S.K. Deb, A microfocus X-ray fluorescence beamline at Indus-2 synchrotron radiation facility., J. Synchrotron Radiat. 20 (2013) 386–9. doi:10.1107/S0909049513001337.

[123] E.-E. Koch, Handbook on synchrotron radiation, Volume 1, Part 2, North Holland Pub. Co., 1983.

[124] M. Sánchez del Río, R.J. Dejus, XOP v2. 4: recent developments of the x-ray optics software toolkit, in: M. Sanchez del Rio, O. Chubar (Eds.), SPIE Opt. …, International Society for Optics and Photonics, 2011: pp. 814115-814115–5. doi:10.1117/12.893911.

[125] P.J. Schilling, E. Morikawa, H. Tolentino, E. Tamura, R.L. Kurtz, C. Cusatis, Installation and operation of the LNLS double-crystal monochromator at CAMD, Rev. Sci. Instrum. 66 (1995) 2214. doi:10.1063/1.1145710.

[126] L. Salvo, M. Su??ry, A. Marmottant, N. Limodin, D. Bernard, 3D imaging in material science: Application of X-ray tomography, Comptes Rendus Phys. 11 (2010) 641–649. doi:10.1016/j.crhy.2010.12.003.

[127] S.R. Stock, Recent advances in X-ray microtomography applied to materials, Int.

Mater. Rev. 53 (2008) 129–181. doi:10.1179/174328008X277803.

[128] A. Limaye, Drishti: a volume exploration and presentation tool, in: S.R. Stock (Ed.), Proc. SPIE - Int. Soc. Opt. Eng., 2012: p. 85060X. doi:10.1117/12.935640.

[129] E. Roessl, A. Thran, G. Martens, T. Istel, R. Proksa, J. Schlomka, Dual-energy x-ray imaging by simultaneous integration and campbelling readout, in: IEEE Nucl. Sci. Symp. Med. Imaging Conf., IEEE, 2010: pp. 2112–2115. doi:10.1109/NSSMIC.2010.5874151.

[130] S. Preibisch, S. Saalfeld, P. Tomancak, Globally optimal stitching of tiled 3D microscopic image acquisitions., Bioinformatics. 25 (2009) 1463–5. doi:10.1093/bioinformatics/btp184.

[131] K.K. Mishra, A.I. Hawari, Phase contrast neutron imaging at a medium intensity neutron source, in: 2009 IEEE Nucl. Sci. Symp. Conf. Rec., IEEE, 2009: pp. 1283–1288. doi:10.1109/NSSMIC.2009.5402356.

[132] W. Treimer, M. Strobl, A. Hilger, C. Seifert, U. Feye-Treimer, Refraction as imaging signal for computerized (neutron) tomography, Appl. Phys. Lett. 83 (2003) 398–400. doi:10.1063/1.1591066.

[133] F. Pfeiffer, C. Grünzweig, O. Bunk, G. Frei, E. Lehmann, C. David, Neutron phase imaging and tomography., Phys. Rev. Lett. 96 (2006) 215505. doi:10.1103/PhysRevLett.96.215505.

[134] B.E. Allman, P.J. McMahon, K.A. Nugent, D. Paganin, D.L. Jacobson, M. Arif, S.A. Werner, Phase radiography with neutrons., Nature. 408 (2000) 158–9. doi:10.1038/35041626.

[135] B.E. Allman, K.A. Nugent, Phase imaging with thermal neutrons, Phys. B Condens. Matter. 385–386 (2006) 1395–1401. doi:10.1016/j.physb.2006.05.203.

[136] N. Kardjilov, S.W. Lee, E. Lehmann, I.C. Lim, E. Steichele, C.M. Sim, P. Vontobel, Applied phase-contrast radiography with polychromatic thermal neutrons, in: Key Eng. Mater., 2004: pp. 1330–1336.

[137] E. Lehmann, K. Lorenz, E. Steichele, P. Vontobel, Non-destructive testing with neutron phase contrast imaging, Nucl. Instruments Methods Phys. Res. Sect. A Accel. Spectrometers, Detect. Assoc. Equip. 542 (2005) 95–99. doi:10.1016/j.nima.2005.01.293.

[138] R.H. MORGAN, The frequency response function. A valuable means of expressing the informational recording capability of diagnostic x-ray systems., Am. J. Roentgenol. Radium Ther. Nucl. Med. 88 (1962) 175–186.

[139] P.R. Vaidya, Use of modulation transfer function in the determination of focal spot dimensions, Insight Non-Destructive Test. Cond. Monit. 42 (2000) 323–326.

[140] I.V. Dulera, R.K. Sinha, High temperature reactors, J. Nucl. Mater. 383 (2008) 183–188. doi:10.1016/j.jnucmat.2008.08.056.

[141] R.K. Sinha, I. V Dulera, Carbon based materials – applications in high temperature nuclear reactors, Indian J. Eng. Mater. Sci. 17 (2010) 321–326.

[142] Q. Zhu, X. Qiu, C. Ma, Oxidation resistant SiC coating for graphite materials, Carbon N. Y. 37 (1999) 1475–1484. doi:10.1016/S0008-6223(99)00010-X.

[143] X. Yang, Q.Z. Huang, Y.H. Zou, X. Chang, Z. an Su, M.Y. Zhang, Z.Y. Xie, Anti-oxidation behavior of chemical vapor reaction SiC coatings on different carbon materials at high temperatures, Trans. Nonferrous Met. Soc. China (English Ed. 19 (2009) 1044–1050. doi:10.1016/S1003-6326(08)60404-5.

[144] J. Chin, P.K. Gantzel, R.G. Hudson, The structure of chemical vapor deposited silicon carbide, Thin Solid Films. 40 (1977) 57–72. doi:10.1016/0040-6090(77)90103-1.

[145] R. Venugopalan, J. Prakash, J. Nuwad, C.G.S. Pillai, A.K. Tyagi, S. Dakshinamoorthy, Morphological study of SiC coating developed on 2D carbon composites using MTS precursor in a hot-wall vertical reactor, Int. J. Mater. Res. (Formerly Zeitschrift Fuer Met. 103 (2012) 1251–1256. doi:10.3139/146.110759.

[146] T. Kaneko, H. Sone, N. Miyakawa, M. Naka, Growth kinetics of silicon carbide chemical vapor deposition from methyltrichlorosilane, Japanese J. Appl. Physics, Part 1 Regul. Pap. Short Notes Rev. Pap. 38 (1999) 2089–2091.

[147] H. Sone, T. Kaneko, N. Miyakawa, In situ measurements and growth kinetics of silicon carbide chemical vapor deposition from methyltrichlorosilane, J. Cryst. Growth. 219 (2000) 245–252. doi:10.1016/S0022-0248(00)00616-3.

[148] C. Lu, L. Cheng, C. Zhao, L. Zhang, Y. Xu, Kinetics of chemical vapor deposition of SiC from methyltrichlorosilane and hydrogen, Appl. Surf. Sci. 255 (2009) 7495–7499. doi:10.1016/j.apsusc.2009.03.069.

[149] S.R. Stock, X-ray microtomography of materials, Int. Mater. Rev. 44 (1999) 141–164. doi:10.1179/095066099101528261.

[150] L. Salvo, P. Cloetens, E. Maire, S. Zabler, J.J. Blandin, J.Y. Buffi??re, W. Ludwig, E. Boller, D. Bellet, C. Josserond, X-ray micro-tomography an attractive characterisation technique in materials science, Nucl. Instruments

Methods Phys. Res. Sect. B Beam Interact. with Mater. Atoms. 200 (2003) 273–286. doi:10.1016/S0168-583X(02)01689-0.

[151] B.D. Metscher, Biological applications of X-ray microtomography: imaging micro- anatomy, molecular expression and organismal diversity, Microsc. Anal. 27 (2013) 13–16.

[152] G. Perfetti, E. Van De Casteele, B. Rieger, W.J. Wildeboer, G.M.H.H. Meesters, X-ray micro tomography and image analysis as complementary methods for morphological characterization and coating thickness measurement of coated particles, Adv. Powder Technol. 21 (2010) 663–675. doi:10.1016/j.apt.2010.08.002.

[153] B. Crean, A. Parker, D. Le Roux, M. Perkins, S.Y. Luk, S.R. Banks, C.D. Melia, C.J. Roberts, Elucidation of the internal physical and chemical microstructure of pharmaceutical granules using X-ray micro-computed tomography, Raman microscopy and infrared spectroscopy, Eur. J. Pharm. Biopharm. 76 (2010) 498–506. doi:10.1016/j.ejpb.2010.08.006.

[154] F. Sondej, A. Bück, K. Koslowsky, P. Bachmann, M. Jacob, E. Tsotsas, Investigation of coating layer morphology by micro-computed X-ray tomography, Powder Technol. 273 (2015) 165–175. doi:10.1016/j.powtec.2014.12.050.

[155] J. Van den Bulcke, M. Boone, J. Van Acker, L. Van Hoorebeke, Three-dimensional x-ray imaging and analysis of fungi on and in wood., Microsc. Microanal. 15 (2009) 395–402. doi:10.1017/S1431927609990419.

[156] S. Noguchi, R. Kajihara, Y. Iwao, Y. Fujinami, Y. Suzuki, Y. Terada, K. Uesugi, K. Miura, S. Itai, Investigation of internal structure of fine granules by microtomography using synchrotron X-ray radiation, Int. J. Pharm. 445 (2013) 93–98. doi:10.1016/j.ijpharm.2013.01.048.

[157] C.A. Schneider, W.S. Rasband, K.W. Eliceiri, NIH Image to ImageJ: 25 years of image analysis, Nat. Methods. 9 (2012) 671–675. doi:10.1038/nmeth.2089.

[158] R.G. Gordon, S. Barry, J.T. Barton, R.N.R. Broomhall-Dillard, Atmospheric pressure chemical vapor deposition of electrochromic tungsten oxide films, Thin Solid Films. 392 (2001) 231–235. doi:10.1016/S0040-6090(01)01033-1.

[159] R. Brütsch, Chemical vapour deposition of silicon carbide and its applications, Thin Solid Films. 126 (1985) 313–318. doi:10.1016/0040-6090(85)90326-8.

[160] Y.S. Kashyap, T. Roy, P.S. Sarkar, P.S. Yadav, M. Shukla, A. Sinha, K. Dasgupta, D. Sathiyamoorthy, Characterization of pyrocarbon coated materials using laboratory based x-ray phase contrast imaging technique, Rev. Sci.

Instrum. 78 (2007) 1–6. doi:10.1063/1.2772780.

[161] H. Miao, H. Zhao, F. Gao, S. Gong, Implementation of FDK Reconstruction Algorithm in Cone-Beam CT Based on the 3D Shepp-Logan Model, in: 2009 2nd Int. Conf. Biomed. Eng. Informatics, IEEE, 2009: pp. 1–5. doi:10.1109/BMEI.2009.5304987.

[162] D. Barbash, J.E. Fulghum, J. Yang, L. Felton, A novel imaging technique to investigate the influence of atomization air pressure on film-tablet interfacial thickness., Drug Dev. Ind. Pharm. 35 (2009) 480–6. doi:10.1080/03639040802438381.

[163] M. Andersson, B. Holmquist, J. Lindquist, O. Nilsson, K.-G. Wahlund, Analysis of film coating thickness and surface area of pharmaceutical pellets using fluorescence microscopy and image analysis, J. Pharm. Biomed. Anal. 22 (2000) 325–339. doi:10.1016/S0731-7085(99)00289-7.

[164] D.-J. Kim, D.-J. Choi, Y.-W. Kim, Effect of reactant depletion on the microstructure and preferred orientation of polycrystalline SiC films by chemical vapor deposition, Thin Solid Films. 266 (1995) 192–197. doi:10.1016/0040-6090(96)80023-X.

[165] K. Choy, Chemical vapour deposition of coatings, Prog. Mater. Sci. 48 (2003) 57–170. doi:10.1016/S0079-6425(01)00009-3.

[166] T. Kingetsu, M. Takehara, T. Yarii, K. Ito, H. Masumoto, Correlation between the oxidation behavior and the microstructure of SiC coatings deposited on graphite substrates via chemical vapor deposition, Thin Solid Films. 315 (1998) 139–143. doi:10.1016/S0040-6090(97)00363-5.

[167] G. Sun, H. Li, Q. Fu, M. Huang, W. Cao, H. Wu, Finite element simulation of the effects of process parameters on deposition uniformity of chemical-vapor-deposited silicon carbide, Comput. Mater. Sci. 46 (2009) 1002–1006. doi:10.1016/j.commatsci.2009.05.005.

[168] K. Dasgupta, M. Roy, a Tyagi, S. Kulshreshtha, R. Venugopalan, D. Sathiyamoorthy, Novel isotropic high-density amorphous carbon composites for moderator applications in low-temperature thermal reactors, Compos. Sci. Technol. 67 (2007) 1794–1801. doi:10.1016/j.compscitech.2006.10.026.

[169] R. Venugopalan, D. Sathiyamoorthy, ARTICLE Development of Carbon / Carbon Composites for Nuclear Reactor Applications BRIEF COMMUNICATION, (2012).

[170] J. Prakash, R. Venugopalan, B. Paul, J. Bahadur, S.K. Ghosh, D. Sathiyamoorthy, Study of thermal degradation behavior of dense and

nanostructured silicon carbide coated carbon fibers in oxidative environments, Corros. Sci. 67 (2013) 142–151. doi:10.1016/j.corsci.2012.10.015.

[171] A.T. DeLaRiva, T.W. Hansen, S.R. Challa, A.K. Datye, In situ Transmission Electron Microscopy of catalyst sintering, J. Catal. 308 (2013) 291–305. doi:10.1016/j.jcat.2013.08.018.

[172] Y.S. Kashyap, P.S. Yadav, P.S. Sarkar, a. Agrawal, T. Roy, A. Sinha, K. Dasgupta, D. Sathiyamoorthy, Application of X-ray phase-contrast imaging technique in the study of pyrocarbon-coated zirconia kernels, NDT E Int. 42 (2009) 384–388. doi:10.1016/j.ndteint.2009.01.004.

[173] Y.S. Kashyap, P.S. Yadav, T. Roy, P.S. Sarkar, M. Shukla, A. Sinha, Laboratory-based X-ray phase-contrast imaging technique for material and medical science applications., Appl. Radiat. Isot. 66 (2008) 1083–90. doi:10.1016/j.apradiso.2007.12.008.

[174] D.S. Grzegorczyk, G. Carta, Adsorption of amino acids on porous polymeric adsorbents—II. Intraparticle mass transfer, Chem. Eng. Sci. 51 (1996) 819–826. doi:10.1016/0009-2509(95)00290-1.

[175] K.K. Yadav, K. Dasgupta, D.K. Singh, L. Varshney, H. Singh, Dysprosium sorption by polymeric composite bead: Robust parametric optimization using Taguchi method, J. Chromatogr. A. 1384 (2015) 37–43. doi:10.1016/j.chroma.2015.01.061.

[176] C. Dwivedi, A. Kumar, J.K. Ajish, K.K. Singh, M. Kumar, P.K. Wattal, P.N. Bajaj, Resorcinol-formaldehyde coated XAD resin beads for removal of cesium ions from radioactive waste: synthesis, sorption and kinetic studies, RSC Adv. 2 (2012) 5557. doi:10.1039/c2ra20054f.

[177] H. Yasuda, H. Tamai, M. Ikeuchi, S. Kojima, Extremely large mesoporous carbon fibers synthesized by the addition of rare earth metal complexes and their unique adsorption behaviors, Adv. Mater. 9 (1997) 55–58. doi:10.1002/adma.19970090112.

[178] S. Lim, K. Suh, Y. Kim, M. Yoon, H. Park, D.N. Dybtsev, K. Kim, Porous carbon materials with a controllable surface area synthesized from metal-organic frameworks., Chem. Commun. (Camb). 48 (2012) 7447–9. doi:10.1039/c2cc33439a.

[179] I. Kruusenberg, N. Alexeyeva, K. Tammeveski, The pH-dependence of oxygen reduction on multi-walled carbon nanotube modified glassy carbon electrodes, Carbon N. Y. 47 (2009) 651–658. doi:10.1016/j.carbon.2008.10.032.

[180] K.-K. Park, J.-B. Lee, P.-Y. Park, S.-W. Yoon, J.-S. Moon, H.-M. Eum, C.-W.

Lee, Development of a carbon sheet electrode for electrosorption desalination, Desalination. 206 (2007) 86–91. doi:10.1016/j.desal.2006.04.051.

[181] K.K. Yadav, D.K. Singh, M. Anitha, L. Varshney, H. Singh, Studies on separation of rare earths from aqueous media by polyethersulfone beads containing D2EHPA as extractant, Sep. Purif. Technol. 118 (2013) 350–358. doi:10.1016/j.seppur.2013.07.012.

[182] K.K. Singh, R. Ruhela, A. Das, M. Kumar, A.K. Singh, R.C. Hubli, P.N. Bajaj, Separation and recovery of palladium from spent automobile catalyst dissolver solution using dithiodiglycolamide encapsulated polymeric beads, J. Environ. Chem. Eng. 3 (2015) 95–103. doi:10.1016/j.jece.2014.11.002.

[183] D. Ag, Methods for Cell Structure Analysis of Polyurethane Foams, Magn. Reson. Imaging. (n.d.).

[184] M. Thirumal, D. Khastgir, G.B. Nando, Y.P. Naik, N.K. Singha, Halogen-free flame retardant PUF: Effect of melamine compounds on mechanical, thermal and flame retardant properties, Polym. Degrad. Stab. 95 (2010) 1138–1145. doi:10.1016/j.polymdegradstab.2010.01.035.

[185] M. Thirumal, D. Khastgir, N.K. Singha, B.S. Manjunath, Y.P. Naik, Effect of foam density on the properties of water blown rigid polyurethane foam, J. Appl. Polym. Sci. 108 (2008) 1810–1817. doi:10.1002/app.27712.

[186] P.D. Edmondson, Y. Zhang, S. Moll, F. Namavar, W.J. Weber, Irradiation effects on microstructure change in nanocrystalline ceria - Phase, lattice stress, grain size and boundaries, Acta Mater. 60 (2012) 5408–5416. doi:10.1016/j.actamat.2012.07.010.

[187] C.K. Saurabh, S. Gupta, J. Bahadur, S. Mazumder, P.S. Variyar, A. Sharma, Radiation dose dependent change in physiochemical, mechanical and barrier properties of guar gum based films, Carbohydr. Polym. 98 (2013) 1610–1617. doi:10.1016/j.carbpol.2013.07.041.

[188] W.B. Herppich, U. Matsushima, W.G. Graf, S. Zabler, M. Dawson, G. Choinka, I. Manke, Synchrotron X-ray CT of rose peduncles - evaluation of tissue damage by radiation, Mater. Test. 57 (2015) 59–63. doi:10.3139/120.110675.

[189] J. Mackerle, Metal matrix composites : ÿnite element and boundary element analyses A bibliography (1997 – 2000), 38 (2002) 659–667.

[190] C. Chateau, L. Gélébart, M. Bornert, J. Crépin, E. Boller, C. Sauder, W. Ludwig, In situ X-ray microtomography characterization of damage in SiCf/SiC minicomposites, Compos. Sci. Technol. 71 (2011) 916–924. doi:10.1016/j.compscitech.2011.02.008.

[191] J.J. Williams, Z. Flom, A.A. Amell, N. Chawla, X. Xiao, F. De Carlo, Damage evolution in SiC particle reinforced Al alloy matrix composites by X-ray synchrotron tomography, Acta Mater. 58 (2010) 6194–6205. doi:10.1016/j.actamat.2010.07.039.

[192] H.M. Zakaria, Microstructural and corrosion behavior of Al/SiC metal matrix composites, Ain Shams Eng. J. 5 (2014) 831–838. doi:10.1016/j.asej.2014.03.003.

[193] J. Martín-Herrero, C. Germain, Microstructure reconstruction of fibrous C/C composites from X-ray microtomography, Carbon N. Y. 45 (2007) 1242–1253. doi:10.1016/j.carbon.2007.01.021.

[194] Y. Feng, Z. Feng, S. Li, W. Zhang, X. Luan, Y. Liu, L. Cheng, L. Zhang, Micro-CT characterization on porosity structure of 3D Cf/ SiCm composite, Compos. Part A Appl. Sci. Manuf. 42 (2011) 1645–1650. doi:10.1016/j.compositesa.2011.07.015.

[195] H. Crostack, J. Nellesen, F. Beckmann, G. Fischer, Porosity analysis of thermally sprayed mullite utilizing synchrotron radiation based microtomography pore SiC Mullite inclusions Mullite SiC, (n.d.) 2–3.

[196] M. De Giovanni, J.M. Warnett, M.A. Williams, N. Haribabu, P. Srirangam, X-ray tomography investigation of intensive sheared Al–SiC metal matrix composites, Mater. Charact. 110 (2015) 258–263. doi:10.1016/j.matchar.2015.11.003.

[197] B. Drach, I. Tsukrov, T. Gross, S. Dietrich, K. Weidenmann, R. Piat, T. Böhlke, Numerical modeling of carbon/carbon composites with nanotextured matrix and 3D pores of irregular shapes, Int. J. Solids Struct. 48 (2011) 2447–2457. doi:10.1016/j.ijsolstr.2011.04.021.

[198] B. Drach, A. Drach, I. Tsukrov, Prediction of the effective elastic moduli of materials with irregularly-shaped pores based on the pore projected areas, Int. J. Solids Struct. 51 (2014) 2687–2695. doi:10.1016/j.ijsolstr.2014.03.042.

[199] S. Hernández, F. Sket, C. González, J. Llorca, Optimization of curing cycle in carbon fiber-reinforced laminates: Void distribution and mechanical properties, Compos. Sci. Technol. 85 (2013) 73–82. doi:10.1016/j.compscitech.2013.06.005.

[200] R. Seltzer, C. González, R. Muñoz, J. Llorca, T. Blanco-Varela, X-ray microtomography analysis of the damage micromechanisms in 3D woven composites under low-velocity impact, Compos. Part A Appl. Sci. Manuf. 45 (2013) 49–60. doi:10.1016/j.compositesa.2012.09.017.

[201] R. Muñoz, V. Martínez, F. Sket, C. González, J. Llorca, Mechanical behavior and failure micromechanisms of hybrid 3D woven composites in tension, Compos. Part A Appl. Sci. Manuf. 59 (2014) 93–104. doi:10.1016/j.compositesa.2014.01.003.

[202] R.. Singh, R. Kishore, T.. Sinha, B.. Kashyap, Hydride blister formation in Zr–2.5wt%Nb pressure tube alloy, J. Nucl. Mater. 301 (2002) 153–164. doi:10.1016/S0022-3115(02)00708-0.

[203] R.. Singh, R. Kishore, T.. Sinha, S. Banerjee, B.. Kashyap, Stress field estimation around a semi-constrained inclusion and its validation by interpreting hydride platelet orientation around a blister in a Zr–2.5Nb alloy, Mater. Sci. Eng. A. 339 (2003) 17–28. doi:10.1016/S0921-5093(02)00115-6.

[204] J.L. Singh, S. Kumar, R. Keswani, S. Muralidhar, A.K. Sengupta, H.N. Singh, K.C. Sahoo, Calandria Tube Contact Location By Ultrasonic Velocity Ratio Measurement Technique, (n.d.).

[205] R. Yasuda, M. Nakata, M. Matsubayashi, K. Harada, Y. Hatakeyama, H. Amano, Application of hydrogen analysis by neutron imaging plate method to Zr-alloy cladding tubes, J. Nucl. Mater. 320 (2003) 223–230. doi:10.1016/S0022-3115(03)00112-0.

[206] E. Sváb, G. Mészáros, Z. Somogyvári, M. Balaskó, F. Körösi, Neutron imaging of Zr-1%Nb fuel cladding material containing hydrogen., Appl. Radiat. Isot. 61 (2004) 471–7. doi:10.1016/j.apradiso.2004.03.072.

[207] Principles of Computerized Tomographic Imaging (Classics in Applied Mathematics): Aninash C. Kak, Malcolm Slaney: 9780898714944: Amazon.com: Books, (n.d.).

[208] Advisory Material for the IAEA Regulations for the Safe Transport of Radioactive Material, (n.d.).

[209] C. Gau, R. Viskanta, Melting and Solidification of a Pure Metal on a Vertical Wall, J. Heat Transfer. 108 (1986) 174. doi:10.1115/1.3246884.

[210] C. Gau, R. Viskanta, Melting and solidification of a metal system in a rectangular cavity, Int. J. Heat Mass Transf. 27 (1984) 113–123. doi:10.1016/0017-9310(84)90243-6.

[211] X. Wang, Y. Fautrelle, An investigation of the influence of natural convection on tin solidification using a quasi two-dimensional experimental benchmark, Int. J. Heat Mass Transf. 52 (2009) 5624–5633. doi:10.1016/j.ijheatmasstransfer.2009.05.030.

[212] J. Szekely, P.S. Chhabra, The effect of natural convection on the shape and movement of the melt-solid interface in the controlled solidification of lead, Metall. Mater. Trans. 1 (1970) 1195–1203. doi:10.1007/BF02900231.

[213] T.E. Gureyev, Y.I. Nesterets, D.M. Paganin, A. Pogany, S.W. Wilkins, Linear algorithms for phase retrieval in the Fresnel region. 2. Partially coherent illumination, Opt. Commun. 259 (2006) 569–580. doi:10.1016/j.optcom.2005.09.072.

9 APPENDICES

Appendix 1: Interaction of X-ray and neutron with matter 244

Appendix 2: Theory of Tomography reconstruction 250

Appendix 3: Parameters of image quality 254

APPENDIX 1: INTERACTION OF X-RAY AND NEUTRON WITH MATTER

X-rays and neutrons, being fundamentally different probes, differ in their way of interaction with matter and provide complementary information in imaging applications. Study of their interaction with matter plays a very important role in development and application of advanced imaging techniques. Sensitivity of X-ray and neutron imaging to various object properties also relies on their interaction modes to the material. Apart from this, design and development of advanced optics and detectors for them are also decided based on their modes of interaction with matter.

a) X-ray interaction

In the hard X-rays energy range (10–150 keV), photoelectric absorption, Compton scattering, and Rayleigh scattering are the three main interaction mechanisms relevant for X-ray imaging applications. Photoelectric absorption is the dominant effect contributing to the attenuation of X-rays in absorption-based transmission imaging at lower energy range (below approx. 25keV). The interaction cross-section of the photoelectric effect is approximately proportional to Z^4/E^3 (Z is the atomic number) and thus decays rapidly at higher energies. Secondary particles ejected in photoelectric absorption like photoelectrons, fluorescence photons and Auger electrons are used in photoelectron microscopy (PEEM) and fluorescence microscopy for elemental mapping and detection of trace elements with very high sensitivity. Compton scattering or incoherent scattering is nearly independent of atomic number Z and considered a serious source of noise in imaging. The attenuation cross section becomes more

dominated by Compton scattering at higher energies as its contribution to X-ray attenuation decreases slower than photoelectric absorption as a function of energy. Rayleigh scattering is the coherent elastic scattering having the dominant effect to the phase shift whereas its contribution to attenuation is mostly negligible.

The most general formulation of X-ray interaction with matter is given by quantum theory of electromagnetic radiation however; a simplified explanation of important modes of interactions can be derived using high frequency approximation of dispersion in the perspectives of Maxwell's classical electromagnetic theory. In this formulation, X-rays considered as electromagnetic waves incident on atomic electrons and force them to oscillate around their equilibrium position. This motion can be described as a series of damped harmonic oscillators with the oscillatory electric field of the incident X-ray as the driving force. The electric susceptibility of the medium χ_e is given by

$$\boldsymbol{\chi_e = \frac{n_a e^2}{m_e \varepsilon_0} \sum_j \frac{F_j}{\omega_j^2 - \omega^2 - i\gamma_j \omega} = \frac{n_a r_e e^2}{4\pi^2 \varepsilon_0} \sum_j \frac{\omega^2 F_j}{\omega_j^2 - \omega^2 - i\gamma_j \omega}} \quad (9.1)$$

Where r_e is the classical electron radius, n_a is the number of atoms per unit volume and summation is extended over all the atoms of oscillator. It is also assumed that each oscillator has strength F_j damping constant γ_j and binding energy ω_j. The sum over all the oscillator strength is assumed to be equal to the atomic number Z of the atom. For X-rays, the frequency of the incident wave is much higher than the resonant frequency of most of the oscillators ($\omega \gg \omega_j$) i.e. the incident photon energy is much higher than the electron binding energies. In addition to that, the absorption per wavelength for X-rays is negligible. Therefore the damping constants are generally small ($\gamma/\omega \ll 1$) and can be neglected. The refractive index of the material

is defined as ratio of wave vector in material medium to that in vacuum; hence, we can write the following relation:

$$n = \frac{k}{k_0} = \frac{\sqrt{\mu\varepsilon}}{\sqrt{\mu_0\epsilon_0}} = \sqrt{(1 + \chi_e)(1 + \chi_m)} \quad (9.2)$$

$$= \sqrt{\mathbf{1} + \boldsymbol{\chi_e}} = \mathbf{1} + \frac{\mathbf{1}}{\mathbf{2}}\boldsymbol{\chi_e} + \cdots \ldots \quad (9.3)$$

Where $\mu = \mu_0(1 + \chi_m)$ and $\epsilon = \epsilon_0(1 + \chi_e)$. As the electric susceptibility (χ_e) is small compared to unity, while magnetic susceptibility (χ_m) is even smaller and hence it was neglected, in arriving at above relation. After putting Eq. (9.1) in the above equation we obtain, the refractive index of the material is

$$\boldsymbol{n = 1 - \frac{1}{2}\frac{n_e r_e e^2 \lambda^2}{4\pi^2 \varepsilon_0} \sum_j F_j} \quad (9.4)$$

For X-rays the equation is generally separated in real and imaginary arguments for the purpose of experimental convenience as shown below

$$\boldsymbol{n = 1 - \delta + i\beta = 1 - \frac{n_e r_e \lambda^2}{2\pi}(f_1 + if_2)} \quad (9.5)$$

Where $\boldsymbol{\delta = \frac{n_e r_e \lambda^2}{2\pi} f_1}$ and $\boldsymbol{\beta = \frac{n_e r_e \lambda^2}{2\pi} f_2}$ (9.6)

The quantity $f = f_1 + if_2$ is known as effective atomic scattering factor. $f_1 \propto Z$ is responsible for phase shift and is dependent upon electron number density whereas $f_2 \propto \mu$ is responsible for the attenuation. This result shows that the phase differences can be easily detected by measuring the scattering in the forward direction and hence it can be combined with the scheme of conventional X-ray imaging techniques to give spatially resolved distribution of electron density or complex refractive index of the material. The wavelength dependent dispersion corrections f_1 and f_2 show resonance

effects near X-ray absorption edges where strong changes in the phase and the amplitude of the scattered wave occur and allow dual energy imaging.

b) Neutron interaction

Neutron interaction, primarily with the nucleus, is either by scattering or absorption. In case of absorption, neutron is absorbed by a nucleus resulting in an unstable, radioactive nucleus that decays with a particular half-life. As the nucleus decays, it may emit a variety of secondary radiation, including α particle, β-particle, γ-rays, neutrons and others heavy ions with different probability of occurrence. On the other hand, scattering process can be further classified in to coherent and incoherent components. Coherent and incoherent scattering process may be elastic if there is no exchange of energy with sample atoms, or inelastic if it is with either gain or loss of energy. Neutron also carries a magnetic moment that can interact with magnetic fields produced by unpaired electrons in materials and scattered out of an incident beam. All of these scattering and absorption processes contribute to the attenuation of the incident neutron beam and give rise to contrast, which can be used for real-space imaging. The strength of the scattering cross section varies non-uniformly across the periodic table and depends not only on the individual element but also on the particular isotope of that element. The total microscopic interaction cross section of neutron is written as the sum of individual scattering and absorption cross sections. The scattering cross sections in the epithermal, thermal, and cold neutron energy ranges have energy dependence however in practice, they are typically taken as constant. Propagation and interaction of neutrons with matter is formulated through quantum theory and Schrodinger equation.

$$\left(-\frac{\hbar^2}{2\mathrm{m}}\nabla^2 + \mathrm{V(r,t)}\right)\Psi(\mathrm{r,t}) = \mathrm{i}\hbar\,\partial_{\mathrm{t}}\Psi(\mathrm{r,t}) \tag{9.7}$$

Depending upon the kind of interactions, different potential are used. For an adiabatic motion in a spatially dependent potential V(r), the wave function ψ(r,t) can be seperated in a time independent and time dependent part $\Psi(r,t) = \Psi(r)e^{-i\omega t}$ where ψ(r) satisfies time independent shrodingeer equation.

$$-\frac{\hbar^2}{2m}\nabla^2\Psi(\mathbf{r}) + V(\mathbf{r})\Psi(\mathbf{r}) = E\,\Psi(\mathbf{r}) \tag{9.8}$$

Where E = ħω is the energy of neutron. This is well known Helmholtz equation also called wave equation i.e. neutron in a time independent field satisfies wave equation.

$$\nabla^2\Psi(r) + \mathbf{K}^2(r)\Psi(r) = 0 \tag{9.9}$$

The refractive index of material is defined as the ratio of spatially dependent wave vectors K(r) to free space wave vector k

$$n(\mathbf{r}) = \frac{\mathbf{K(r)}}{k} = \sqrt{1 - \frac{\mathrm{V(r)}}{E}} \tag{9.10}$$

Where wave vectors for medium are defined by $\mathbf{K}^2(\mathbf{r}) = \frac{2m}{\hbar^2}[\mathrm{E} - \mathrm{V}(\mathbf{r})]$ and for vacuum, it is given by $\mathbf{k}^2 = \frac{2m}{\hbar^2}\mathrm{E}$. For neutron-nucleus interaction, the motion is described by Fermi pseudo potential i.e.

$$V(r) = \sum_j \frac{2\pi\hbar^2}{m}\,\mathrm{b}\,\delta(\mathrm{r} - \mathrm{r_j}) \tag{9.11}$$

Averaged over a macroscopic volume for non-magnetic material with atomic density N and bound coherent scattering length b_c this gives the effective optical potential

$$V(r) = \frac{2\pi\hbar^2}{m}b_c N \tag{9.12}$$

If absorption and incoherent scattering is also included in the neutron-nuclear interaction, the scattering length is a complex value and refractive index is given by

$$n = 1 - \frac{\lambda^2 N}{2\pi}\sqrt{b_c^2 - \left(\frac{\sigma_r}{2\lambda}\right)^2} + i\frac{\sigma_r N\lambda}{4\pi}\ where \tag{9.13}$$

$\sigma_r = \sigma_a + \sigma_i$ is the total interaction cross section

$$n = 1 - \delta + i\beta \tag{9.14}$$

This equation (9.14) is exactly similar to the expression obtained for X-rays (9.5). Therefore we find that X-ray and neutron interaction with matter, being different at fundamental scale is similar at macroscopic scale and can be formulated in terms of their complex refractive index. When passed through matter, X-rays and neutron undergo reflection, refraction, diffraction, attenuation and scattering phenomena, which are well described by various components of their complex refractive indices. Hence, X-ray and neutron imaging can be formulated and applied in identical manner in micro-imaging applications. However, because of difference in their fundamental interaction, the information provided in imaging application is different and complimentary in nature.

APPENDIX 2: THEORY OF TOMOGRAPHY RECONSTRUCTION

Two basic theories for tomography reconstruction are explained here namely Radon transform theory and the Fourier slice theorem/filtered backprojection.

a) Radon transform

The Radon transform is projection transformation of a two-dimensional function onto polar coordinate space, which transforms lines through an image to points in the Radon domain. Analytically, the measured projection images can be described by a Radon Transform of the object function corresponding to one angular position. If the object is represented by the two dimensional scalar function f(x, y) which describe some physical property of object at position (x, y) then the radon transform is given by

$$p_\theta(t) = \iint_{-\infty}^{\infty} f(x,y)\delta(x\cos\theta + ysin\,\theta - t)dxdy \qquad (9.15)$$

Here we have used (x, y) co-ordinate space for object whereas (t, z) in polar co-ordinate system is used for camera system. $\theta$is the projection angle and δ is the Dirac delta function.$p_\theta(t)$ a function of $\theta$and t is known as Radon transform of f(x, y). Radon transform map every point (x, y) in object space onto a sinusoidal line in the (θ, t) space hence Radon transform is also called sinogram. The distribution of a quantity related to object physical properties such as object density, is then reconstructed from the projections of many different angles (or the sinogram). This is the inversion of the Radon transform or the back projection. The back projection operation simply propagates the measured sinogram back into the image space along the projection paths, where each point in the Radon domain is transformed back to a straight line in

the image. In the parallel beam geometry, the slices of the sample corresponding to different heights in the sample can be treated independently. To obtain a complete 3D distribution, one must reconstruct slices for every value of z. The simple back projection image is however, not exactly the same as the original image but is badly blurred. This is because the back projection operation is not a reversible process of the Radon transform. To be truly reversible this requires the inverse Radon transform associated an infinite number of projections and zero-width pixels.

b) Fourier slice theorem

The Fourier slice theorem relates the Fourier transform of the object distribution and its projections. The one-dimensional Fourier transform of a single projection corresponds to a single radial line through the centre of the frequency image. The two-dimensional Fourier transform of the function f(x, y) is given by

$$F(u,v) = \iint_{-\infty}^{\infty} f(x,y) e^{-i2\pi(ux+vy)} dxdy \qquad (9.16)$$

Similarly, the one dimensional Fourier transform of radon transform or projection data is given by

$$p_\theta(w) = \int_{-\infty}^{\infty} p_\theta(t) e^{-i2\pi wt}\, dt \qquad (9.17)$$

The Fourier slice theorem relates the projection $p_\theta(t)$and the function f(x, y) in Fourier space. The Fourier transform $p_\theta(w)$ for angle θ gives the values of *F*(u, v) along a line through the origin and rotated by angle $\theta$with respect to the horizontal axis i.e.

$$p_\theta(w) = F(w\cos\theta\,, w\sin\theta) \qquad (9.18)$$

c) Filtered back projection

Following the Fourier slice theorem, if enough projections are collected for various rotation angles, they will fill up the entire frequency space of the object. It should then be possible to reconstruct the object by simply performing a two-dimensional inverse Fourier transform. The filtered backprojection is based on this assumption and usually derived from the definition of inverse Fourier transform of F (u, v).

$$f(x,y) = \iint_{-\infty}^{\infty} F(u,v) e^{i2\pi(ux+vy)} du dv \qquad (9.19)$$

By introduction of polar co-ordinates representation of (u, v), substitution of t = x cosθ + y sin θ, use of the Fourier slice theorem and rearrangement of integration variables

$$f(x,y) = \int_{0}^{\pi} \int_{-\infty}^{\infty} |w| \, P_{\theta}(w) e^{i2\pi wt} dw d\theta \qquad (9.20)$$

Here, the outer integral describes the so-called backprojection. Inversion algorithms based on this equation are called filtered backprojection algorithms. Note that the backprojection operation requires the knowledge of the position of the rotation axis (t = 0) in the recorded projection data. The inner integral is referred to as the filtered projection. The term 'filtered' refers to the frequency filter $|w|$ called ramp filter, which is implemented to correct the blurring caused by high frequency losses during tomography data acquisition. Due to this insufficient sampling and bandwidth limitation majority of the blurring and other artefacts arise in the reconstruction. There are varieties of possibilities to choose this filter and derive reconstruction algorithms from Equation (9.20).The main difference between these filters lies in the way, in

which the filtering is implemented. A filter function $H(w)$ is generally introduced in the above equation as

$$f(x,y) = \int_0^{\pi} \int_{-\infty}^{\infty} H(w)\, P_\theta(w) e^{i2\pi wt} dw d\theta \text{ with } H(w) = B(w)|w| \qquad (9.21)$$

The factor $|w|$ in the filter is an essential part of the reconstruction, while the factor $B(w)$ is used to suppress noise at high frequencies at the cost of a decreased resolution. Filter functions are discussed by Huesman *et al.* [82].

APPENDIX 3: PARAMETERS OF IMAGE QUALITY

Applicability of X-ray or neutron micro-imaging techniques for the qualitative visualization of distributed phases and structures in the materials or for quantitative analysis of micro-structural properties such as porosity, anisotropy, orientation etc. depends on the quality of images produced which is usually measured in terms of resolution, contrast and signal to noise ratio [31,50,64]. The definitions of various parameters used for qualifying image quality are discussed here.

a) Resolution:

Spatial resolution refers to the ability of an imaging system to record fine detail and measured in terms of minimum spacing resolved also called Limiting Spatial Resolution (LSR). The reciprocal of it is called the Spatial Frequency, which is generally expressed in line pairs/mm (LP/mm) or cycles/mm. A more complete approach to assess spatial resolution is provided by Fourier methods in which different factors contributing to image spatial resolution are analysed mathematically by measuring response of imaging system to a sharp edge input. Due to unsharpness created by factors in the imaging system, image of the sharp edge becomes spread out over a broader area than its ideal. The effect is seen in the plot profile, which consists of spread (tail) extending around the edge. This type of profile is called the Line Spread Function (LSF). The same type of effect can be seen in 2 dimensions using a pin hole and is called the Point Spread Function (PSF).When the Fourier Transform of an LSF is calculated, then the imaging system's response to sine waves of all spatial frequencies is obtained. This response is called the Modulation Transfer Function (MTF). It can be

seen that the modulation falls off with increasing spatial frequency. The limiting spatial resolution is sometimes defined as the frequency where the modulation drops to 4%.

b) Contrast

Image contrast is the measure of visibility of object features relative to the local background in the image and may differ for different objects in the same X-ray/neutron image depending upon their densities, atomic numbers and thicknesses. Contrast across the boundary of the object is expressed mathematically in terms of maximum and minimum intensity/gray values by the following equation

$$Contrast = \frac{I_{max} - I_{min}}{I_{max} + I_{min}} \tag{9.22}$$

Sensitivity of an imaging system or technique to distinguish smallest object contrast is a measure of its merit and called contrast sensitivity. If the imaging system has high contrast sensitivity, objects with lower-contrast will also be visible. Contrast sensitivity of PCI is several orders of magnitude higher than absorption contrast as discussed before. Apart from improved sensitivity, it offers additional edge enhancement therefore improves object contrast for objects differing in their complex refractive index. The edge enhancement effects in PCI can be quantified in terms of edge enhancement index (EEI) which compares the degree of edge enhancement relative to the absolute change in optical density across the edge. EEI is given by

$$EEI = \frac{(P-T)/(P+T)}{(H-L)/(H+L)} \tag{9.23}$$

Where P and T are the peak and trough intensity values at the edge, and H and L represent the intensity values that would result at these locations if there were no edge

enhancement (determined by projecting a line derived from finite number of adjacent pixels) at the high and low intensity regions next to the edge [64].

c) Signal to noise ratio (S/N)

S/N characterises the quality of image by measuring strength of signal as compared to noise and defined as the ratio of the effective signal and the noise at each point of the image. It measures the capability of effectively distinguishing features in an image for qualitative and quantitative analysis. There are usually two origins of noise in image, first the experimental additive noise, which is of integral nature and proportional to the spatial area of detector and temporal interval of measurement whereas the second is counting noise, which has a statistical origin usually, modelled with Poisson statistics. Signal to noise ratio for an image is given by

$$SNR = \frac{Signal}{Noise} = \sqrt{tP_{0\,image}S_{pixel}}Contrast \qquad (9.24)$$

Where t is the integration time, S_{pixel} is the area of detector pixel, $P_{0\,image}$ is the photon flux of the spherical wave in the image plane in absence of object given by $P_{0\,image} = \frac{P_{\Sigma}}{\Omega R^2}$ where R is source to detector distance. Hence signal to noise ratio depends on integration time, incident beam flux, detector pixel size, source to detector distance, and image contrast [50,213].